A Comparison of Lorentz Trajectories with the Guiding Center Approximation for High Energy Particles

Une Comparaison des Trajectoires de Lorentz avec L'Approximation du Centre de Guidage pour les Particules de haute Énergie

A Thesis Submitted to the Division of Graduate Studies
of the Royal Military College of Canada
by

Mathew William Staikos, B.E.Sc

In Partial Fulfillment of the Requirements for the Degree of
Master of Science

April 2022

Acknowledgments

I would like to take this time to thank my thesis supervisor, Dr. Konstantin Kabin, for his guidance and financial support throughout the development of this thesis.

I would also like to thank the faculty leads of the International Space Mission (ISM) training program, Dr. Ron Vincent and Dr. L Sangalli, for fostering my academic endeavours.

Lastly, I would like to thank the Natural Sciences and Engineering Research Council of Canada (NSERC), specifically the Collaborative Research and Training Experience (CREATE) program, for the financial support that made pursuing my master's degree possible.

Abstract

The Guiding Center (GC) approximation is a widely used technique for reducing the computational power needed to model the motion of charged particles in magnetic fields. It is well known that the accuracy of the GC approximation increases as the energy of plasma particles becomes smaller. However, the accuracy of the GC approximation is hard to assess in any specific case. To quantify GC accuracy, we compare the GC approximation with full Lorentz trajectories by employing numerical integration to solve differential Equations of motion in various magnetic fields. Specifically, we consider particle motion in a magnetic field with a constant gradient, in the equatorial plane of a magnetic dipole, in the equatorial plane of a non-axisymmetric field, which is illustrative of the stretched magnetotail in the terrestrial magnetosphere, and in a 3-dimensional magnetic dipole. The particle motion has analytic solutions in some of these magnetic fields, which we describe and use in our analysis. For the first two fields we discuss in detail various methods for selecting the initialization point for the GC approximation based solely on the particle's initial position and velocity vectors. We established multiple options for GC initialization and discuss the effects of the starting point on the accuracy of computing the drift velocity. We also discuss the possibility to replicate the magnetic moment, drift velocity or gyroperiod exactly. Since conservation of the magnetic moment, or 1st adiabatic invariant, is an essential assumption used in the GC approximation we discuss in detail the accuracy of this conservation. For axisymmetric, and non-axisymmetric magnetic fields, the conservation of the canonical angular momentum and its consequences is also discussed. To analyze the effect asymmetry has on these conserved quantities we simulate a plasma particle crossing the magnetotail for which three different models are considered. As a means of assessing the accuracy of the GC approximation, we consider an ensemble of particles that differ only in their initial phase. Such particles are indistinguishable in GC theory as the GC approximation collapses all phases onto the same GC trajectory. Thus, by analyzing the phase effects, we illustrate the limitations of the GC approximation thoroughly. Through this process we were able to quantify the secular error the GC approximation incurs every drift period. We find that in some cases, if the magnetic field is a smooth function of the coordinates, the errors in the GC approximation are exponentially small in the velocity of the particle. In other cases, if the magnetic field is represented by a piece-wise linear function, these errors are proportional to some power of the particle velocity. Lastly, we tested the GC theory assumption that the equatorial pitch angle is a conserved quantity. While this error decreases with particle velocity as well, there are noticeable variations in the pitch angle for consecutive crossings of the equatorial plane, even for relatively small velocities. We quantify the deviation of the equatorial pitch angle for a bounce period as a function of the velocity. The results obtained in this thesis can be used to estimate the accuracy of the Guiding Center approximation in a variety of magnetic fields.

Résumé

L’approximation du centre guide (CG) est une technique très répandue pour réduire la puissance de calcul nécessaire à la modélisation du mouvement des particules dans des champs magnétiques. Le fait que l’exactitude de l’approximation du CG augmente quand l’énergie des particules du plasma devient plus petite est bien connu. Cependant, l’exactitude de l’approximation du CG est difficile à évaluer pour des cas spécifiques. De façon à quantifier l’exactitude du CG, nous comparons l’approximation du CG avec les trajectoires de Lorentz complètes en utilisant l’intégration numérique pour résoudre les équations différentielles du mouvement dans plusieurs types de champs magnétiques. Plus spécifiquement, nous considérons le mouvement des particules dans un champ magnétique avec un gradient constant, dans le plan équatorial d’un dipôle magnétique, dans le plan équatorial d’un champ non axisymétrique, ce qui est représentatif de l’étirement de la magnétoqueue, et pour un dipôle magnétique en trois dimensions. Les équations du mouvement des particules possèdent des solutions analytiques pour certain de ces champs que nous décrivons et utilisons dans notre analyse. Pour les deux premiers types de champs, nous examinons en détail plusieurs méthodes de sélection des points d’initialisation pour l’approximation du CG en nous basant uniquement sur la position et le vecteur vitesse initiaux de la particule. Nous avons établi plusieurs options cette initialisation et nous discutons les effets de ce point initial sur l’exactitude du calcul de la vitesse de dérive. Nous considérons aussi la possibilité de reproduire exactement le moment magnétique, la vitesse de dérive et la période de rotation. Puisque la conservation du moment magnétique, aussi appelé le premier invariant adiabatique, est une hypothèse essentielle utilisée pour l’approximation du CG, nous discutons en détail l’exactitude de sa conservation. Pour les champs magnétiques axisymétriques et non axisymétriques, la conversation du moment angulaire canonique et ses effets sont aussi discutés. Pour analyser l'effet de l'asymétrie sur ces quantités conservées, nous simulons une le mouvement d’une particule de plasma traversant la magnétoqueue pour laquelle trois modèles différents sont considérés. Afin d'évaluer l’exactitude de l'approximation CG, nous considérons un ensemble de particules qui ne diffèrent que par leur phase initiale. De telles particules sont indiscernables dans la théorie CG car l'approximation CG ramène toutes les phases sur la même trajectoire GC. Ainsi, en analysant les effets de phase, nous illustrons minutieusement les limites de l'approximation CG. Grâce à ce processus, nous avons pu quantifier l'erreur séculaire que l'approximation CG entraîne à chaque période de dérive. Nous constatons que dans certains cas, si le champ magnétique est une fonction lisse des coordonnées, les erreurs dans l'approximation CG sont exponentiellement petites pour la vitesse de la particule. Dans d'autres cas, si le champ magnétique est représenté par une fonction linéaire par morceaux, ces erreurs sont proportionnelles à une certaine puissance de la vitesse de la particule. Enfin, nous avons testé l'hypothèse de la théorie CG selon laquelle l'angle d’attaque équatorial est une quantité conservée. Bien que cette erreur diminue également avec la vitesse de la particule, il existe des variations notables de l'angle d’attaque pour des traversées consécutives du plan équatorial, même pour des vitesses relativement faibles. Nous quantifions la déviation de l'angle d’attaque équatorial pour une période de rebond en fonction de la vitesse. Les résultats obtenus dans cette thèse peuvent être utilisés pour estimer l’exactitude de l'approximation du centre guide dans une variété de champs magnétiques.

Contents

Acknowledgments i
Abstract ii
Résumé iii
List of Figures vi
Nomenclature x
1. Introduction 1
1.1 Research Motivation 1
1.2 Scope and Objectives 1
1.3. Thesis Outline 3
2. Theory 5
2.1 Lorentz Force 5
2.2 Motion in Uniform Magnetic Field 6
2.3 Guiding Center (GC) Approximation 8
2.4 Canonical Momentum 11
2.5 First Adiabatic Invariant, Magnetic Moment 12
2.6 Other Adiabatic Invariants 14
2.7 Matlab 14
2.8 Elliptic Integrals 16
3. Particle Motion in a Magnetic Field with a Constant Gradient 17
3.1 Analysis of the Magnetic Field with Constant Gradient 17
3.2 GC Approximation for the Magnetic Field with Constant Gradient 19
3.3 Detailed Examination of Particle Trajectory 19
3.4 Analysis of the Magnetic Moment 27
3.5 Guiding Center Starting Location 32
3.6 Conclusion 34
4. Particle Motion in Equatorial Plane of a Magnetic Dipole 36
4.1 Analysis of the Axisymmetric Magnetic Field 36
4.2 GC Approximation for the Radial Magnetic Field Gradient 40
4.3 Code Accuracy 40
4.4 Detailed Examination of Particle Trajectory 41
4.5 Analysis of the Magnetic Moment 48
4.6 Alternative Guiding Center Starting Location 53
4.7 Conclusion 55

5. Particle Motion in the Equatorial Plane of a Non-Axisymmetric Magnetic Field. Magnetic Dipole and Magnetotail 57
5.1 Description of Non-Axisymmetric Magnetic Field 57
5.2 Brief Examination of Particle Trajectory 64
5.3 Phase Distribution 70
5.4 Diffusion of the Canonical Angular Momentum and Magnetic Moment. 74
5.5 Diffusion of Particle Trajectory Boundaries 80
5.6 Conclusion 83
6. Particle Motion in Three Dimensions in a Magnetic Dipole 86
6.1 Analysis of Three-Dimensional Magnetic Field 86
6.2 Analytical Properties of 3D Trajectories 88
6.3 GC Approximation for the 3D Magnetic Dipole 89
6.4 Particle Trajectory and Code Accuracy 91
6.5 Phase Distribution Problem 93
6.6 Analysis of Variations in Velocity 94
6.7 Analysis of Variations in Pitch Angle 105
6.8 Analysis of Variations in Azimuthal Angle 110
6.9 Conclusion 116
7. Summary 118
8. References 122
9. Appendix: Matlab Code 125

List of Figures

Figure 1.1: Near-Earth space environment highlighting the location of various plasmas [2]. 2
Figure 1.2: Compression and stretching of Earth's magnetic field lines [1]. 4
Figure 2.1: Gyration of charged particles in a uniform magnetic field. 7
Figure 2.2: Helical trajectory of an ion in a uniform magnetic field. 8
Figure 2.3: Gyration of charged particles in a non-uniform magnetic field. 10
Figure 2.4: Relative error in P_y (left) and v (right). 15
Figure 3.1: Trajectory of an ion in a magnetic field with a constant gradient. 19
Figure 3.2: Trajectory of an ion for one gyroperiod. 20
Figure 3.3: 1st, 2nd, 3rd and final iterations of the gyrocenter with corresponding points for one gyroperiod. 23
Figure 3.4: 1st, 2nd, 3rd and final iterations of the gyrocenter using our threshold velocity for one gyroperiod 24
Figure 3.5: GC integration using the trajectory, 1st gyrocenter and converged gyrocenter as starting locations for one gyroperiod. 25
Figure 3.6: Tracing Error as a function of velocity for v = 0.01 to v = 30. 26
Figure 3.7: Tracing Error for GC integration initiated between x_{min} and x_{max} for v = 0.1 (blue) and v = 1 (red). 27
Figure 3.8: Zeroth-order magnetic moment approximation using B at the particle trajectory, 1st gyrocenter and converged gyrocenter, normalized by the exact expression at v = 25 (top) and v = 2.5 (bottom). 29
Figure 3.9: Various magnetic moment approximations and the exact expression for one gyroperiod normalized by the exact expression. 30
Figure 3.10: Magnetic moment approximation error as a function of velocity from v = 0.01 to v = 30. 31
Figure 3.11: Normalized x position along the trajectory where μ, T_g and v_D equal their respective exact expression as a function of velocity from v = 0.01 to v = 30. 33
Figure 3.12: GC initialization options overlayed onto the trajectory, 1st gyroradius and converged gyrocenter for one gyroperiod. 34
Figure 4.1: Magnetic dipole field lines in the Earth's meridional plane. 37
Figure 4.2: A typical trajectory of a particle in the equatorial field of a magnetic dipole. 39
Figure 4.3: Trajectory of ion in the equatorial plane of a magnetic dipole. 41
Figure 4.4: Trajectory of an ion for one gyroperiod. 42
Figure 4.5: 1st, 2nd, 3rd and final iteration of gyrocenter and corresponding points for one gyroperiod. 43
Figure 4.6: 1st, 2nd, 3rd and final iteration of gyrocenter for v = 3.5 for one gyroperiod. 44
Figure 4.7: GC integration using trajectory, 1st gyrocenter and converged gyrocenter as starting locations for one gyroperiod. 46
Figure 4.8: Tracing error for v = 0.01 to v = 3.02. 47
Figure 4.9: Tracing error of GC drift between r_{min} and r_{max} of the particle trajectory for v = 0.1 (blue) and v = 0.2 (red). 48
Figure 4.10: Normalized magnetic moment (2.18) at the trajectory, 1st gyrocenter and converged gyrocenter at v = 3 (top) and v = 0.3 (bottom). 50
Figure 4.11: Various magnetic moment approximations and the exact expression for one gyroperiod. 51
Figure 4.12: Error in approximate magnetic moments vs exact expression for v = 0.01 to v = 3.02 for one gyroperiod. 52

Figure 4.13: Normalized r distance along the trajectory where μ, T_g and T_d equal their respective exact expression for v = 0.01 to v = 3.48. 54
Figure 4.14: GC initialization options overlayed onto trajectory, 1st gyroradius and converged gyrocenter for one gyroperiod. 55
Figure 5.1: $f(\varphi)$ factor as a function of φ. 59
Figure 5.2: Contour plot of the magnetic field strength of B_z (T) in the equatorial plane for small ∇φ. 60
Figure 5.3: Variations of B_z as a function of r for multiple values of φ. 61
Figure 5.4: Contour plot of the magnetic field strength of B_z (T) in an equatorial plane large ∇φ. 62
Figure 5.5: Derivative of $f(\varphi)$ for cases small ∇φ is in blue and large ∇φ is in red. 63
Figure 5.6: Contour plot of the magnetic field strength of B_z (T) in an equatorial plane for piecewise linear. 64
Figure 5.7: Trajectory of a particle in the equatorial plane of a non-axisymmetric field for one drift period. 65
Figure 5.8: Particle transition from bound to unbound trajectory due to weaker magnetic field in the tail. 66
Figure 5.9: Normalized canonical angular momentum over one drift period. 67
Figure 5.10: Magnetic moments over one drift period. 67
Figure 5.11: Trajectory in a magnetic field using large ∇φ for full T_d (left) and half T_d piece-wise (right). 69
Figure 5.12: Comparison of exact drift period in dipole vs drift period of numerical integrator using small ∇φ. 69
Figure 5.13: Initialization of various particles phase-shifted to have the same starting line. 71
Figure 5.14: Discontinuity example of 10 phases $\delta = 0$ to $\pi/8$, at start and end of drift period. .. 72
Figure 5.15: Endpoints of the trajectory for a 1000 particle with different phases in axisymmetric dipole with v = 6 R_E/s (left) and in non-axisymmetric field with v = 3.5 R_E/s (right). 72
Figure 5.16: Endpoints of trajectory for 1000 phases in non-axisymmetric field with v = 6 R_E/s. 73
Figure 5.17: Final phase dependence on the initial phase in a non-axisymmetric field (left) and in an axisymmetric dipole (right). The particle is initiated with $m_0 = 1.673 \cdot 10^{-27}$ kg, $q = 1.602 \cdot 10^{-19}$ C, r_0 = [7, 0] R_E and v_0 = [0, 3.5] R_E/s. The magnetic field is out of the page with $M = 3.1 \cdot 10^{-5}$ TR_E^3. 73
Figure 5.18: Normalized canonical angular momentum difference for one drift period for v = 2.5 R_E/s through 6.5 R_E/s. 75
Figure 5.19: Normalized canonical angular momentum difference for one drift period over 500 Phases. 76
Figure 5.20: Normalized magnetic moment difference for one drift period for v = 2.5 R_E/s through 6.5 R_E/s. 76
Figure 5.21: Normalized difference in canonical angular momentum (top) and magnetic moment (bottom) for one drift period in a pure dipole with v = 6 R_E/s. 77
Figure 5.22: Average and amplitude of $\Delta P_\varphi / P_0$ for all three magnetic fields. 78
Figure 5.23: Average and amplitude of $\Delta \mu_{Exact} / \mu_0$ for all three magnetic fields. 80
Figure 5.24: Normalized difference in r_{min} and r_{max} after one drift period across all phases for v = 6.5, 6 and 5.5 R_E/s. 81
Figure 5.25: Average normalized difference in r_{min} and r_{max} after one drift period from v = 1 to 6.5 R_E/s. 82
Figure 5.26: Log plot of Fourier series coefficient a_1 as a function of velocity. 83
Figure 6.1: Eight 3D magnetic field lines crossing the equatorial plane at r = 10 R_E. 87

Figure 6.2: Illustration of ion trajectory and bounds for a half bounce period in ρ-z coordinates. 89
Figure 6.3: Example trajectory in 3D for half a bounce period. 92
Figure 6.4: Magnetic moment for half a bounce period. 93
Figure 6.5: Illustration of the phase distribution problem. 94
Figure 6.6: $\Delta\alpha_{eq}$ for 1000 velocities from v = 0.01 to 10 R_E/s. Integrated for half a bounce period. 95
Figure 6.7: $\Delta\mu/\mu_0$ for 1000 velocities from v = 0.01 to 10 R_E/s. Integrated for half a bounce period The particle is initiated with $M = 3.1\cdot10^{-5}\,TR_E^3$, $m_0 = 1.673\cdot10^{-27}$ kg, $q = 1.602\cdot10^{-19}$ C, r_0 = [7, 0, 0] R_E and $v_0 = v[\sin(\alpha_{eq})\cos(\xi), \sin(\alpha_{eq})\sin(\xi), \cos(\alpha_{eq})]$ R_E/s. $\alpha_0 = \pi/4$ and $\xi = \pi/2$. $\Delta\mu/\mu_0$ is in blue, minimum and maximum lines of best fit are black dashed lines and the average line of best fit is the black line. 96
Figure 6.8: α_{eq} at every equatorial crossing for v = 1 R_E/s. Integration time = 1300s. 97
Figure 6.9: α_{eq} at every equatorial crossing for v = 1 R_E/s (top row), 3 R_E/s (middle row) and 7 R_E/s (bottom row). Integration time = 1300s/v (left column) and 2600/v (right column). 98
Figure 6.10: Maximum oscillation range of α_{eq} for 1000 velocities between v = 0.01 to 10 R_E/s. Integration time = 332s/v. 99
Figure 6.11: ρ-z plot for v = 9.52 R_E/s. Integration time = 154.03s. 101
Figure 6.12: ρ-z plot for v = 4.34 R_E/s (left) and v = 9 R_E/s (right). Integration time = 1300s/v. 102
Figure 6.13: Calculation of λ_m using GC approximation for velocities from v = 0.01 to 10 R_E/s. Integrated for half a bounce period. 102
Figure 6.14: Calculation of T_b using GC approximation for velocities from v = 0.01 to 10 R_E/s. Integrated for half a bounce period. 103
Figure 6.15: Calculation of T_d using GC approximation for velocities from v = 0.01 to 10 R_E/s. The particle is initiated with $M = 3.1\cdot10^{-5}\,TR_E^3$, $m_0 = 1.673\cdot10^{-27}$ kg, $q = 1.602\cdot10^{-19}$ C, r_0 = [7, 0, 0] R_E and $v_0 = v[\sin(\alpha_{eq})\cos(\xi), \sin(\alpha_{eq})\sin(\xi), \cos(\alpha_{eq})]$ R_E/s. $\alpha_0 = \pi/4$ and $\xi = \pi/2$. The numerical solution is in blue, GC theory is in red and our modification to GC theory is in green. 104
Figure 6.16: $\Delta\alpha_{eq}$ for 1000 pitch angles from α_0 = 0 to 89°. Integrated for half a bounce period. 105
Figure 6.17: $\Delta\mu/\mu_0$ for 1000 pitch angles from α_0 = 0 to 89°. Integrated for half a bounce period. 106
Figure 6.18: Maximum oscillation range of α_{eq} for 1000 pitch angles from α_0 = 0 to 89°. Integration time = 66.4s. 107
Figure 6.19: Calculation of λ_m using GC approximation for 1000 pitch angles from α_0 = 0 to 89°. The particle is initiated with $M = 3.1\cdot10^{-5}\,TR_E^3$, $m_0 = 1.673\cdot10^{-27}$ kg, $q = 1.602\cdot10^{-19}$ C, r_0 = [7, 0, 0] R_E and $v_0 = v[\sin(\alpha_{eq})\cos(\xi), \sin(\alpha_{eq})\sin(\xi), \cos(\alpha_{eq})]$ R_E/s. v = 5 R_E/s and $\xi = \pi/2$. The numerical solution is in blue, GC theory is in red and our modification to GC theory is in green. 108
Figure 6.20: Calculation of T_b using GC approximation for 1000 pitch angles from α_0 = 0 to 89°. The particle is initiated with $M = 3.1\cdot10^{-5}\,TR_E^3$, $m_0 = 1.673\cdot10^{-27}$ kg, $q = 1.602\cdot10^{-19}$ C, r_0 = [7, 0, 0] R_E and $v_0 = v[\sin(\alpha_{eq})\cos(\xi), \sin(\alpha_{eq})\sin(\xi), \cos(\alpha_{eq})]$ R_E/s. v = 5 R_E/s and $\xi = \pi/2$. The numerical solution is in blue, GC theory is in red and our modification to GC theory is in green. 109
Figure 6.21: Calculation of T_d using GC approximation for 1000 pitch angles from α_0 = 0 to 89°. Integrated for half a bounce period. 110
Figure 6.22: $\Delta\alpha_{eq}$ for 1000 azimuthal angles from $\xi = 0$ to 2π. Integrated for half a bounce period. 111
Figure 6.23: $\Delta\alpha_{eq}$ for 1000 azimuthal angles from ξ = 0 to 2π for v = 0.15 R_E/s (left), 1.5 R_E/s (right). Integrated for half a bounce period. 112
Figure 6.24: $\Delta\mu/\mu_0$ as for 1000 azimuthal angles from ξ = 0 to 2π. Integrated for half a bounce period. 112

Figure 6.25: Calculation of λ_m using GC approximation for 1000 azimuthal angles from ξ = 0 to 2π. Integrated for half a bounce period. 113
Figure 6.26: Calculation of T_b using GC approximation for 1000 azimuthal angles from ξ = 0 to 2π. Integrated for half a bounce period. 114
Figure 6.27: Calculation of T_d using GC approximation for 1000 pitch angles from α_0 = 0 to 89°. Integrated for half a bounce period. 115

Nomenclature

a_0	zeroth-order Fourier coefficient
a_1	first-order Fourier coefficient
a_2	second-order Fourier coefficient
a_3	third-order Fourier coefficient
a_x	acceleration in x-direction
a_y	acceleration in y-direction
A	vector potential
α	pitch angle
α_{eq}	equatorial pitch angle
α_{lc}	loss cone angle
B	magnetic field strength at a specific location
B_0	constant magnetic field strength
B_m	magnetic field strength at a magnetic mirror
B_E	magnetic field strength of Earth at the equatorial surface
β	variable magnetic field strength
c	speed of light
γ	relativistic factor
d	derivative
δ	phase angle
Δ_s	neutral line crossing parameter
E	electric field
ε	rate of magnetic field change
$f(\varphi)$	magnetotail on/off function
$f_1(\varphi)$	first component of $f(\varphi)$
F	force
gc	gyrocenter
GC	Guding Center
I	adiabatic invariant
J	longitudinal invariant (second adiabatic invariant)
k	elliptic modulus
K	elliptic integral of the first kind
κ	curvature of magnetic field line
L	Lagrangian
L_s	shell/Mcllwainian parameter
λ	latitude angle measured from the origin of the equatorial plane
λ_m	latitude angle corresponding to a magnetic mirror
m	relativistic mass
m_0	rest mass
M	magnetic field strength of an external field
M_E	magnetic dipole moment of Earth
μ	magnetic moment (first adiabatic invariant)
μ_0	magnetic moment in a uniform magnetic field
μ_0	magnetic permeability in a non-uniform magnetic field
μ_1	first-order approximation of magnetic moment
μ_2	second-order approximation of magnetic moment

μ_{T2}	Taylor expansion of magnetic moment up to second-order term
μ_{Exact}	exact expression for the magnetic moment
n	normal to magnetic field line that lies in the r-z plane
η	elliptic characteristic
o	is ultimately smaller than
O	is of the same order as
ω_g	gyrofrequency
Θ	colatitude angle measured from the positive z-axis
Ω_b	bounce frequency
Ω_d	drift frequency
P	canonical (generalized) momentum
P_y	canonical momentum in the y-direction
P_φ	canonical angular momentum in the φ direction
φ	azimuthal angle measured counter clockwise from the positive x-axis
Φ_d	drift invariant (3^{rd} adiabatic invariant)
Φ	scalar potential
Π	elliptic integral of the third kind
q	charge
r	radius
r_0	initial position/radius
r*	radial position where v is directed in radial direction
r_{eq}	equatorial radius
r_g	gyroradius/Larmor radius
r_{gc}	gyrocenter
r_{max}	maximum trajectory bounds in the radial direction
r_{min}	minimum trajectory bounds in the radial direction
r_{Td}	radial position where $T_d = T_{d\_Exact}$
r_{Tg}	radial position where $T_g = T_{g\_Exact}$
r_μ	radial position where $\mu_0 = \mu_{Exact}$
Rad	radians
R_E	radius of Earth at the equator (6378km)
ρ	radius of x and y components in 3D
s	arc length
s_m	arc length between mirror points
sgn	sign of
t	time
T	period
T_b	bounce period
T_d	drift period
T_{d_Exact}	exact expression for drift period
T_g	gyroperiod
T_{g_Exact}	exact expression for gyroperiod
τ	tangential to the magnetic field line that lies in the r-z plane
v($\dot{r}$)	velocity
v_0	initial velocity
v*	velocity of circular motion at r_*
$v_\parallel$	velocity parallel to magnetic field lines
$v_\perp$	velocity perpendicular to magnetic field lines

v_n	velocity normal to magnetic field line that lies in r-z plane
$v_x(x')$	velocity in x-direction
$v_y(y')$	velocity in y-direction
v_z	velocity in z-direction
v_C	curvature drift velocity
v_D	drift velocity
v_{D_Exact}	exact expression for drift velocity
v_G	gradient drift velocity
v_φ	velocity in the φ direction
W	kinetic energy
x	position in x-direction
x_0	initial position in the x-direction
x_{max}	maximum trajectory bounds in x
x_{min}	minimum trajectory bounds in x
x_{Tg}	x position where $T_g = T_{g\_Exact}$
x_{VD}	x position where $v_D = v_{D\_Exact}$
x_μ	x position where $\mu_0 = \mu_{Exact}$
ξ	angle between r and v vectors measured counterclockwise
Ξ	elliptic integral of the second kind
y_0	initial position in the y-direction
y	position in y-direction
z_0	initial position in z-direction
z	position in z-direction

1. Introduction

1.1 Research Motivation

My desire to research this thesis topic stems from my two strongest educational interests. The first is my passion for space. Growing up my childhood love for science fiction instilled in me a sense of exploration and an aspiration to improve myself. This conviction is what motivated me to understand the world around me on both a microscopic and macroscopic scale, as represented by the study of the atom and space in my degree pursuits of chemical engineering and space physics. My secondary passion is nuclear fusion, which is derived from my interests in the atom. It is the overlap of these two interests which led me to choose a thesis that involved both plasma physics and magnetic fields. This is because current techniques for achieving sustained nuclear fusion involve the use of magnetic fields to confine plasmas, while the significance of plasmas and magnetic fields in our universe is prevalent. If one-day nuclear fusion becomes viable as a means of spacecraft propulsion then it would be my dream to work in that field. In the meantime, I hope I can help accelerate this reality or at the very least learn enough to understand it. Lastly, my desire to explore boundaries while pushing my own is one of the reasons I chose to pursue a master's degree in a difficult subject like physics. It was a test to simply prove to myself that I can do it.

1.2 Scope and Objectives

Around 99% of the matter in the known universe is made out of plasma, the fourth state of matter [1]. Due to this vast amount of matter, there are various types of plasmas found in the universe. These include, but are not limited to, artificial plasmas such as lasers and ion thrusters, terrestrial plasmas such as lightning and fire, and space plasmas such as the ionosphere, plasmasphere, the Van Allen belts, the ring current, the plasma sheet the magnetosheath and the sun. In general, most plasmas in the universe originate from the sun in the form of solar wind, coronal mass ejection, cosmic rays and solar radiation which ionizes the atmosphere of planets. An illustration of some of the plasmas surrounding Earth is given in Figure 1.1.

A plasma is an ionized gas and thus it is uniquely susceptible to the effects of an externally applied electromagnetic force. This ionized nature makes plasma particles charge carriers. Due to this charge it is known that at rest a plasma particle generates a local electric field, while in motion it generates a local magnetic field at right angles to the electric field and velocity [3]. Due to the various types of plasma, there are four main subcategories used for studying the motion of plasmas in electromagnetic fields. These are single-particle motion, magnetohydrodynamics, multifluid theory and kinetic theory. In single-particle motion we neglect the collective behaviour and assume an environment without collision. This is often used in low-density plasmas. On the other extreme, we have magnetohydrodynamics which is good for understanding collective behaviour and averages values such as density and velocity. It is suitable for highly conductive plasma with low wave frequency. Multi-fluid theory is similar to magnetohydrodynamics but takes into account the effects of different particles within the plasma. This is suitable for high-frequency wave propagation as the differences in components of the plasma cause the high-frequency waves. Lastly, we have the kinetic theory which relies on a statistical approach, rather than solving the Equations of motion. It requires certain simplifying assumptions and thus there are different 'flavours' of kinetic theory [1].

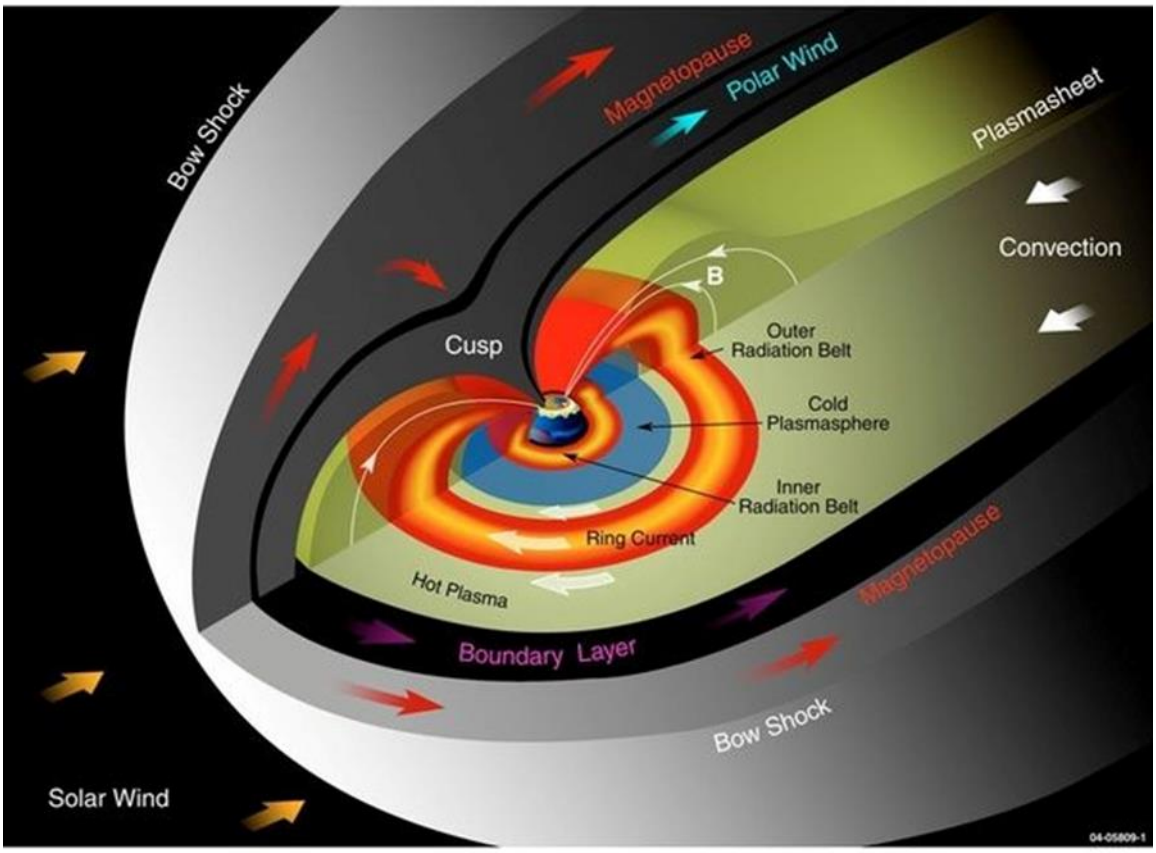

Figure 1.1: Near-Earth space environment highlighting the location of various plasmas [2].

In this thesis, we focus on studying the high-energy Van Allen belt plasmas which are confined by Earth's magnetosphere, the locations of which were illustrated in Figure 1.1. To study these plasma particles, it is common to view them from the perspective of single-particle motion, thus, an environment without collision is assumed. In addition, the single-particle theory is only valid for modelling plasmas where diamagnetism is assumed to be negligible [3]. This occurs when the electromagnetic field produced by the motion of the charged particle is small relative to the applied field guiding its motion [3]. Van Allen belt particles meet this condition as their local electromagnetic fields are small relative to Earth. Overall a basic review of single-particle motion is needed to understand the motion of Van Allen belt particles in Earth's magnetic field. In three dimensions the motion of a plasma particle moves in three distinct ways. In order of decreasing frequency the first distinct motion is the gyration around magnetic field lines. The second is the bouncing between mirror points along magnetic field lines. The third is the drift around the Earth as a result of the magnetic field gradient and curvature. All of these motions are explained in more detail throughout the thesis. What is important to know is the higher frequency gyrations make modelling these plasma particles computationally resource intensive. A common approach to avoid this is using the guiding center (GC) approximation to eliminate the gyrating motion. This is done by assuming the particle lies on a GC within the gyrating path of the particle. However, the validity of this approximation is inversely proportional to the energy of the plasma particle. This is why we are particularly interested in the high-energy Van Allen belt particles.

In this thesis our main objective is to study and improve upon the applicability of the guiding center (GC) approximation for modelling high energy particles. We do this by analyzing various GC initialization options, the underlying assumptions of GC theory and by quantifying errors associated with the GC approximation, in relation to the actual motion of the plasma particle. This provides those that wish to implement the GC approximation, under any particular study, to do so with a predictable scale of deviation from the actual motion of the plasma particle.

1.3. Thesis Outline

In this thesis we solve differential equations of motion numerically to model the trajectories of plasma particles and their GC approximation. This is done to evaluate the accuracy of the GC approximation at high energies and to quantify secular errors that accumulate as a result of the underlying assumption of GC theory. Before our analysis, we present the basics of plasma physics theory to establish the fundamental knowledge needed for understanding this thesis. In the overview of the theory, we discuss the motion of plasma particles in magnetic fields, how the GC theory allows for the approximations of said motion, the conserved quantities upon which the GC approximation is based and the numerical integrator used to generate our models. Additionally, we briefly touch on elliptic integrals as they are expressed in a short-handed form in various analytical solutions within this thesis.

We start with the two-dimensional motion of a plasma particle in a magnetic field with a constant gradient. This is done because any two-dimensional magnetic field can be locally approximated by a field with a constant gradient. Here we evaluate various locations to initialize the GC approximation based solely on the initial position and velocity vectors. The results are then measured against the actual trajectory of the particle to establish the accuracy of the GC approximation, particularly at higher velocities.

In the second section we analyze the motion of a plasma particle confined to the equatorial plane of a magnetic dipole. This is done to simulate a more Earth-like environment since at distances less than four Earth radii, R_E = 6,378km, the terrestrial magnetic field lines are often approximated as a magnetic dipole [4]. This is visualized in Figure 1.2 below.

Our choice to confine the particle to the equatorial plane is due to the desire to employ analytical equations that exist for equatorial mirroring particles. Again, we follow the same process as the first section and evaluate various locations to initialize the GC approximation. The section is applicable for modelling high-energy plasma particles trapped in the inner Van Allen belts shown in Figure 1.1.

In the third section we evaluate the motion of a plasma particle confined to the equatorial plane of a non-axisymmetric magnetic field. This is done to simulate the outer sections of Earth's magnetic field since the terrestrial magnetic field lines start to compress on the dayside and stretch on the nightside at distances greater than four R_E as a result of solar wind pressure. This effect is also visualized in Figure 1.2. To introduce this asymmetry we add a magnetotail component to our dipole magnetic field. This is done using three different magnetotails for thoroughness, as space weather causes the shape of the magnetotail to be dynamic [4]. Additionally, we relied on magnetic field symmetry on the dayside to apply conserved quantities used in previous Sections. Thus we analyze the effects asymmetry has on these conservated quantities by modelling a particle for one drift period. Allowing it to transverse a dipole field on the dayside and a non-axisymmetric

magnetotail on the nightside. Quantifying these effects allows us to demonstrate the deviation of the GC approximation from the real trajectory when applied in non-axisymmetric conditions. Specifically, this section is applicable for modelling high-energy plasma particles trapped in the outer Van Allen belts shown in Figure 1.1.

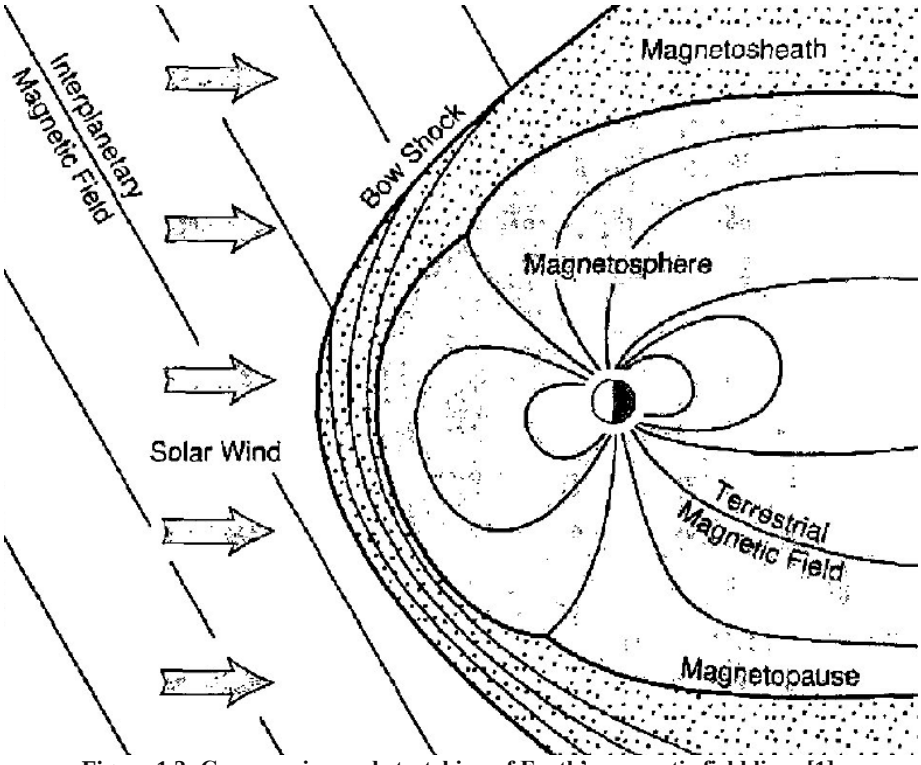

Figure 1.2: Compression and stretching of Earth's magnetic field lines [1].

In the fourth section we evaluate the motion of a plasma particle in three dimensions of a magnetic dipole. This is done to simulate a more Earth-like environment as it is rare for particles to be confined to the equatorial plane. Like the previous section it also allows us to evaluate the deviation of the GC approximation from the real trajectory. This is based on the GC theory assumption that the equatorial pitch angle is a conserved quantity. In this section we show that the actual motion of a plasma particle results in a changing equatorial pitch angle. We thus quantify this error to improve upon GC Equations. Though this section uses a magnetic dipole, which is more applicable in modelling the inner Van Allen belt high energy particles, we explore aspects of outer Van Allen belt particles as well. One example is the exploration of the upper limit of energies found in both Van Allen belts. For the inner Van Allen belt, this is 100 keV and 100 MeV for electrons and protons respectively, while the outer Van Allen belt contains mostly electrons at a maximum energy of 10 MeV [2].

2. Theory

2.1 Lorentz Force

We begin with a brief review of Lagrangian mechanics. To understand the motion of an object as it moves through space, with respect to time, a relationship between position, velocity and acceleration is needed. This is normally done in classical mechanics with Newton's Equations of motion, but these Equations are dependent on the coordinate system. In contrast, the Euler-Lagrange equation takes the same form in any system, regardless of the coordinates chosen. The Euler-Lagrange equation is more common in classical and analytical mechanics because of this and is given by Equation (2.1) [5]. Here *r* represents the position of the object, in our case the plasma particle, and the time derivative, velocity, is denoted with the standard dot above. In all equations, the bolded terms represent vectors to distinguish from scalar variables.

$$\frac{\mathrm{d}}{\mathrm{dt}}\left(\frac{\partial \mathrm{L}}{\partial \dot{\mathbf{r}}}\right) = \frac{\partial \mathrm{L}}{\partial \mathbf{r}} \tag{2.1}$$

In this equation, *L* represents the Lagrangian which is given by Equation (2.2) for our electrodynamic case [5]. In electrodynamics, the potential energy contains both the vector potential $\boldsymbol{A}(r, t)$ and scalar potential $\Phi(r, t)$ associated with the magnetic and electric fields respectively. In addition, *m* is mass and *q* is the charge of the plasma particle.

$$\mathrm{L} = \frac{\mathrm{m}\dot{\mathbf{r}}^2}{2} + \mathrm{q}(\dot{\mathbf{r}} \cdot \mathbf{A} - \Phi) \tag{2.2}$$

From Maxwell's Equations, we know the expressions for the magnetic field strength (*B*) and electric field strength (*E*) are given in terms of their respective potentials as demonstrated in Equations (2.3)and (2.4) respectively.

$$\mathbf{B} = \nabla \times \mathbf{A} \tag{2.3}$$

$$\mathbf{E} = -\nabla\Phi - \frac{\partial \mathbf{A}}{\partial \mathrm{t}} \tag{2.4}$$

Applying the Lagrange to the Euler-Lagrange Equation yields the electromagnetic Equation of motion known as the Lorentz force. This force governs the motion of a charged particle moving in an electromagnetic field and is given by Equation (2.5) below [1].

$$\mathbf{F} = \frac{\mathrm{d}(\mathrm{m}\mathbf{v})}{\mathrm{dt}} = \mathrm{q}(\mathbf{E} + [\mathbf{v} \times \mathbf{B}]) \tag{2.5}$$

In this Equation, $\boldsymbol{v}$ is the velocity of the particle. In this thesis, only the effects of *B* are examined, and therefore $\boldsymbol{E}$ is set to 0 for all cases analyzed. This means that $\Phi = 0$ and $\boldsymbol{A}$ is independent of time. Under this condition, the magnitude of the velocity vector and the kinetic energy of the particle remains constant, as a magnetic field can not do work on a particle. This is proven by dot-multiplying Equation (2.5) by velocity and integrating it once [1]. Since v is constant than it should be noted that *m* in Equation (2.5) can be taken outside the derivative.

Due to the absence of $\boldsymbol{E}$ Equation (2.5) is valid to use for both relativistic and non-relativistic plasma particles so long as the relativistic definition is used for the mass. This is needed because the mass of relativistic particles deviates from the rest mass (m_0) of a particle at sufficiently high velocities. Since $\boldsymbol{E} = 0$ throughout this thesis, the relativistic factor (γ) is also constant for any particular v.The relativistic mass is given by Equation (2.6), where and c is the speed of light [6].

$$m = \gamma m_0 = \frac{m_0}{\sqrt{1 - \frac{v^2}{c^2}}} \tag{2.6}$$

2.2 Motion in Uniform Magnetic Field

The direction the Lorentz force acts on a charged particle is at right angles to both the velocity and the magnetic field vectors. In the simplest case, a magnetic field with a constant strength causes a charged particle to gyrate in a circular motion when the velocity is directed perpendicular to the magnetic field lines. This gyrating motion is periodic and thus the time it takes for a charged particle to complete one gyration is known as the gyroperiod. The reciprocal of this is known as the gyrofrequency and it is displayed along with the gyroperiod below in Equations (2.7) and (2.8) respectively [3].

$$\omega_g = \frac{|q|B}{m} \tag{2.7}$$

$$T_g = \frac{2\pi}{\omega_g} \tag{2.8}$$

In addition, the distance between the particle at any point along its trajectory and the center of its rotation is known as the Larmor radius or gyroradius. The analytical solution for this radial distance is given by Equation (2.9), where $v_\perp$ is the perpendicular velocity relative to $\boldsymbol{B}$ [3].

$$r_g = \frac{mv_\perp}{|q|B} \tag{2.9}$$

This gyrating motion is illustrated for both a proton and an electron in Figure 2.1, where the rest mass used is $1.673 \cdot 10^{-27}$ kg and $9.109 \cdot 10^{-31}$ kg respectively. In addition, the magnitude of the charge used is $1.602 \cdot 10^{-19}$ C. In Figure 2.1 the dependence of the Lorentz force on both the mass and the charge of the particle is displayed. Where the sign of the charge affects the direction of rotation. While the mass is inversely proportional to the acceleration caused by the Lorentz force. Based on Equation (2.9) this would result in a gyroradius difference too large between an electron and a proton to be visualized since the rest mass of a proton is roughly 1850 times that of an electron. To counteract this the electron was initialized with 10 times the energy, with the proton and electron being assigned energies of 1 MeV and 10 MeV respectively. At these energies, the proton is non-relativistic while the electron is relativistic. The velocity associated with this kinetic energy is directed in the XY plane. The magnetic field strength was given a value of 0.1 T and was directed in the positive z-direction. Compared to the magnetic fields in space a 0.1 T magnitude is much stronger and is used here only for illustration purposes. Under these conditions, the

corresponding T_g and r_g for the proton are $6.57 \cdot 10^{-7}$s and 1.45 m respectively. For the electron, T_g and r_g are $7.34 \cdot 10^{-9}$s and 0.35 m respectively.

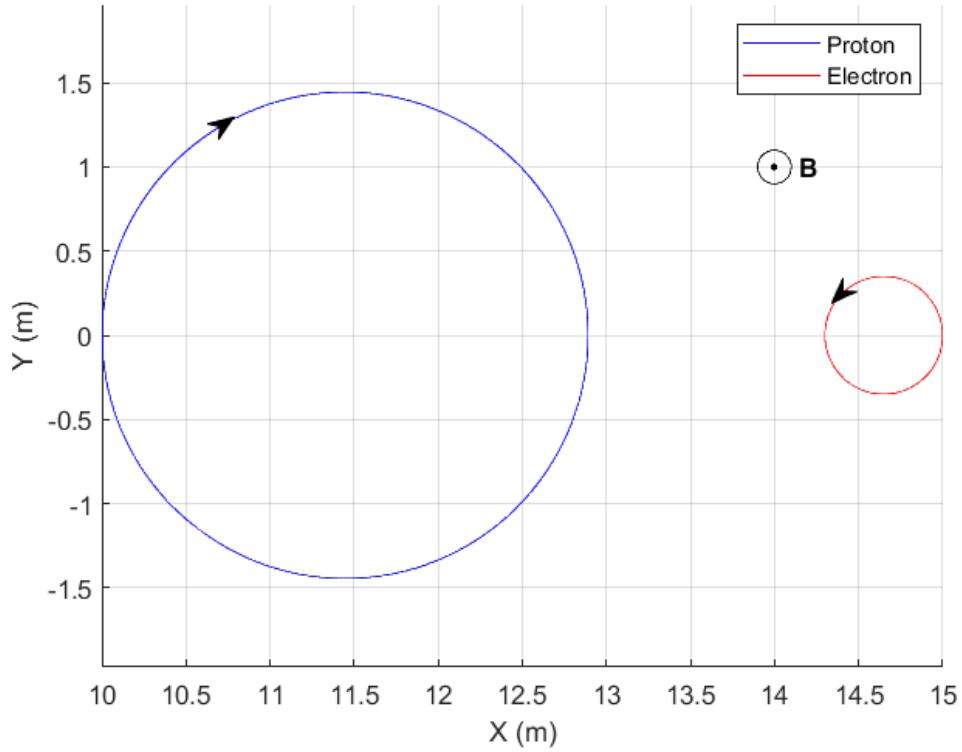

Figure 2.1: Gyration of charged particles in a uniform magnetic field. The ion is initiated with $m_0 = 1.673 \cdot 10^{-27}$ kg, $q = 1.602 \cdot 10^{-19}$ C $r_0 = [10, 0]$ m, $v_0 = [0 , 1.3828 \cdot 10^7]$ m/s. The election is initiated with $m_0 = 1.673 \cdot 10^{-27}$ kg, $q = -1.602 \cdot 10^{-19}$ C, $r_0 = [15, 0]$ m, $v_0 = [0, 2.9964 \cdot 10^8]$ m/s. The magnetic field is out of the page with $B_z = 0.1$ T. The gyration of the ion is shown in blue and the electron in red.

In the event the plasma particle velocity has components in both the perpendicular and parallel directions, with respect to the magnetic field lines, then the motion of the plasma particle is helical. This is visualized in Figure 2.2 by using the proton with the same conditions as Figure 2.1 and distributing 10% of the total velocity to the parallel velocity ($v_\parallel$). The arrow represents a single magnetic field line passing through the gyrocenter of the particle.

Lastly, the angle made between the velocity vector and the magnetic field vector is known as the pitch angle (α) and is defined by Equation (2.10) [1]. The pitch angle is an important quantity and is extensively used in Chapter 6.

$$\alpha = \cos^{-1}\left(\frac{\mathbf{v} \cdot \mathbf{B}}{|\mathrm{v}||\mathrm{B}|}\right) = \tan^{-1}\left(\frac{\mathrm{v}_\perp}{\mathrm{v}_\parallel}\right) \tag{2.10}$$

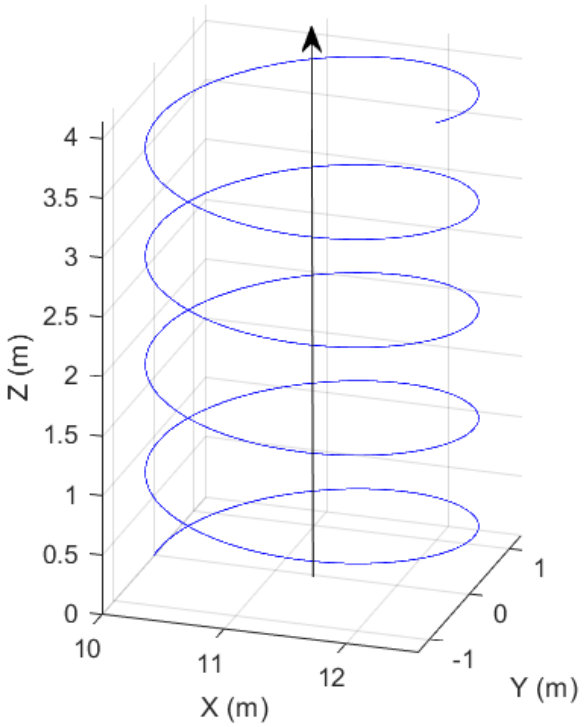

Figure 2.2: Helical trajectory of an ion in a uniform magnetic field. The ion is initiated with $m_0 = 1.673 \cdot 10^{-27}$ kg, $q = 1.602 \cdot 10^{-19}$ C $r_0 = [10, 0]$ m, $v_0 = [0, \ 1.2445 \cdot 10^7, 1.383 \cdot 10^6]$ m/s. The magnetic field is out of the page with B_z = 0.1 T. The trajectory of the ion is shown in blue and a magnetic field line in black.

2.3 Guiding Center (GC) Approximation

In this section, we introduce the basics of the GC approximation. Using Equation (2.5) it is possible to model the exact particle motion to complete specification. However, in many cases of practical importance, its direct numerical solution is too time-consuming. For example, the gyroperiods calculated in Figure 2.1 were $6.57 \cdot 10^{-7}$s and $7.34 \cdot 10^{-9}$s for the proton and electron respectively. This requires a lot of computational power because numerical time steps need to be significantly smaller than the gyroperiod. The GC approximation allows for a significant reduction in this computational time by averaging over the gyroperiod. In this approach, the particle is effectively collapsed into the gyrocenter. This is the most common way of tracing particle motion in Earth's magnetosphere. For example, the energetic plasma particles trapped in the Van Allen belts. Overall a thorough assessment of the GC accuracy is the main goal of this thesis.

In Figure 2.2 the arrow representing the magnetic field line also doubles as a visualization of the moving center of the rotation for the plasma particle. In plasma physics this is commonly referred to as the gyrocenter. The gyrocenter is a vectorized form of the gyroradius Equation and is given by Equation (2.11) below [7].

$$\mathbf{r}_{gc} = \mathbf{r} + \frac{m}{qB^2}[\mathbf{v} \times \mathbf{B}] \tag{2.11}$$

For the case of a uniform magnetic field, the gyrocenter of a particle is a straight line coinciding with the magnetic field line passing through the center of the helix of the particle trajectory. Knowing this, it becomes possible to replace the helical motion of the charged particles with a simple line that acts to approximate the real trajectory. This serves as an example of what is being attempted by the GC approximation. If the magnetic field is nonuniform the position of the instantaneous gyrocenter throughout the particle motion follows a more complicated trajectory. However, in many cases, the motion of a particle is represented as a fast gyration around the relatively slow-moving center of gyration. This is the essence of the GC approximation. In the simplest form of the GC approximation, it is common to average over the gyrations and assume that the particle is collapsed into the GC. In practice, this means only the GC trajectory is examined. One disadvantage of this is the loss of gyration differences across phases since the GC converges at the same point for all phase variations [6].

Overall, the GC approximation is applicable when the gyrations about the GC are relatively much faster than the drift of the GC. In addition, to apply the GC in a time-dependent magnetic field the field variation over the gyroradius should be small. Therefore, the validity of the approximation decreases as the velocity, or energy, of the particle increases [6]. To determine the independent Equations of motion for the GC, the particle motion must be examined under all non-uniform magnetic field circumstances. Commonly these Equations of motion are known as drifts. In a non-uniform magnetic field, the magnetic field strength is a function of the position of the particle. Under this condition, when the velocity is initialized perpendicular to the magnetic field, like in Figure 2.1, the gyrating motion of the charged particle becomes cycloidal due to the change in the magnetic field strength changing the magnitude of the Lorentz force. Applying a magnetic field with a constant gradient that increases as a function of x allows for a visualization of this cycloidal motion in Figure 2.3. Here the conditions are the same as in Figure 2.1, except now B_z = (0.1 + 0.01x) T and the energy of both particles are increased by a factor of four for ease of visualization. The gyrocenter in black is governed by Equation (2.11). The magnetic field here is just used as an illustration, this type of field is discussed in detail in Chapter 3 of this thesis.

In Figure 2.3 the addition of the black line shows that the gyrocenter moves roughly along the center of a charged particle trajectory, though not exactly, as was the case with a uniform magnetic field. Therefore, in a non-uniform field, the variation of the gyrocenter illustrates the increased difficulty in applying the GC approximation, as there is no longer a single x position in which the gyrocenter remains. In general, the variations of the gyrocenter are a result of magnetic field inhomogeneity, measured in any direction. This magnetic field gradient causes the charged particle's gyroradius to decrease in areas of stronger magnetic field strength, and increase in areas of weaker magnetic field strength. This is demonstrated by the formation of cusps along the gyrocenter. Overall this gradient causes a net drift perpendicular to both the magnetic field vector and the associated magnetic gradient. This net drift is what is being approximated by the GC gradient drift equation. In Figure 2.3 this corresponds to a net drift in the y-direction, as the gradient is in the x-direction and the magnetic field is in the z-direction. The opposite direction in drift is a result of the drift equation being a function of the charge as displayed in Equation (2.12) [8]. Here ∇B is the gradient for the magnitude of the magnetic field.

$$\mathbf{v}_G = \frac{m v_\perp^2}{2qB^3}[\mathbf{B} \times \nabla B] \tag{2.12}$$

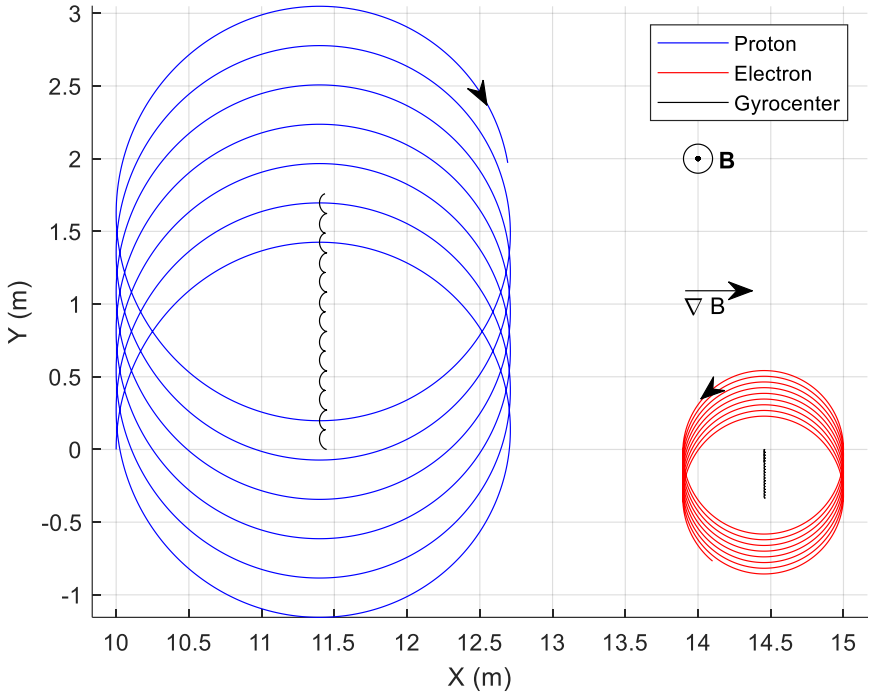

Figure 2.3: Gyration of charged particles in a non-uniform magnetic field. The ion is initiated with m_0 = $1.673 \cdot 10^{-27}$ kg, q = $1.602 \cdot 10^{-19}$ C r_0 = [10, 0] m, v_0 = [0 , $2.7590 \cdot 10^{7}$] m/s. The election is initiated with m_0=$1.673 \cdot 10^{-27}$ kg, q = $-1.602 \cdot 10^{-19}$ C, r_0 = [15, 0] m, v_0 = [0, $2.9998 \cdot 10^{8}$] m/s. The magnetic field is out of the page with B_z = (0.1 + 0.01x) T. The trajectory of the ion is shown in blue, the electron in red and their gyrocenters in black.

The gradient drift is proportional to the kinetic energy of the particle in the perpendicular direction, which is due to the particle experiencing more inhomogeneity by travelling farther along the gradient. Additionally, charged particles drifting in opposite directions cause a current to form.

When the magnetic field is perpendicular to a certain plane the gradient drift becomes the only drift experienced by the particles moving in this plane. A common example of this is the magnetic equatorial plane of a dipole field. Particles confined to the equatorial plane of a dipole field are discussed in Chapters 4 and 5.

The next GC Equation of motion becomes applicable when the charged particle moves along the magnetic field lines and the field lines are not straight. This is the drift due to the curvature of the magnetic field lines. Similar to gradient drift, the curvature drift also contributes to the ring current and drift velocity, which is why it is often combined into one Equation. Unlike the gradient drift, the curvature drift is derived from the parallel kinetic energy component of the particle. Due to this motion along the curved line a centripetal force is experienced [1]. The resultant drift is shown below in Equation (2.13) [8].

$$\mathbf{v}_C = \frac{m v_{\parallel}^2}{qB^3}[\mathbf{B} \times \nabla B] \tag{2.13}$$

Overall, the curvature drift is proportional to the kinetic energy of the particle in the parallel direction. It is directed at right angles to the radius of curvature and the magnetic field lines. Additionally, magnetic field curvature also contributes to current formation. Current formation as a result of magnetic curvature and gradients is how the ring current of Earth is formed, this was illustrated in Figure 1.1 [1]. In the event the magnetic field is cylindrically symmetric it becomes possible to combine the gradient and curvature drift equations into one governing equation of motion. This is done because, under this condition, the direction of both drifts is the same. The resultant total magnetic drift Equation is given by Equation (2.14).

$$\mathbf{v_D} = \frac{m\left(v_{\parallel}^2 + \frac{1}{2}v_{\perp}^2\right)}{qB^3}[\mathbf{B} \times \nabla B] \tag{2.14}$$

Other common guiding center drifts, include but are not limited to, the *E* x *B* drift, the polarization drift and the gravity drift. The *E* x *B* represents the direction of drift when an electric and magnetic field contributes to the Lorentz force. While *E* accelerates a particle along the electric field vector, *B* rotates the particle, as previously displayed in 2 and Figure 2.2. Once turned the electric field acts to decelerate the particle. This drift is not charge or mass dependent. The polarization drift is applicable when there are slow time variations in the electric field. The direction of this drift is along the same vector line as the electric field and depends on the charge. Usually, an oscillating electric field causes the polarization drift to oscillate with a 90^o phase shift. This drift is also proportionate to mass and therefore the polarization current is mainly carried by the ions. Lastly, gravity drift acts in the direction perpendicular to both the gravity vector and the magnetic field. It is charge dependent and proportionate to the mass. Like the polarization drift, the difference in mass means the gravitational effects on electrons are ignored [1]. Overall the *E* x *B* and polarization drifts are not discussed in this thesis because we restrict our study to the $E = 0$ condition. The gravity drift is ignored due to it being typically much weaker than the other Equation of motion [1]. The only exception to this is near strong gravitational fields, such as the surface of a sun, however, conditions such as this are not examined in this thesis.

2.4 Canonical Momentum

An important quantity defined in Lagrangian mechanics is the generalized canonical momentum (*P*). This generalized momentum, canonically conjugate to *r*, is given by Equations (2.15) and (2.16) [9].

$$\frac{dP}{dt} = \frac{\partial L}{\partial r} \tag{2.15}$$

$$P = \frac{\partial L}{\partial \dot{r}} = mv + qA \tag{2.16}$$

In the case that the Lagrangian does not depend on the coordinate *r*, which in our case means that A does not depend on *r*, then the corresponding Lagrange Equation becomes $dP/dt = 0$

and *P* is always a conserved quantity. If the magnetic field possesses some form of symmetry, such as axial symmetry, then there are conserved components of the canonical momentum. Magnetic fields discussed in Chapters 3, 4, 5 and 6 all have some form of symmetry, and conservation of the corresponding components of *P* are important in the discussions of these Chapters. If the Lagrangian does depend on *r* then the canonical momentum conjugate to this coordinate is not conserved.

For two-dimensional problems the conservation of *P* allows, at least in principle, to reduce the integration of the equations of motion to quadratures. In three dimensions, however, there are never enough known conservation laws to integrate the equations of motion completely. Nevertheless, even in three dimensions, the conservation of *P* allows us to show that the motion of a particle is restricted to certain areas. Finally, it is used for assessment of the accuracy of the numerical method used to integrate the equations of motion in Chapters 3, 4, 5 and 6.

2.5 First Adiabatic Invariant, Magnetic Moment

In addition to the canonical momentum, another relevant quantity defined in classical mechanics is the adiabatic invariant. An adiabatic invariant is a quantity that varies very slowly relative to the changing system. It is known that the motion of a charged particle in an external magnetic field is periodic and that for every periodic motion, there is an associated adiabatic invariant (*I*) [9]. The general form, for all of the adiabatic invariants, is given by Equation (2.17) [5]. It should be noted that this equation can also be written as a definite integral when the conservation of canonical angular momentum is conserved under the assumption magnetic fields are axisymmetric straight lines [10].

$$I = \oint P \, dr \tag{2.17}$$

The first adiabatic invariant is associated with the periodic motion of a particle gyrating around a magnetic field, as in Figure 2.1. This quantity is known as the magnetic moment of the particle when the field is uniform. It is often interpreted as the product of the current loop about the magnetic field and the area encompassed by this loop. It is given by Equation (2.18) [1]. For a non-uniform field Equation (2.18) represents the permeability of a vacuum μ and has a value of $4\pi \cdot 10^{-7}$ N/A^2 [1]. The magnetic moment, in this case, is more complicated and is discussed later in this sub-section.

$$\mu_0 = m\frac{v_\perp{}^2}{B} \tag{2.18}$$

It should be noted here that the normalization for the magnetic moment varies in literature, in Equation (2.18) we define normalization as the constant value terms in front of $v_\perp{}^2/B$. A normalization of *m* was chosen in this paper for both simplicity and unit consistency. The importance of the conservation of the magnetic moment is that it is the basis of the GC approximation, since the collapse of all phases onto the GC is only allowed if μ_0 is conserved [11]. We are thus constrained to systems that conserve the magnetic moment to apply the GC approximation. Therefore, it should be noted that one condition where the magnetic moment becomes invalid is when the time variation of the magnetic field becomes comparable to the

gyrofrequency [3]. Overall, the GC approximation is widely used in plasma physics which is examining the conservation of μ_0 is important.

For any non-uniform magnetic fields, Equation (2.18) only represents the first term in an infinite Talyor series expansion. In addition, an exact expression for the adiabatic invariant can be calculated analytically, but only exist for a few specific magnetic fields [9]. While the Taylor series expansion applies more generally. The Taylor series of the magnetic moment needs to be examined in this paper since the validity of the GC approximation depends on the magnetic moment. For high energies, this requires more accurate forms of the magnetic moment. For general magnetic fields, the Taylor series expansion has been solved up to the second-order term. The generalized form, with our normalization factor *m*, is given by Equations (2.19), (2.20) and (2.21). This Equation only remains valid for static magnetic fields with axial symmetry [12].

$$\mu = \mu_0 + \frac{m}{q}\mu_1 + \left(\frac{m}{q}\right)^2 \mu_2 \tag{2.19}$$

$$\mu_1 = \frac{m}{B^2}\left(\left(\frac{2\sin\theta}{r} + \frac{1}{B}\frac{\partial B}{\partial \tau}\right) v_\perp v_\parallel v_\varphi - 2\left(\frac{\partial_\theta}{\partial \tau}\right) v_\parallel{}^2 v_\varphi - \frac{1}{B}\left(\frac{\partial B}{\partial n}\right)\left(v_\perp{}^2 + v_\varphi{}^2\right) v_\varphi\right) \tag{2.20}$$

$$\mu_2 = \frac{m}{B^3}\left(a_1 v_\parallel{}^4 + a_2 v_\parallel{}^3 v_n + a_3 v_\parallel{}^2 v_n{}^2 + a_4 v_\parallel{}^2 v_\varphi{}^2 + a_5 v_\parallel v_n{}^3 + a_6 v_\parallel v_n v_\varphi{}^2 + a_7 v_n{}^4 + a_8 v_n{}^2 v_\varphi{}^2 + a_9 v_\varphi{}^4\right) \tag{2.21}$$

Here expressions for the first-order and second-order Taylor series expansions are expressed in cylindrical coordinates *r*, φ, *z*. Additionally, τ and *n* represent the tangential and normal directions relative to the magnetic field line that lies in the r-z plane, making an angle θ with the *z*-axis. In relation to this magnetic field we define $v_\perp{}^2 = v_n{}^2 + v_\varphi{}^2$. The *a* coefficients for the second-order expansions are found in Gardner [12].

For a uniform magnetic field Equation (2.19) simplifies to Equation (2.18) and represents the exact solution of the magnetic moment. However, if the magnetic field is non-uniform, then μ_0 oscillates at the gyrofrequency around an exact solution. Exact analytical expressions for the first adiabatic invariant were developed for the magnetic field with a constant gradient and the equatorial plane of the magnetic dipole [11]. They are discussed further in Chapters 3 and 4.

One of the main benefits of all adiabatic invariants of motion is that they are approximately conserved in most non-static magnetic fields. The main condition for this is that the time variations of the system are relatively slow. If we make *B* functions of time then it is true that as *t* approaches $-\infty$ or ∞ then $I(t = -\infty) \approx I(t = \infty)$. Here *I* is used simply as an example for any adiabatic invariant. Assuming these time variations are smooth, or all-time derivatives of $B(t)$ and $E(t)$ are continuous, then the adiabatic invariant is conserved exponentially well for any n-th derivative. If ε represents how fast the magnetic field changes, with ε being proportional to the maximum of the time derivative, we can write $\Delta I = I(t = \infty) - I(t = -\infty) = o(\varepsilon^n)$. In the event of a discontinuity at the n-th derivative then the difference between $I(t = -\infty)$ and $I(t = \infty)$ becomes algebraic $\Delta I = O(\varepsilon^n)$ [11]. The notation used here is standard for describing the rate at which a function changes as its argument grows or shrinks. Where *O* means 'is of the same order as' and o means 'is ultimately

smaller than' [13]. If the normalized difference of the magnetic moment, $\Delta\mu/\mu_i$, is graphed against a range of ε it is shown that for a continuous function $\Delta\mu/\mu_i$ is proportional to the generic exponential form $e^{(\#/\varepsilon)}$. In contrast, the same process applied to a discontinuous piece-wise linear function follows the power-law form $\varepsilon^{\#}$ [11].

2.6 Other Adiabatic Invariants

The first adiabatic invariant is associated with the periodic gyration of a particle around a magnetic field line already discussed. In many magnetic fields there are two additional periodic motions a particle exhibits. These are the bouncing between mirror points and the drift around the Earth, the motions of which are illustrated later when they become relevant. In addition to the first adiabatic invariant associated with the gyration of the particle, it is possible to define two more adiabatic invariants associated with the bounce motion and the drift motion. These are known as the second and third adiabatic invariants respectively. Although we do not use these expressions in this thesis, they are included here for completeness. The second and third adiabatic invariants are usually defined as Equations (2.22) and (2.23) and are alternatively called the longitudinal (J) and drift Φ_d invariants respectively. Here < > denotes the average, s_m the magnetic field line length between mirror points and B_E the magnetic field strength of Earth at the equatorial surface [1].

$$J = 2ms_m\langle v_{\parallel}\rangle \tag{2.22}$$

$$\Phi_d = \frac{2\pi m}{q^2}B_E\mu_0 \tag{2.23}$$

It should be noted, that these expressions are not exact. Similar to Equation (2.18) they are just the first terms of asymptotic expansions for these quantities. First and second-order corrections for the second and third adiabatic invariants are calculated in Siambis *et al* [14], Northrop *et al* [15] and Northrop *et al* [16].

2.7 Matlab

Matlab is one of the most popular and common software packages for numerical engineering and scientific calculations. It is used in this thesis to analyze the motion of plasma particles in various magnetic fields. Matlab is used to solve the ordinary differential equations of motion numerically in various externally prescribed magnetic fields. The main tool used for this purpose is Matlab's ode45 subroutine. Ode45 solves non-stiff ordinary differential Equations with medium accuracy. Matlab does have other ordinary differential equation solvers for various accuracy requirements and stiff conditions, however, ode45 is always used first since it applies to most situations. For this thesis ode45 is sufficient.

The numerical solutions implemented by ode45 use algorithms from the Runge-Kutta family [17]. Specifically, it uses embedded methods of the 4^{th} and 5^{th} order of Cash–Karp type. The difference between the 4^{th} and 5^{th} order solutions is used to adjust the time steps as needed to maintain the desired accuracy of the integrator, ensuring the outputted data is smooth. The accuracy settings in ode45 are controlled by setting the value of two parameters, the relative tolerance and the absolute tolerance of the integration. The relative tolerance is usually an adequate threshold for stopping the integrator when a solution has met the desired accuracy. However, if the solution is

around 0 then absolute tolerance is needed. In this thesis, the relative and absolute tolerances are set to 10^{-10} and 10^{-14}. For reference, a tolerance of 10^{-3} in Matlab corresponds to a 0.1% accuracy [17]. To test the accuracy of this code we can use conserved quantities to estimate the numerical error of our Matlab simulation. This is demonstrated in Figure 2.4 below which shows the absolute numerical error in two conserved quantities. For this example, the magnetic field with a constant gradient in the *x*-direction from Figure 2.3 is used. For this field the conserved quantities are the velocity and the *y*-component of canonical momentum P_y. Here it is shown that the code has a relative numerical error between the order of 10^{-11} and 10^{-13}, which is more than sufficient for most purposes.

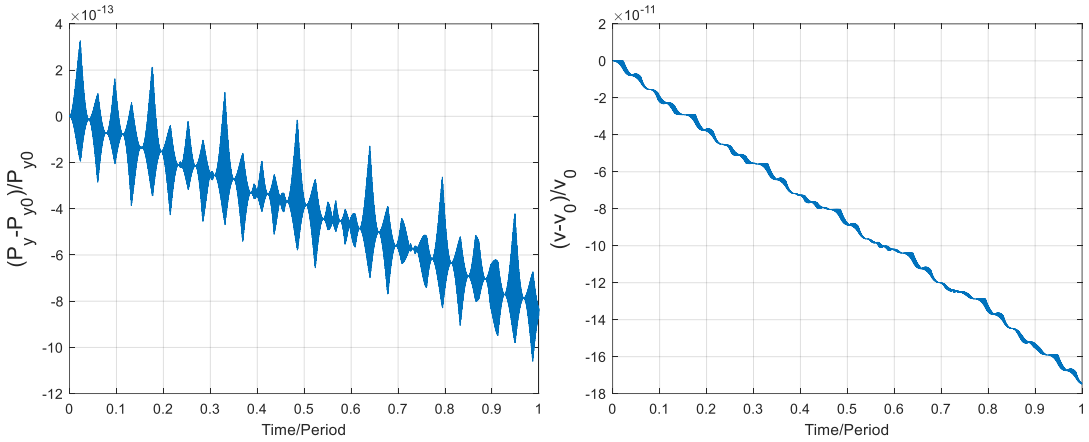

Figure 2.4: Relative error in P_y (left) and v (right). Same conditions as Figure 2.1 for ion.

For most ode45 integration in this thesis, the runtime was in the order of seconds and minutes. However, for slow velocity particles that drifted around the Earth, the runtime increased to the order of hours. Most of these were run overnight due to this time limitation. The computer used to run these simulations was equipped with an AMD Ryzen 7 5700U processor and a 16 GB Radeon Graphics (1.80 GHz) RAM. This is a high-end commercially available laptop at the time of writing.

Ode45 is used in two different modes. First, for some calculations, the numerical integration of ode45 is carried out for a specified time. Alternatively, ode45 allows for the ability to terminate the integration when a certain condition is reached, such as a single gyroperiod or a single drift period around the Earth. This is controlled using Matlab's 'events' functionality. Ode45 is used to integrate either Lorentz Equations of motion or GC Equations. In the case of the Lorentz equation of motion, both the initial position and velocities are needed. Ode45 then takes these initial conditions and applies them in a separate function that calculates the *x*, *y* and *z* components of the Lorentz acceleration. With the initial velocity, the solver uses the initial acceleration outputs to generate new position and velocity vectors. This process continues until the time limit or events condition is reached. Thus generating an array of position and velocity vectors that will be analyzed and visualized. For the GC Equations the process is the same, but only the initial position is needed as GC Equations are in terms of velocity. Matlab also has a built-in function for evaluating elliptic integrals, which are used in this thesis to evaluate the exact expression of the adiabatic invariant. This function takes the form [K, Ξ] = ellipke(k). Where the argument k ranges from 0 to 1, while K and Ξ represent the complete elliptic integrals for the first and second kind respectively.

2.8 Elliptic Integrals

Elliptic integrals are used to calculate the arclength of an ellipse similar to how inverse trigonometric functions are used to calculate the arclength of a circle [18]. Elliptic integrals provide solutions to a wide set of problems. Using standard notation, we define the elliptic integral of the first kind in Equation (2.24), here k is the elliptic modulus and the specific formulations of k are introduced when needed in later chapters.

$$K(k) = \int_0^1 \frac{dt}{\sqrt{(1 - t^2)(1 - k^2t^2)}} \tag{2.24}$$

In addition to the completed elliptic integral of the first kind there are two other complete elliptic integrals. The complete elliptic integral of the second kind is given by Equation (2.25) [18].

$$\Xi(k) = \int_0^1 \frac{\sqrt{1 - k^2t^2}dt}{\sqrt{1 - t^2}} \tag{2.25}$$

The complete elliptic integral of the third kind is given by Equation (2.26), here η is the elliptic characteristic [18].

$$\Pi(\eta, k) = \int_0^1 \frac{dt}{(1 - \eta t^2)\sqrt{(1 - t^2)(1 - k^2t^2)}} \tag{2.26}$$

3. Particle Motion in a Magnetic Field with a Constant Gradient

3.1 Analysis of the Magnetic Field with Constant Gradient

As an example, we analyze the motion of a particle in a magnetic field with a constant gradient. Although this magnetic field is very simple it is often used to illustrate the general properties of particle motion. Furthermore, any two-dimensional magnetic field can be locally approximated by a field with a constant gradient. The expression for the magnetic field used in this section is given by Equation (3.1), where the coordinate system chosen is cartesian (*x*, *y*, *z*). Properties of a charged particle moving in this magnetic field has been studied by Kabin [11], Brizard [19] and Seymour [20].

$$\mathbf{B} = (B_0 + \beta x)\,\hat{\mathbf{e}}_\mathbf{z} \tag{3.1}$$

For this magnetic field we use generic units. B_0 and β represent the constant and variable magnetic field strength respectively and are both set to a value of 1 for simplicity. The motion of a plasma particle in this field is constricted to the XY plane if the initial velocity of the particle is in the XY plane [11]. Therefore, it should be noted that velocity is always perpendicular to the magnetic field in this case. Applying the definition of a magnetic field given by Equation (2.3) it becomes possible to determine the magnetic vector potential presented below by Equation (3.2).

$$\mathbf{A} = \left(B_0 x + \beta \frac{x^2}{2}\right)\hat{\mathbf{e}}_\mathbf{y} \tag{3.2}$$

The vector potential is used to determine the canonical momentum established in Equation (2.16). However, since *A* depends on the *x* coordinate, but not the *y* coordinate, only the *y*-component of the canonical momentum is conserved. Substituting Equation (3.2) into Equation (2.16) gives the following expression for P_y.

$$P_y = mv_y + q\left(B_0 x + \beta \frac{x^2}{2}\right) \tag{3.3}$$

In Equation (3.1) the magnetic field has a value of 0 when $x = -B_0/\beta$, for our field this corresponds to a value of $x = -1$. This location is known as the neutral line or magnetic field reversal line and it serves as an important distinction between two types of trajectories. The first are particles that do not cross this neutral line and the second are ones that do cross it. In this section, we only consider the motion of particles that do not cross the neutral line as the GC approximation does not work for neutral line crossing particles. In addition, particles that do not cross the neutral line are more typical in space physics [11]. The equation used to determine if a particle crosses the neutral line is given by Equation (3.4), where Δ_s represents the separatrix [11].

$$\Delta_s = B_0{}^2 + 2\frac{\beta}{q}P_y - 2\left|\frac{\beta}{q}\right| mv \tag{3.4}$$

Using the conservation of momentum, it is shown that if $\Delta_s > 0$ then the trajectory of a particle does not cross the neutral line, and if $\Delta_s < 0$ then it does. Separating these two types of trajectories is the neutral line where the $\Delta_s = 0$. Neutral line crossing only occurs if the velocity is large relative to the initial *x*-position. The further from the neutral line, the larger *v* must be to cross it. This is because a higher *v* causes the gyroradius to increase, widening the trajectory until the point of crossing. Examining the non-crossing neutral line particles exclusively shows that these particles drift in a strip parallel to the *y*-axis due to the gradient drift cross-product given in Equation (2.12). The edges of this strip are determined from the conservation of the canonical momentum and the fact that $v_x = 0$ at the edge of the strip. At the edge the velocity is directed in the *y*-direction, thus indicating the x_{min} and x_{max} positions relative to the neutral line. These bounds of motion are given by Equations (3.5) and (3.6), where sgn represents taking only the positive or negative sign from the expression within its brackets.

$$x_{min} = \frac{2\left(P_y - \mathrm{sgn}(qB)mv\right)}{qB_0 + \mathrm{sgn}(B_0 + \beta x_0)q\sqrt{\Delta_s}} \tag{3.5}$$

$$x_{max} = \frac{2\left(P_y + \mathrm{sgn}(qB)mv\right)}{qB_0 + \mathrm{sgn}(B_0 + \beta x_0)q\sqrt{\Delta_s + 4\left|\frac{\beta}{q}\right| mv}} \tag{3.6}$$

Equation (3.6) further shows that particles not crossing the neutral line are always bound to some strip. In this field, no particle can approach $x = \infty$. This is implied by the fact the square root term cannot be negative for our case. This is the intuitive conclusion as well since the magnetic field equation is not bound by any *y*-location limits.

For magnetic field (3.1), it is possible to determine the exact expressions for both the gyroperiod and the drift velocity. Due to this, it is also possible to express the general solution for the equations of motion in terms of Jacobi elliptic functions. The period and the drift velocity are therefore expressed in terms of complete elliptic integrals [20]. These expressions are given by Equations (3.7) and (3.9).

$$T_{g\_Exact} = \left(x_{max} + \frac{B_0}{\beta}\right)\frac{k^2}{v}K(k) \tag{3.7}$$

$$k = 4\frac{mv_\perp}{|q|B_{max}x_{max}} \tag{3.8}$$

$$v_{D\_Exact} = \frac{\Delta y}{T_{g\_Exact}} = \mathrm{sgn}(qB)v\left(\frac{2}{k^2}\left[1 - \frac{\Xi(k)}{K(k)}\right] - 1\right) \tag{3.9}$$

3.2 GC Approximation for the Magnetic Field with Constant Gradient

For the magnetic field defined in Equation (3.1), $\nabla B = [\beta, 0, 0]$, substituting this into Equation (2.12) we arrive at the following expression for the GC drift.

$$\mathbf{v_D} = \frac{m v_\perp^2}{2q(B_0 + \beta x)^2} \beta \, \hat{\mathbf{e}}_y \tag{3.10}$$

For small velocities, Equation (3.10) is recovered by expanding Equation (3.9) into a Taylor Series. Similarly, the gyroperiod given by Equation (2.7) is reached by expanding Equation (3.7) for small velocities. It is important to note, that these expressions depend on the value x. For example, at x_{min} the guiding center drift velocity is at a maximum and at x_{max} the guiding center drift velocity is at a minimum. Therefore, it is important to use the correct initial x-position to initialize the GC to ensure that the GC does not overshoot or fall short of replicating the true trajectory of the particle. Finding the ideal x-position to initialize the GC is one of the main goals of this study. This is done exclusively using the initial particle position and velocity vectors.

3.3 Detailed Examination of Particle Trajectory

As an illustration, we initialize a particle with a position of $r_0 = [10, 0]$ and a velocity of $v_0 = [0, -25]$, and a $m_0 = 1$. The trajectory is shown in Figure 3.1 for multiple gyrations using $q = 1$ to represent an ion, the electron is not shown as the analysis is very similar. The main difference is the drift in the opposite direction, which was already illustrated in Figure 2.3. From this point forward only the ion is further analyzed, though the results of this chapter are still applicable to the electron. It should be noted that all trajectories for this case are initialized with the velocity in the negative y-direction.

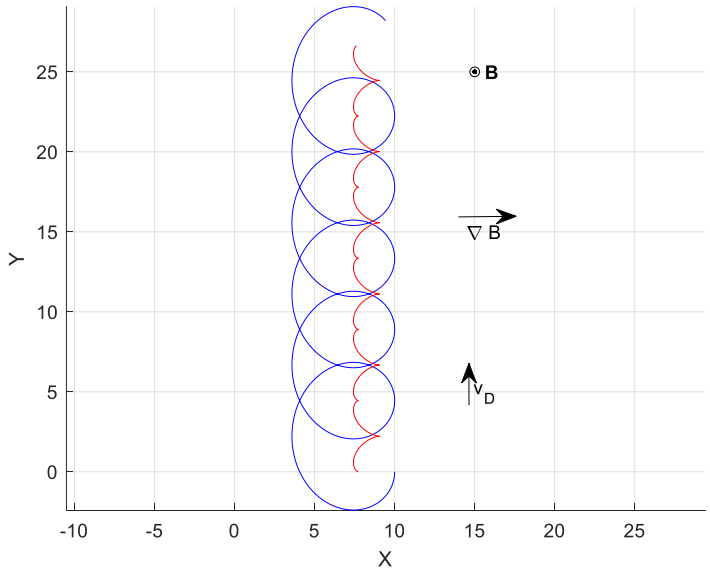

Figure 3.1: Trajectory of an ion in a magnetic field with a constant gradient. The ion is initiated with $m_0 = 1$, $q = 1$ $r_0 = [10, 0]$, $v_0 = [0 , -25]$. The magnetic field is out of the page with $B_z = (1 + x)$. The trajecory is shown in blue and gyrocenter in red.

In Figure 3.1 the particle trajectory in blue is determined by integrating the Lorentz force Equation (2.5) and the gyrocenter position in red is calculated using Equation (2.11). The change in the radius of curvature of the trajectory is a result of the magnetic field increasing in the positive *x*-axis direction. The elongated trajectory at x_{min} on the left, or the shortened trajectory at x_{max} on the right, is a result of the magnetic field getting stronger along the positive *x*-axis.

The vertical drift in the y-direction of the particle is to be expected based on the magnetic field gradient Equation (3.10). With the magnetic field in the *z*-direction and the gradient in the *x*-direction, the particle must drift in the *y*-direction. The direction of motion along the *y*-axis is determined by the charge, with the ion drifting upward. Lastly, it should be noted that the ion is initialized at x_{max} for all figures in this chapter unless otherwise specified.

For our purposes, it is sufficient to analyze the motion of the particle over a single gyroperiod. Although the analytical expression for the gyroperiod is available from Equation (3.7), we can easily terminate the numerical calculation using Matlab functionality. We initialize all particles in our simulation with $v_x = 0$ and we implement in Matlab an events function that terminates the integration when the *x* component of the velocity reaches zero again. Since the motion in this magnetic field is exactly periodic, we do not need to analyze longer periods of time. A typical particle trajectory restricted to one gyroperiod is presented in Figure 3.2 for the same initial conditions given in Figure 3.1.

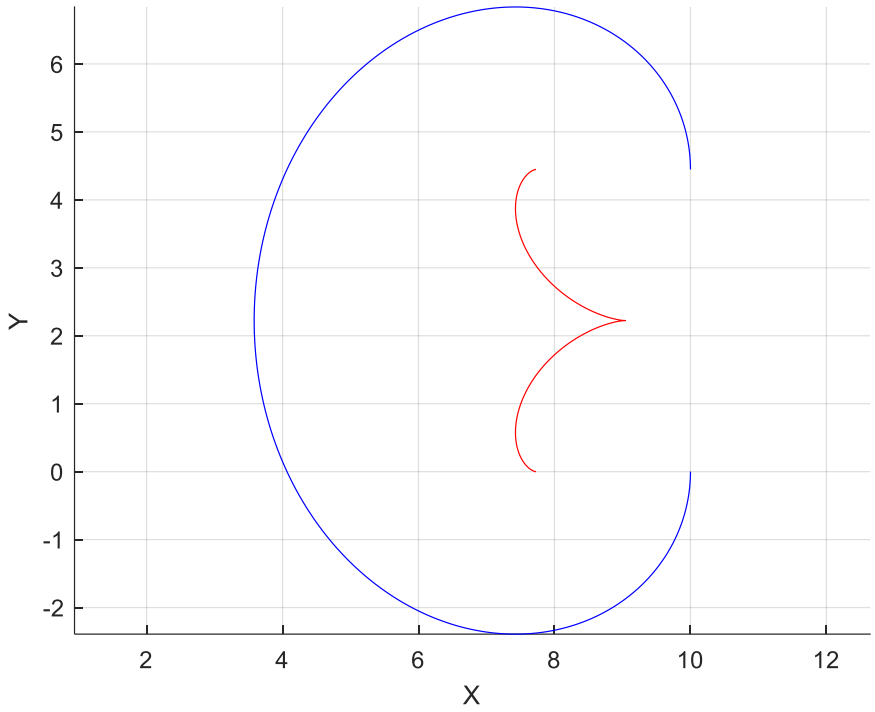

Figure 3.2: Trajectory of an ion for one gyroperiod. The ion is initiated with $m_0 = 1$, $q = 1$ $r_0 = [10, 0]$, $v_0 = [0 , -25]$. The magnetic field is out of the page with $B_z = (1 + x)$. The trajectory is shown in blue and the gyrocenter in red.

To approximate the trajectory in Figure 3.2 it is necessary to pick an initial point to integrate Equation (3.10), our GC drift velocity. It is conventional practice to use the initial gyrocenter position in red to do this because, at relatively low velocities, the gyrocenter is always roughly at the mean between x_{min} and x_{max}. At this relatively high velocity, we show that the red gyrocenter varies substantially in the x-direction during a gyroperiod and is often not at the mean of the particle trajectory in blue. In addition, using the particle trajectory to integrate our GC drift equation is obviously insufficient because the initial position can vary anywhere between x_{min} and x_{max}. For this reason, we analyze the evolute of a curve in an attempt to produce an alternative to the gyrocenter for GC initiation.

Mathematically, the evolute is defined as the locus of the centers of curvature of a given curve [21]. For a curve given in parametric form $x(t)$, $y(t)$, the equations of the evolute are given by Equations (3.11) and (3.12).

$$x(t) = x_0(t) - \frac{y'(t)\left(x'(t)^2 + y'(t)^2\right)}{x'(t)y''(t) - y'(t)x''(t)} \tag{3.11}$$

$$y(t) = y_0(t) + \frac{x'(t)\left(x'(t)^2 + y'(t)^2\right)}{x'(t)y''(t) - y'(t)x''(t)} \tag{3.12}$$

For our case, we recognize that $x(t) = x$, $y(t) = y$, $x'(t) = v_x$, $y'(t) = v_y$, $x''(t) = a_x$ and $y''(t) = a_y$ which allows us to reduce the evolute Equations (3.11) and (3.12) to Equations to (3.13) and (3.14) respectively.

$$x = x_0 - \frac{v_y\left(v_x^2 + v_y^2\right)}{v_x a_y - v_y a_x} \tag{3.13}$$

$$y = y_0 + \frac{v_x\left(v_x^2 + v_y^2\right)}{v_x a_y - v_y a_x} \tag{3.14}$$

Finally, using the Lorentz force Equation (2.5) and the fact that v^2 is a constant of motion we can re-write the evolute as Equations (3.15) and (3.16).

$$x = x_0 + \frac{mv_y}{qB} \tag{3.15}$$

$$y = y_0 + \frac{mv_x}{qB} \tag{3.16}$$

This coincides with the gyrocenter position calculated in Equation (2.11). These Equations show that the local curvature radius of a particle trajectory is given by the gyroradius evaluated based on the magnetic field at the particle position. Therefore, the position of the gyrocenter coincides with the evolute in Figure 3.2.

We now try to improve the accuracy of the GC approximation by improving the initiation point of the gyrocenter. It is known that the GC approximation more accurately models the particle trajectory if the magnetic field applied in Equation (3.10) is averaged [6]. To do this we introduce iterations to the gyrocenter calculation. For epicycloid trajectories, a similar procedure was done in a paper by Fancong Zen [6]. However, in this paper, the iterative procedure was only applied to a single point and not along the entire trajectory [6]. For this paper, we use the vectorized form of the gyroradius from Equation (2.11). Here *B* is a function of *r* and can be taken at any location. In the original application, the gyrocenter is calculated using the magnetic field at the location of the particle. In the next iteration, we use *B* at the gyrocenter to determine a new gyrocenter location. Clearly this iterative process can be repeated, giving rise to the following.

$$\mathbf{r}_{gc(i)} = \mathbf{r} + \frac{m}{q(B_0 + \beta x_{r_{gc(i-1)}})} [v_y, -v_x, 0] \tag{3.17}$$

This equation is used to generate a series of new gyrocenter positions. Typically, these iterations converge, although for sufficiently large velocities they may diverge. The convergence criteria for Equation (3.17) are discussed later in Figure 3.4. The letter *i* distinguishes the iteration number. For the first iteration, we use the position of the particle. From here on out the final convergence of this Equation will be known as the converged gyrocenter, while the previously discussed gyrocenter will be known as the first gyrocenter.

Next, the converged gyrocenter is added to the figure of one gyroperiod along with a few of the gyrocenter iterations to provide a visualization of this process. For further clarity, an additional plot of the corresponding points along the trajectory, 1st gyrocenter and converged gyrocenter is generated. Both plots are seen in Figure 3.3 below for the same initial conditions as before. The black line here represents the limit of iterations to reach convergence.

On Figure 3.3 the transitions between the 1st, 2nd and 3rd iterations are shown to slowly converge towards the final converged gyrocenter. The number of iterations was set to 12 to reach this convergence, though the 10th and higher iterations practically coincide with the converged result. This is because, at the 10th iteration, the result changes on the order of 10^{-4}. We define this as the minimum accuracy to be considered convergent because the naked eye can no longer detect changes in the black converged gyrocenter at subsequent iterations without zooming in on Figure 3.3. To ensure the result in Figure 3.3 is converging, a comparison was done on the difference at 100 iterations. Under this iteration number changes were on the order of 10^{-6}, since this is smaller than 10^{-4} it was concluded that this process was convergent.

The cusps of the converged gyrocenter serve as a common point between all iterations greater than 1, since they all intersect the same point on the 1st iteration. This point is more easily visualized using the stars in Figure 3.3. From this it is clear that the converged gyrocenter cusps correspond to the 3rd star on either side of the particle trajectory. This occurs when the entire velocity is directed in the *x*-direction. Therefore, it is concluded that the converged gyrocenter and the 1st iteration share a common point when velocity is in the same direction as the gradient. Alternatively, this point is thought of as the most stable point for the gyrocenter iterations. Thus it is also concluded the most unstable point is when velocity is in the *y*-direction, or perpendicular to the gradient. More specifically this occurs at x_{min}. This is visualized on Figure 3.3 by noticing how

far the 1st gyrocenter iteration protrudes away from the middle of the particle trajectory. At higher velocities, this point approaches and surpasses x_{max}, this is shown on Figure 3.4. When this happens, the iterative gyrocenter procedure requires more iterations to reach convergence. This further illustrates our need for a different approach when applying the GC approximation at high energies.

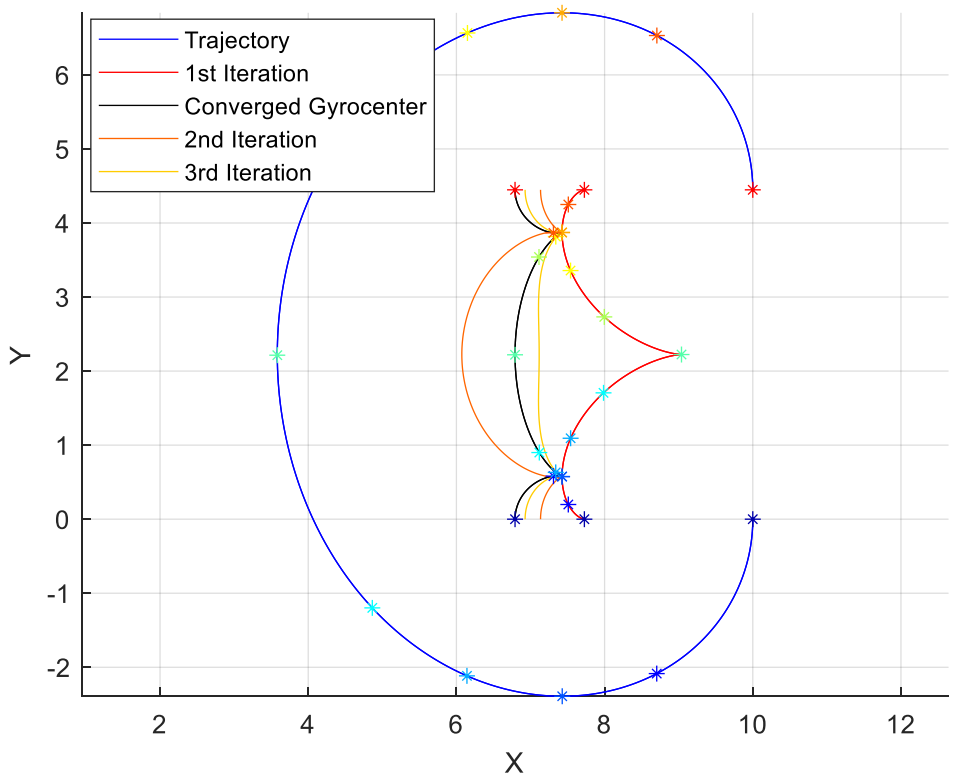

Figure 3.3: 1st, 2nd, 3rd and final iterations of the gyrocenter with corresponding points for one gyroperiod. The ion is initiated with $m_0 = 1$, $q = 1$ $r_0 = [10, 0]$, $v_0 = [0 , -25]$. The magnetic field is out of the page with $B_z = (1 + x)$. The trajectory is shown in blue, 1st gyrocenter in red, 2nd gyrocenter in orange, 3rd gyrocenter in yellow and final gyrocenter in black.

To compare the difference in the converged gyrocenter at a higher velocity a value of $v = 30$ was chosen. This value was chosen because it is the highest integer available before the neutral line crosses occurs. The threshold speed for neutral line crossing was determined by using the separatrix definition of $\Delta_s = 0$ in Equation (3.4) and solving for the velocity. The result is given by Equation (3.18). For the initial conditions of this case, this results in a $v = 30.25$ to cross the $x = -1$ neutral line.

$$v = \frac{B_0^2 + 2\beta\frac{p_y}{q}}{2m\left|\frac{\beta}{q}\right|} \tag{3.18}$$

The gyrocenter iterations for $v = 30$ are displayed in Figure 3.4.

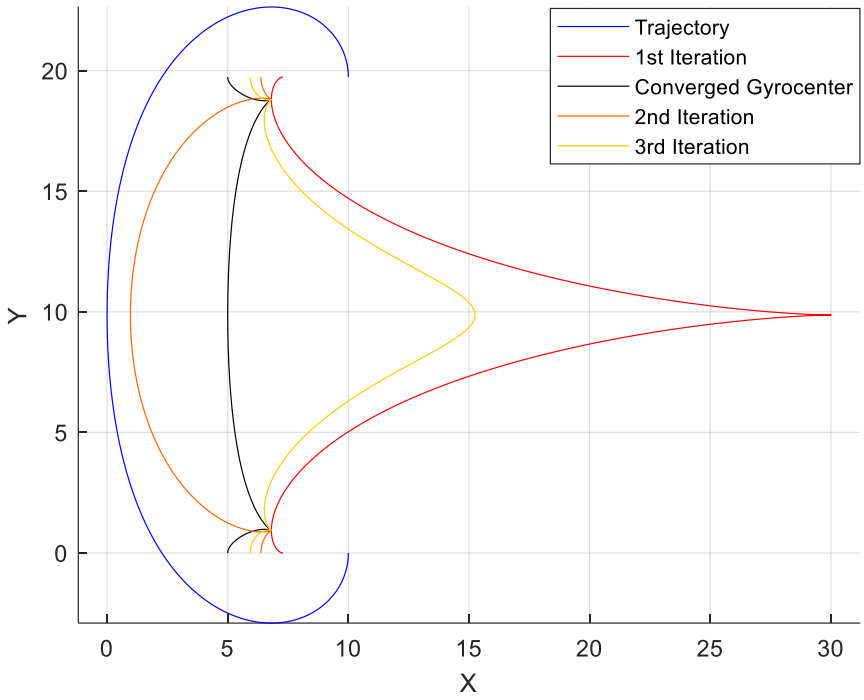

Figure 3.4: 1st, 2nd, 3rd and final iterations of the gyrocenter using our threshold velocity for one gyroperiod. The ion is initiated with $m_0 = 1$, $q = 1$ $r_0 = [10, 0]$, $v_0 = [0 , -25]$. The magnetic field is out of the page with $B_z = (1 + x)$. The trajectory is shown in blue, 1st gyrocenter in red, 2nd gyrocenter in orange, 3rd gyrocenter in yellow and final gyrocenter in black.

In Figure 3.4 it took roughly 30 iterations to reach our desired convergence threshold of 10^{-4}. Zooming in on Figure 3.4 there were small-scale improvements even around 100 iterations, though these were smaller than 10^{-4}. These improvements were all around the aforementioned unstable point of x_{min}. Overall, the iterative gyrocenter converged for the highest velocity that did not cross the neutral line. This process aids in illustrating the fact that the GC approximation works well for small velocities and not so well for large velocities. Lastly, it is known that the iterated gyroperiods differ from the exact ones at higher velocities. Due to this, the GC approximation suffers from the secular errors that accumulate over multiple gyroperiods [6]. However, a means to avoid this is discussed later in Section 3.5.

Next, we consider the selection of the initial point for the GC drift equation. In this case, the drift velocity is in the *y*-direction and it depends on the initial *x* position only, as the *x*-position determines *B*. Thus, to calculate the change in the position of the GC we need simply to multiply the GC drift velocity, Equation (3.10), by the timeframe we consider. We can also use ode45 to integrate Equation (3.10), which is a more general approach. In Figure 3.5 the particle trajectory (blue), 1st gyrocenter (red) and converged gyrocenter (black) are shown with the thin lines. The thicker lines are the results of applying the GC approximation by integrating Equation (3.10) using the initial positions of the particle trajectory, 1st gyrocenter and converged gyrocenter. Clearly, if we use the position of the particle as the starting point for the GC approximation then we severely underestimate the GC drift, as the blue thick line endpoint is far from the blue thin line endpoint in Figure 3.5. This is because we used x_{max} as our initial point. If we used x_{min} then we would be

overestimating the GC drift. Using the 1st gyrocenter this approximation still underestimates the drift, but is clearly more accurate than using the particle position. Finally, using the converged gyrocenter we get the most accurate estimation of the particle drift.

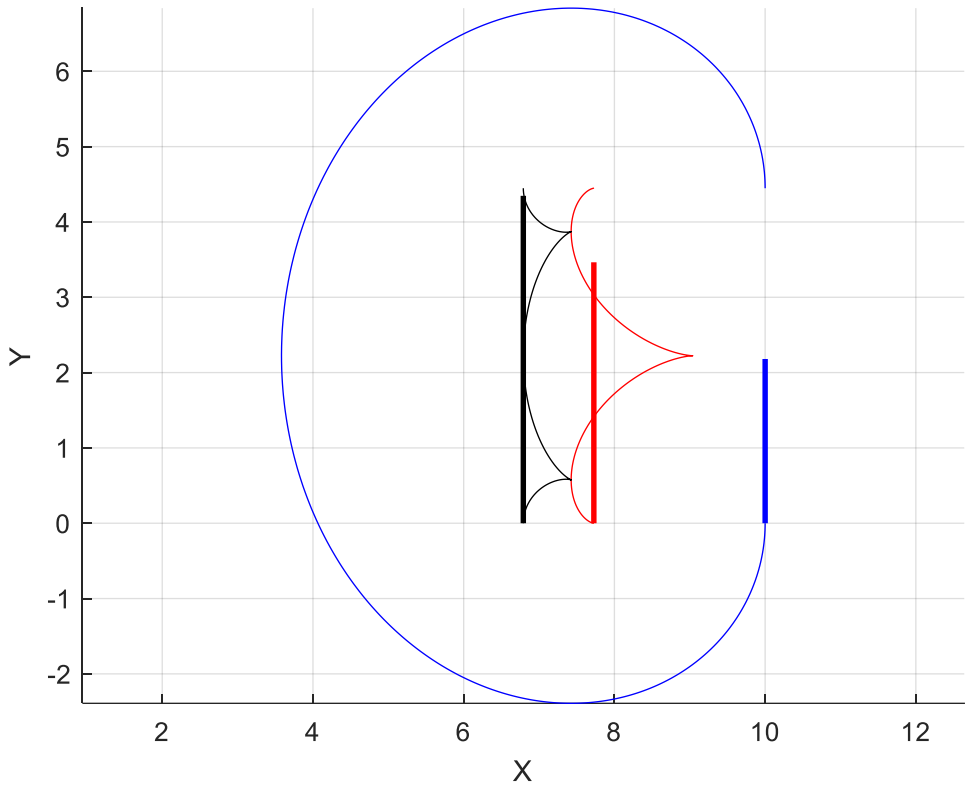

Figure 3.5: GC integration using the trajectory, 1st gyrocenter and converged gyrocenter as starting locations for one gyroperiod. The ion is initiated with $m_0 = 1$, $q = 1$ $r_0 = [10, 0]$, $v_0 = [0 , -25]$. The magnetic field is out of the page with $B_z = (1 + x)$. . The trajectory is shown in blue, 1st gyrocenter in red and converged gyrocenter in black, with the same colour thicker lines corresponding to GC integration.

Note that we used the values based on the initial point of our particle trajectory, which corresponded to x_{max}. However, in practical calculations, the initial point is likely to be arbitrary. If the particle trajectory is used, the possible starting points for the GC calculation would vary between x_{min} and x_{max}, and the result would vary between underestimating and overestimating the GC drift. The same applies to either the 1st iteration of the converged gyrocenter. However, in these cases, the range of the variation in the x-direction is considerably smaller. Thus, either of these methods improves the consistency of the GC drift calculation and increases the accuracy when compared to using the particle position. Still, the final position of the GC drift underestimates the converged gyrocenter in Figure 3.5. To quantify our accuracy we now take the difference in y between the endpoints of the thinner lines and the correspondingly coloured thicker lines. We call this difference in endpoints the tracing error and plot it as a function of velocity. The range of which is from $v = 0.01$ to $v = 30$. This is done on a log scale and is given in Figure 3.6.

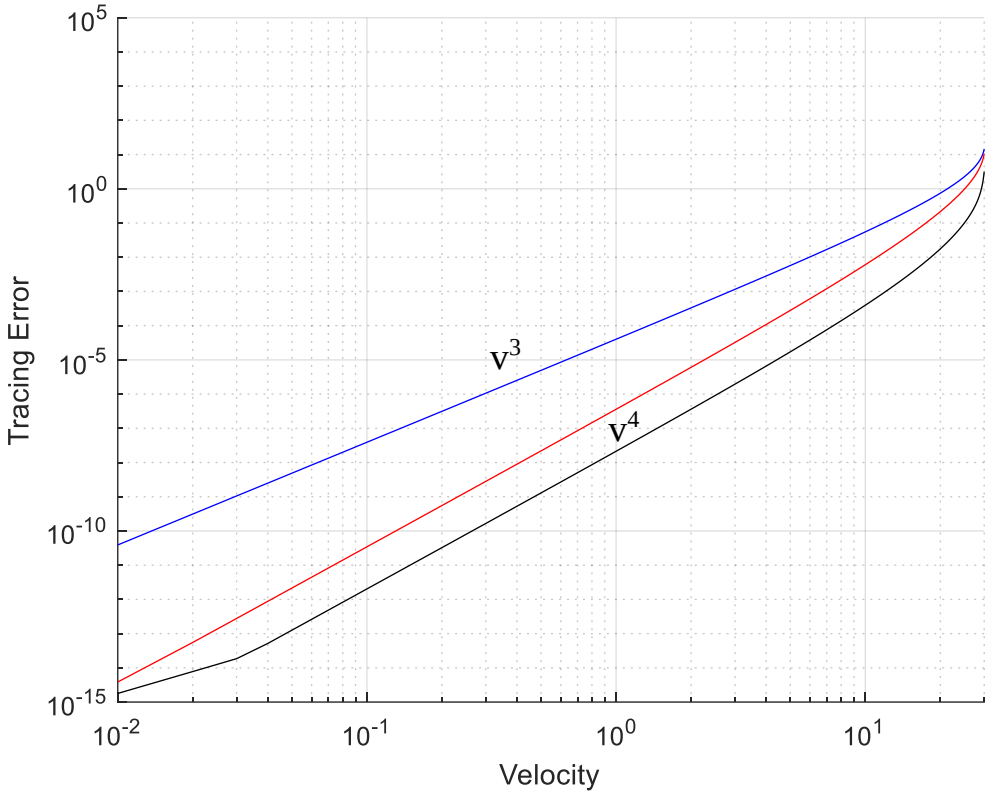

Figure 3.6: Tracing Error as a function of velocity for v = 0.01 to v = 30. The ion is initiated with m_0 = 1, q = 1 r_0 = [10, 0], v_0 = [0 , -v]. The magnetic field is out of the page with B_z = (1 + x). Tracing error for the trajectory is shown in blue, 1st gyrocenter in red and converged gyrocenter in black.

In Figure 3.6 it is shown that as v goes to 0 all GC approximations, regardless of initial position, converge to the exact GC drift. To determine the relationship between tracing error and velocity we multiplied our initial tracing error value at v = 0.01 by velocity raised to some power, $v^{\#}$. Varying this power until the results matched that of Figure 3.6 allowed us to determine the relationship between tracing error and velocity. The tracing error in this plot is proportional to v^3 for the trajectory, while the 1st gyrocenter and converged gyrocenter are proportional to v^4. It is clear, and also to be expected, that the tracing error is smallest when using the converged gyrocenter at every velocity in this range. Compared to the 1st gyrocenter, the converged gyrocenter reduced the tracing error by a factor of 17 for most velocities, where the red and black lines of Figure 3.6 are parallel. At the highest velocity of v = 30 the tracing error was reduced by a factor of 4. The deviation from the linear shape at the high velocity extreme is attributed to the breaking down of the GC approximation, while the change at the low extreme is due to numerical accuracy limitations.

The GC approximation is initialized at x_{max} in Figure 3.5 and Figure 3.6. Thus the conclusion that tracing error is proportional to v^3 has only been proven for the x_{max} condition. To test the proportionality of v^3, for any point along the particle trajectory, we distribute the GC approximation starting location between x_{min} and x_{max}. For this analysis, we use 250 points for

sufficient resolution. Like before, the distance travelled by the GC approximation is measured against the true drift of the particle. This is the vertical distance between the starting point and endpoint of the trajectory in Figure 3.5. We now select two velocities from Figure 3.6 to compare the difference in their tracing errors from x_{min} and x_{max}. This is done for $v = 0.1$ and $v = 1$ and is displayed on the semilog plot in Figure 3.7. Here we normalize the x-axis such that 0 corresponds to x_{min} and 1 corresponds to x_{max}.

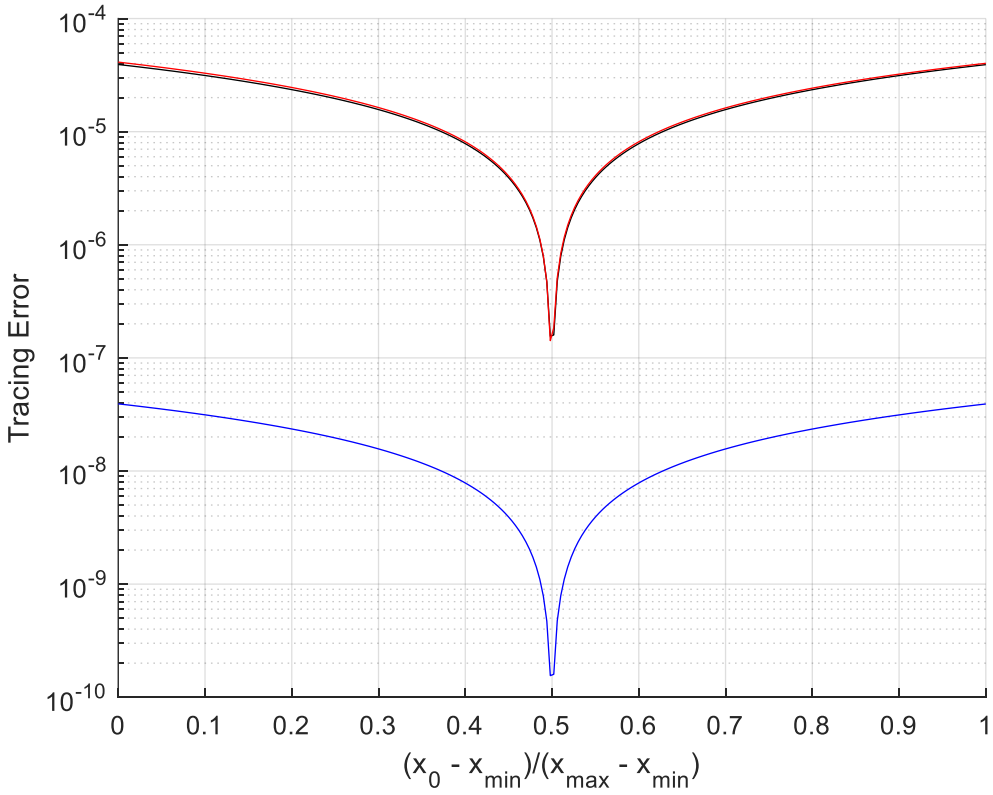

Figure 3.7: Tracing Error for GC integration initiated between x_{min} and x_{max} for $v = 0.1$ (blue) and $v = 1$ (red). The ion is initiated with $m_0 = 1$, $q = 1$ $r_0 = [x_{min}$ to $x_{max}, 0]$, $v_0 = [0, -v]$. The magnetic field is out of the page with $B_z = (1 + x)$.The black line is the blue line multiplied by 10^3.

In Figure 3.7 the blue corresponds to $v = 0.1$ and the red corresponds to $v = 1$. Unsurprisingly the smallest tracing error occurs at the mean of x_{min} and x_{max} for these relatively low velocities, while the largest tracing error occurs at the extremes. The most important part of Figure 3.7 is the black line. It is the tracing error results of $v = 0.1$ multiplied by our proportionality of v^3, for this situation this is 10^3. Since the black line coincides with the results of $v = 1$ we thus conclude that tracing error is always proportionate to v^3 when using the particle trajectory as a GC starting point, regardless of the location between x_{min} and x_{max}.

3.4 Analysis of the Magnetic Moment

The use of the magnetic moment allows for a more in-depth analysis of the GC approximation accuracy, as the GC approximation requires that the first adiabatic invariant be

conserved. Conventionally Equation (2.18) is used to determine the magnetic moment, however, this is only an approximation and thus we attempt to improve upon it. To further increase accuracy, the second-order Taylor expansion of the magnetic moment is also derived for this magnetic field. This is done by applying the magnetic field with a constant gradient (3.1) to the general second-order Taylor series expansions (2.19). The resulting formula is given by Equation (3.19) [10]. In addition, since the magnetic field can be taken along any path for the Taylor series expansion, both the actual ion trajectory and the converged gyrocenter are used.

$$\mu_{T2} = \frac{\mu}{m}\left(1 - u_y + \frac{3}{8}\left(u^2 + u_y{}^2\right)\right) \tag{3.19}$$

$$u = \sqrt{u_x{}^2 + u_y{}^2} \tag{3.20}$$

$$u_x = \frac{v_x}{v_*} \tag{3.21}$$

$$u_y = \frac{v_y}{v_*} \tag{3.22}$$

$$v_* = \frac{qB^2}{\beta m} \tag{3.23}$$

In addition, an exact analytical solution for the adiabatic invariant exists for this magnetic field in the form of elliptic integrals. It is given by Equation (3.24) [11]. Here K and Ξ are elliptic integrals of the first and second type respectively, as introduced in Section 2.6 [10].

$$\mu_{Exact} = \frac{\mu}{m}\left(\frac{2}{3\pi}\right)\frac{\sqrt{1 + 2\left(u + u_y\right)}}{u^2}\left(\left(1 + 2u_y\right)\Xi(k) - \left(1 - 2\left(u - u_y\right)\right)K(k)\right) \tag{3.24}$$

$$k = \frac{4u}{1 + 2(u + u_y)} \tag{3.25}$$

We consider all of our different approximations of the magnetic moment. Since we know that the exact adiabatic invariant remains constant along the trajectory, we use Equation (3.24) as a basis of comparison for our various approximations of μ. We start by analyzing the application of Equation (2.18) using the magnetic field along the ion trajectory, the 1st gyrocenter and the converged gyrocenter. The result is displayed in Figure 3.8 for one gyroperiod, where it is shown that the approximations of μ oscillate at the same rate as the gyrofrequency. All quantities are normalized to the exact value of the adiabatic invariant given by Equation (3.24), which is also shown with a cyan line. Analyzing the application of Equation (2.18) was done for velocity values of $v = 25$ and $v = 2.5$, displayed in the top and bottom panels of Figure 3.8 respectively.

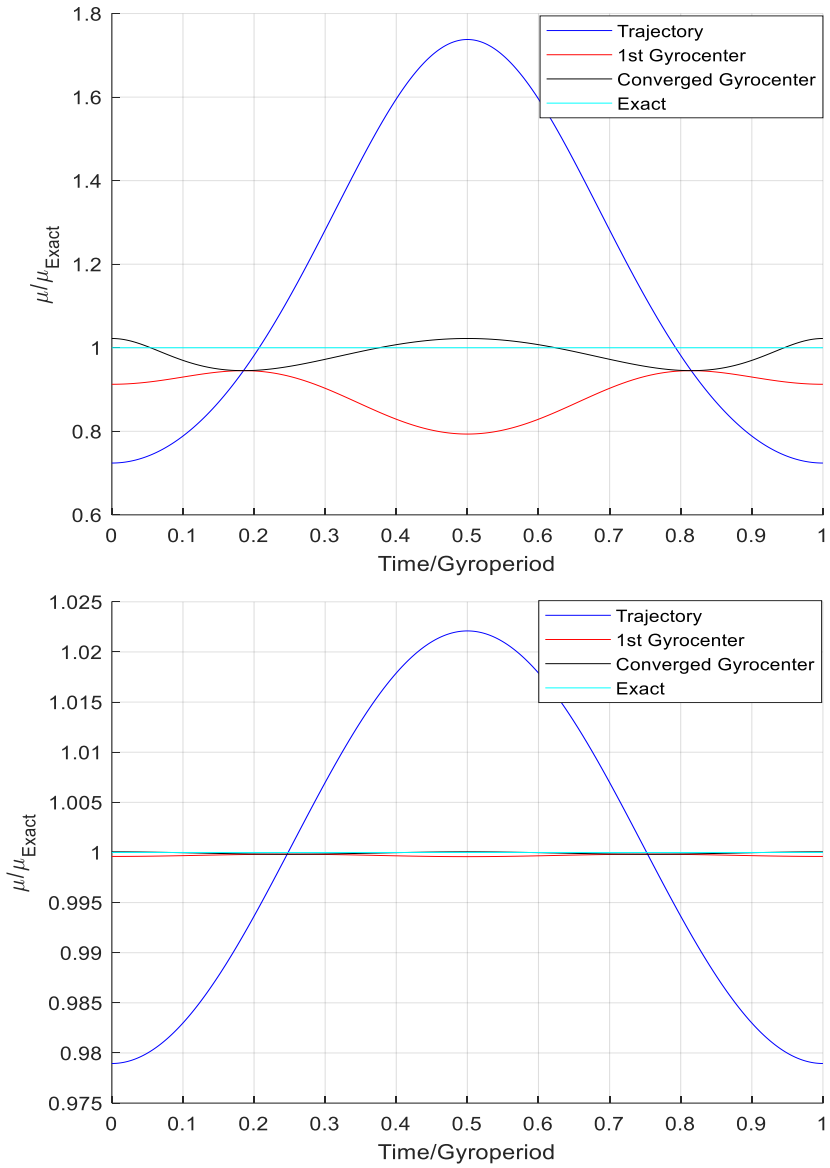

Figure 3.8: Zeroth-order magnetic moment approximation using *B* at the particle trajectory, 1st gyrocenter and converged gyrocenter, normalized by the exact expression at *v* = 25 (top) and *v* = 2.5 (bottom). The ion is initiated with m_0 = 1, *q* = 1 r_0 = [10, 0], v_0 = [0 , - *v*]. The magnetic field is out of the page with B_z = (1 + x). Magnetic Moment for trajectory is shown in blue, 1st gyrocenter in red and converged gyrocenter in black and exact expression in cyan.

The top panel shows that the exact solution is not centred at the mean of the oscillations for any of the magnetic moments. Clearly, the magnetic moment computed based on the magnetic field along the location of the particle exhibits the largest variation and is, therefore, the least accurate. The amplitude deviates by a maximum of 70% from the exact solution. Comparatively the 1st gyrocenter and converged gyrocenter deviate by a maximum of 20% and 5% respectively from the exact solution. Unsurprisingly it is clear that the converged gyrocenter is the most accurate. The asymmetry on the top panel is attributed to the relatively high velocity of *v* = 25.

Reducing this by a factor of 10 to $v = 2.5$, as shown on the bottom panel, validates this dependence on the velocity. This is demonstrated by the increased symmetry of all trajectories about the exact solution. The symmetry on the bottom panel shows why the 1st gyrocenter is a valid GC initiation point at relatively lower velocities, while the top panel further validates the use of the converged gyrocenter at higher velocities since it more accurately replicates the exact solution of μ than the 1st gyrocenter.

For further comparison, we now apply the Taylor series expansion for the magnetic moment, which was established in (3.19). This is done using the magnetic field along the particle trajectory and the converged gyrocenter in an attempt to improve the magnetic moment accuracy. The result for one gyroperiod is given in Figure 3.9.

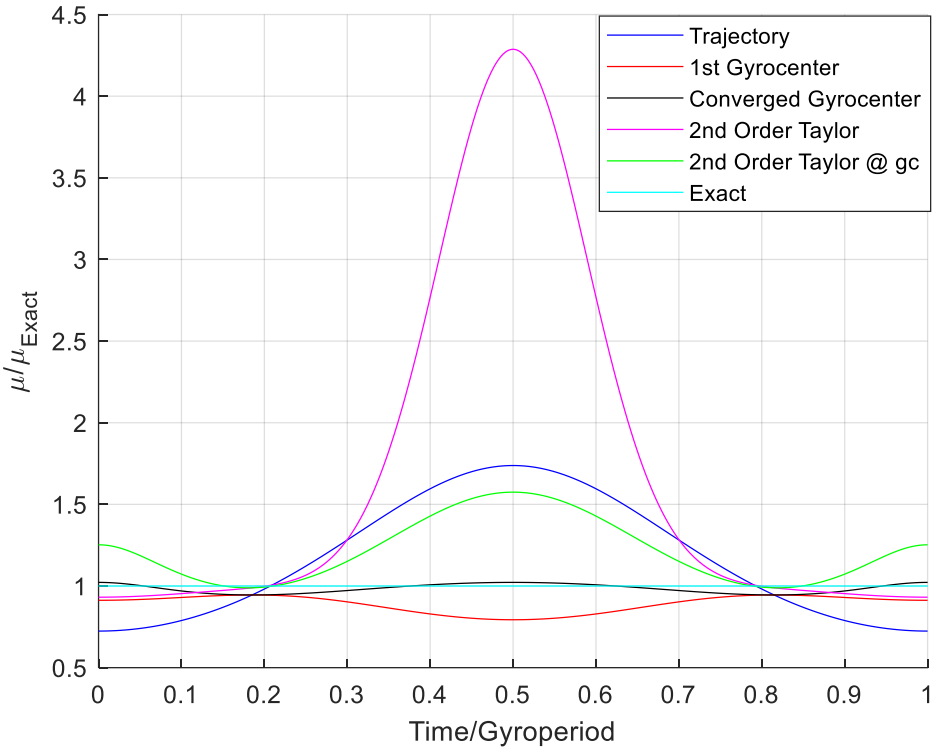

Figure 3.9: Various magnetic moment approximations and the exact expression for one gyroperiod normalized by the exact expression. The ion is initiated with $m_0 = 1$, $q = 1$ $r_0 = [10, 0]$, $v_0 = [0 , -25]$. The magnetic field is out of the page with $B_z = (1 + x)$. Equation (2.18) using B at the trajectory is shown in blue, 1st gyrocenter in red and converged gyrocenter in black. Equation (3.19) using B at the trajectory is shown in magenta and converged gyrocenter in green. The exact expression is in cyan.

At this relatively high velocity it is seen that the Taylor series expansions do not increase the accuracy of the magnetic moment. However, due to the dependency on velocity, the potential to be more accurate at different velocities exists. With all magnetic moments established, a correlation between velocity and the magnetic moment error is generated. This error is the difference between the exact solution and the farthest amplitude point. This corresponds to the most unstable point along the trajectory, which was established in Section 3.3 as x_{min} due to the

weaker magnetic field. The correlation of the magnetic moment error with velocity is graphed on a log plot from a velocity of $v = 0.01$ to $v = 30$ and displayed below in Figure 3.10.

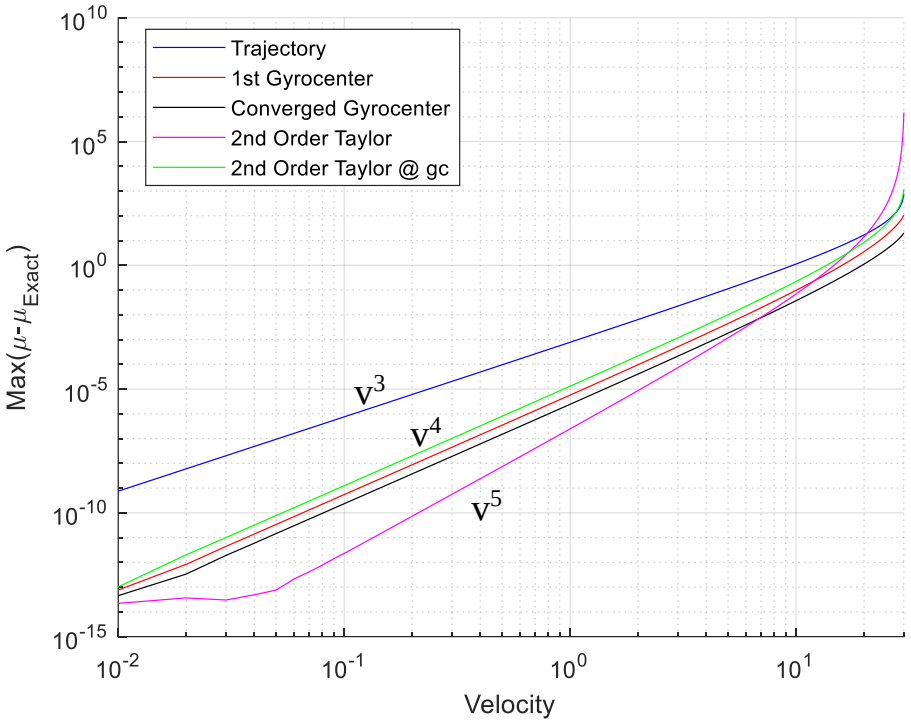

Figure 3.10: Magnetic moment approximation error as a function of velocity from $v = 0.01$ to $v = 30$. The ion is initiated with $m_0 = 1$, $q = 1$ $r_0 = [10, 0]$, $v_0 = [0 , -v]$. The magnetic field is out of the page with $B_z = (1 + x)$. Equation (2.18) using B at the trajectory is shown in blue, 1st gyrocenter in red and converged gyrocenter in black. Equation (3.19) using B at the trajectory is shown in magenta and converged gyrocenter in green. The exact expression is in cyan.

Figure 3.10 shows the magnetic moment error scales as a power law with velocity, where $v^{\#}$ is determined by the steepness of the slope. From Figure 3.10 it was determined that error using Equation (2.18) along the particle trajectory is proportional to v^3 and changes the slowest of all the magnetic moments. The magnetic moment error using Equation (2.18) at the 1st gyrocenter, converged gyrocenter and using (3.19) at the converged gyrocenter are proportional to v^4. The steepest curve corresponds to using the 2nd order Taylor expansion (3.19) at the particle trajectory and is proportional to v^5. Therefore, the application of Equation (2.18) along the converged gyrocenter is the most accurate method of calculating the magnetic moment at, or above, a velocity of roughly 6.5, while at, or below this threshold, the 2nd order Taylor expansion taken along the trajectory is the most accurate. All other methods of calculating the magnetic moment are inferior to both of these for the entire velocity range. The deviation of the linear sloped shape at the high velocities is attributed to the breaking down of the GC approximation. For low velocities, the deviation of the linear sloped shape is attributed to numerical errors as the calculation is approaching machine accuracy. Since this paper is examining the application of the GC approximation for higher energy particles this means the converged gyrocenter continues to be our basis of comparison for GC initiation.

3.5 Guiding Center Starting Location

The converged gyrocenter is the best starting point for the GC, but it is still imperfect, as established by the tracing error in Figure 3.5. This tracing error is analyzed further by investigating three more starting point options. First, we note that there exist positions, along the *x*-axis, where the local magnetic moment, gyroperiod and drift velocity have the same value as their respective exact value. As an example, x_μ is defined by rearranging Equation (2.18) for *x* and substituting μ_{Exact}, Equation (3.24), for μ_0. The result is given by Equation (3.26). The same process is repeated for determining the exact *x* location of the gyroperiod (x_{Tg}) and the drift velocity (x_{VD}) by rearranging Equations (2.7) and (3.10) for *x*. The exact value used for the gyroperiod and drift period are given by Equations (3.7) and (3.9) respectively. However, these exact values can more easily be determined by using the integration time of the Matlab code with the events functionality set for one gyroperiod, now integration time = Equation (3.7) and the Δy/(integration time) = Equation (3.9). Substituting these values into x_{Tg} and x_{VD} results in (3.27) and (3.28) respectively.

$$x_\mu = \frac{\left(\frac{mv^2}{\mu_{Exact}} - B_0\right)}{\beta} \tag{3.26}$$

$$x_{Tg} = \frac{\left(\frac{2\pi m}{T_{g\_Exact}|q|} - B_0\right)}{\beta} \tag{3.27}$$

$$x_{VD} = \frac{\left(\sqrt{\left(\frac{m}{q}\right)\left(\frac{v^2}{2v_{D\_Exact}}\right)(\beta)} - B_0\right)}{\beta} \tag{3.28}$$

The values of these x positions are normalized by subtracting the x_{min} and dividing by x_{max} - x_{min}, limiting them to values between 0 and 1. This results in a relative *x*-position value of 0.5 corresponding to the center of the strip of the particle motion. As the velocity decreases all three *x*-position Equations converge at this value which is validated by graphing the relative *x*-positions over the velocity range from $v = 0.01$ to $v = 30$. The graph is displayed in Figure 3.11.

Figure 3.11 shows that the *x*-position of the drift velocity deviates the least from 0.5 as velocity is increased, this is followed by the magnetic moment, with the gyroperiod deviating the most. The direction of deviation varies as the magnetic moment deviates towards x_{max}, while the gyroperiod and drift velocity deviate towards x_{min}. Lastly, it is shown that there is never a single *x*-position that will satisfy the exact solution for all three quantities. Thus, in practical calculations, one might need to choose which is more important for a particular simulation.

While the exact values for the first adiabatic invariant and gyrofrequency are sometimes very desirable, the typical application of GC focuses on the transport of the particle, thus accurately reproducing the drift velocity is the main goal. Equation (3.28) allows us to match the drift velocity used in the GC approximation to the precise drift velocity of the particle, which is determined from the exact solution of the full equations of motion for this particular magnetic field. Overall x_{VD} is

typically the best choice for GC initialization. Furthermore, Equation (3.28) can be applied approximately to any two-dimensional magnetic field. Thus, we envision the following procedure for calculating the starting point for GC calculations. First, given a magnetic field, one needs to calculate its gradient, a necessary step for GC calculations regardless of the initialization procedure. Second, one would use Equation (3.28) to initialize the GC calculation. This procedure accounts for both the magnetic field strength and its gradient in GC initialization and thus is likely to always be superior to the conventional method of making a single step with the 1st gyrocenter. Assessment of how well this procedure performs in comparison with, for example, the iterated gyrocenter approach for general fields requires additional analysis.

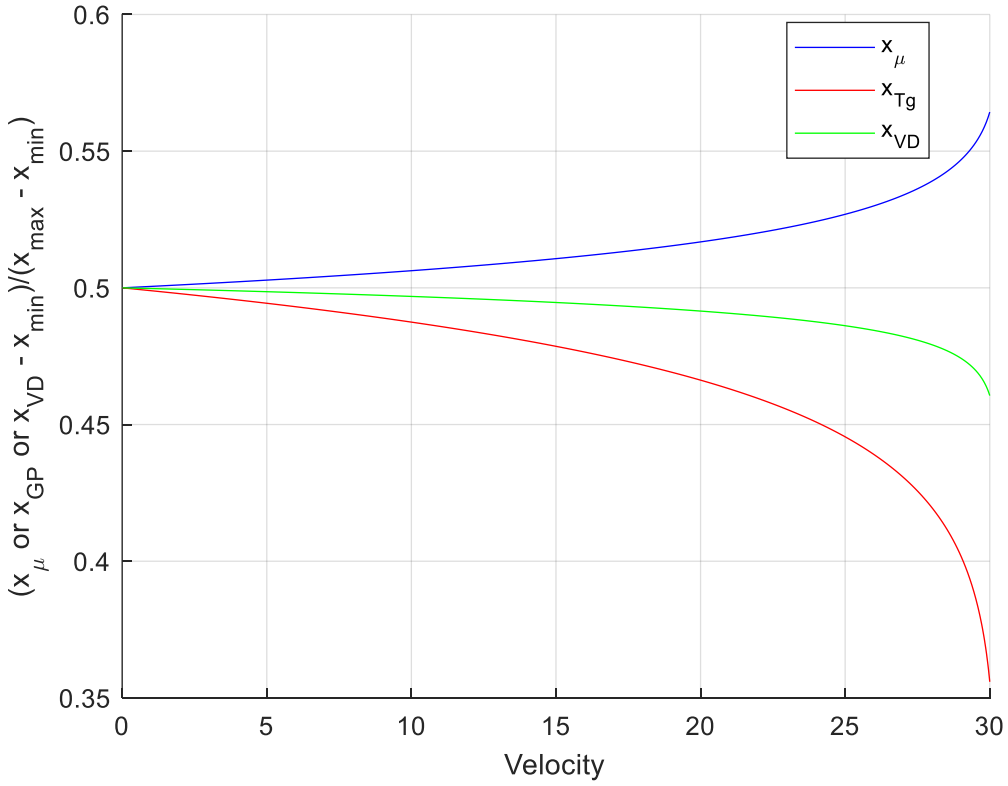

Figure 3.11: Normalized x position along the trajectory where μ, T_g and v_D equal their respective exact expression as a function of velocity from v = 0.01 to v = 30. The ion is initiated with m_0 = 1, q = 1 r_0 = [10, 0], v_0 = [0 , -v]. The magnetic field is out of the page with B_z = (1 + x). x_μ is shown in blue, x_{Tg} in red and x_{VD} in green.

Taking our new positions of x_μ, x_{Tg} and x_{VD} and overlaying them onto the ion trajectory for one gyroperiod at v = 25 yields Figure 3.12.

Comparing this figure with Figure 3.5 indicates x_{VD} in green models the drift velocity exactly, as to be expected. Recall in Figure 3.5 that initiating the GC at the converged gyrocenter resulted in slightly underestimating the GC drift. In Figure 3.12 x_{VD} is positioned at a slightly weaker magnetic field position than the converged gyrocenter in black, therefore, the GC will drift slightly further than before, thus improving upon the GC initiated at the converged gyrocenter.

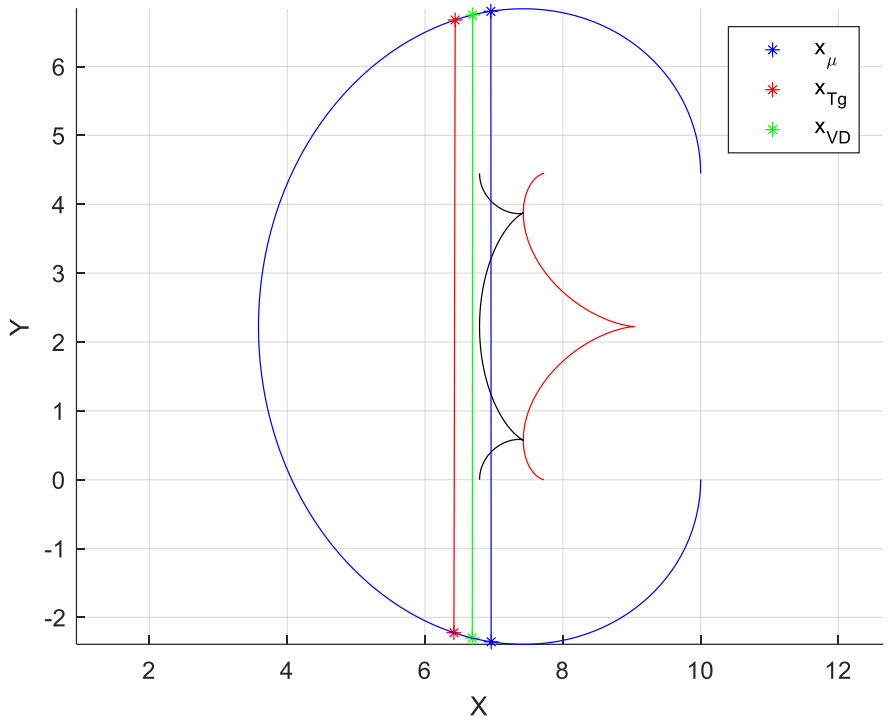

Figure 3.12: GC initialization options overlayed onto the trajectory, 1st gyroradius and converged gyrocenter for one gyroperiod. The ion is initiated with m_0 = 1, q = 1 r_0 = [10, 0], v_0 = [0 , -25]. The magnetic field is out of the page with B_z = (1 + x). The trajectory is shown in blue, 1st gyrocenter in red and the converged gyrocenter in black. Vertical lines correspond to the initialization options for x_μ is shown in blue, x_{Tg} in red and x_{VD} in green.

3.6 Conclusion

In this section, we analyzed in detail the motion of charged particles in a magnetic field with a constant gradient in the *x*-direction. Although this is a very simple field, it is used to illustrate many of the issues occurring in complex fields. These include how to choose an initial point for the GC approximation and what method should be used to most accurately approximate the magnetic moment. This field is also useful because any two-dimensional magnetic field can be locally approximated by a magnetic field with a constant gradient. For this magnetic field some important analytical expressions exist, which allow full and detailed analysis of the accuracy of the GC approximation.

We discussed several methods for calculating the initial starting point for the GC approximation from the particle's position and velocity vectors. We note that other methods have also been used by Kabin [22] or Brizard [19]. Brizard, for example, used the average *x* value for the particle trajectory [19]. However, this requires either using analytical results, which are not available other than for very specific magnetic fields, or numerical integration of a particle over at least one gyroperiod. In this thesis, we do not consider such possibilities and focus exclusively on the techniques for computing the GC initial position based exclusively on the initial position and velocity of the charged particle.

The first method used to evaluate the GC initial position was the application of the gyrocenter Equation (2.11). This restricted the range of variation in the x-direction when compared to using the particle position, thus, improving the consistency of the GC drift calculation. At higher velocities, it was shown that x_{min} was an unstable point in the application of Equation (2.11), and even increased x_{max} of the gyrocenter past x_{max} of the actual particle trajectory. To improve upon the 1st gyrocenter, iterations were introduced to average the variation in B across the range of x positions. This resulted in the converged gyrocenter trajectory (3.17), which further restricted the range of variation in the x-direction. In addition, the converged gyrocenter remained confined to the particle's x_{max} at high velocities. To confirm the improvement of the converged guiding center a log plot was generated across a wide range of velocities for the error in GC drift. This validated that the converged gyrocenter had a smaller tracing error across all velocities. This error was a factor of 17 smaller than at the 1st gyrocenter for most velocities, reducing to a factor of 4 at the velocity extreme of $v = 30$. It was also determined that the tracing error was proportion to v^3 when initiating the GC approximation at the particle position and v^4 when at the 1st gyrocenter or converged gyrocenter.

The existence of exact analytical expressions for the magnetic moment, gyroperiod and drift velocity allowed for the determination of an x-position that corresponded to an equivalent value of the exact solution. These resulted in Equations (3.26), (3.27), and (3.28) respectively. It was found that these three x-positions shared no overlap for a range of velocities, except for their convergence towards the mean x-position at low velocities. Thus, the choice to initiate the GC approximation at any three of these x-positions depends on which expression takes priority for a given situation. In general, the typical application of GC prioritizes accurately modelling the drift velocity, and thus using x_{VD} is the preferred choice in most situations. However, it is still very desirable to match the exact values for the first adiabatic invariant and gyrofrequency in certain situations.

Different methods of measuring the accuracy of the GC approximation were determined by using the GC approximation condition that the 1st adiabatic invariant is conserved. Using the exact magnetic moment as a basis of comparison, various methods for calculating the magnetic moment were compared. This was done on a log plot using the zeroth-order Equation of μ (2.18) and the Taylor series approximation Equation of μ (3.19). Here the value of B used was taken along the particle trajectory, 1st gyrocenter and converged gyrocenter for Equation (2.18), and along the particle trajectory and converged gyrocenter for Equation (3.19). The result was that the zeroth-order converged gyrocenter is the most accurate method of calculating the magnetic moment at or above a velocity of roughly 6.5. The error between this calculation of μ and the exact solution was proportional to v^4. For velocities less than 6.5 the 2nd order Taylor expansion taken along the trajectory of the particle is the most accurate. The error between this calculation of μ and the exact solution was proportional to v^5.

4. Particle Motion in Equatorial Plane of a Magnetic Dipole

4.1 Analysis of the Axisymmetric Magnetic Field

In this chapter, we explore the accuracy of the GC approximation for a magnetic field that is commonly found in space physics. For example, at distances less than four R_E, the terrestrial magnetic field is often approximated as a magnetic dipole, because the inner field lines are shielded by the outer magnetic field lines, which stretch and compress due to solar wind pressure, as illustrated in Figure 1.2. The effects of the asymmetry that arises from this stretching and compressing are analyzed in more detail in Chapter 5 of this thesis. The field of a magnetic dipole is often expressed in spherical coordinates (r, φ, λ) where r is the radial distance from the origin, φ is the angle made with the positive x-axis measured counter-clockwise and λ is the magnetic latitude. The conventional expression for a magnetic dipole is given by Equation (4.1).

$$\mathbf{B} = \frac{\mu_0 M_E}{4\pi r^3}(-2\sin\lambda\,\hat{\mathbf{e}}_\mathbf{r} + \cos\lambda\hat{\mathbf{e}}_{\boldsymbol{\lambda}}) \tag{4.1}$$

Here M_E is Earth's magnetic dipole moment and has a value of $8.05\cdot10^{22}\text{Am}^2$. Magnetic fields are usually visualized with magnetic field lines. The differential Equation for the field lines is given by Equation (4.2). Here s represents the arc length of the magnetic field lines.

$$\frac{d\mathbf{r}}{ds} = \frac{\mathbf{B}}{B} \tag{4.2}$$

This equation is integrated to give Equation (4.3) [1].

$$r = \rho\cos^2\lambda \tag{4.3}$$

Here ρ is the interception of a magnetic field line with the magnetic equator. The result of employing our magnetic field line expressions, Equations (4.2) and (4.3), is visualized in Figure 4.1, where the dipole field is displayed for the meridional plane along the x-axis. Figure 4.1 shows that in the equatorial plane, when $z = 0$, the magnetic field only has a vertical component. Thus, charged particles with velocities in the equatorial plane remain restricted to this plane. These are known as equatorially mirroring particles. Thus, it is typical for the population of the equatorially mirroring particles to be considered separately from particles that are not confined to this plane. This is often done in literature to simplify the analysis, such as in Kabin *et al* [23], Li *et al* [24] [25] and Sarris *et al* [26] [27]. Similarly, we focus on the dynamics of equatorially mirroring particles exclusively.

Since the magnetic field in the equatorial plane only has a vertical component, it is convenient to express Equation (4.1) in cartesian coordinates of x, y, and z. Applying this $z = 0$ condition results in Equation (4.1) reducing to Equation (4.4). In this equation, the magnetic field is always in the positive z-direction. The motion of particles in the equatorial plane of a dipole similar to Equation (4.4) has been analytically studied extensively, some examples include Zeng

et al [6], Avrett [28]**,** Juarez [29] and Brizard *et al* [30].

$$\mathbf{B} = \frac{\mathrm{M}}{\mathrm{r}^3}\,\hat{\mathbf{e}}_{\mathbf{z}} \tag{4.4}$$

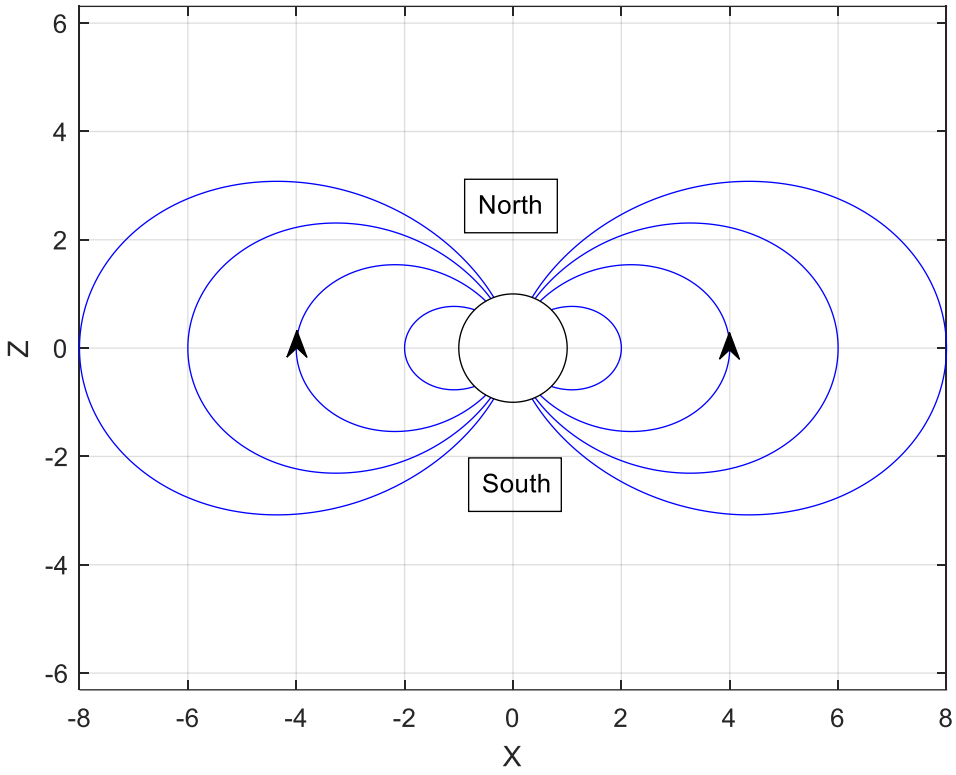

Figure 4.1: Magnetic dipole field lines in the Earth's meridional plane. Field lines are given in blue and Earth's position is in black.

In Equation (4.4) M is the dipole moment of Earth expressed such that $M = \mu_0 M_E/4\pi$. For the dipole magnetic field in this Chapter, we use generic units, with an M value of 1000. Since Equation (4.4) is inversely proportional to r^3, it is also noted that the magnetic gradient is in the radial direction pointing towards the origin. The magnetic vector potential corresponding to this field is given by Equation (4.5).

$$\mathbf{A} = -\frac{\mathrm{M}}{\mathrm{r}^2}\hat{\mathbf{e}}_{\boldsymbol{\varphi}} \tag{4.5}$$

The vector potential is useful to determine the canonical momentum established in Equation (2.16). Since A does not depend on φ, the φ-component of the canonical momentum is conserved. Substituting Equation (4.5) into Equation (2.16) and only using the φ-component of velocity P_φ is given by Equation (4.6).

$$P_\varphi = mv_\varphi - \frac{qM}{r^2} \tag{4.6}$$

$$v_\varphi = \frac{xv_y - yv_x}{r} \tag{4.7}$$

Alternatively, $v_\varphi = v\sin\xi$ where ξ is the angle between the position vector $\boldsymbol{r}$ and the velocity vector $\boldsymbol{v}$ measured counter-clockwise. These definitions and the typical trajectory of a particle moving between r_{min} and r_{max}, defined later, are illustrated in Figure 4.2. In this figure the blue trajectory represents an ion with initial conditions of $r_0 = [7, 0]$, $v_0 = [0, 3]$, $m_0 = 1$ and $q = 1$.

By applying P_φ with $v_\varphi = v\sin\xi$ the radial limits of motion for bound particles are determined. These are illustrated by the black dashed lines in Figure 4.2. This is done by realizing the particle is at r_{min} and r_{max} when ξ is at 90^o and -90^o respectively. Substituting these conditions into P_φ results in r_{min} and r_{max} when rearranging for r. These parameters, however, are most conveniently represented using an auxiliary variable r^*. We note that the expression for P_φ simplifies when $\xi = 0^o$ or 180^o. Under this condition, r represents the position when the velocity of the particle is radially directed, we introduce r^* to represent this value. There is a particular class of trajectories in this magnetic field which are simply circles centred on the dipole location. The velocity for this kind of motion is obtained simply by equating the Lorentz force with the centripetal acceleration required for circular motion. We call v^* the speed of this circular motion at the location of r^* [22]. The location of r^* is illustrated by the red dashed line in Figure 4.2. The expressions for r^* and v^* are given by Equations (4.8) and (4.9) below.

$$r^* = \left|\frac{qM}{P_\varphi}\right| \tag{4.8}$$

$$v^* = \frac{|qM|}{m(r^*)^2} \tag{4.9}$$

Applying this notation and simplifying the results we express the radial minimum and maximum limits of the trajectory in Equations (4.10) and (4.11) respectively [22].

$$r_{min} = \frac{2r^*}{1 + \sqrt{1 + \frac{4v}{v^*}}} \tag{4.10}$$

$$r_{max} = \frac{2r^*}{1 + \sqrt{1 - \frac{4v}{v^*}}} \tag{4.11}$$

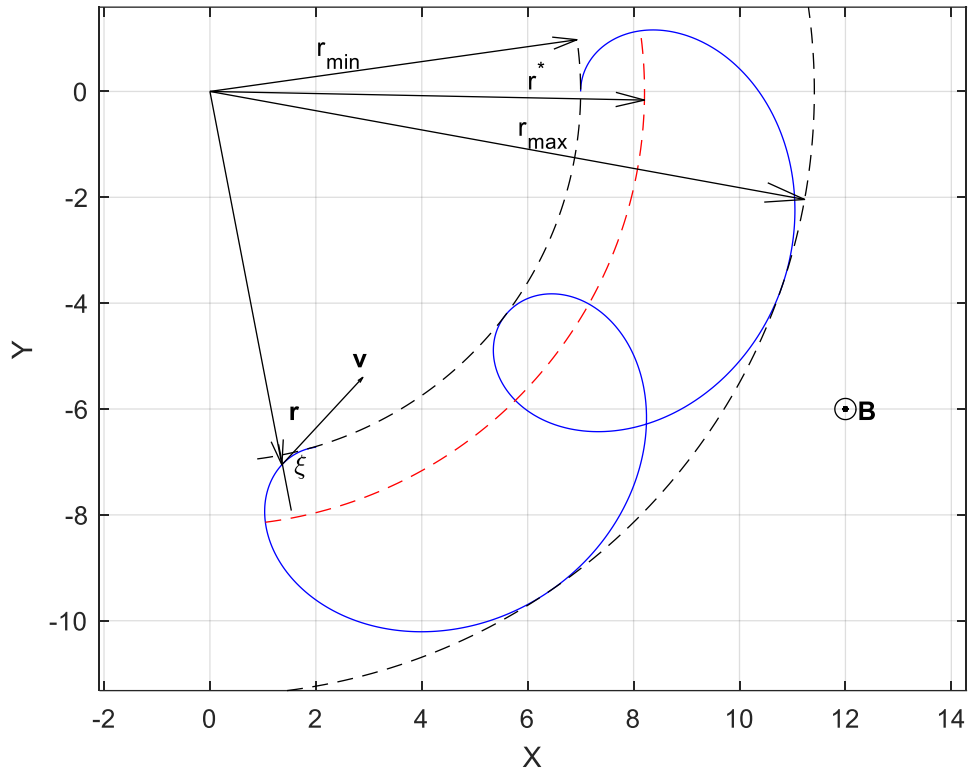

Figure 4.2: A typical trajectory of a particle in the equatorial field of a magnetic dipole. The particle is initiated with m_0 = 1, q = 1 r_0 = [7, 0] and v_0 = [0, 3]. The magnetic field is out of the page with M = 1000. The trajectory is the blue line, r_{min} and r_{max} are the black dashed lines and r^* is the red dashed line.

If $v > v^*/4$ r_{max} becomes undefined and the particle motion becomes unbounded. Meaning that the trajectory of the particle is no longer confined by Earth's magnetic dipole. Cosmic rays generally fall in this category, but in this thesis, only bound particles are examined [31].

The motion of charged particles in the equatorial plane of a dipole is known to have analytical solutions for the Equations of motion. These are expressed in terms of Jacobi elliptic functions [6]. The analytical solutions for the gyroperiod and the drift period are presented below in Equations (4.12) and (4.13) respectively, where the drift period is the complete rotation around the origin of the coordinate system [28].

$$T_{g\_Exact} = \frac{2r_*}{v}\int_{r_*/r_{min}}^{r_*/r_{max}} \frac{d\left(\frac{r^*}{r}\right)}{\left(\frac{r^*}{r}\right)^2\sqrt{1-\left(\frac{v^*}{v}\right)^2\left(\frac{r^*}{r}\right)^2\left(1-\frac{r^*}{r}\right)}} = \frac{2r^*}{v} I2\left(\frac{v}{v^*}\right) \tag{4.12}$$

This expression can be reduced to a combination of elliptic integrals of the first, second and third kind [28], however we do not use that formulation here. The solution for the drift period is given by (4.13) [6].

$$T_{d\_Exact} = -\mathrm{sgn}(qB)\frac{r^*}{v^*}\frac{I2\left(\frac{v}{v^*}\right)}{\int_{r^*/r_{max}}^{r^*/r_{min}} \frac{\left(1-\frac{r^*}{r}\right) d\left(\frac{r^*}{r}\right)}{\sqrt{1-\left(\frac{v^*}{v}\right)^2\left(\frac{r^*}{r}\right)^2\left(1-\frac{r^*}{r}\right)}}} = -\mathrm{sgn}(qB)\frac{r^*}{v^*}\frac{I2\left(\frac{v}{v^*}\right)}{I1\left(\frac{v}{v^*}\right)} \quad (4.13)$$

The inclusion of the negative sign here is because φ is conventionally measured counterclockwise from the *x*-axis. This ensures that ions drift clockwise in a positive *z*-directed magnetic field, and electrons drift counterclockwise. Overall, it is clear that the particle trajectory in the equatorial field of a magnetic dipole only depends on three parameters. These are *v*, *v** and *r**. This provides a very convenient method of scaling for any situation that varies in initial conditions [6].

4.2 GC Approximation for the Radial Magnetic Field Gradient

For the magnetic field in Equation (4.4), $\nabla B = [-3Mx/r^5, -3My/r^5, 0]$, substituting this into Equation (2.12) yields the following expression for the GC drift.

$$\mathbf{v_D} = \frac{3mv_\perp{}^2 r}{2qM}\left(y\hat{\mathbf{e}}_\mathbf{x} - x\hat{\mathbf{e}}_\mathbf{y}\right) \quad (4.14)$$

From this equation, we know that the drift velocity increases with *r* and is directed azimuthally in the φ-direction. For small *v*, Equation (4.14) can also be derived by expanding the change in radial position ($\Delta\varphi$) of a particle into a Taylor Series and dividing by Equation (4.13). Similarly, the gyroperiod given by Equation (2.7) is determined by expanding Equation (4.12) for small velocities. It is important to note, that these expressions depend on the value of *r*. For example, at r_{min} the GC drift velocity is at a minimum and at x_{max} the GC drift velocity is at a maximum. Therefore, it is important to use the correct initial r position to initialize the GC to ensure the GC does not overshoot or fall short of replicating the true trajectory of the particle. Finding the ideal *r* position to initialize the GC is one of the goals of this thesis. This is done by investigating various procedures of GC initialization using only the initial position and velocity of the particle. Using Equation (4.14) we can express the drift period of the particle as Equation (4.15) [6].

$$T_d = \frac{4\pi}{3}\frac{qM}{mv^2 r} \quad (4.15)$$

4.3 Code Accuracy

Prior to analyzing the particle trajectory, it is important to quantify the accuracy of the numerical integrator for this code. The absolute relative error is determined in the same manner as in Figure 2.4. Here we use the normalized difference of conserved quantities and their initial values. The conserved quantities for this case are P_φ and *v*. The resultant relative numerical error for one drift period was determined to be on the order of 10^{-11} for both P_φ and *v*. This is more than sufficient for our purposes.

4.4 Detailed Examination of Particle Trajectory

As an illustration, we initialize an ion with the same conditions as Figure 4.2 and integrate the Lorentz force, Equation (2.5), for one drift period. It should be noted that all trajectories for this case are initialized with the entire velocity pointed in the positive *y*-direction or φ-direction. The trajectory for approximately one drift period is shown in Figure 4.3. In this figure, the integration time was somewhat arbitrarily set to 53s so the trajectory does not stop at exactly one drift period. Using Matlab's events functionality to model exactly one drift period is possible but was deemed unnecessary here. Note that the trajectory, in general, is not a closed curve, since the ratio of the drift period to the gyration period is usually not a rational number.

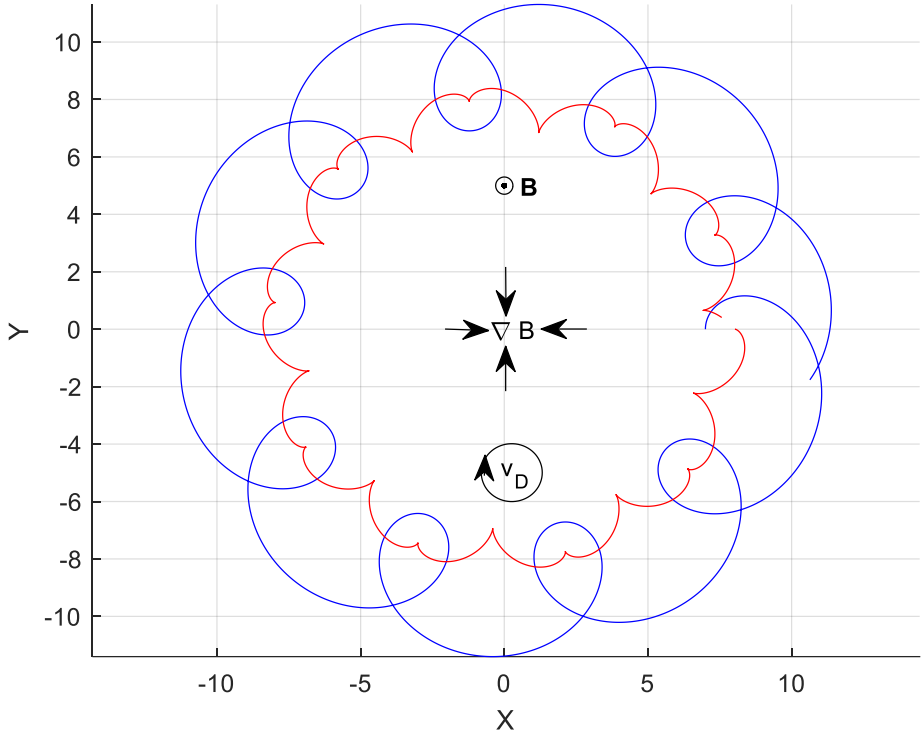

Figure 4.3: Trajectory of ion in the equatorial plane of a magnetic dipole. The particle is initiated with m_0 = 1, q = 1 r_0 = [7, 0] and v_0 = [0, 3]. The magnetic field is out of the page with M = 1000. The trajectory is shown in blue and gyrocenter in red.

In Figure 4.3 the blue line is the ion trajectory and the red line is the gyrocenter position calculated using Equation (2.11). The change in the radius of curvature of the trajectory is a result of the magnetic field increasing towards the origin in the radial direction. This radial-gradient stretches trajectory at r_{max} and compresses trajectory at r_{min}. With the magnetic field in the positive *z*-direction and the gradient in the radial direction, the particle must experience a drift in the φ direction, the direction of which is determined by the charge, with an electron drifting counterclockwise and an ion drifting clockwise, with the ion shown in Figure 4.3. The direction of the drift ensures that an ion initialized on the positive *x*-axis is always at r_{min} when with $v_x = 0$ and v_y is positive.

Similarly to Section 3.3, it is sufficient to analyze the motion of the particle over a single gyroperiod. Although an analytical expression for the gyroperiod is available in Equation (4.12), we can more easily terminate the numerical calculation using Matlab functionality as we did for the magnetic field with a constant gradient. We initialize all particles in our simulation with $v_r = 0$ and we implement an event function that terminates the integration when the radial component of the velocity reaches zero again. A typical ion trajectory for one gyroperiod is shown below in Figure 4.4 for the same initial conditions as in Figure 4.3.

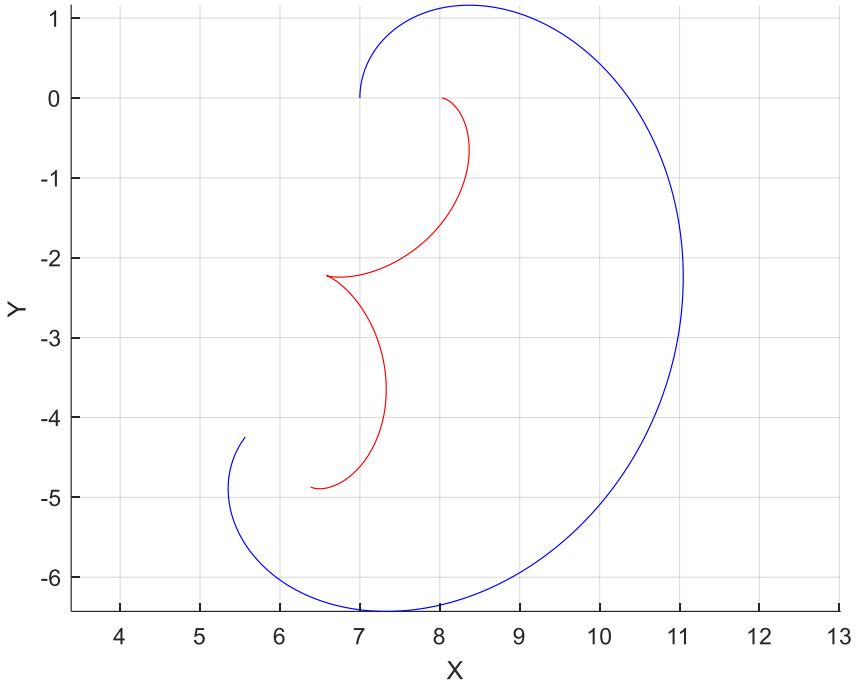

Figure 4.4: Trajectory of an ion for one gyroperiod. The particle is initiated with m_0 = 1, q = 1 r_0 = [7, 0] and v_0 = [0, 3]. The magnetic field is out of the page with M = 1000. The trajectory is shown in blue and gyrocenter in red.

To reiterate the red line in this plot shows the gyrocenter position which is mathematically equivalent to the evolute curve, or the center of the curvature as established in Equations (3.11) through (3.16).

Similarly to Section 3.3, we try to improve the accuracy of the GC approximation by averaging the magnetic field applied in Equation (4.14) [6]. To do this we introduce iterations to the gyrocenter calculation from Equation (2.11) to determine the location of the averaged magnetic field. The resulting gyrocenter iteration formula is given by Equation (4.16).

$$\mathbf{r}_{gc(i)} = \mathbf{r} + \frac{mr^3_{r_{gc(i-1)}}}{qM}[v_y, -v_x] \tag{4.16}$$

We use this equation to iterate the gyrocenter position until it converges or to determine if the gyrocenter diverges. To generate Equation (4.16), we substituted the magnetic field, Equation (4.4), into Equation (2.11), our gyrocenter formula. The letter i distinguishes the iteration number.

The initial condition is such that r^3 is taken at the trajectory of the particle. Like Chapter 2 we refer to the final convergence limit of this Equation as the converged gyrocenter position, while the center of curvature of the trajectory is referred to as the 1st gyrocenter.

Following the same procedure as in Chapter 2, we plot our iteration procedure in Figure 4.5. In this figure we show the location of the gyrocenter at the 1st, 2nd and 3rd iteration as well as the final converged position. In addition, the corresponding points along the trajectory, 1st iteration and converged gyrocenter are indicated with stars of the same colour for easier interpretation.

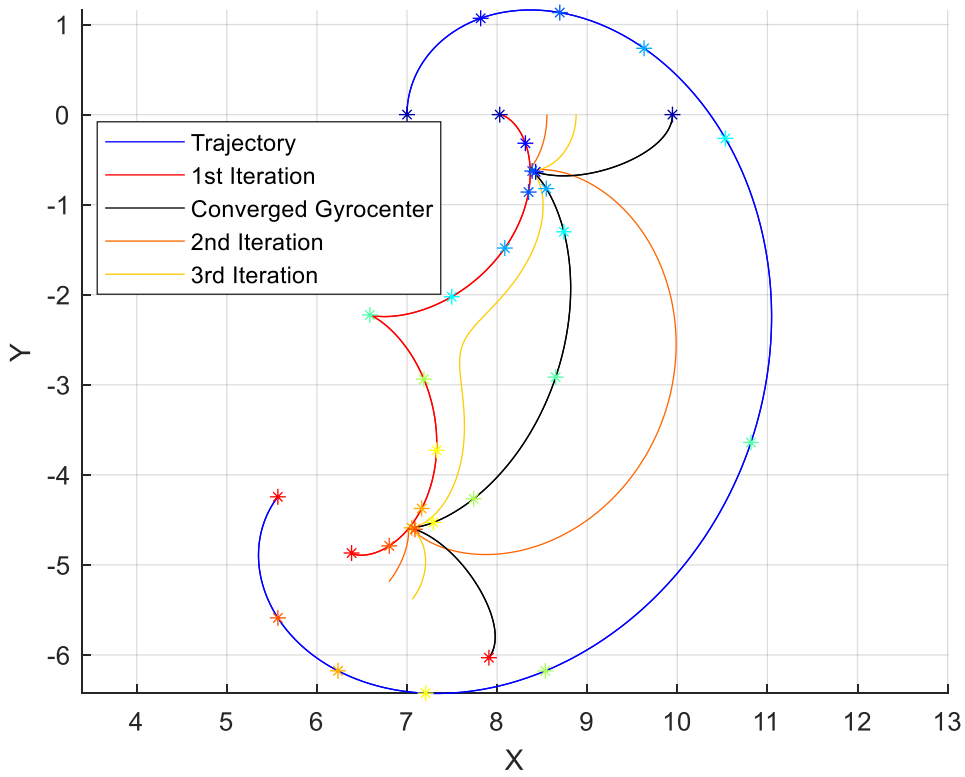

Figure 4.5: 1st, 2nd, 3rd and final iteration of gyrocenter and corresponding points for one gyroperiod. The particle is initiated with m_0 = 1, q = 1 r_0 = [7, 0] and v_0 = [0, 3]. The magnetic field is out of the page with M = 1000. The trajectory is shown in blue, 1st gyrocenter in red, 2nd gyrocenter in orange, 3rd gyrocenter in yellow and the final gyrocenter in black.

In Figure 4.5 the 1st, 2nd and 3rd iterations are shown to slowly converge towards the final converged gyrocenter. To reach the converged result a total of 25 iterations were used. However, at the 20th iteration, the difference between the iterations is on the order of 10^{-4}, our convergence threshold from Chapter 3. To ensure this result is converging a comparison was done on the difference at 100 iterations. Under this iteration number, changes were on the order of 10^{-6}. Therefore, it was concluded that the result shown in Figure 4.5 is indeed fully converged.

The cusps of the converged gyrocenter serve as a common point between all iterations greater than one, as seen by the fact they all intersect the same point on the 1st iteration. This point is more easily visualized by viewing the stars in Figure 4.5. Here it is clear that the converged gyrocenter cusps correspond to the 3rd star on either side of the ion's trajectory. This occurs at the

point where the velocity of a particle is directed in the radial direction. Therefore, it is concluded that the converged gyrocenter and the 1st iteration share a common point when velocity is in the same direction as the gradient of the magnetic field. This point is considered the most stable point for the gyrocenter iterations, where the converged limit is achieved on the very first iteration. Intuitively it can also be concluded that the most unstable point, where the iterations take the longest time to converge, occurs where the velocity is completely in the φ-direction, or perpendicular to the magnetic field gradient. More specifically this occurs at r_{min} and r_{max}. This is visualized by noticing that the green star on the 1st gyrocenter iteration is close to r_{min}, and is not near the center of the particle trajectory. However, at even higher velocities, this point does return close to the center of the particle trajectory. This is only because the particle is approaching unbound conditions and r_{max} increases rapidly at higher velocities, causing the 1st gyrocenter to also move with it. This is shown in Figure 4.6.

To illustrate the difference in gyrocenter iteration we examine a higher velocity of $v = 3.5$. The higher velocity of $v = 3.5$ was chosen because it is close to the threshold speed above which the particle becomes unbound [22]. The unbound velocity was determined by using applying the unbound condition of $v > v^*/4$. For the initial conditions of this case, this results in $v = 3.5015$ for a particle to become unbound. The results of 11 iterations for $v = 3.5$ are shown in Figure 4.6.

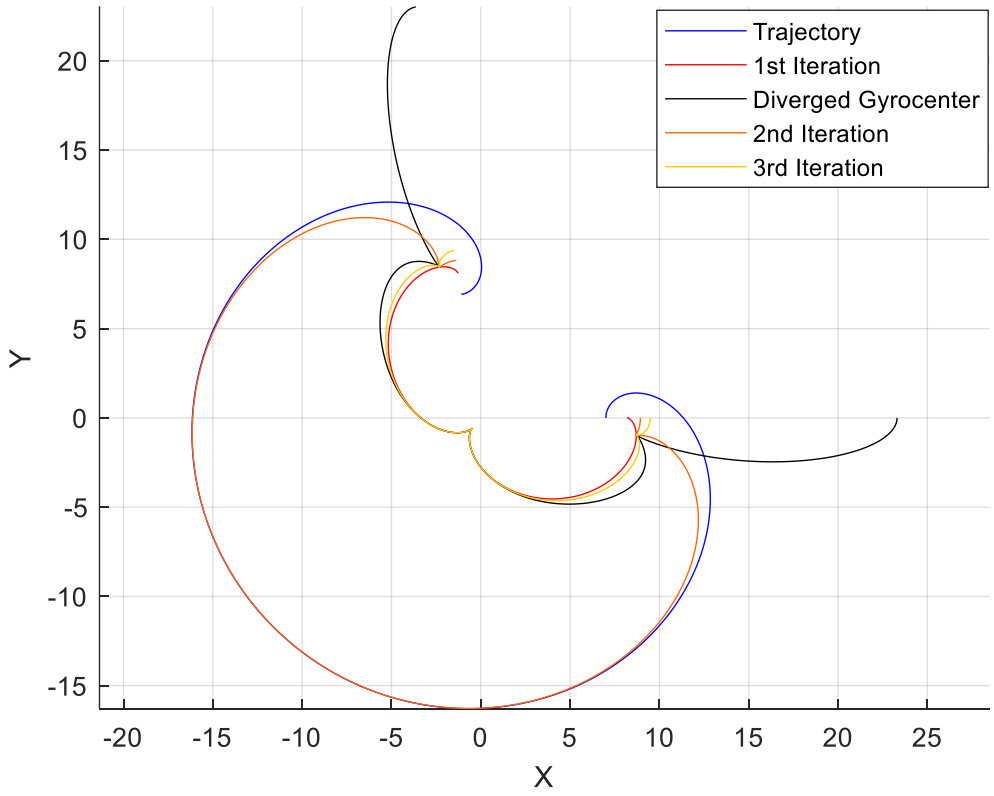

Figure 4.6: 1st, 2nd, 3rd and final iteration of gyrocenter for $v = 3.5$ for one gyroperiod. The particle is initiated with $m_0 = 1$, q = 1 $r_0 = [7, 0]$ and $v_0 = [0, v]$. The magnetic field is out of the page with $M = 1000$. The trajectory is shown in blue, 1st gyrocenter in red, 2nd gyrocenter in orange, 3rd gyrocenter in yellow and final gyrocenter in black.

Contrasting Figure 4.6 with Figure 4.5 it is shown that convergence was not reached. This is seen by the protrusion of the final iteration in black outside the actual particle trajectory, this protrusion increases as the iteration numbers are increased. The number of iterations used in this figure was 11, though the gyrocenter iterations fully diverge at iterations ≥ 14. At these iterations, the scale of the diverged gyrocenter is much larger than the particle trajectory, which is why we chose to show the results of 11 iterations. Overall, at $v = 3.5$, or relatively high velocities, the gyrocenter iterations diverge before the unbound threshold of 3.5015 is reached. This divergence first appears at r_{min}, which is the most unstable point along the particle trajectory. This is not surprising, since the gyrocenter position at the 2nd iteration is displaced onto the particle trajectory. Numerical calculations from Zeng *et al* show that this iterative procedure converges when $v < 0.204v^*$ [6]. For the initial conditions of this case, this results in $v = 3.0217$ for gyrocenter iterations to diverge. This indicates that the GC approximation also breaks down before unbound velocity thresholds are reached.

We would like to point out that the gyrofrequency calculated using Equation (2.7) differs from the exact value given by Equation (4.12) when using the magnetic field at the converged gyrocenter, and this difference becomes more pronounced as the velocity increases. Gyrofrequency is typically not a particularly important parameter within the GC approximation, but it is used, for example, if the trajectory of the particle is approximated with cycloids. If either the drift velocity or the gyrofrequency used in the cycloid approximation is inaccurate, the GC approximation suffers from secular error [6]. This is examined in more detail in Section 4.6.

We now discuss the effects of different GC starting locations for the integration of the GC drift velocity given by Equation (4.14). For the equatorial plane of a magnetic dipole, the magnitude of the drift velocity depends on the initial r position only, increasing proportionally with r^2. Thus, to calculate the arc length travelled along the φ-direction of the GC we need simply to multiply the GC drift velocity by the time interval we consider. Instead, we use ode45 to integrate the GC drift velocity, which is a more general approach. This is done by using the starting locations of the particle trajectory, the 1st gyrocenter and the converged gyrocenter to integrate Equation (4.14). The result is displayed in Figure 4.7. In this figure the thicker lines represent the GC approximation while the thinner lines represent the particle trajectory, the 1st gyrocenter and the converged gyrocenter. It should be noted here that, unlike the magnetic field with a constant gradient, the GC approximation overestimates the drift velocity when it is evaluated at the converged gyrocenter. In addition, it is not clear if the converged gyrocenter improves upon the 1st gyrocenter at this relatively high velocity. When using the initial position of the particle the GC approximation underestimates the actual drift, however, this is to be expected since the particle is initialized at r_{min} where B is the strongest. If initialized at r_{max} the GC approximation would thus overestimate the drift the most. Using the 1st gyrocenter this approximation still underestimates the drift, but is clearly more accurate than using the particle position.

In Figure 4.7 the particle trajectory is initialized at r_{min}, but we note that in the practical application the particle will not always be initialized at r_{min}, instead, it would follow a probability of distribution between r_{min} and r_{max}. Thus, the probability of distribution between these limiting values would result in various underestimating or overestimating of the true particle drift. The same logic applies to either the 1st gyrocenter or the converged gyrocenter, but the variation in drift inaccuracy would be smaller since these curves are more tightly constrained in the r-direction.

Therefore, the overestimation or underestimation of the drift velocity is considerably reduced and either of these methods improves the consistency of the GC drift calculation. Still, the GC drift initialized at the converged gyrocenter significantly overestimates the particle's true drift. This is a result of $v = 3$ approaching divergence conditions.

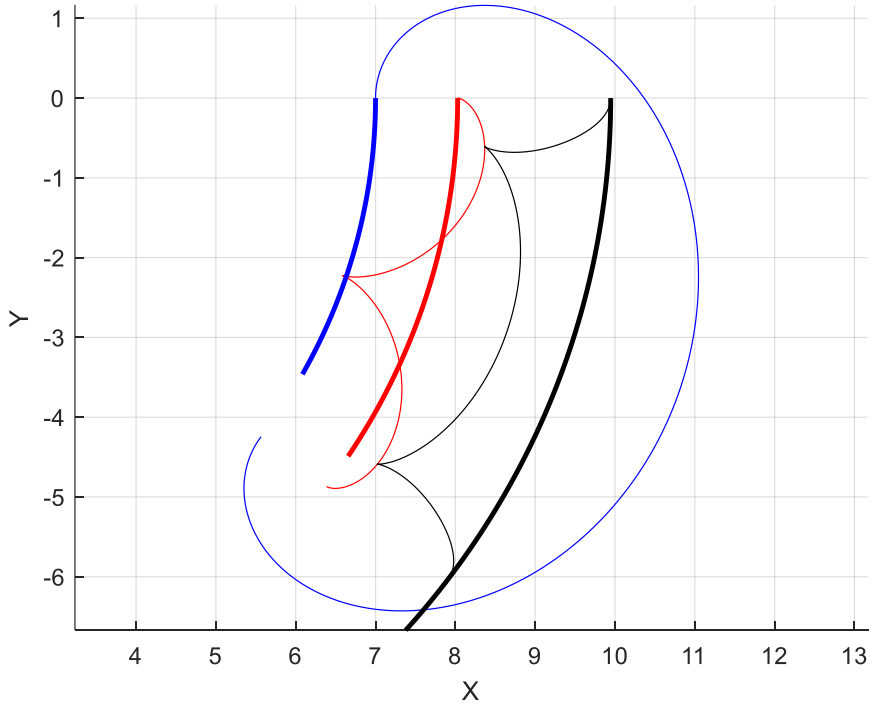

Figure 4.7: GC integration using trajectory, 1st gyrocenter and converged gyrocenter as starting locations for one gyroperiod. The particle is initiated with $m_0 = 1$, q = 1 $r_0 = [7, 0]$ and $v_0 = [0, 3]$. The magnetic field is out of the page with $M = 1000$. The trajectory is shown in blue, 1st gyrocenter in red and converged gyrocenter in black, with the same colour thicker lines corresponding to the GC approximation.

To quantify the error in the drift velocity associated with different possibilities for initialization of a GC simulation we plot the arclength error after one gyroperiod as a function of the particle velocity. This process is applied to the particle position, the first gyrocenter and the converged gyrocenter. The tracing error plot is shown in Figure 4.8 below on a log-log scale. The range of velocities for which the calculations are carried is from $v = 0.01$ to $v = 3.02$, to coincide with the divergence threshold.

Figure 4.8 shows that the GC tracing error is proportional to v^3 when using the position of the particle as a starting point and is proportional to v^4 when using both the 1st gyrocenter and converged gyrocenter. This scaling is the same as for the magnetic field with a constant gradient in Section 3.3 and likely holds for general magnetic fields as well. Figure 4.8 also shows that using the converged gyrocenter at high velocities is worse than using the 1st gyrocenter above $v = 2.7$ and reaches trajectory error at the divergence threshold of $v = 3.0217$. However, the converged gyrocenter does offer significant improvement for $v < 2$, at these velocities the converged gyrocenter is a factor of three smaller in tracing error when compared to the 1st gyrocenter. The

deviation from the linear shape at the high velocity extreme is attributed to velocities approaching the gyrocenter divergence threshold. At the low-velocity extreme, numerical limitations affect the calculation of the arc length as changes in the φ position of the particle get significantly small and are thus hard to calculate numerically.

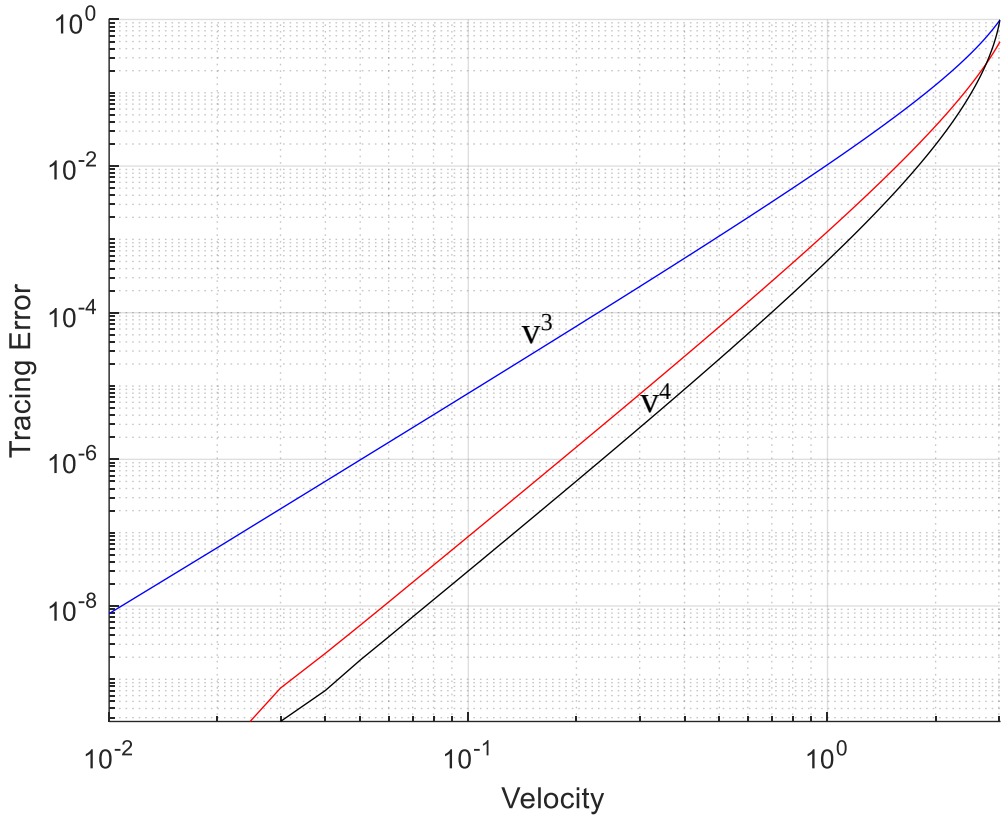

Figure 4.8: Tracing error for v = 0.01 to v = 3.02. The particle is initiated with m_0 = 1, q = 1 r_0 = [7, 0] and v_0 = [0, v]. The magnetic field is out of the page with M = 1000. Tracing error for trajectory is shown in blue, 1st gyrocenter in red and converged gyrocenter in black.

In the discussion above, when using the particle position as the starting point, the GC approximation is initialized at r_{min} in Figure 4.7 and Figure 4.8. Thus, the tracing error proportional to v^3 has only been proven for the r_{min} condition. Of course, initializing the GC calculation at one of the extremes, such as r_{min} and r_{max} gives the largest error. To test the proportionality of v^3, for any point along the particle trajectory, we distribute the GC approximation starting location between r_{min} and r_{max}. For this analysis, we use 250 points to achieve sufficient resolution. Like previously, the distance travelled by the GC approximation is compared to the true drift of the particle for one gyroperiod. Since the GC trajectory is circular, we use the difference in arc length, as we did in Figure 4.8. For comparison to the GC approximation endpoints, we must determine the endpoint of the particle at every point between r_{min} and r_{max}. Thus, we use the change in φ from Figure 4.7 and the r-value at each GC initialization point to calculate the corresponding arc length of the particle's trajectory. We now select two velocities from Figure 4.8 to compare the difference in their tracing errors from r_{min} and r_{max}. This is done for v = 0.1 and v = 0.2 and is displayed on the

semi-log plot in Figure 4.9. In this figure we normalize the *x*-axis such that 0 corresponds to r_{min} and 1 corresponds to r_{max}.

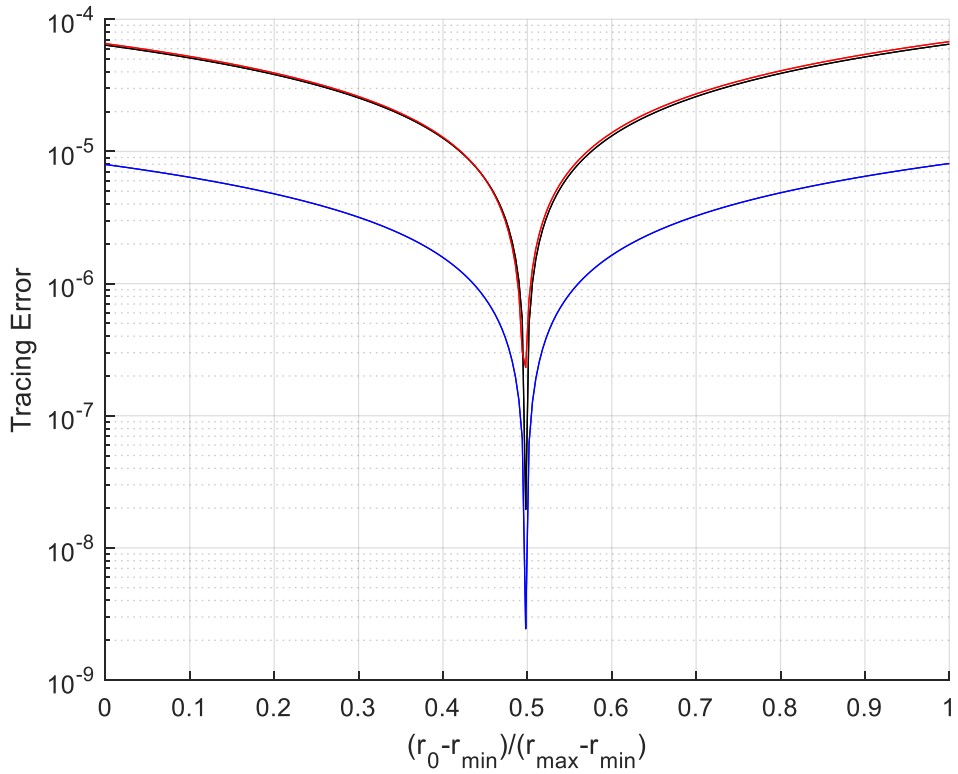

Figure 4.9: Tracing error of GC drift between r_{min} and r_{max} of the particle trajectory for v = 0.1 (blue) and v = 0.2 (red). The particle is initiated with m_0 = 1, q = 1 r_0 = [r_{min} to r_{max}, 0] and v_0 = [0, v]. The magnetic field is out of the page with M = 1000. The black line is the blue line multiplied by 2^3.

In Figure 4.9 the blue line corresponds to v = 0.1 and the red line corresponds to v = 0.2. Unsurprisingly the smallest tracing error occurs at the mean of r_{min} and r_{max} for these relatively low velocities, while the largest tracing error occurs at the extremes. The most important part of Figure 4.9 is the black line. It is the tracing error results of v = 0.1 multiplied by our proportionality of v^3, for this situation this is 2^3. Since it coincides with the results of v = 0.2 we thus conclude that tracing error is always proportionate to v^3 when using the particle trajectory as a GC starting point. Regardless of the location between r_{min} and r_{max}. The deviation of the black line from the red at 0.5 is to be expected. This is because tracing error approaches zero faster at 0.5 when velocity is decreased, or the number of points used between r_{min} and r_{max} increases.

4.5 Analysis of the Magnetic Moment

We now analyze the magnetic moment as a means to measure the accuracy of the GC approximation. First, we derive the 2nd order expansion for the magnetic moment for use later in this section. This is done by applying the magnetic field given by Equation (4.4) to our general form of μ given by Equation (2.19). The resulting formula is given by Equation (4.17) [10]. In this expression for μ, the magnetic field is supposed to be evaluated at the particle position.

$$\mu_{T2} = m\frac{v^2}{B}\left(1 + 3\frac{m}{qrB}v_\varphi + \left(\frac{m}{qrB}\right)^2\left(6{v_\varphi}^2 + \frac{15}{4}v^2\right)\right) \tag{4.17}$$

For this particular magnetic field, the exact expression for the magnetic moment can be calculated, this is given by Equation (4.18) [10].

$$\mu_{Exact} = \left|\frac{q}{\pi}\frac{P_\varphi}{m}\right|\left(\pi - \sqrt{1+k}\,\Xi\left(\frac{2k}{1+k}\right)\right) \tag{4.18}$$

$$k = \frac{4qMv}{m\left(\frac{P_\varphi}{m}\right)^2} \tag{4.19}$$

The normalization used in the original paper by Kabin [9] is slightly different from that used in this thesis, thus Equation (4.18) is converted to our notation. To make k unitless, P_φ is divided by m to account for differences in normalization choices between this paper and Kabin [10]. For the same reason, q/π is multiplied at the beginning of the equation. In this expression, Ξ is the complete elliptic integral of the second kind as introduced in Section 2.6. This version of the adiabatic invariant remains exactly constant along the entire trajectory of the particle, while other approximations for the adiabatic invariant oscillate at the gyrofrequency due to the change in magnetic field strength along the trajectory of the particle. In the following, we normalize the various approximations for the adiabatic invariant with the value of the exact invariant.

We start by comparing the zeroth-order magnetic moment given by Equation (2.18) to the exact solution given by Equation (4.18). Applying Equation (2.18) using the value of the magnetic field strength along the ion trajectory (blue), the 1st gyrocenter (red) and converged gyrocenter (black) we generate Figure 4.10. These colours are consistent for all magnetic moment plots generated in this section. The values displayed here are normalized with the exact solution of the adiabatic invariant. Thus, the exact solution is represented by the horizontal cyan line at a value of one. This was done for one gyroperiod at a velocity of $v = 3$ and $v = 0.3$.

On the top panel, the exact solution does not correspond to the mean of oscillation for any of the approximate magnetic moments. Though the converged gyrocenter is relatively close to the exact expression, the area above the cyan line is still clearly larger than below. Viewing the size of the amplitude variations it is clear that the magnetic moment calculated along the particle trajectory is the least accurate, at most this amplitude deviates 120% from the exact solution. In comparison, the 1st gyrocenter deviates a maximum of 50%, while the converged gyrocenter deviates a maximum of 30%. Thus, it is clear the converged gyrocenter is the most accurate method when using the zeroth-order magnetic moment given by Equation (2.18). This differs from the results in tracing error accuracy from the previous section, where the 1st gyrocenter was superior to the converged gyrocenter at $v = 3$. Thus showing that the converged gyrocenter is more valuable in magnetic moment approximations than GC initialization at relatively high velcoities. The asymmetry in the exact solution in the top panel is attributed to the relatively high velocity of the particle. On the bottom panel, we decrease the velocity by a factor of 10 to show that the application

of Equation (2.18) is much closer to the exact solution. This is demonstrated by the increased symmetry and the decreased deviation in maximum amplitude. The symmetry on the bottom panel shows that the 1st gyrocenter, at relatively lower velocities, provides a very reasonable approximation to the true gyrocenter position.

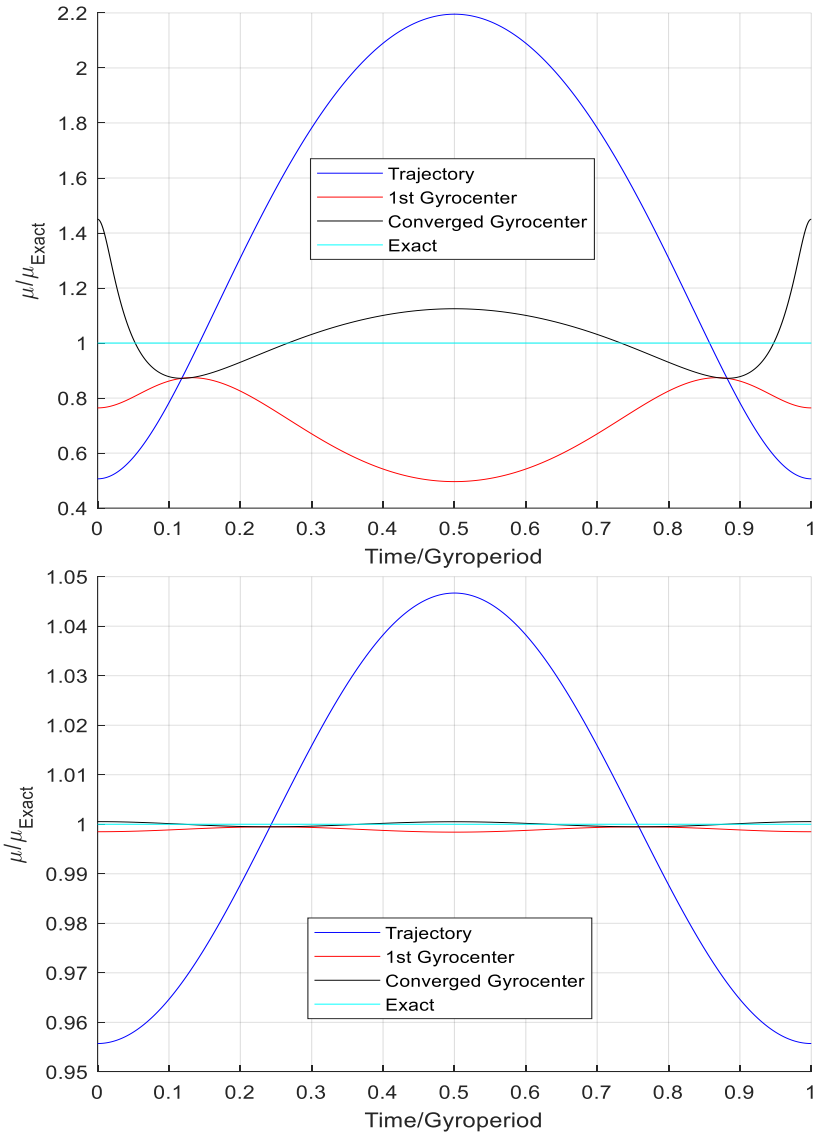

Figure 4.10: Normalized magnetic moment (2.18) at the trajectory, 1st gyrocenter and converged gyrocenter at v = 3 (top) and v = 0.3 (bottom). The particle is initiated with m_0 = 1, q = 1 r_0 = [7, 0] and v_0 = [0, v]. The magnetic field is out of the page with M = 1000. The magnetic moment for trajectory is shown in blue, 1st gyrocenter in red, converged gyrocenter in black and exact expression in cyan.

For further comparison, we now apply the second-order version of the magnetic moment, which is given by Equation (4.17). This is done using B along the particle trajectory. Despite the formulation of Equation (4.17) being derived for the trajectory of the particle we also use B at the converged gyrocenter in an attempt to improve Equation (4.17) further. All approximations of the magnetic moment are now displayed in Figure 4.11.

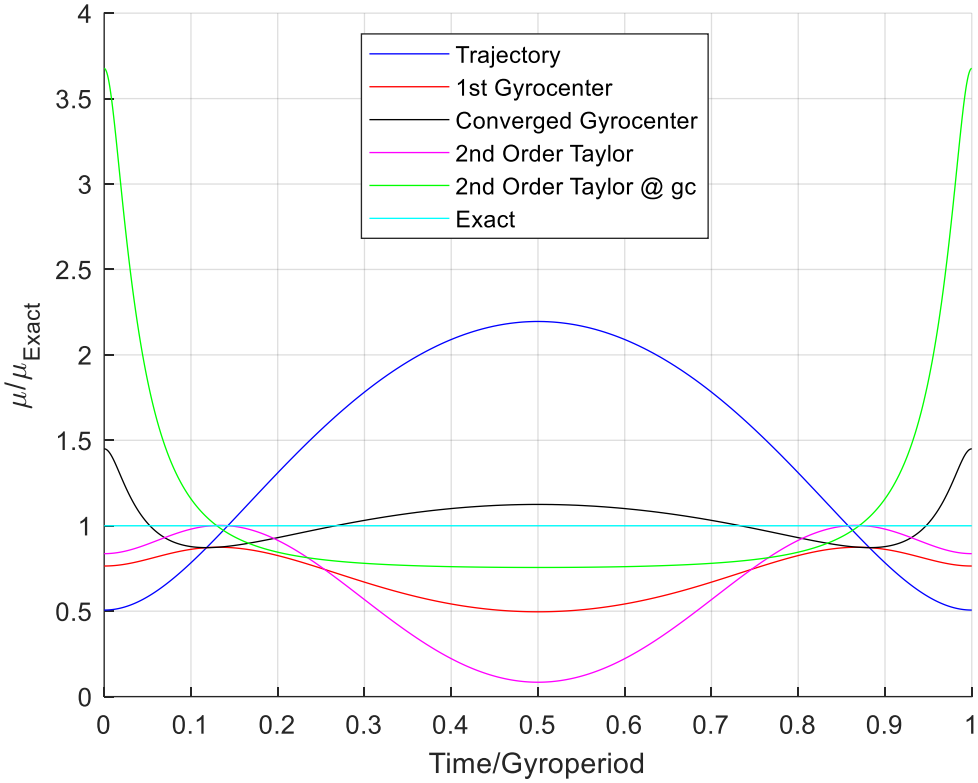

Figure 4.11: Various magnetic moment approximations and the exact expression for one gyroperiod. The particle is initiated with m_0 = 1, q = 1 r_0 = [7, 0] and v_0 = [0, 3]. The magnetic field is out of the page with M = 1000. Magnetic moment (2.18) using the trajectory is shown in blue, 1st gyrocenter in red and converged gyrocenter in black. Magnetic moment (4.17) using the trajectory is shown in magenta and converged gyrocenter in green. The exact expression is in cyan.

At this relatively high velocity the second-order Taylor series expansion does not increase the accuracy of the magnetic moment calculation when compared to Equation (2.18) applied at the converged gyrocenter. Quantified the maximum amplitude deviation from the exact solution is 320% for μ_{T2} when using B at the converged gyrocenter (green) and 90% for μ_{T2} when using B at the actual trajectory (magenta). Interestingly these maximum deviation points do not occur at the same points along the trajectory, but do occur at the iteration unstable points of r_{min} and r_{max}. Thus, maximum deviation occurs at opposite radial extremes for the 1st gyrocenter and the converged gyrocenter. Therefore, there is a gyrocenter iteration in which r_{min} changes to r_{max} as the maximum deviation point. We note that the Taylor series expansion given by Equation (4.17) is based on the position of the particle. Thus, applying it to the gyrocenter position is, strictly speaking, not justified. However, it is natural to check if using the converged gyrocenter instead of the particle position improves the accuracy of this calculation. Clearly, as Figure 4.11 shows, it does not.

Next, we calculate the maximum deviation of μ from μ_{Exact} across a wide range of velocities. We define this measurement as the error in this calculation. The dependence of the magnetic moment error on the velocity is graphed on a log plot from a velocity of v = 0.01 to v = 3.02 and is displayed below in Figure 4.12.

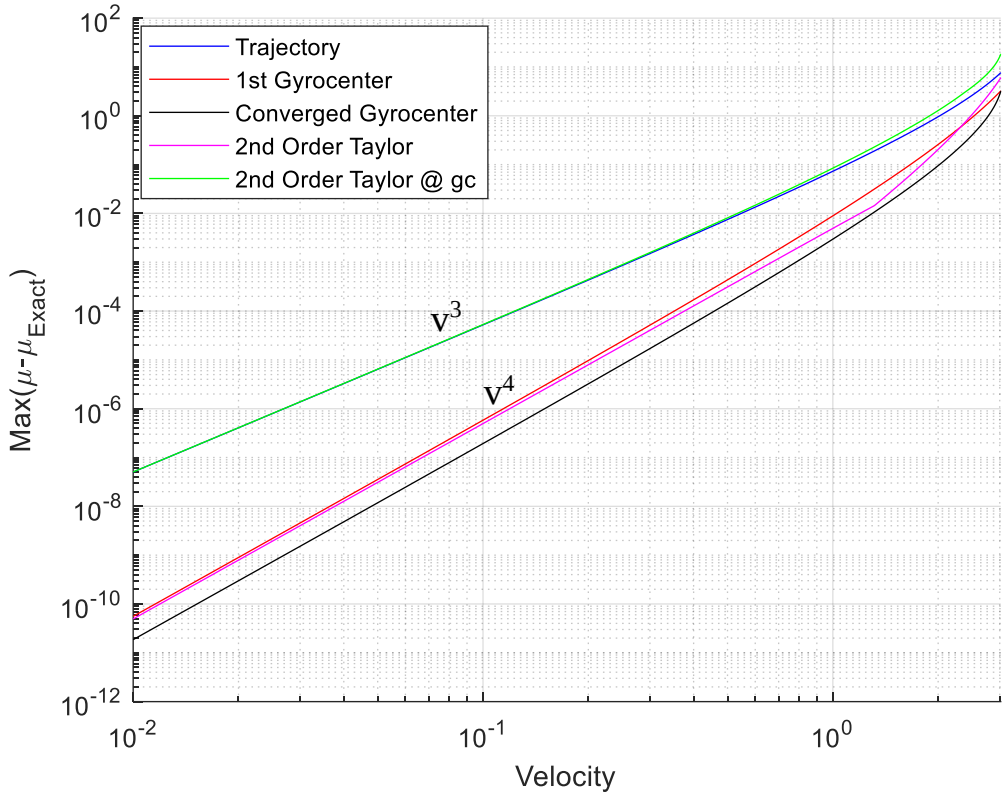

Figure 4.12: Error in approximate magnetic moments vs exact expression for v = 0.01 to v = 3.02 for one gyroperiod. The particle is initiated with m_0 = 1, q = 1 r_0 = [7, 0] and v_0 = [0, v]. The magnetic field is out of the page with M = 1000. Magnetic moment (2.18) using the trajectory is shown in blue, 1st gyrocenter in red and converged gyrocenter in black. Magnetic moment (3.19) using the trajectory is shown in magenta converged gyrocenter in green. The exact expression is in cyan.

Figure 4.12 shows the differences in magnetic moment error calculations as a function of velocity. For Equation (2.18) using B at the particle trajectory and Equation (4.17) using B at the converged gyrocenter, the error is proportional to v^3. This is the slowest rate of convergence for all of the magnetic moments. For Equation (2.18) using B at the 1st gyrocenter and converged gyrocenter, along with Equation (4.17) using B at the particle trajectory, the error is proportional to v^4. For all velocities analyzed the application of Equation (2.18) at the converged gyrocenter is the most accurate method of calculating the magnetic moment. This is different from our analysis of the magnetic field with a constant gradient, where the most accurate approximation was a combination of the 2nd order Taylor expansion using B along the trajectory of the particle and Equation (2.18) using B at the converged gyrocenter. Another difference is that the calculation of the 2nd order Taylor expansion using B at the particle trajectory and the converged gyrocenter are now proportionate to v^3 and v^4 respectively, while before they were proportionate to v^4 and v^5 respectively. In addition, at a v = 1.34, the calculation of Equation (4.17) at the particle trajectory kinks upwards. At v = 1.34 the error changes from being proportional to v^4 to v^6. The reason for this change is not immediately clear and is simply noted for thoroughness as it has no significant impact on the results. Lastly, the deviation of the linear sloped shape at the high velocities is attributed to the breaking down of the GC approximation.

Lastly, Figure 4.12 shows that using the second-order expansion for the magnetic moment gives results very close to using the basic formula for the magnetic moment applied at the first-order gyrocenter position.

4.6 Alternative Guiding Center Starting Location

Similar to the magnetic field with a constant gradient, radial positions between r_{min} and r_{max} exist where B is such that using Equations (2.18), (2.7) and (4.15) give exact results for calculating the adiabatic invariant, the gyroperiod, and the drift velocity. In this Chapter, we use the drift period instead of the drift velocity as the results are equivalent. Like before, these locations are analyzed in an attempt to improve the GC initialization. For the equatorial plane of a magnetic dipole, the location of these exact solutions is achieved by substituting the exact solutions into their respective B-dependent equations. Since B is a function of r, we simply rearrange for r. The final forms of these three Equations are given by Equations (4.20), (4.21) and (4.22). Here r_{μ}, r_{Tg} and r_{Td} are the radial locations where the exact value is achieved for μ, T_g and T_d respectively

$$r_{\mu} = \sqrt[3]{\frac{\mu_{exact} M}{mv^2}} \tag{4.20}$$

$$r_{Tg} = \sqrt[3]{\frac{T_{g\_Exact}|q|M}{2\pi m}} \tag{4.21}$$

$$r_{Td} = T_{d\_Exact}\left(\frac{4\pi}{3}\right)\left(\frac{|q|M}{mv^2}\right) \tag{4.22}$$

The radial positions where these exact values are achieved are now plotted as a function of velocity for v = 0.01 to v = 3.5. These values of r were normalized by subtracting r_{min} and dividing by r_{max} - r_{min} so that a value of zero corresponds to r_{min} and a value of one corresponds to r_{max}. Thus, when the velocity decreases all three r-positions converge at the mean of the particle's bounds, represented by 0.5, as expected. This is displayed in Figure 4.13 below.

From Figure 4.13 it is determined that the radial location of r_{Tg} deviates the least from 0.5 up until a velocity of 3.2, at this point, r_{Td} has the least deviation from 0.5. Additionally, r_{μ} deviates the most out of all exact locations up until a velocity of 3.4, at this point, r_{Tg} has the most deviation from 0.5. Ideally, all three exact quantities would be conserved, but in practical applications, one needs to choose between trade-offs in accuracy between μ, T_g and T_d, as demonstrated in Figure 4.13. Since conservation of T_g is only really used for epicycloid fits the best GC starting location for really high energy particles lies between r_{Td} and r_{μ}. However, in most applications the drift period takes priority and thus the location of r_{Td} is the preferred location for the GC approximation. How this compares to the converged gyrocenter is left for future work.

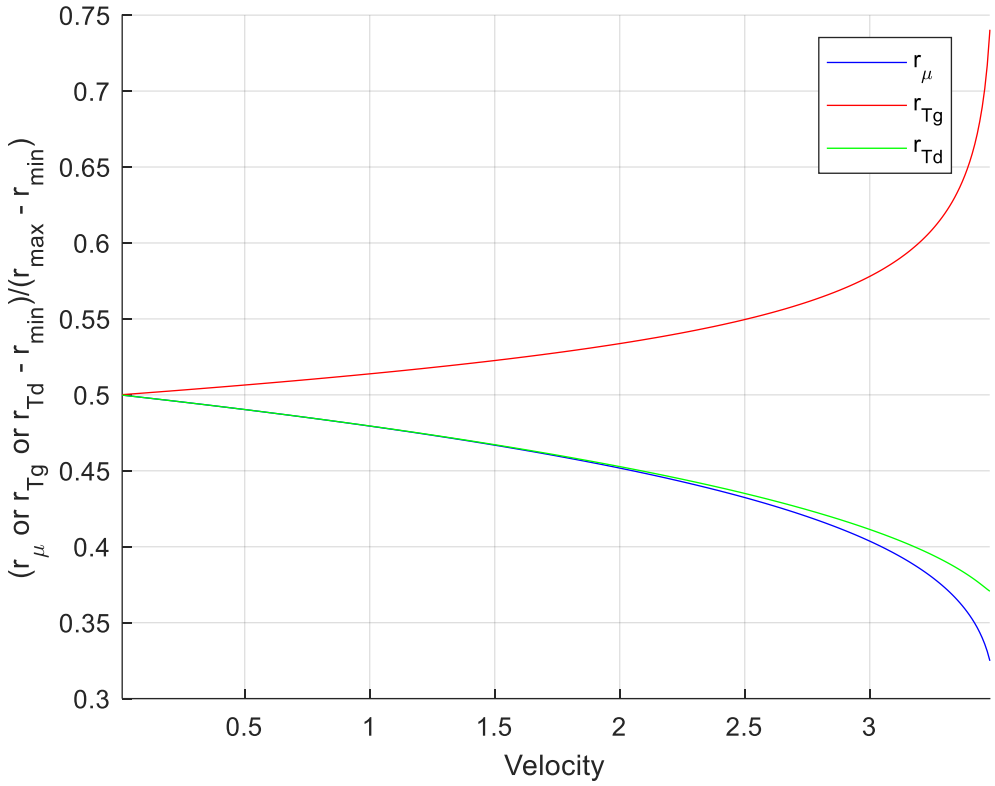

Figure 4.13: Normalized *r* distance along the trajectory where μ, T_g and T_d equal their respective exact expression for v = 0.01 to v = 3.48. The particle is initiated with m_0 = 1, q = 1 r_0 = [7, 0] and v_0 = [0, v]. The magnetic field is out of the page with M = 1000. The magnetic moment is shown in blue, gyroperiod in red and drift period in green.

The direction of deviation should also be noted as towards r_{min} for the location of r_μ and r_{Td} and towards r_{max} for r_{Td}. Contrasting this with the results from the constant gradient analysis in Section 3.5 one notices that the direction of deviation is opposite for the exact μ and exact T_g locations. This is attributed to the direction of the gradient of the magnetic field with respect to the particle bounds. In this chapter, r_{min} corresponds to B maximum, while in Chapter 3, x_{min} corresponded to B minimum, the opposite is true for the maximum boundary. The reason why r_{Td} did not change deviation direction, when compared to x_{VD} from Chapter 3, is because the drift period and drift velocity are inversely proportional. Taking these exact radial locations and overlaying them onto the ion trajectory for one gyroperiod at v = 3 yields Figure 4.14.

Comparing this figure with Figure 4.7 illustrates that the location of r_μ, r_{Tg} and r_{Td} all improve the tracing error at a velocity of v = 3. This is because the GC approximation initiated at the converged gyrocenter significantly overestimated the drift. In Figure 4.14 r_μ, r_{Tg} and r_{Td} are all positioned at a stronger B position than the converged gyrocenter, and therefore the GC drift is more accurate. Quantifying this accuracy is left for future work. Overall we have shown that there exist multiple locations for GC initialization that improve upon the conventional application of the 1st gyrocenter.

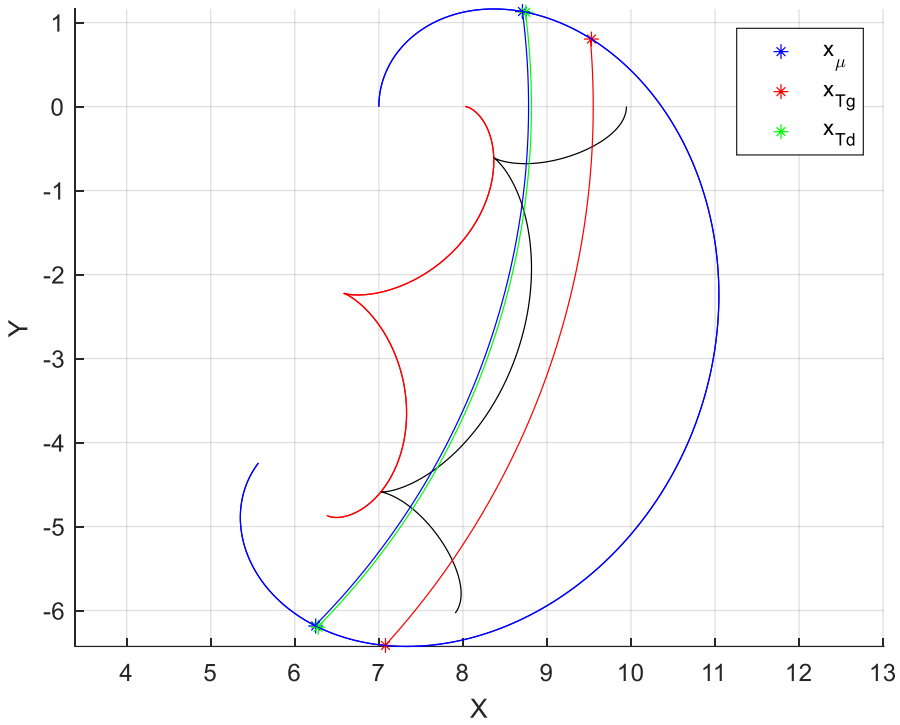

Figure 4.14: GC initialization options overlayed onto trajectory, 1st gyroradius and converged gyrocenter for one gyroperiod. The particle is initiated with m_0 = 1, q = 1 r_0 = [7, 0] and v_0 = [0, 3]. The magnetic field is out of the page with M = 1000. The trajectory is shown in blue, 1st gyrocenter in red and the converged gyrocenter in black. Arc lines corresponding to the initialization option for r_μ are shown in blue, r_{Tg} in red and r_{Td} in green.

4.7 Conclusion

In this chapter, we analyzed in detail the motion of charged particles confined to the equatorial plane of a magnetic dipole. The existence of analytical solutions for equatorially mirroring particles allowed for a more in-depth analysis of this particular field. Specifically an axisymmetric magnetic field with a gradient in the inward radial direction. This magnetic field is used to illustrate the accuracy of the GC approximation applied to particles in the inner magnetosphere region, such as particles in the inner Van Allen Belts centred at 1.5 R_E [2].

Topics discussed in this section were how to choose an initial point for the GC approximation, and what method should be used to calculate the magnetic moment. The fact that this magnetic field has symmetry ensures the conservation of the canonical angular momentum, which was used to provide analytical Equations for the particle bounds.

To evaluate GC initial position options, we started by adding iterations to the gyrocenter Equation (2.11) to average the value of B. This restricted the radial range of the gyrocenter for every iteration until a converged gyrocenter was reached. Thus, when compared to using the particle position, the consistency of the GC drift calculation was improved. Analyzing these iterations at higher velocities showed the existence of stable and unstable points along the gyroperiod. For the

unstable point, this occurred at r_{min} and r_{max}, when the velocity was completely directed in φ or perpendicular to the gradient. For the stable point, this occurred when the velocity was completely directed in the radial direction or parallel along the gradient. At very high velocities the gyrocenter iteration diverges before unbound threshold speeds were reached. This occurs when $v > 0.204v^*$ [6]. To check if the converged gyrocenter improved the GC approximation a log plot was generated across a wide range of velocities for the tracing error in GC drift. From this graph it was determined that the tracing error in modelling the particle's drift was proportionate to v^4 when initialized at the converged gyrocenter, or 1st gyrocenter, and was proportionate to v^3 when initialized at the particle trajectory. Although the tracing error for both the converged gyrocenter and the first approximation decrease at a rate of v^4, this error is consistently a factor of 3 smaller for the converged gyrocenter up until $v = 2$. At $v = 2.7$, the 1st gyrocenter becomes a better GC initiation point because the velocity is approaching our iteration divergence threshold of 3.0217.

Ideally, when using the GC approximation, we would like to model the drift period, magnetic moment and gyrofrequency exactly. In an attempt to determine an r position where this occurs we used the exact expression of drift period, magnetic moment and gyrofrequency that exist for *t* equatorial mirroring particles in a magnetic dipole. Unfortunately, these three points never coincide, except in the limit as *v* approaches 0. Thus, in the practical application of the GC approximation, one must choose between trade-offs in accurately measuring μ, r_{Tg} or r_{Td}. For most applications of the GC approximation, we wish to match the drift period exactly. However, there are applications when accurately measuring μ or T_g is more desirable. An in-depth analysis of the converged gyrocenter vs r_μ, r_{Tg} and r_{Td} is left for future work, but findings here show that the locations of r_μ, r_{Tg} and r_{Td} offer improvement at relatively high velocities, especially those above $v = 3.0217$. Overall, all methods of GC initialization rely only on the initial position and velocity of the charged particle. This adds flexibility to plasma particle modelling as it eliminates the need to first model the actual trajectory of the charged particle.

Lastly, we investigated different methods of calculating the first adiabatic invariant. In the standard GC approximation, the adiabatic invariant is assumed to be constant, a crucial assumption of the GC formalism. Even if the simplest zeroth-order approximation (2.18) for the adiabatic invariant is used there are several different possibilities where *B* is evaluated. It can be evaluated either at the instantaneous particle position or at the gyrocenter, which itself is calculated by several different methods. The magnetic moment was also expanded into a Taylor series in an attempt to improve the accuracy of the calculation. To establish a basis of comparison the oscillations of these magnetic moments were compared to the exact solution of the magnetic moment. To quantify our results we used the maximum difference between the exact solution and these oscillations to measure the error in measuring the magnetic moment. This was then plotted on a log plot for velocities that ranges from 0.01 to 3.02. It was found that applying (2.18) using B at the particle trajectory and (4.17) using *B* at the converged gyrocenter had a proportionality of v^3. For (2.18) using *B* at the 1st gyrocenter and converged gyrocenter, along with (4.17) using *B* at the particle trajectory, we have a proportionality of v^4. Overall, the best method was determined to be using (2.18) at the converged gyrocenter because it had the least error for all velocity values.

5. Particle Motion in the Equatorial Plane of a Non-Axisymmetric Magnetic Field. Magnetic Dipole and Magnetotail

5.1 Description of Non-Axisymmetric Magnetic Field

In this chapter, we continue to analyze charged particles with velocities in the equatorial plane and are thus confined to it, but now introduce asymmetry to the magnetic field. In the previous Chapters, we relied on magnetic field symmetry to apply the canonical momentum, magnetic moment and other analytical expressions to determine GC initialization options. In this chapter, we analyze the effects asymmetry has on the conservation of these quantities for one drift period. Quantifying the effects on magnetic moment specifically allows us to demonstrate the deviation of the GC approximation from the real trajectory. Asymmetry in the magnetic field mimics the outer Sections of the Earth's magnetosphere, where the magnetic field is compressed on the dayside and stretched on the nightside as a result of solar wind pressure, thus leading to asymmetry. Specifically, magnetic field compression occurs at a distance of $r > 4R_E$ on the dayside, while stretching of the magnetotail occurs at a distance of $r > 5R_E$ on the nightside [4]. This process was illustrated in Figure 1.2. High energy particles in the asymmetric portions of Earth's magnetic field are found in the outer Van Allen belts. These represent the primary application for the GC approximation in this thesis, as we are measuring the validity of GC approximation for high-energy particles.

In this chapter we use the geocentric solar magnetospheric (GSM) coordinate system. In this coordinate system the positive *z*-axis is aligned with the magnetic north, the positive *x*-axis is aligned from the Earth to the Sun, ignoring the dipole tilt, and the *y*-axis points from dawn to dusk, this completes the right-hand coordinate system.

The magnetic field used in this section is a modification of our axisymmetric dipole introduced in Equation (4.1), which was simplified in Equation (4.4). To introduce asymmetry we subtract magnetic field strength from the dipole on the nightside to mimic magnetotail stretching. This magnetic field is based on models developed in papers by Kabin *et al* [23] and Kabin *et al* [32]. These models were developed for the specific purpose of investigating the night-time transition between the mostly dipolar region to the stretched magnetotail and were inspired by ground-based riometer measurements and optical observations of auroras [33]. This model allows for a relatively simple parametrization of the night-side transition region and allows the control of the thickness of the night-side cross-tail current sheet, its strength, and the location of the transition. The location of this sheet is given by the label plasma sheet in Figure 1.1. Although not particularly computationally expensive by itself, this model is still too slow to be used directly while integrating the Lorentz equations of particle motion. Therefore, a heuristic fit to a numerical model was developed in the paper by Kabin *et al* [23] approximating the parametrization of the magnetotail. This parametrization is in the equatorial plane only and has a fitting error accuracy better than 10^{-4}, which leads to a slight deviation of the fields from perfect self-consistency in time-dependent simulations, but does not affect our calculations [23]. This approximated model is time-dependent, as the focus of the paper by Kabin *et al* [23] was the study of a substorm dipolarization. This is interpreted as the tailward motion of the transition region. In this thesis, we focus on steady-state magnetic fields, so in the equations below we choose $t = 0$, which corresponds to the state of the magnetosphere before a

substorm. Under this condition, the magnetotail is centred as 6 R_E. In the equatorial plane, the magnetic field is given by Equation (5.1), here a and b_1 through b_5 represent components of the heuristic fit to a numerical model [23].

$$\mathbf{B} = \frac{M}{r^3} - f(\varphi)\frac{b_1}{a^{2.884}}\left[\frac{e^{a^{2.46}} - b_4}{e^{a^{2.46}} + b_5}\right]^{2.065}\widehat{\mathbf{e_z}} \tag{5.1}$$

$$a = (r + b_2)/b_3 \tag{5.2}$$

$$b_1 = 648.9661 - 183.7327\tanh(1.6101t - 3.8109) \tag{5.3}$$

$$b_2 = 0.2019 - 0.0859\tanh(1.6258t - 4.1687) \tag{5.4}$$

$$b_3 = 3.3338 + 0.2906\tanh(1.6013t - 3.9748) \tag{5.5}$$

$$b_4 = 1.3820 - 0.2966\tanh(1.8191t - 5.1973) \tag{5.6}$$

$$b_5 = 93.1713 + 50.4476\tanh(1.6306t - 4.3549) \tag{5.7}$$

In Equation (5.1) the first term is the dipole from Section 4.1, Equation Here M represents the equatorial strength of Earth's magnetic field at the surface, while r represents the radial distance from the center of the Earth in R_E [23]. For this magnetic field, we use $M = 3.1\cdot10^{-5}\,TR_E^3$ because we are quantifying the effects for real Earth-like conditions, unlike the previous sections where we used generic units for the magnetic field. The second term in Equation (5.1) represents the magnetotail. A notable limitation of this model is that it is only applicable in the equatorial plane, however, this is sufficient for our purposes. Another limitation is that this model was designed to work only for radius values greater than 3 R_E. This is not a significant limitation for our purposes since we are considering particle trajectories outside this radius.

Since the magnetic field in the equatorial plane is always in the z-direction, $\nabla\cdot B = 0$ for any functional dependence on x and y.

This magnetic field model was further modified to limit the tail magnetic field to a certain azimuthal range, centred at midnight or $\varphi = \pi$. Here φ is the azimuthal angle. This was necessary as the original magnetotail model was axisymmetric [23]. This was achieved by including the factor $f(\varphi)$ in Equation (5.1). This $f(\varphi)$ is from an unpublished paper by *Kabin et al* that also similarly modelled a magnetotail. The function $f(\varphi)$ is given by the combination of Equations (5.8) and (5.8), with the angle φ in degrees, measured counterclockwise from noon.

$$f_1(\varphi) = \frac{1}{c_0}\left[1 + \tanh\left(\frac{55^o - (\varphi - 180^o)}{20^o}\right)\right]\left[1 + \tanh\left(\frac{55^o + (\varphi - 180^o)}{20^o}\right)\right] \tag{5.8}$$

$$f(\varphi) = \frac{f_1(\varphi)}{c_1}\left[1 + \tanh\left(\frac{110^o - (\varphi - 180^o)}{5^o}\right)\right]\left[1 + \tanh\left(\frac{110^o + (\varphi - 180^o)}{5^o}\right)\right] \tag{5.9}$$

In Equations (5.8) and (5.8) $c_0 = (1 + \tanh(11/4))^2$ and $c_1 = (1 + \tanh(110/5))^2$ to simply

ensure that an exact value of 1 is achieved on the nightside at midnight. This is done so that *f(φ)* ranges from 0 to 1, and acts as an on/off switch to subtract magnetic field strength, as shown by Equation (5.1). In addition, the need for two lines of *f(φ)* was to prevent numerical limitations from affecting our measured results. Originally we employed only Equation (5.8), which does not completely go to 0 but is instead in the order of 10^{-6}. Although this appears to be a fairly small number, it turns out that even this small degree of asymmetry visibly affects the conservation of the canonical angular momentum and magnetic moment, discussed later in section 5.4. Thus, we applied a second *f(φ)*, Equation ((5.9), to decrease our numerical limitation. With both Equations (5.8) and (5.8) our *f(φ)* does a better job at approaching 0 and is in the order of 10^{-18}. This value is smaller than machine epsilon in our numerical calculations and does not affect the results in any visible way.

Overall the most important values in *f(φ)* are 55º and 20º from Equation (5.8). Here the value of 55º represents the azimuthal angle where the transition from a dipolar to tail-like field takes place, measured from the negative *x*-axis. The value of 20º represents the width of this transition. Figure 5.1 shows an illustration of our *f(φ)* given by Equations (5.8) and (5.8) in blue, where we label it small phi-gradient (∇φ) to differentiate it from two additional versions of *f(φ)*, which are presented here for comparative purposes and are introduced later.

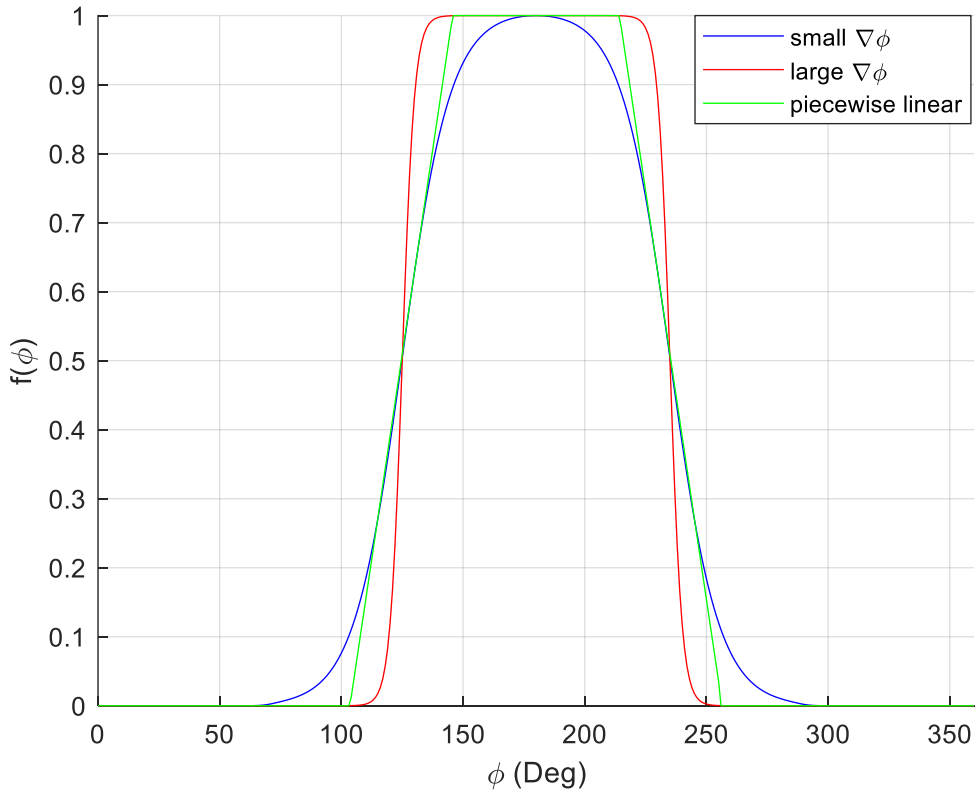

Figure 5.1: *f(φ)* factor as a function of *φ*. Small ∇φ is shown in blue, large ∇φ is shown in red and the piecewise linear is shown in green.

The magnetic field given by Equation (5.1), with *f(φ)* given by Equations (5.8) and (5.8), is visualized in the contour plot in Figure 5.2. The magnetic field on the dayside is clearly

axisymmetric, while on the nightside there is an obvious deviation from this symmetry. Since the magnetotail has a weaker magnetic field, the contours of constant *B* pass closer to the Earth on the nightside than on the dayside. To reiterate our function *f(φ)* controls where the transition from the tail current region to the dayside dipolar magnetic field takes place, as well as the steepness of this transition.

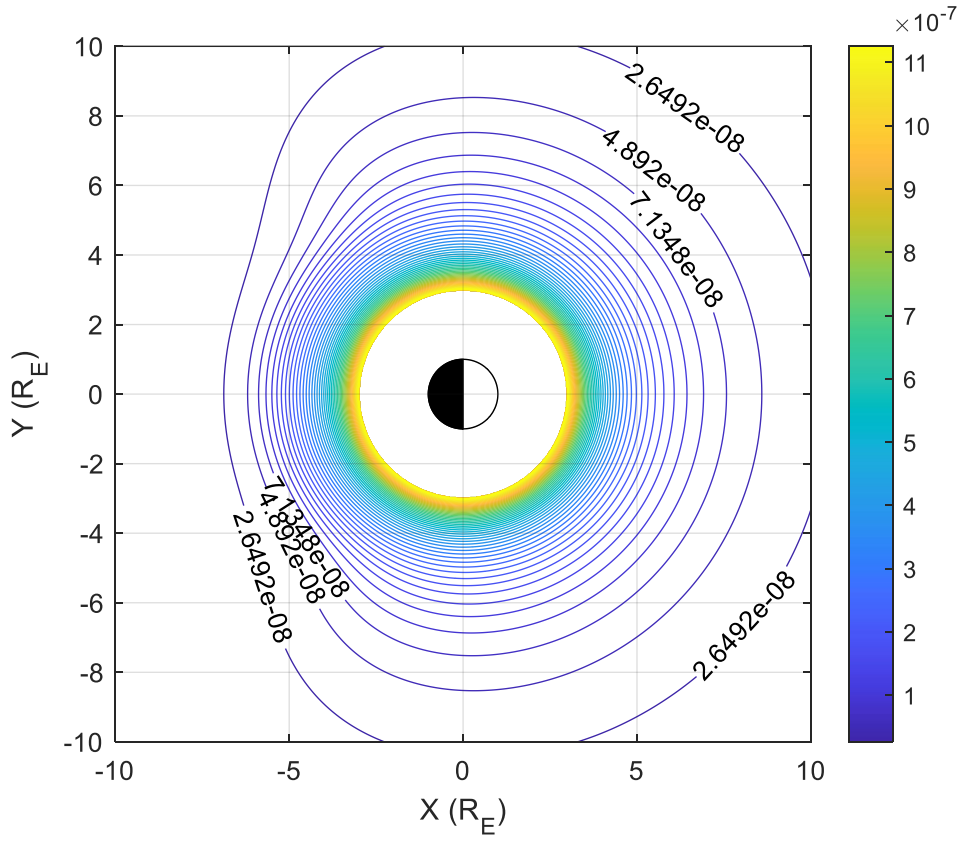

Figure 5.2: Contour plot of the magnetic field strength of B_z (T) in the equatorial plane for small ∇φ. Magnetic field strength is displayed for outermost contour lines. Earth is represented by a circle with a radius of 1 R_E, the dayside is in white and the nightside is in black.

Plotting the magnetic field strength as a function of radius also helps illustrate the effects of the magnetotail on the rate of change of *B*, this is shown in Figure 5.3. This was done for multiple values of φ in radians, measured from the positive *x*-axis.

In Figure 5.3 the black line represents the magnetic field strength along the positive *x*-axis. This illustrates the spatial variations in the magnetic field strength for the magnetic dipole side, while the red and green represent two radial slices of the magnetotail. The red line corresponds to the negative *x*-axis or midnight, and it has the most pronounced dip in strength due to the *f(φ)* factor being a maximum value of 1 here. Comparing this to the black line representing the dayside shows that the magnetic field strength drops approximately by a factor of 10. The green line corresponds to a value of *f(φ)* between 0 and 1 and illustrates a segment of the magnetotail transition. Overall, the magnetotail effects start to occur at $r = 4.5\ R_E$, here the spatial variations in B increase until $r = 6.5\ R_E$, where the spatial variations in B become proportional to r^3 again.

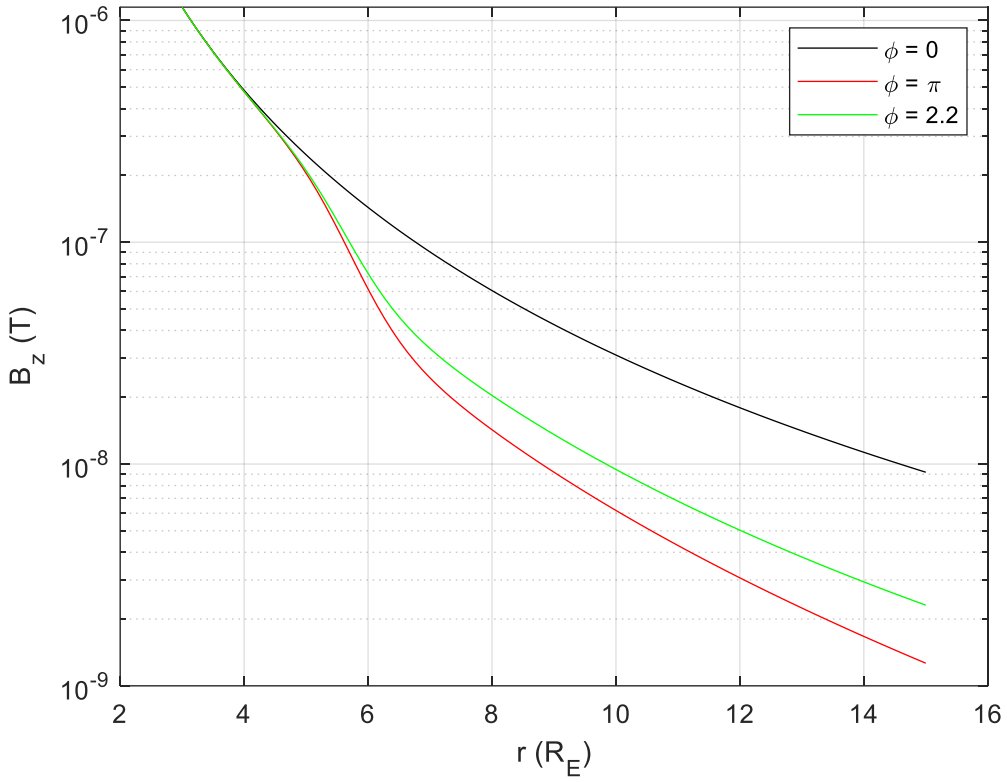

Figure 5.3: Variations of B_z as a function of r for multiple values of φ. The black line represents $\varphi = 0$, the red line is $\varphi = \pi$ and the green line is $\varphi = 0$.

In addition to this magnetic field, two additional non-axisymmetric fields are analyzed in this chapter. This is done in order to illustrate the effects of magnetic field gradient steepness on particle trajectories and the conservation of the adiabatic invariants. Furthermore, Earth's outer magnetosphere is known to change shape due to space weather conditions, which we define as variations in the solar radiation pressure that hits Earth's magnetosphere. Thus, analyzing various magnetotails serves to illustrate the dynamic nature of the magnetotail. We now introduce two new magnetic fields, that are still governed by Equation (5.1) but employ a different *f(φ)* factor to simulate differences in the transition region of the magnetotail as illustrated earlier in Figure 5.1. The first new magnetic field uses a narrower, and therefore, steeper, transitional region. This is achieved by changing the value 20° in Equation (5.8) to a lower value of 5°. For clarity, we referred to our first case as small ∇φ, thus we refer to this one as large ∇φ based on their respective *f(φ)* transition ranges. Overall, the steeper transition in *f(φ)* is given by Equations (5.10) and (5.11), where the correction term c_0 becomes $c_0 = (1 + \tanh(11))^2$ and c_1 is the same as before.

$$f_1(\varphi) = \frac{1}{c_0}\left[1 + \tanh\left(\frac{55^o - (\varphi - 180^o)}{5^o}\right)\right]\left[1 + \tanh\left(\frac{55^o + (\varphi - 180^o)}{5^o}\right)\right] \tag{5.10}$$

$$f(\varphi) = \frac{f_1(\varphi)}{c_1}\left[1 + \tanh\left(\frac{110^o - (\varphi - 180^o)}{5^o}\right)\right]\left[1 + \tanh\left(\frac{110^o + (\varphi - 180^o)}{5^o}\right)\right] \tag{5.11}$$

The magnetic field is given by Equation (5.1), calculated using this definition of *f(φ)* is shown as a contour plot in Figure 5.4. Comparing Figure 5.2 and Figure 5.4 shows that the gradient in the azimuthal direction is much steeper in the tail for this field. This is also illustrated by contrasting the blue and red lines from Figure 5.1

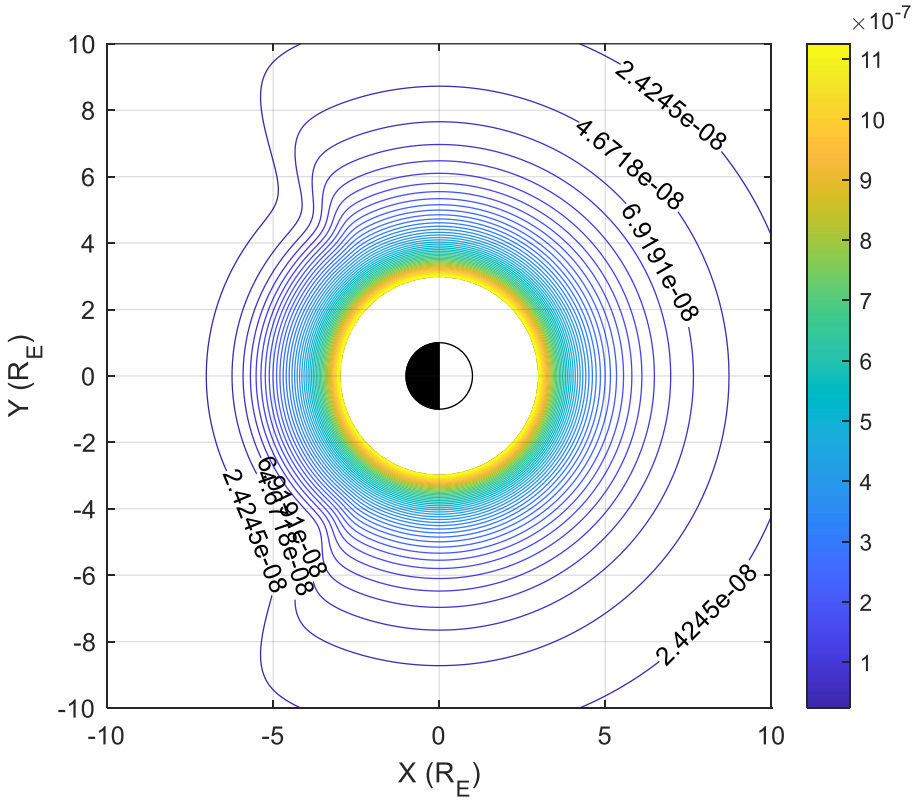

Figure 5.4: Contour plot of the magnetic field strength of B_z (T) in an equatorial plane large ∇φ. Same layout as Figure 5.2.

For the magnetic field shown in Figure 5.2 and Figure 5.4, the magnetic field changes smoothly with the azimuthal angle. Thus the magnetic fields specified by Equations (5.8) and (5.10) are continuously differentiable. As one more example we consider a magnetic field in which *f(φ)* is expressed by a piece-wise linear function. In this case, while the magnetic field is continuous, its derivative is not. We use this example to examine the effects of non-smooth variations of the magnetic field on particle trajectories. It is known that the dependence on smooth, or not smooth, variation in the magnetic field significantly affects the conservation of adiabatic invariants [11] [34]. Therefore, we compare the smooth and non-smooth magnetic fields in this chapter.

The piecewise linear version of *f(φ)* was implemented using if statements. The linear slope was chosen to be equal to the maximum derivative of our small ∇φ definition of *f(φ)*. The derivatives for both Equations (5.8) and (5.10), small ∇φ and large ∇φ respectively, are displayed in Figure 5.5. The choice of using the derivative of small ∇φ was done to make small ∇φ the pivotal magnetic field. This way large ∇φ becomes a variation in the rate of transition, when compared to small ∇φ, and the piece-wise linear function becomes a variation in the style of transition, when compared to small ∇φ.

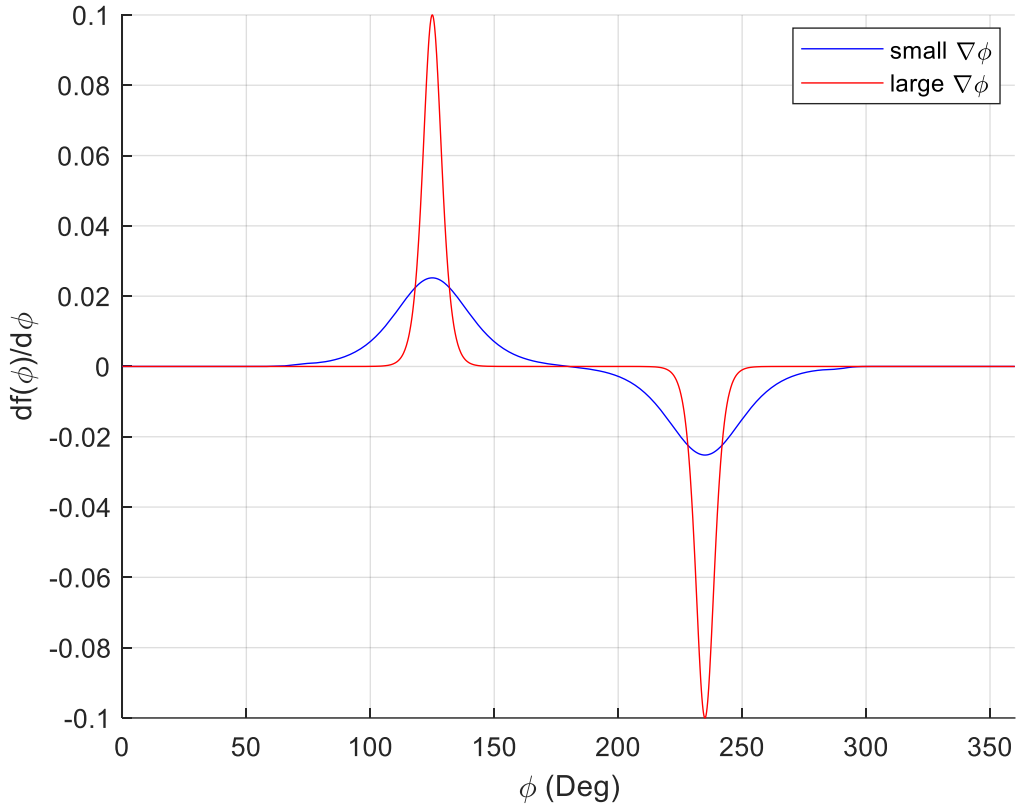

Figure 5.5: Derivative of *f(φ)* for cases small ∇φ is in blue and large ∇φ is in red.

Figure 5.5 shows that the maximum value for d*f(φ)*/d*φ* for small ∇φ is 0.02369 and occurred at $\varphi = 130$. Using this we created the piecewise linear function given by Equation (5.12), which was shown in Figure 5.1 with a green line.

$$\begin{gathered} f(\varphi) = 0 \text{ if } 256 \le \varphi \le 103 \\ 0.02369\varphi - 2.45216 \text{ if } 103 < \varphi < 146 \\ -0.02369\varphi + 6.07624 \text{ if } 214 < \varphi < 256 \\ 1 \text{ if } 146 \le \varphi \le 214 \end{gathered} \tag{5.12}$$

The contour plot for this magnetic field is shown in Figure 5.6. In comparison with Figure 5.2 and Figure 5.4, it shows sharp changes in the magnetic field contour lines at the azimuthal angles where *f(φ)* changes the slope.

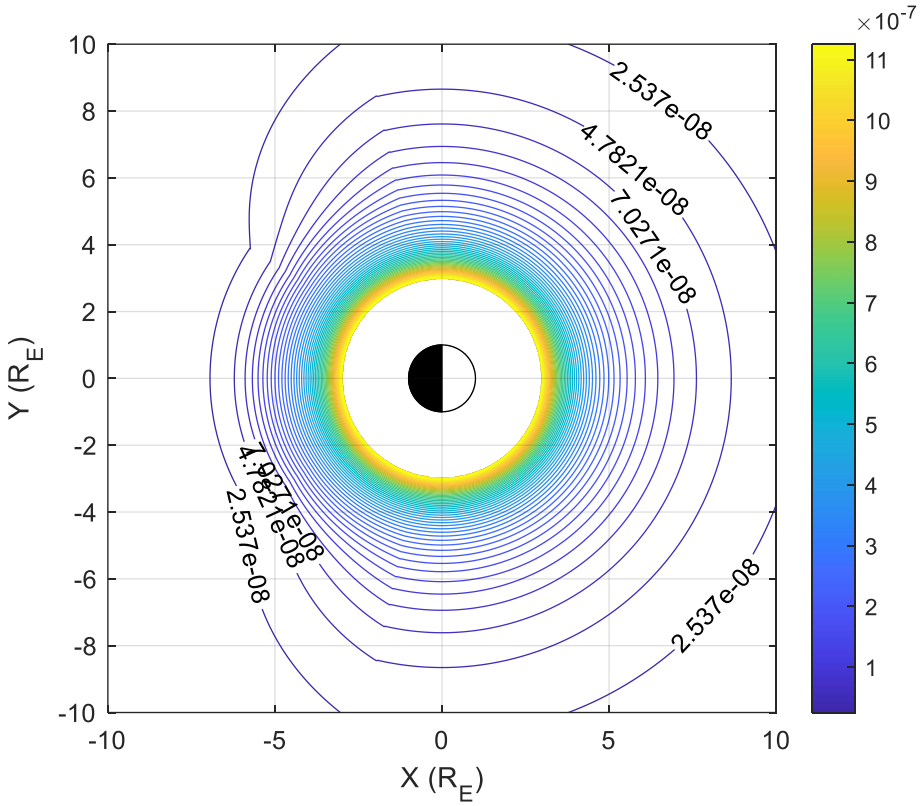

Figure 5.6: Contour plot of the magnetic field strength of B_z (T) in an equatorial plane for piecewise linear. Same layout as Figure 5.2.

5.2 Brief Examination of Particle Trajectory

The charged particles in this chapter are initialized on the axisymmetric dayside of the magnetic field for all three variations of the model. This is done so conserved quantities remain intact for the initial and final parts of the particle's drift period. While the particle is in the axisymmetric part of the magnetic field the Equations for the conserved quantities are the same in this section as the ones derived for the magnetic dipole (4.4) in Section 4.1. This is because Equation (5.1) reduces to Equation (4.4) when $f(\varphi) = 0$. While the particle is on the dayside, the P_φ, r_{min}, r_{max}, T_{d_Exact} and μ_{Exact} remain constant.

In regards to code validation, we reference the results from Section 4.3, as the magnetic field conditions are the same for the dayside. Thus, it is concluded that the code has a relative numerical error on the order of 10^{-11} for P_φ and v. It is shown in Section 5.4 that this numerical limitation is reached during our analysis and thus constrained the range of velocities examined. This is discussed in more detail in Section 5.4. Overall, it does not limit our ability to draw conclusions from the results.

As an example, we consider the motion of a proton with initial conditions of $m_0 = 1.673 \cdot 10^{-27}$ kg, $q = 1.602 \cdot 10^{-19}$ C, $r_0 = [7, 0]$ R_E and $v_0 = [0, 6]$ R_E/s in the small $\nabla\varphi$ magnetic field. The rest mass and charge values were chosen to replicate a hydrogen ion. The initial position, r_0,

was chosen to start on the dayside, with a value of 7 R_E chosen to have the ion pass through the magnetotail's steepest spatial variation, as established in Figure 5.3. An initial velocity of 6 R_E/s was chosen to get a particle gyration range of approximately 2 R_E for ease of visualization. At this velocity, the ion has a kinetic energy of 7.74 MeV. Comparatively the rest energy of an ion is 9.39 MeV . Figure 5.7 shows the trajectory of the ion for one drift period.

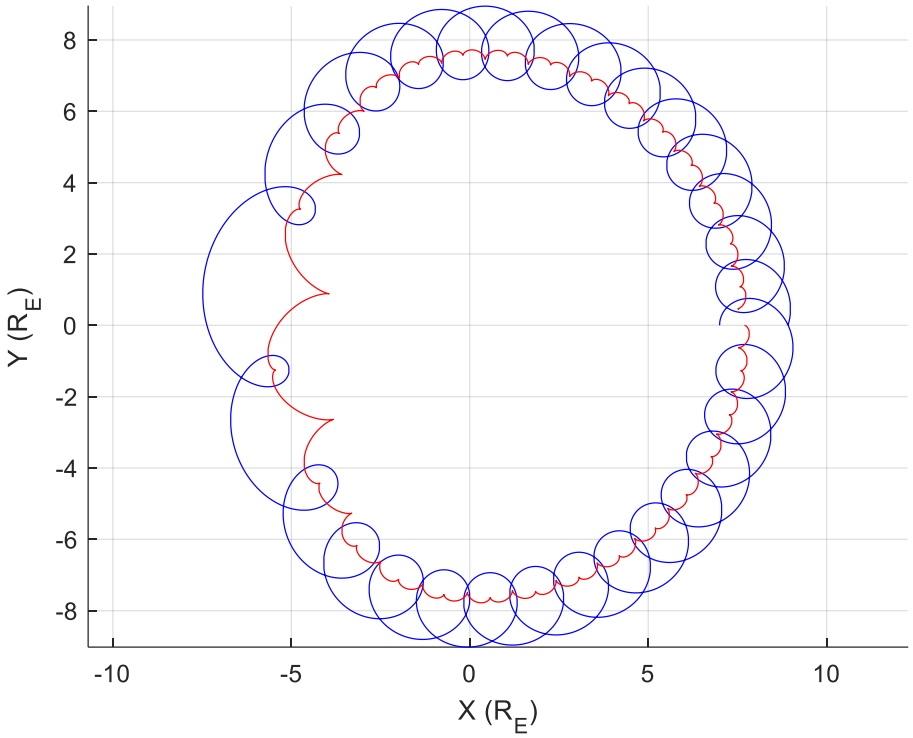

Figure 5.7: Trajectory of a particle in the equatorial plane of a non-axisymmetric field for one drift period. The particle is initiated with $m_0 = 1.673 \cdot 10^{-27}$ kg, $q = 1.602 \cdot 10^{-19}$ C, $r_0 = [7, 0]$ R_E and $v_0 = [0, 6]$ R_E/s. The magnetic field is out of the page with $M = 3.1 \cdot 10^{-5}$ TR_E^3. The trajectory is shown in blue and the 1st gyrocenter in red.

In Figure 5.7 the particle trajectory is displayed in blue and the 1st gyrocenter is in red. The gyrations become larger and longer in the magnetotail region as a result of the weaker magnetic field there. In addition, the r_{min} and r_{max} of the particle's motion also change. Like before we only examine bound particles for this thesis. On the dipole side, the particles become unbound if $v > v^*/4$, as r_{max} becomes undefined. Based on this definition the particle becomes unbound for our initial conditions when $v > 10.15$ R_E/s. However, a lower practical threshold exists when taking into consideration that the particle must travel into a weaker B in the magnetotail. Due to the asymmetry of the magnetic field in this region, an analytical expression for unbound thresholds does not exist. Instead, it is determined through trial and error of numerical integration. For this scenario, with the v_0 in the y-direction and $x_0 = 7$ R_E, it was determined this occurs for a $v > 7$ R_E/s. At velocities slightly above 7 R_E/s it took multiple drift periods for the particle to become unbound by Earth's magnetic field. If we restrict the particle to one drift period then the unbound condition occurs at a $v > 7.98$ R_E/s. An example of such a trajectory is shown in Figure 5.8. Overall, this process illustrates the need to consider magnetic field asymmetry when evaluating unbound threshold velocities.

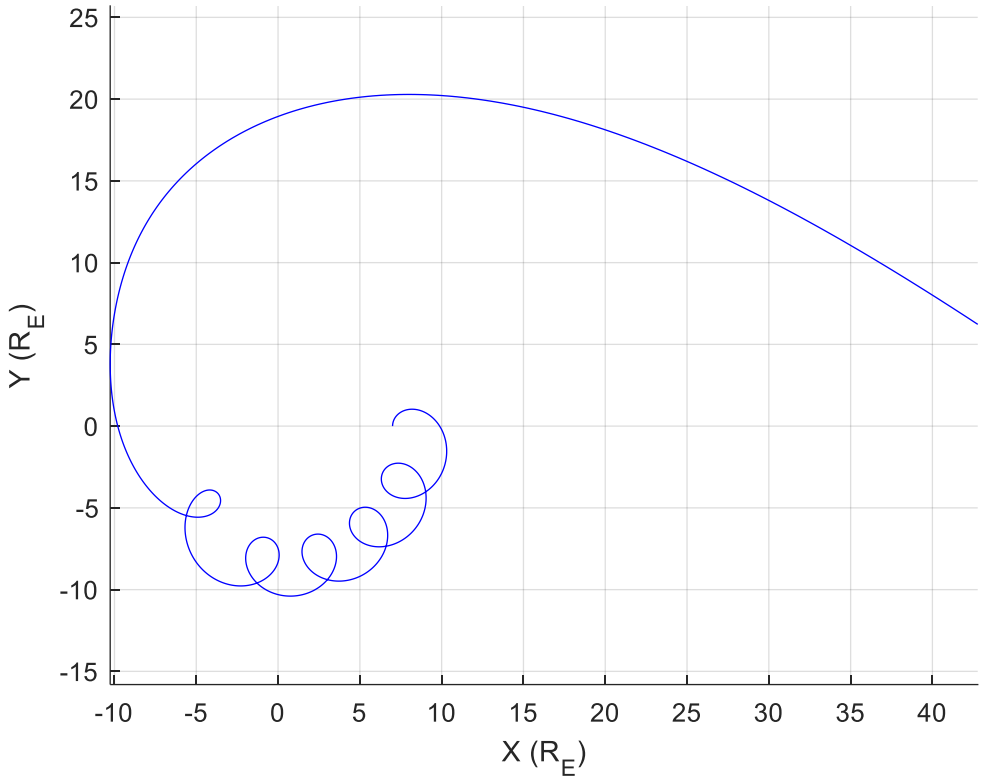

Figure 5.8: Particle transition from bound to unbound trajectory due to weaker magnetic field in the tail. The particle is initiated with $m_0 = 1.673 \cdot 10^{-27}$ kg, $q = 1.602 \cdot 10^{-19}$ C, $r_0 = [7, 0]$ R_E and $v_0 = [0, 7.98]$ R_E/s. The magnetic field is out of the page with $M = 3.1 \cdot 10^{-5}$ TR_E^3.

Now we consider the conservation of the canonical angular momentum and the first adiabatic invariant in this field. Figure 5.9 shows the canonical angular momentum of a particle from Figure 5.7 as a function of time. On the dayside, in the dipole magnetic field area, the canonical momentum is given by Equation (4.6) and is conserved. In Figure 5.9 this part of the trajectory corresponds to the initial horizontal part of the plot. As the particle moves into the tail field area, Equation (4.6) no longer represents the canonical angular momentum because the field now depends on the azimuthal angle, meaning the canonical momentum is no longer conserved. In Figure 5.9 this corresponds to the central area where the momentum oscillates. Eventually, when the particle enters the region of the dipolar magnetic field again, the canonical momentum is conserved again, this is illustrated by the plot of $P\varphi$ in Figure 5.9 becoming a horizontal line again.

Similar considerations apply to the first adiabatic invariant. Figure 5.10 shows the time variation of the exact adiabatic invariant (4.18), as well as approximation (2.18) for the trajectory and 1st gyrocenter as a function of time. In the dipolar region, the exact value of the adiabatic invariant is given by (4.18), and it remains constant along the particle trajectory. In the tail region, this value oscillates, since expression (4.18) does not apply to this magnetic field. It becomes constant again when the particle renters the dipolar region. The approximations for the trajectory and 1st gyrocenter oscillate with every gyration even in the dipolar field region, but the amplitude of these oscillations becomes significantly larger in the tail field area. This is shown in Figure 5.10

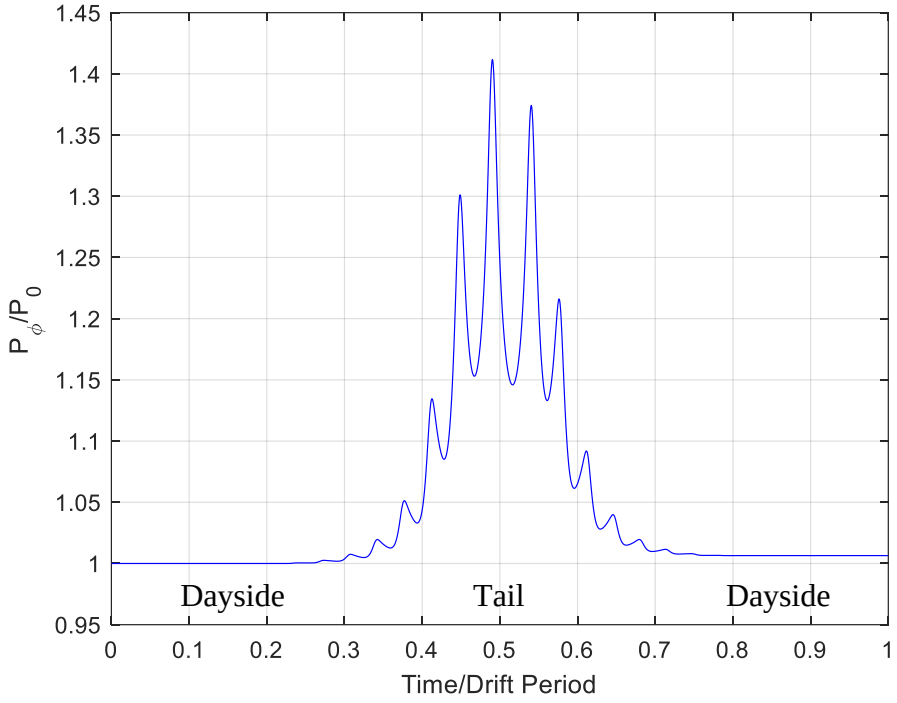

Figure 5.9: Normalized canonical angular momentum over one drift period. The particle is initiated with m_0 = $1.673 \cdot 10^{-27}$ kg, q = $1.602 \cdot 10^{-19}$ C, r_0 = [7, 0] R_E and v_0 = [0, 6] R_E/s. The magnetic field is out of the page with M = $3.1 \cdot 10^{-5}$ TR_E^3.

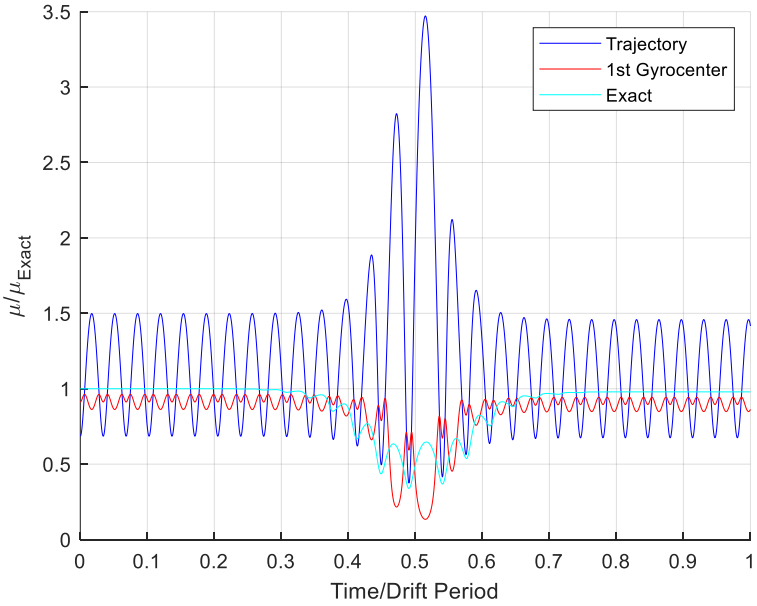

Figure 5.10: Magnetic moments over one drift period. The particle is initiated with m_0 = $1.673 \cdot 10^{-27}$ kg, q = $1.602 \cdot 10^{-19}$ C, r_0 = [7, 0] R_E and v_0 = [0, 6] R_E/s. The magnetic field is out of the page with M = $3.1 \cdot 10^{-5}$ TR_E^3. The exact expression for the magnetic moment is in cyan, the approximate expression using the trajectory is in blue and using the 1st gyrocenter is in red.

Figure 5.9 and Figure 5.10 show that both the canonical angular momentum and the exact value of the magnetic moment return to a value close, but not exactly equal, to their initial values after passing through the magnetotail area. For the adiabatic invariant this behaviour is expected [11]. However, this is a significant result for the canonical momentum as the only expectation is that it returns to a constant value in the dipolar region, but there is no obvious reason to expect it to be close to the starting value. In the GC approximation, however, the return to the original value for both the canonical momentum and the adiabatic invariant is expected because of the dawn-dusk symmetry of the magnetic field. This symmetry of the magnetic field results in the GC drift path being a closed curve. Thus, one can expect a particle that is well described by the GC approximation to remain within the same r_{min} and r_{max} bounds after passing through the tail region. Thus, small deviations from the initial value of P_φ and the μ_{Exact} represent the deviation from the GC theory. Thus the GC approximation will incur cumulative secular errors with every drift. Section 5.4 aims to quantify this error over a range of velocities by measuring the difference between the final and starting values of P_φ and μ_{Exact}. Quantifying this allows for the GC approximation to be applied so long as the error is tolerable for any particular application. This provides some guidelines on accuracy for applications of the GC approximation in non-axisymmetric conditions.

The differences between final and initial values of P_φ and μ_{Exact} are also calculated for large $\nabla\varphi$ and the piece-wise linear function versions of the non-axisymmetric magnetic field. An example of the particle's trajectory in both of these magnetic fields is given in Figure 5.11. The same initialization considerations used in Figure 5.7 are used here except for the following. An initial velocity of $v_0 = 5$ R_E/s is used in large $\nabla\varphi$ because it was determined that an initial velocity of $v_0 = 6$ R_E/s resulted in the particle becoming unbound. For the piece-wise linear function $r_0 = [7, 0]$ R_E and $v_0 = [0, 6]$ R_E/s became $r_0 = [0, -7]$ R_E and $v_0 = [6, 0]$ R_E/s. This is because the particle for the piecewise linear function was only modelled for half a drift period and thus was initialized on the negative *y*-axis. This was done to save computational time as the magnetic field model becomes exactly dipolar on the dayside, thus the calculation of the particle trajectory on the dayside is not necessary and only wastes our computational resources. The computational time is a notable limitation of the analysis discussed in more detail in Section 5.4. Modelling half a drift period was not done for small $\nabla\varphi$ or large $\nabla\varphi$ magnetic fields as the numerical limitations of the code were reached before the need to reduce computational time. Overall the left panel of Figure 5.11 clearly shows the effects of a narrower φ range for $f(\varphi)$ as the particle deviates from the projected path more sharply than in Figure 5.7, while the right panel of Figure 5.11 is visually very similar to the Figure 5.7.

Regardless of which magnetic field is used, the weaker *B* in the magnetotail region causes the particle's gyroradius to increase and gyrofrequency to decrease. Thus, the particle spends less time traversing the magnetotail region than it otherwise would if the magnetic field were a dipole. To quantify this time difference we use the exact expression for the drift period, given by Equation (4.13), to represent the particle's drift period in a dipole. To represent the drift period with our magnetotail we use our numerical integration time with Matlab's events functionality set to stop the integrator after one drift period. This is done using the magnetic field of small $\nabla\varphi$ for a velocity range of 1 R_E/s to 6.5 R_E/s. The result is shown in Figure 5.12. In this figure the decrease in drift period due to a weaker magnetotail is quantified. The reasoning for the limited range of velocities and 0.5 R_E/s intervals is explained in subsequent sections.

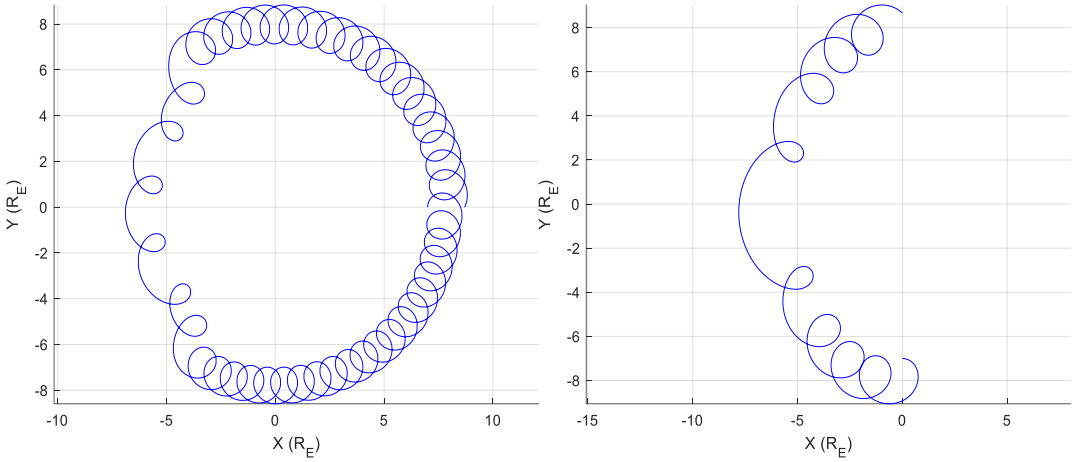

Figure 5.11: Trajectory in a magnetic field using large ∇φ for full T_d (left) and half T_d piece-wise (right). The particle is initiated with $m_0 = 1.673 \cdot 10^{-27}$ kg, $q = 1.602 \cdot 10^{-19}$ C. $r_0 = [7, 0]$ R_E and $v_0 = [0, 5]$ R_E/s (left). $r_0 = [0, -7]$ R_E and $v_0 = [6, 0]$ R_E/s (right). The magnetic field is out of the page with $M = 3.1 \cdot 10^{-5}$ TR_E^3.

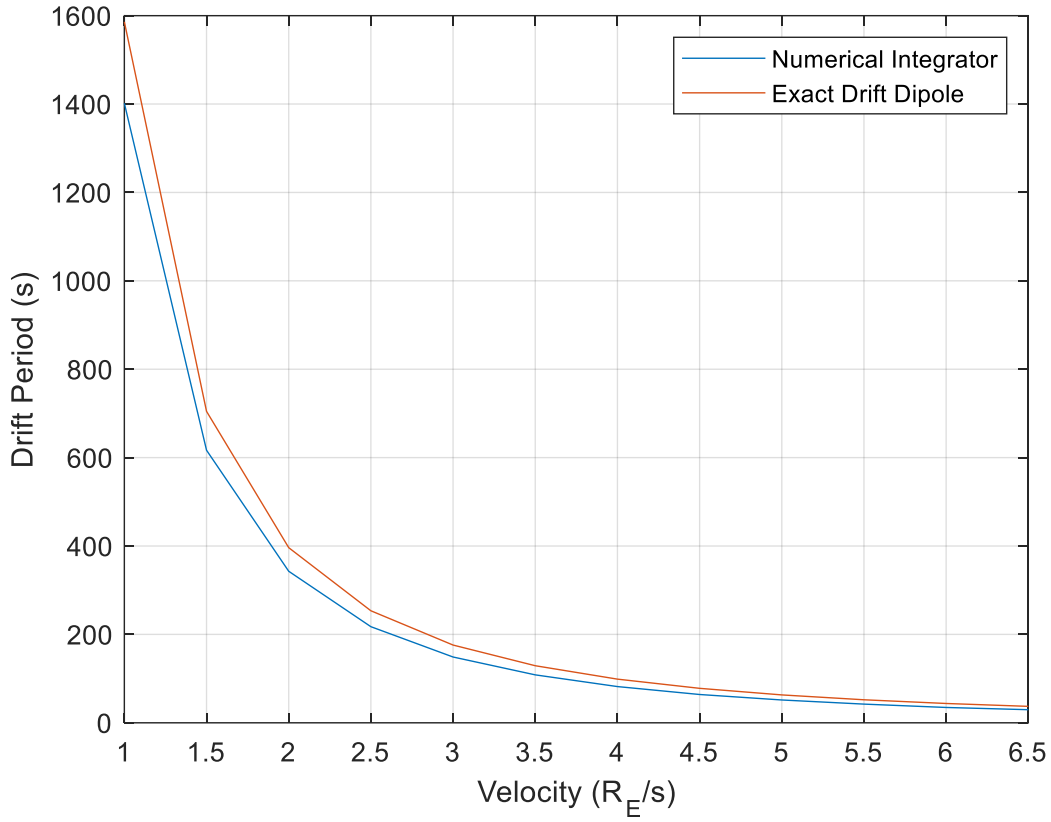

Figure 5.12: Comparison of exact drift period in dipole vs drift period of numerical integrator using small ∇φ. The particle is initiated with $m_0 = 1.673 \cdot 10^{-27}$ kg, $q = 1.602 \cdot 10^{-19}$ C, $r_0 = [7, 0]$ R_E and $v_0 = [0, 6]$ R_E/s. The magnetic field is out of the page with $M = 3.1 \cdot 10^{-5}$ TR_E^3.

5.3 Phase Distribution

The GC approximation is based on averaging the trajectory of a particle. Due to this multiple particle trajectories average to the same GC trajectory. In this section, we describe a procedure for generating an ensemble of particles that all have an identical GC approximation. These particles are indistinguishable from the point of view of GC theory. The initial conditions for these particles are generated in such a way that they are all characterized by the same value of P_φ, μ_{Exact} and velocity. Due to the shared value of $P_{\varphi,}$ these particles also have the same values for r_{min} and r_{max}. The only difference between these particles is their initial phase, which is, unobservable within the GC formalism. In Section 5.4 we show that certain properties of the motion depend on the initial phase, and this dependence becomes more prominent as the velocity of the particle increases. Thus the dependence of the results on the phase of the particle indicates the breakdown of the GC approximation.

Figure 5.13 illustrates our procedure for generating particles with different phases and identical energies, P_φ, and μ_{Exact}. The blue line in Figure 5.13 is the gyroperiod of a particle initiated at $r_0 = [7, 0]$ R_E and $v_0 = [0, 6]$ R_E/s, which is the same as Figure 5.7 discussed earlier. Using this trajectory, we calculate the velocity components of the particle at any point along the gyroperiod. This is illustrated in Figure 5.13 by the several black lines tangential to the blue trajectory. We then rotate these velocities to the same initial starting line at $y = 0$ shown by the black solid line. The red dashed lines in Figure 5.13 shows this rotation and the red vectors illustrate the new velocity vectors. We define the phase, δ, of the particle in such a way that $\delta = 0$ at our initial point, where v_0 is in the positive y-direction, and $\delta = 2\pi$ at the end of the gyroperiod. This allows us to write the initial velocity as $v_0 = v[\sin(\delta), \cos(\delta)]$ R_E/s. Using this definition of velocity, we generate v_{x0} and v_{y0} for all phases between 0 and 2π.

We now distribute the velocity vectors along the same starting line, the positive x-axis. To do this we use the r_{min} equation to determine x_0 for each phase. This is done because our initial phase, $\delta = 0$, is initiated at r_{min}, thus $x_0 = r_{min}$ at initialization. Additionally, since $y_0 = 0$, the y component of our becomes v_φ. Applying this results in our expression for x_0 being given by Equation (5.13).

$$x_0 = \frac{P_\varphi + \sqrt{P_\varphi{}^2 + 4mqMv\cos\delta}}{2mv\cos\delta} \tag{5.13}$$

Due to the dependency on P_φ in this approach, it should be noted this process is limited to initialization on the dipole side only. Overall, this entire phase distribution process is visualized in Figure 5.13 below.

In Figure 5.13 five of the particle's local velocity vectors are displayed in black at five different positions along the trajectory for one gyroperiod, the corresponding values of the phase are shown. The corresponding red velocity vectors show r_0 and v_0 for each phase. To provide sufficient resolution 200 to 1000 particles with different phases are used in subsequent sections of this chapter.

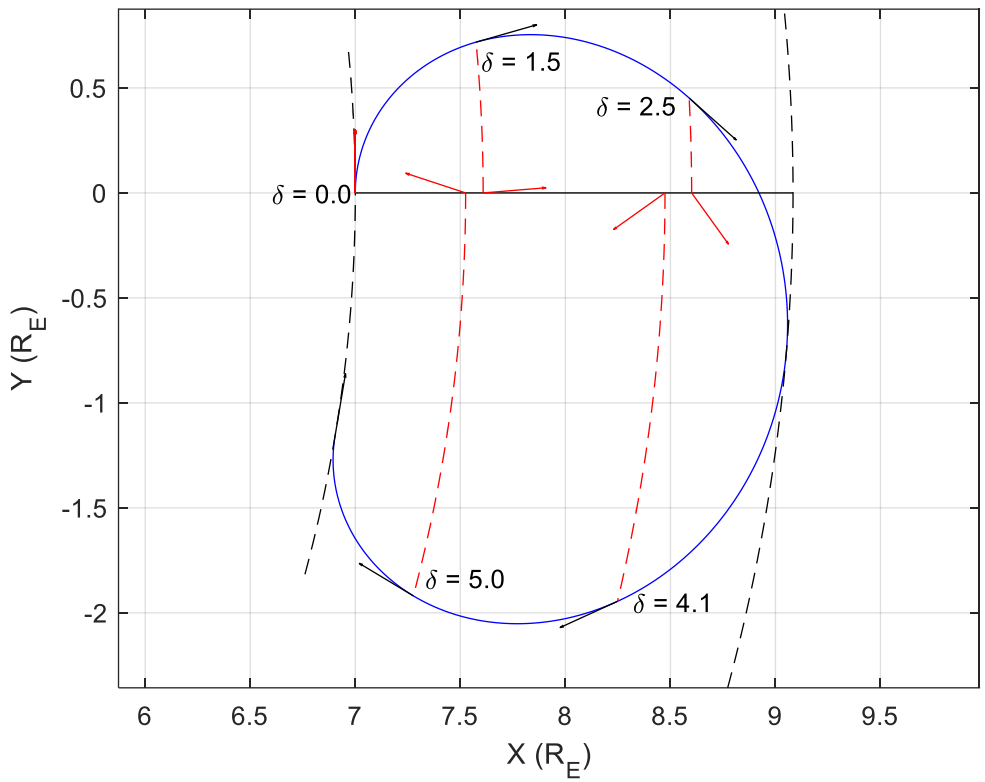

Figure 5.13: Initialization of various particles phase-shifted to have the same starting line. The particle is initiated with $m_0 = 1.673 \cdot 10^{-27}$ kg, $q = 1.602 \cdot 10^{-19}$ C, $r_0 = [7, 0]$ R_E and $v_0 = [0, 6]$ R_E/s. The magnetic field is out of the page with $M = 3.1 \cdot 10^{-5}$ TR_E^3. The trajectory is shown with a blue line, r_{min} and r_{max} with black dashed lines, starting line with a solid black line, local velocity vectors with black arrows, phase shift with res dashed lines and phase shifter velocity vectors with red arrows.

During our initial attempts, we simply used Matlab's events functionality to stop the integration when the particle returned to the positive x-axis, this ensured that the simulation corresponded to a single drift period. However, due to differences in phases, this created discontinuities in the data. These discontinuities appeared because different phases cross the $y = 0$ line at different parts of their gyration. Thus, trajectories for some initial phases had an extra gyration compared to some other initial phases. This is illustrated in Figure 5.14 by the two darkest blue lines being separated from the rest of the phases. For this figure and the remaining figures in the phase distribution section, we used the small $\nabla\varphi$ version of the magnetic field for illustration.

This separation of the phase endpoints causes complications in the calculation of P_φ and μ_{Exact}. To resolve this issue Matlab's events stopping condition of stopping at the positive x-axis was only used for the first phase. The time corresponding to this calculation was recorded and all the trajectories for the remaining phases were then integrated for the same time as the first one. Using this method, it is clear that all phases of particle tracing stop in the same vicinity. To illustrate the pattern the endpoints of each phase are graphed in Figure 5.15. On the left panel of Figure 5.15 we use our original, relatively high velocity of $v = 6$ R_E/s in a pure dipole field. This is done to determine if phase mixing is dependent on magnetic field asymmetry. The dipole field used is based on (5.1) with $f(\varphi)$ always set to 0 to remove the magnetotail component. On the right panel

of Figure 5.15, we use our non-axisymmetric magnetic field with a reduced velocity of v = 3.5 R_E/s. Overall the oval shape of Figure 5.15 shows that phases are not mixing up and the particles are coming back in the same order as the left. Stars are used to display the location of phases 0, $\pi/2$, π and $3\pi/2$.

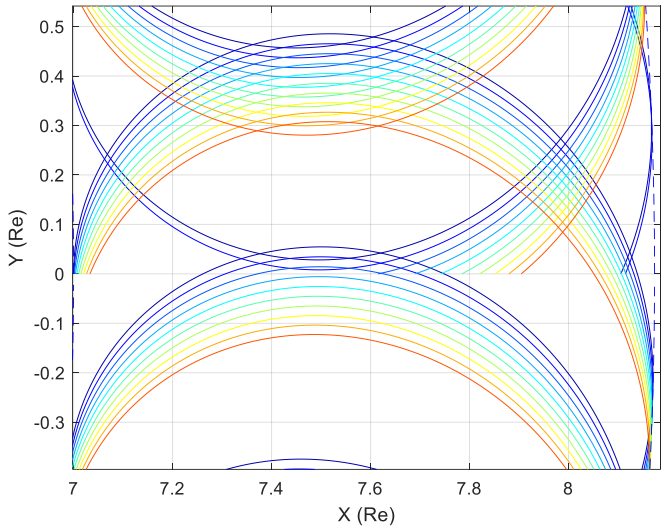

Figure 5.14: Discontinuity example of 10 phases δ = 0 to π/8, at start and end of drift period. The particle is initiated with m_0 = 1.673·10^{-27} kg, q = 1.602·10^{-19} C, r_0 = [x_0 (5.13), 0] R_E and v_0 =[sin(δ), cos(δ)] R_E/s. The magnetic field is out of the page with M = 3.1·10^{-5} TR_E^3.

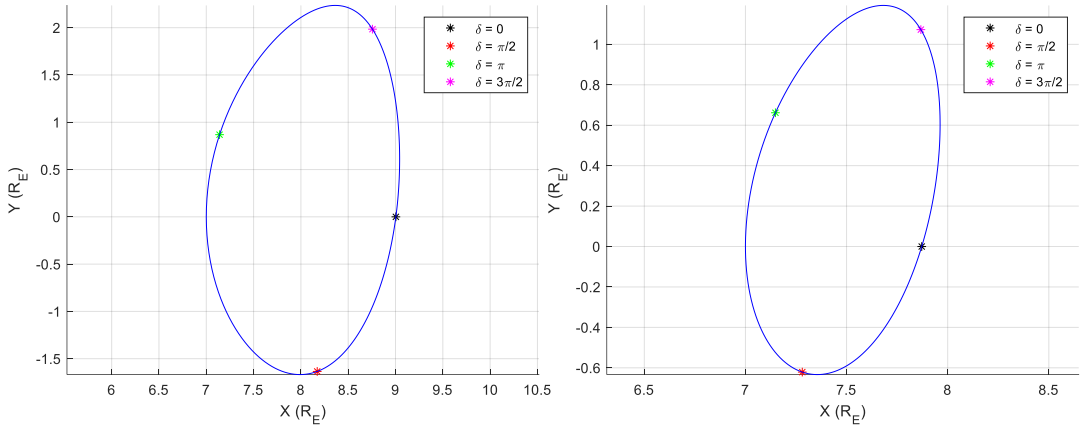

Figure 5.15: Endpoints of the trajectory for a 1000 particle with different phases in axisymmetric dipole with v = 6 R_E/s (left) and in non-axisymmetric field with v = 3.5 R_E/s (right). The particle is initiated with m_0 = 1.673·10^{-27} kg, q = 1.602·10^{-19} C, r_0 = [7, 0] R_E and v_0 = [0, v] R_E/s. The magnetic field is out of the page with M = 3.1·10^{-5} TR_E^3.. Phase 0, pi/2, pi, and 3pi/2 are marked with stars in black, red, green and magenta respectively.

From Figure 5.15 it is clear that calculating P_φ and μ_{Exact} using these endpoints eliminates our discontinuity problem as the line of endpoints shows that every adjacent phase has an adjacent endpoint. We now present the same phase graph in Figure 5.16 for our original v = 6 R_E/s, with the non-axisymmetric magnetic field. At this relatively high velocity, the phase endpoint pattern becomes more complex, indicating that we are approaching a limit in the applicability of the GC assumption. From Figure 5.15 and Figure 5.16 we conclude that the complex pattern of Figure 5.16 is attributed to the relatively high velocity and not field asymmetry.

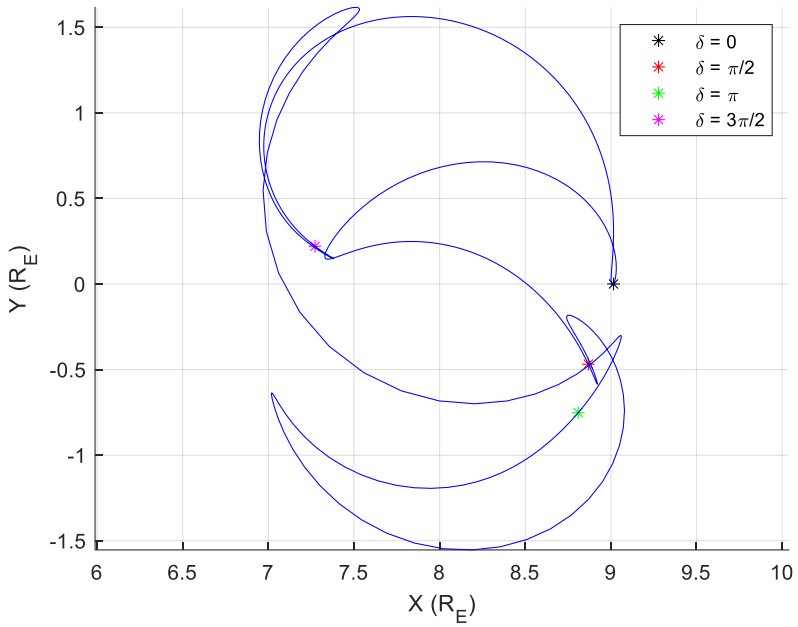

Figure 5.16: Endpoints of trajectory for 1000 phases in non-axisymmetric field with v = 6 R_E/s. The particle is initiated with m_0 = 1.673·10^{-27} kg, q = 1.602·10^{-19} C, r_0 = [7, 0] R_E and v_0 = [0, 6] R_E/s. The magnetic field is out of the page with M = 3.1·10^{-5} TR_E^3. Phase 0, pi/2, pi, and 3pi/2 are marked with stars in black, red, green and magenta respectively.

To illustrate that the initial phases do not mix for axisymmetric fields with relatively slow initial velocities we examine v = 3.5 R_E/s further. Figure 5.17 shows the final phase as a function of the initial phase for both the non-axisymmetric field and the pure dipole field. A factor of π is added to adjust the range of results from -π and π to 0 and 2π. The nearly identical left and right panels of Figure 5.17 show the result of this comparison and visually validates that phase endpoints are not dependent on magnetic field asymmetry for relatively low velocities. The shape of Figure 5.17 demonstrates a sinusoidal relationship between the final and initial phases. The discontinuity between 0 and 2π is expected and simply reflects the periodicity of the functions.

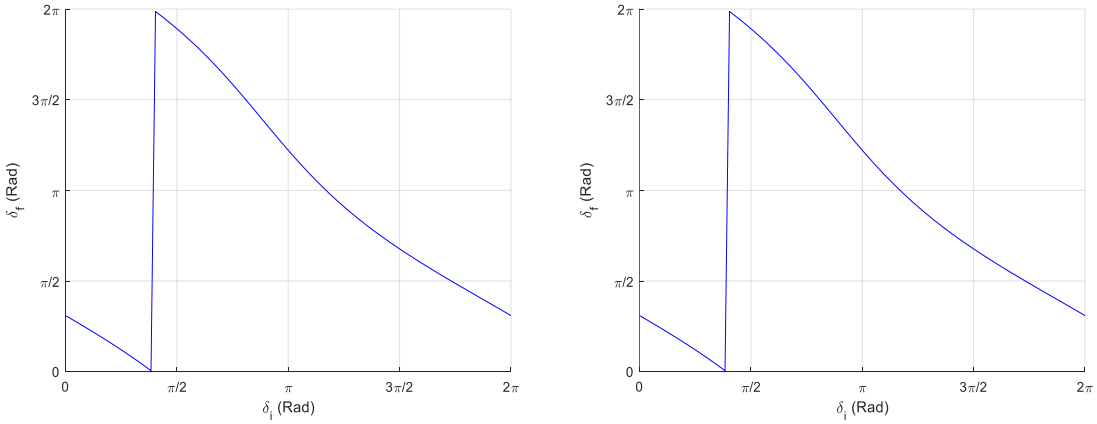

Figure 5.17: Final phase dependence on the initial phase in a non-axisymmetric field (left) and in an axisymmetric dipole (right). The particle is initiated with m_0 = 1.673·10^{-27} kg, q = 1.602·10^{-19} C, r_0 = [7, 0] R_E and v_0 = [0, 3.5] R_E/s. The magnetic field is out of the page with M = 3.1·10^{-5} TR_E^3.

5.4 Diffusion of the Canonical Angular Momentum and Magnetic Moment.

In this section, we analyze the difference between the final and starting values of P_φ and μ_{Exact} across all phases. The starting and final values correspond to the straight-line Sections of Figure 5.13. The change in P_φ and μ_{Exact} as the particles pass through the non-dipolar region can be interpreted as diffusion: an ensemble of particles with identical GC parameters at the beginning of the simulation becomes an ensemble of particles with somewhat different parameters after one drift period. Measuring this diffusion in P_φ and μ_{Exact} is done over a range of velocities that varies by intervals of 0.5 R_E/s. For every velocity analyzed we integrate 200-1000 particles corresponding to different initial phases for an entire drift. At high velocities, the time this took using an AMD Ryzen 7 5700U CPU was on the order of hours and increased as the velocity decreased. For this reason, the number of particles with different phases was reduced for small velocities. Often this code was left to run overnight. For this reason, we computed data in sets and then compiled the data together later. It should be noted that it is possible to dramatically reduce the computation time by using cluster parallel processing. Another reason preventing us from performing this calculation was numerical accuracy limits for relatively small velocities, as our results show that the ΔP_φ and $\Delta\mu_{Exact}$ quickly decrease with velocity, and at some point become comparable to the numerical accuracy of the calculation. While it is possible to extend our results to smaller particle speeds by using higher-order numerical integrators and possibly quadruple precision arithmetic, we did not pursue this because of the lack of time.

For our small $\nabla\varphi$ magnetic field, we start with velocities of 6.5 R_E/s, 6.0 R_E/s and 5.5 R_E/s. We then continue to decrease the velocity by 0.5 R_E/s intervals and generate new sets of three. The compiled results for the normalized values of P_φ are displayed in Figure 5.18. The highest velocity of 6.5 R_E/s was chosen based on the fact that the threshold velocity for the particle motion to become unbound for this case is just over 7 R_E/s. Furthermore, this velocity exceeds the limit at which the GC approximation can be applied comfortably, as Figure 5.16 indicated that the GC approximation starts to break down at a velocity of 6 R_E/s. Thus, the velocity of 6.5 R_E/s is, in essence, the largest velocity that is relevant for our study.

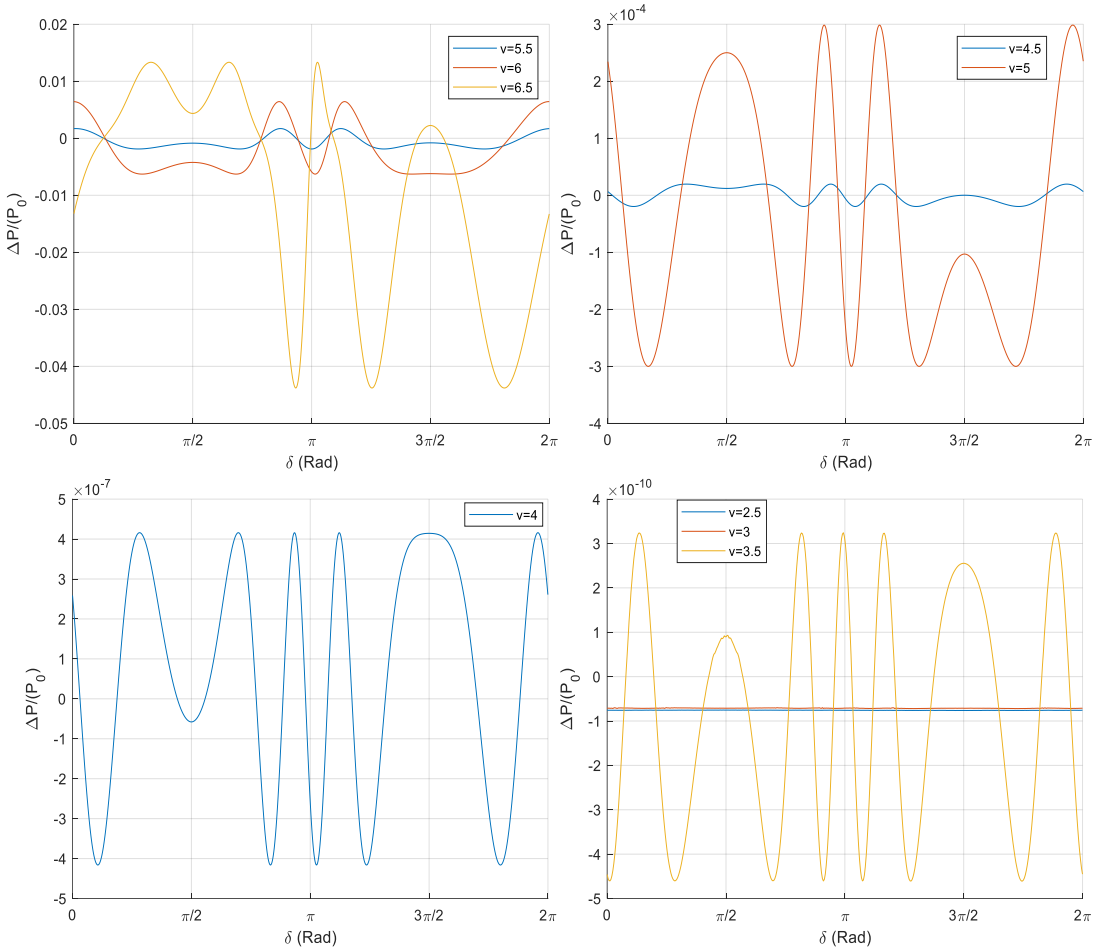

Figure 5.18: Normalized canonical angular momentum difference for one drift period for v = 2.5 R_E/s through 6.5 R_E/s. The particle is initiated with $m_0 = 1.673 \cdot 10^{-27}$ kg, $q = 1.602 \cdot 10^{-19}$ C, r_0 = [x_0 (5.13), 0] R_E and v_0 = v[sin(δ), cos(δ)] R_E/s. The magnetic field is out of the page with $M = 3.1 \cdot 10^{-5}$ TR_E^3.The top left panel is v = 6.5, 6 and 5.5 R_E/s; the top right panel is v = 5 and 4.5 R_E/s; the bottom left panel is v = 4 R_E/s; The bottom right panel is v = 3.5, 3 and 2.5 R_E/s

Figure 5.18 shows a complicated pattern of variation of $\Delta P_\varphi/P_0$ as a function of the initial phase. Additionally, the magnitude of $\Delta P_\varphi/P_0$ is shown to reduce from a scale on the order of 10^0 to 10^{-10} over this very narrow velocity range. This indicates a very rapid decline in the change of P_φ as a function of velocity. Due to this rapid decline, the data for the relatively low velocities of 2.5 R_E/s and 3.0 R_E/s were a result of numerical error and were thus omitted. This is visually validated by graphing the results of 2.5 R_E/s and 3.0 R_E/s alone and is given in Figure 5.19. Here we know our numerical limitations are reached based on the fact that the scale in Figure 5.19 is on the order of 10^{-11}, which coincides with our numerical limitation discussed earlier. In addition, the patterns in Figure 5.19 are clearly different from the waveforms in Figure 5.18. In principle, calculations for lower velocities could be achieved with a higher-order numerical integrator.

The same numerical limitation is also reached at these velocities for $\Delta\mu_{Exact}/\mu_0$. We now discuss similar graphs for $\Delta\mu_{Exact}/\mu_0$ and display them in Figure 5.20. In this figure the main difference between the results of $\Delta\mu_{Exact}/\mu_0$ and $\Delta P_\varphi/P_0$. is that the $\Delta P_\varphi/P_0$ decreases more rapidly

than $\Delta\mu_{Exact}/\mu_0$ as a function of velocity. This is seen by the order of magnitude decreasing to 10^{-8} for $\Delta\mu_{Exact}/\mu_0$, versus 10^{-10} for $\Delta P_\varphi/P_0$, over the same velocity range.

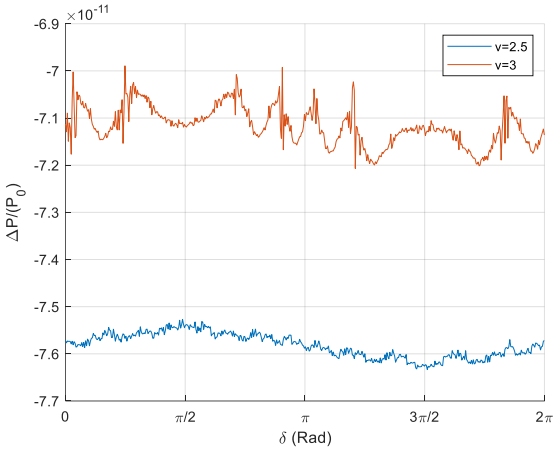

Figure 5.19: Normalized canonical angular momentum difference for one drift period over 500 Phases. The particle is initiated with $m_0 = 1.673\cdot10^{-27}$ kg, $q = 1.602\cdot10^{-19}$ C, $r_0 = [x_0\ (5.13), 0]$ R_E and $v_0 = v[\sin(\delta), \cos(\delta)]$ R_E/s. The magnetic field is out of the page with $M = 3.1\cdot10^{-5}$ TR_E^3. Results for $v = 2.5$ R_E/s are in blue and $v = 3$ R_E/s are in red.

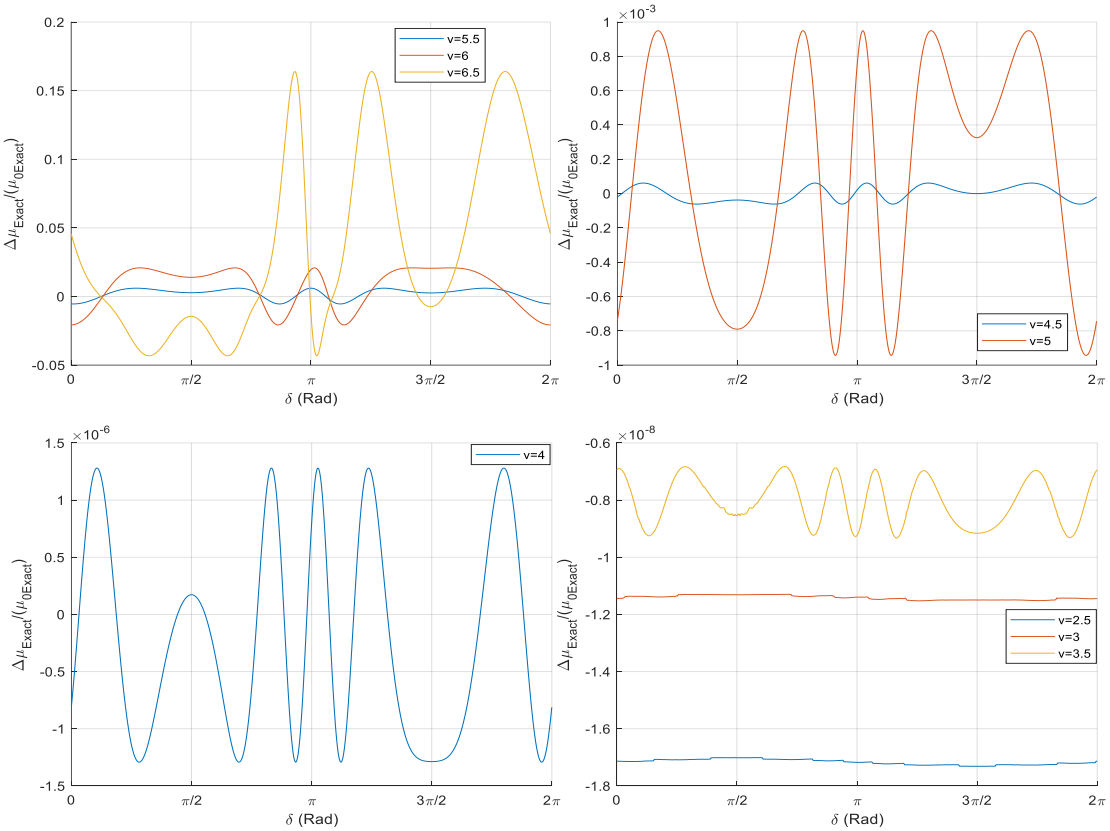

Figure 5.20: Normalized magnetic moment difference for one drift period for $v = 2.5$ R_E/s through 6.5 R_E/s.The particle is initiated with $m_0 = 1.673\cdot10^{-27}$ kg, $q = 1.602\cdot10^{-19}$ C, $r_0 = [x_0\ (5.13), 0]$ R_E and $v_0 = v[\sin(\delta), \cos(\delta)]$ R_E/s. The magnetic field is out of the page with $M = 3.1\cdot10^{-5}$ TR_E^3. The top left panel is $v = 6.5$, 6 and 5.5 R_E/s; the top right panel is $v = 5$ and 4.5 R_E/s; the bottom left panel is $v = 4$ R_E/s; The bottom right panel is $v = 3.5$, 3 and 2.5 R_E/s

To ensure the results displayed in Figure 5.18 and Figure 5.20 were in fact due to magnetic field asymmetry similar plots were produced for $\Delta P_\varphi/P_0$ and $\Delta\mu_{Exact}/\mu_0$ for a pure magnetic dipole field. This was only done for a velocity of 6 R_E/s and is displayed in Figure 5.21. The results show that the data does not show regular variations and the amplitude of the variations is on the order of 10^{-9} or 10^{-10}. This is characteristic of the numerical precision used in our simulations. Compared to the results of v = 6 R_E/s in Figure 5.18 and Figure 5.20 this validates diffusion occurs due to magnetotail asymmetry.

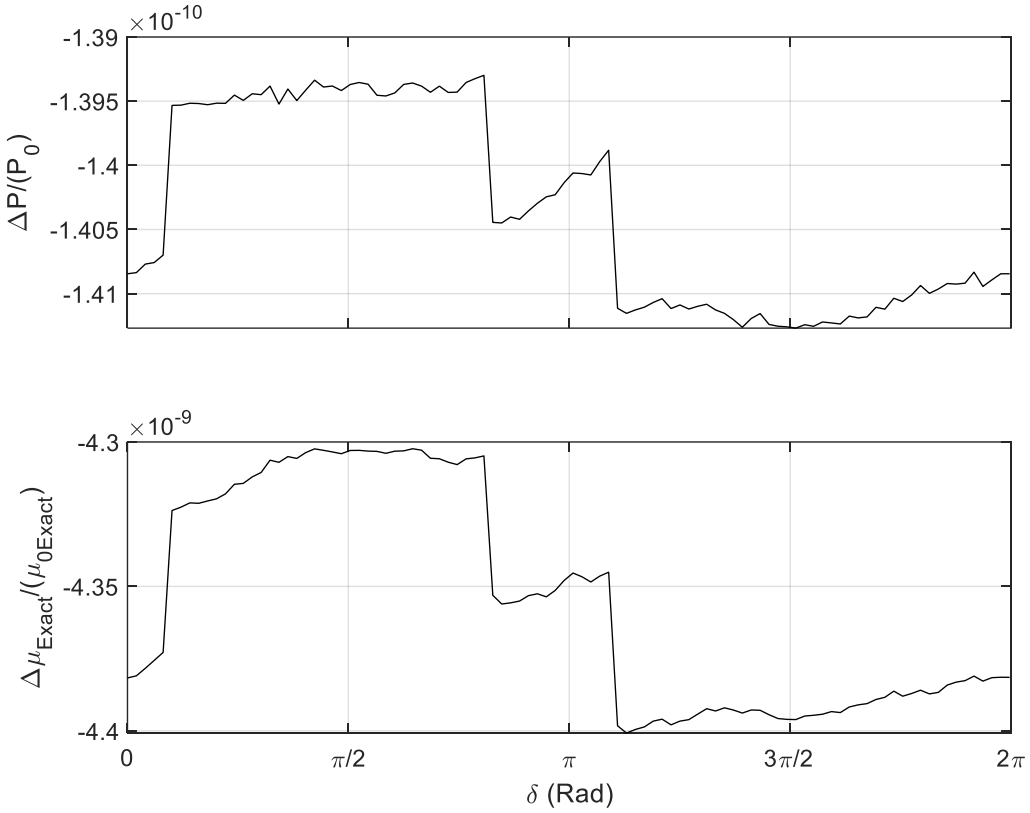

Figure 5.21: Normalized difference in canonical angular momentum (top) and magnetic moment (bottom) for one drift period in a pure dipole with v = 6 R_E/s. The particle is initiated with $m_0 = 1.673\cdot10^{-27}$ kg, $q = 1.602\cdot10^{-19}$ C, r_0 = [x_0 (5.13), 0] R_E and $v_0 = v$[sin(δ), cos(δ)] R_E/s. The magnetic field is out of the page with $M = 3.1\cdot10^{-5}$ TR_E^3.

Figure 5.18 and Figure 5.20 illustrate the dependence of $\Delta P_\varphi/P_0$ and $\Delta\mu_{Exact}/\mu_0$ on the phase of the particle. Since the GC approximation assumes all phases are condensed onto a single GC trajectory the very existence of these variations demonstrates the limitations of the GC approximation. In the following we use two measures to quantify the violation in the conservation of $\Delta P_\varphi/P_0$ and $\Delta\mu_{Exact}/\mu_0$. The first measure we use is simply the average of the data in Figure 5.18 and Figure 5.20. The second method uses the maximum amplitude of $\Delta P_\varphi/P_0$ and $\Delta\mu_{Exact}/\mu_0$ for any phase.

A similar analysis was performed for large $\nabla\varphi$ and the piece-wise linear function magnetic fields. The plots of $\Delta P_\varphi/P_0$ and $\Delta\mu_{Exact}/\mu0$ as a function of initial phases are not included here

because they are redundant to the patterns illustrated in Figure 5.18 and Figure 5.20. What is important is the $\Delta P_\varphi/P_0$ and $\Delta\mu_{Exact}/\mu_0$ as a function of velocity. However, a notable difference in the calculations performed in these magnetic fields is the range of velocity we were able to use. For large $\nabla\varphi$ we used velocities that ranged between v = 2 R_E/s and v = 5 R_E/s. The choice of 5 R_E/s was due to the threshold speed limitation of this magnetic field and the choice of 2 R_E/s was due to the numerical limitations. For the piece-wise linear function, we used velocities that ranged between v = 1 R_E/s and v = 6.5 R_E/s. Since the piece-wise linear function is based on small $\nabla\varphi$ they share the same upper limit of v = 6.5 R_E/s. The lowest velocity of 1 R_E/s was chosen because of the time limitations of the calculations. At v = 1 R_E/s, the code ran for upwards of 12 hours and thus lower velocities were not pursued.

Combining the results of $\Delta P_\varphi/P_0$, for all three magnetic fields, allows us to generate Figure 5.22 below, here < > represents the average across phases and Δ represents the maximum amplitude across phases.

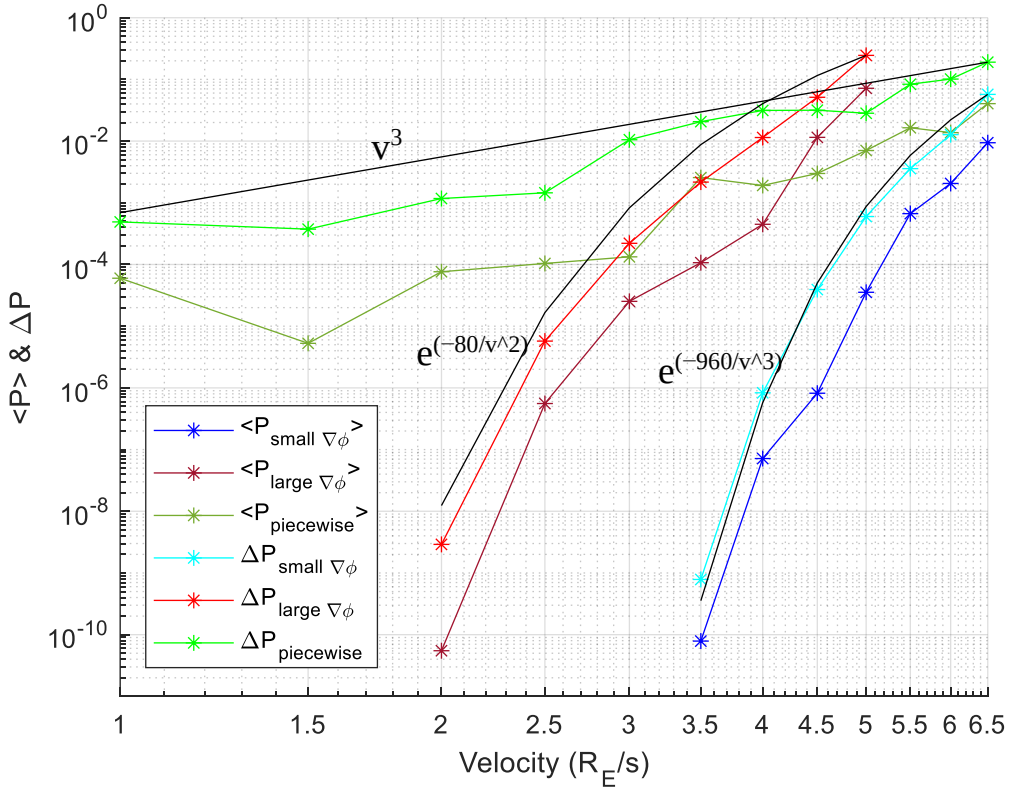

Figure 5.22: Average and amplitude of $\Delta P_\varphi/P_0$ for all three magnetic fields. A The particle is initiated with m_0 = $1.673\cdot10^{-27}$ kg, q = $1.602\cdot10^{-19}$ C, r_0 = [x_0 (5.13), 0] R_E and v_0 = v[sin(δ), cos(δ)] R_E/s. The magnetic field is out of the page with M = $3.1\cdot10^{-5}$ TR_E^3. Results for large $\nabla\varphi$ are in blue, small $\nabla\varphi$ are in red and piecewise linear are in green. The darker colour corresponds to the average and the lighter to the amplitude.

For a smooth magnetic field profile, $\Delta P_\varphi/P_0$ decreases very rapidly with velocity. Figure 5.22 suggests that the diffusion of $\Delta P_\varphi/P_0$ is an exponentially small function of the velocity. This is illustrated by the shape of the red and blue lines representing large $\nabla\varphi$ and small $\nabla\varphi$ respectively. For large $\nabla\varphi$ the line of best fit, given in black, demonstrates that $\Delta P_\varphi/P_0$ is proportional to e^{-80/v^2}.

For small ∇φ the line of best fit demonstrates the diffusion of $\Delta P_\varphi/P_0$ is proportional to e^{-960/v^3}. To reiterate the difference between these two cases was a factor of four in their respective $f(\varphi)$ Equations. Based on the black lines of best fit no correlation between this factor of four in the exponents is obvious, further analysis is required to understand this behaviour. In the future, it would be worthwhile to perform additional simulations for additional velocity values and to extend the range of the velocities used by increasing the accuracy of the calculations by using a higher-order numerical integrator. If $f(\varphi)$ is a piecewise linear function, and thus has a non-continuous derivative, then it is concluded that the diffusion of $\Delta P_\varphi/P_0$ follows a power-law relationship. This is illustrated by the shape of the green lines, where the corresponding black line of best fit is proportional to v^3. Figure 5.22 also shows that the average deviation from the initial value is considerably smaller than the amplitude, but they both follow approximately the same pattern as a function of v.

The radical difference in the accuracy with which $\Delta P_\varphi/P_0$ is conserved between the smooth and non-smooth magnetic variations is not entirely surprising. Similar behaviour is known for the adiabatic invariants. When the time variation of the parameters of the system is smooth, then the change between the final and initial states of the invariant is an exponentially small function of the rate of change of the system parameter. This has been shown in papers by Kabin [11], Chandrasekhar [35] and Littlewood [34]. However, to the best of our knowledge, this kind of behaviour has not been discussed for the canonical momentum. This result might have considerable theoretical importance for future studies of systems that are almost symmetric.

Figure 5.23 presents a plot similar to Figure 5.22 but for $\Delta\mu_{Exact}/\mu_0$. In this figure, the trends are very similar to Figure 5.22 and the same conclusions are drawn. A notable difference is that all corresponding data points for $\Delta P_\varphi/P_0$ are smaller than for $\Delta\mu_{Exact}/\mu_0$. Thus showing that canonical momentum under the considered conditions is conserved better than the magnetic moment. It should also be noted that the difference in the level of conservation of the adiabatic moment for smooth and non-smooth field variations was also explored for $\Delta\mu_{Exact}/\mu_0$ in a paper by Kabin [11]. However, Kabin examined a magnetic field with a constant gradient similar to our Chapter 3, and focused on time-dependent magnetic fields, while we study exclusively the effects of spatial variations. Despite this difference, the same conclusion of smooth functions being exponentially proportional to velocity and piecewise functions being power-law proportional was reached [11].

Figure 5.22 and Figure 5.23 show particles with different phases disperse as a result of passing through a non-axisymmetric magnetic field. Since different phases are indistinguishable in the GC approximation, this process may be represented as a diffusion, where a population of particles with initially identical GC parameters passes through a region of field asymmetry and comes out as a population with slightly different GC parameters. Naturally, this process repeats every time the particles pass through the magnetotail, thus the errors in the initial GC approximation are secular. After multiple transits through the magnetotail, the initial delta-function distribution of particles becomes wider thus this is a diffusion process. Further analysis of these results, as well as other magnetic fields, would allow us to calculate the velocity-dependent diffusion coefficient for the GC approximation, thus allowing us to mimic the effect of the initial phases of the particles. This project is potentially very important in the context of magnetospheric modelling, but is too time-consuming to be attempted as a part of this thesis. It is therefore left for future work.

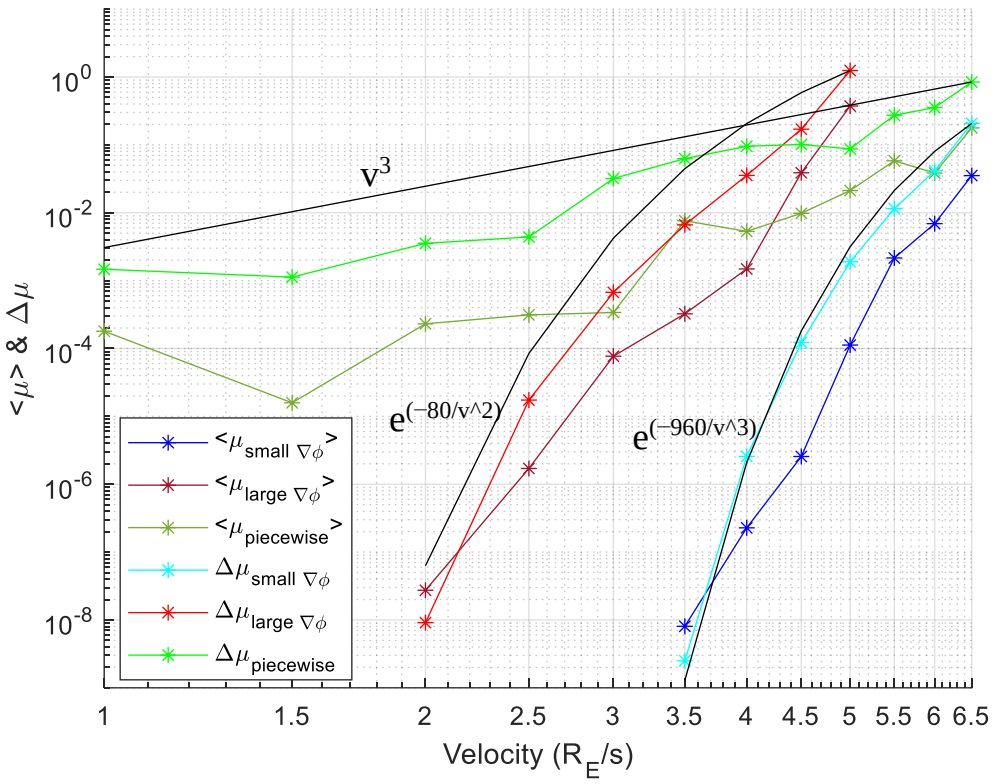

Figure 5.23: Average and amplitude of $\Delta\mu_{Exact}/\mu_0$ for all three magnetic fields. The particle is initiated with m_0 = $1.673\cdot10^{-27}$ kg, q = $1.602\cdot10^{-19}$ C, r_0 = [x_0 (5.13), 0] R_E and v_0 = v[sin(δ), cos(δ)] R_E/s. The magnetic field is out of the page with M = $3.1\cdot10^{-5}$ TR_E^3. Results for large ∇φ are in blue, small ∇φ are in red and piecewise linear are in green. The darker colour corresponds to the average and the lighter to the amplitude.

5.5 Diffusion of Particle Trajectory Boundaries

As discussed in the previous section, the generalized angular momentum of a particle is dependent on the initial phase of the particle. Therefore, r_{min} and r_{max} of the particle are also dependent on the initial phase as well. Note, that in the GC approximation these quantities also remain constant. We now examine the diffusion of the particle boundaries due to magnetic field asymmetry. This analysis is only done for the small ∇φ magnetic field. Overall the goal is to determine if there is a net drift outward or inward on the ensemble of particles that differ only in their initial phase. This drift has the potential to be quite important since in the GC it is directly associated with energy gain or loss. For example, if particles conserve their magnetic moment, then moving closer to the Earth, into the region of a stronger magnetic field implies energy gain by the particle. The reverse is true for a particle moving further away from the Earth [23]. To determine the net drift we plot the change in r_{min} and r_{max}, normalized by their respective initial values, as a function of the initial phase. The velocity range is from 1 R_E/s to 6.5 R_E/s, and not 3.5 R_E/s to 6.5 R_E/s like before, as r_{min} and r_{max} remained accurate in the numerical calculation at lower velocities. The results for velocities 5.5 R_E/s, 6 R_E/s and 6.5 R_E/s are displayed below in Figure 5.24. Velocities from 1 R_E/s to 5 R_E/s are not included because it hinders visualization and the data is very similar to the cosine shape corresponding to v = 5.5 R_E/s in Figure 5.24

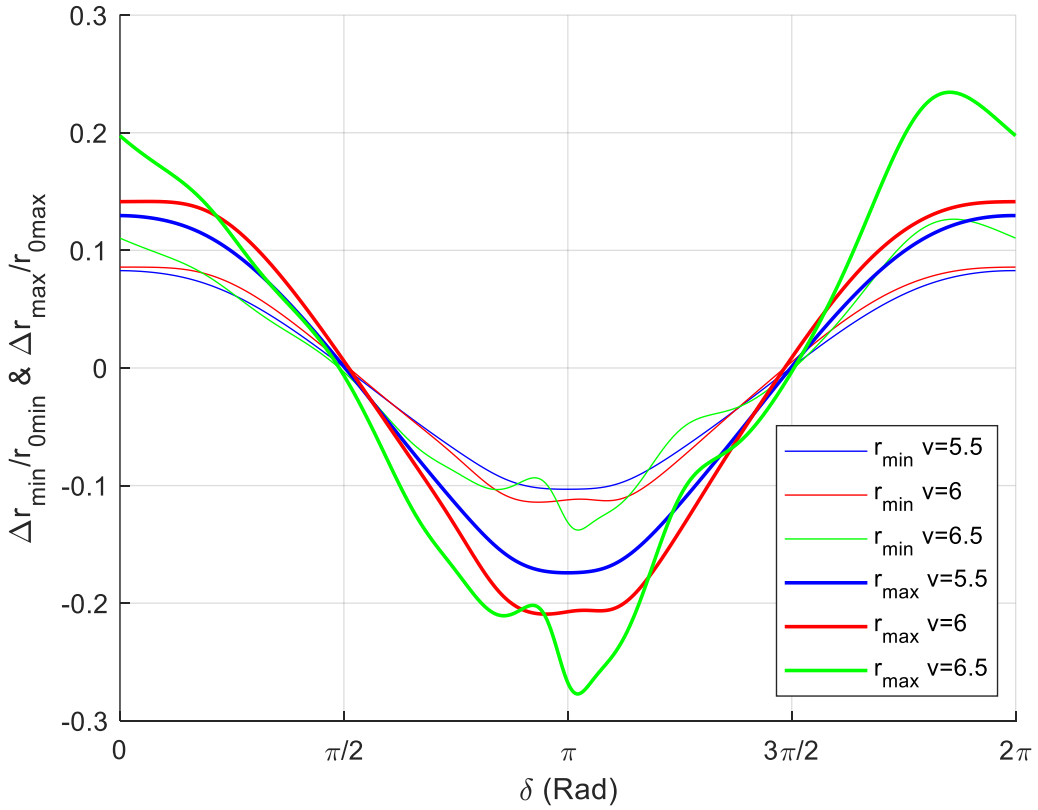

Figure 5.24: Normalized difference in r_{min} and r_{max} after one drift period across all phases for v = 6.5, 6 and 5.5 R_E/s. The particle is initiated with $m_0 = 1.673 \cdot 10^{-27}$ kg, $q = 1.602 \cdot 10^{-19}$ C, r_0 = [x_0 (5.13), 0] R_E and v_0 = v[sin(δ), cos(δ)] R_E/s. The magnetic field is out of the page with $M = 3.1 \cdot 10^{-5}$ TR_E^3.

This figure shows that particles with an initial phase between π/2 and 3π/2 drift inwards, towards Earth, while particles outside this phase range drift outwards, away from Earth. Based on our definition of phases the interval between π/2 and 3π/2 corresponds to when the particle is initialized closer to r_{max}. For relatively small particle speeds, the dependence of r_{min} and r_{max} on δ is remarkably close to a cosine function. As the velocity increases, however, this profile starts to deviate from cosine significantly, as seen at v = 6.5 R_E/s in Figure 5.24. Another way of characterizing the inward or outward diffusion of particles crossing the magnetotail is to calculate the average over the phase displacement. The result is displayed in Figure 5.25 showing the average change in r_{min} and r_{max} as a function of velocity.

Overall Figure 5.25 shows that the normalized change in r_{min} and r_{max} are positive for velocities of 2 R_E/s or less, and negative for velocities of 2.5 R_E/s or more. Thus indicating a diffusion outward for lower velocities and a diffusion inward for higher velocities. The spike in the data between 6 R_E/s and 6.5 R_E/s is attributed to approaching the upper limits of validity for this analysis. Lastly, it is shown that r_{max} moves further inward than r_{min} for inward diffusion as velocity is increased, thus the trajectory bounds tighten for inward drifting particles.

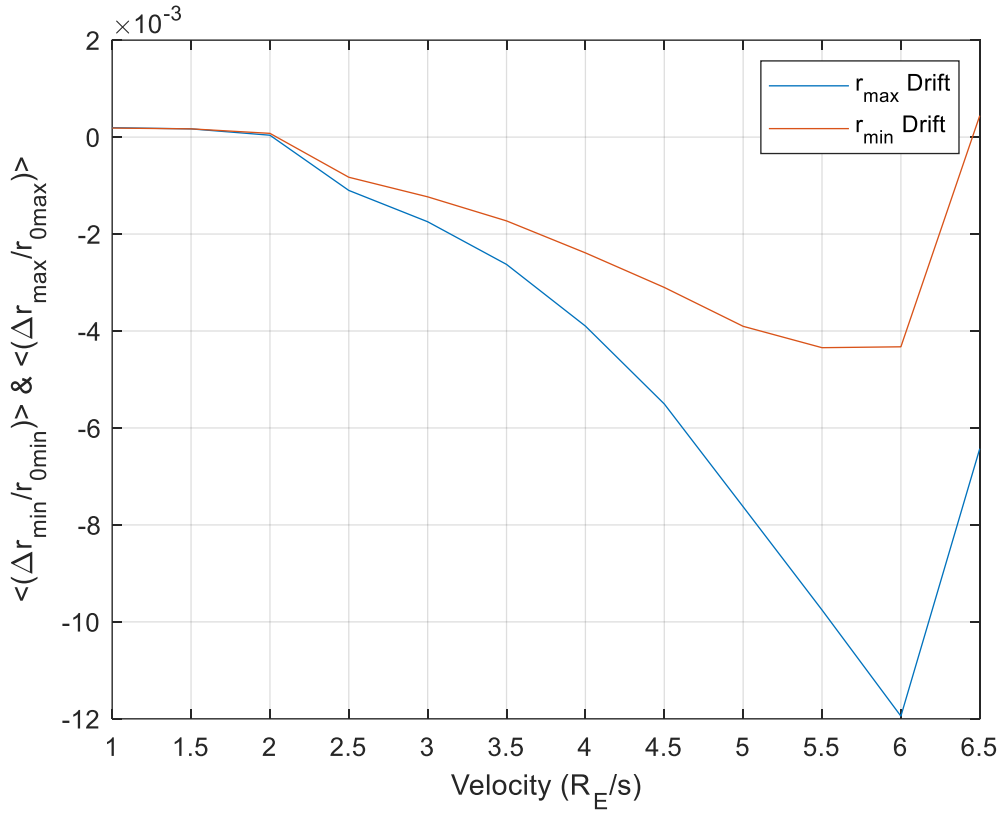

Figure 5.25: Average normalized difference in r_{min} and r_{max} after one drift period from v = 1 to 6.5 R_E/s. The particle is initiated with $m_0 = 1.673 \cdot 10^{-27}$ kg, $q = 1.602 \cdot 10^{-19}$ C, r_0 = [x_0 (5.13), 0] R_E and $v_0 = v[\sin(\delta), \cos(\delta)]$ R_E/s. The drift of r_{min} is in red and the drift r_{max} is in blue.

Since $\Delta r_{min}/r_{min0}$ and $\Delta r_{max}/r_{max0}$ in Figure 5.24 appear to be close to basic trigonometric functions, specifically cosines, a Fourier series expansion is done to simplify the analysis of velocity dependence. To fit these graphs a 3rd order Fourier expansion is used, meaning four coefficients are calculated. These coefficients are labelled a_0, a_1, a_2 and a_3. Thus the Fourier expansion takes the following form:

$$\frac{\Delta r_{min}}{r_{min0}} \text{ or } \frac{\Delta r_{max}}{r_{max0}} = a_0 + a_1\cos(\delta) + a_2\cos(2\delta) + a_3\cos(3\delta) \tag{5.14}$$

Applying Equation (5.14) to every plot in Figure 5.24 allows us to generate values for a_0, a_1, a_2 and a_3 for every velocity used in that figure. Since most of the functions from Figure 5.24 appear to be shaped like a cosine function it was unsurprising that the coefficient a_1 had the most predictable shape. Furthermore, a_1 had significantly higher values across all velocities when compared to a_0, a_2 and a_3, making it the dominant coefficient. Therefore all other coefficients are ignored. They were only calculated to verify that a_1 is indeed sufficient to describe the shape of the curve. Plotting a_1 as a function of velocity on a log scale resulted in the generations of Figure 5.26, where the red and blue lines correspond to $\Delta r_{min}/r_{min0}$ and $\Delta r_{max}/r_{max0}$ respectively.

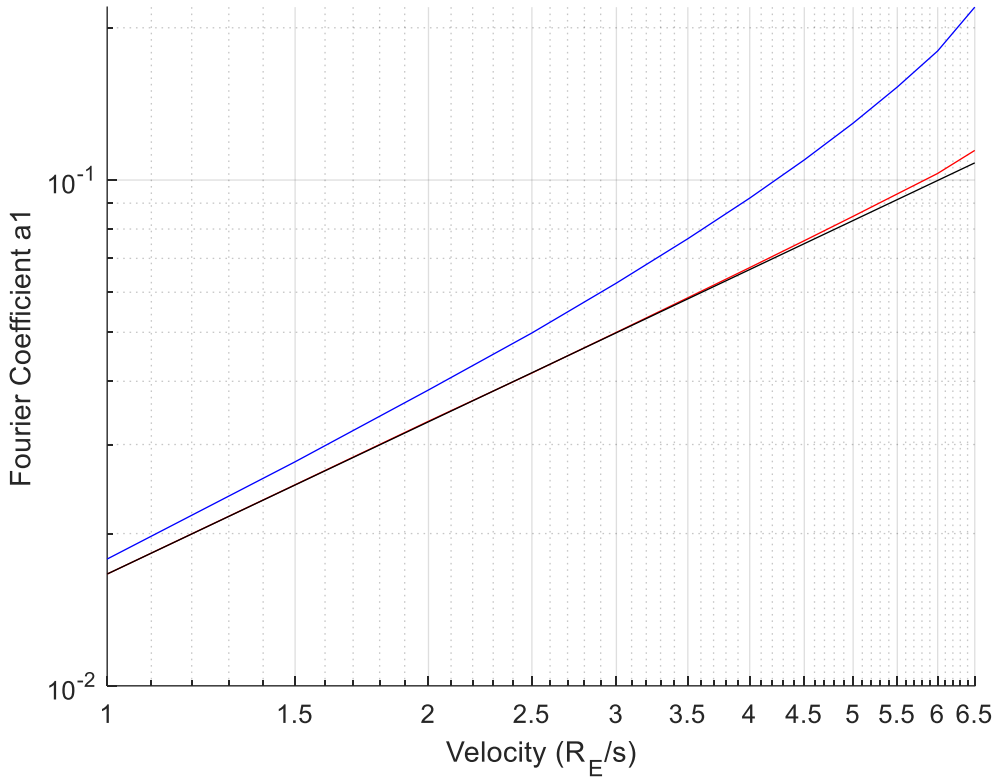

Figure 5.26: Log plot of Fourier series coefficient a_1 as a function of velocity. r_{min} is in red and r_{max} is in blue. Black is the value of a_1 for r_{min} at v = 1 R_E/s, multiplied by v^1.

In Figure 5.26 the black line is the value of a_1 for $\Delta r_{min}/r_{min0}$ at v = 1 R_E/s, multiplied by v^1. Thus Figure 5.26 shows that the cosine shapes of $\Delta r_{min}/r_{min0}$ are proportionate to v^1. In regards to $\Delta r_{max}/r_{max0}$ in blue, the same conclusion is true for relatively low velocities. For relatively high velocities it is clear that a_1 deviates from the v^1 proportionality for the cosine shapes of $\Delta r_{max}/r_{max0}$. This is attributed to the results of Figure 5.25 where it was shown that $<\Delta r_{max}/r_{max0}>$ moves more rapidly further inwards than $<\Delta r_{min}/r_{min0}>$.

5.6 Conclusion

In this chapter, we analyzed in detail the effects of magnetic field asymmetry on the conservation of canonical angular momentum and the first adiabatic invariant of the particle. Specifically, we analyzed particles that are confined to the equatorial plane of a magnetic dipole, modified by a tail current sheet on the nightside. Since the GC approximation is dependent on the conservation of the magnetic moment this is an important test of the GC accuracy and the range of applicability. This analysis is relevant to the high-energy particles in the outer Van Allen belt [1] [36] [37] [38].

In this chapter, we considered three separate versions of the magnetotail to demonstrate the differences arising from the magnetic field gradients. The magnetotail fields differed by a function that made the magnetic field weaker when the particle was at a certain φ location. This

function, $f(\varphi)$, ranged from 0 to 1. The first two magnetic fields relied on an $f(\varphi)$ that was smooth to gradually achieve the transition from the dipolar magnetic field on the dayside to the tail-like field on the nightside. The first was denoted as small $\nabla\varphi$ based on the slower transition in $f(\varphi)$. The second was denoted as large $\nabla\varphi$ based on the faster transition in $f(\varphi)$. The last magnetic field examined relied on an $f(\varphi)$ that was a piecewise linear function. The slope for the linear part of function $f(\varphi)$ was chosen to correspond to the maximum derivative of $f(\varphi)$ for small $\nabla\varphi$.

We described a procedure to initialize the particle which differs only in the initial phases. Since the GC approximation assumes all phases are collapsed onto the GC, these particles are indistinguishable in the GC approximation. Thus, by analyzing the effect of the initial phase of the particle we assessed the accuracy of the GC approximation. The detailed calculations following thousands of particles with different phases were quite time-consuming, which was a limiting factor in our study. This ultimately put a constraint on the range of velocities analyzed and the number of velocities analyzed.

The magnetic field used in this section was axisymmetric on the dayside which assured strict conservation of the canonical angular momentum and the adiabatic invariant. The magnetic field on the nightside was not axisymmetric which resulted in the violation of these conservation laws. Somewhat surprisingly it was found that the canonical angular momentum returns close to its original value after the particle has passed through the asymmetric magnetotail. It was furthermore shown that the change in the canonical momentum is exponentially small in velocity if the magnetic field variation is smooth. To the best of our knowledge, this is a new result that may be important in theoretical plasma physics. If the magnetic field variation is a piece-wise linear function, the change in ΔP_φ is only proportional to v^3. A similar level of conservation is well-known for the adiabatic invariants, but this is the first time it is observed for the canonical momentum. The change in the canonical momentum and the adiabatic invariant as a result of crossing the magnetotail area is considered a diffusion process. Although this process cannot be explicitly modelled in the GC approximation, it can be added to it as a statistical diffusion process.

Analysis of the conservation of the adiabatic moment in the same situation yielded similar results. For a smooth variation of the magnetic field, the change in the magnetic moment of a particle after passing through the magnetotail was exponentially small in the velocity. If the variation of the magnetic field was a piece-wise linear function, the change in the adiabatic invariant was proportional to v^3. This result agrees with the general theory of the adiabatic invariants.

Finally, the effects of asymmetry on r_{min} and r_{max} were examined because they rely on the conservation of canonical momentum. For particles initiated closer to r_{max}, with initial phases between $\pi/2$ and $3\pi/2$, it was found that both r_{min} and r_{max} decreased. Therefore, these particles drift inward. In contrast, for particles initiated closer to r_{min}, outside phases $\pi/2$ and $3\pi/2$, it was found that r_{min} and r_{max} increased, thus these particles drift outward. This relatively small drift of the particles arising from passing through the magnetotail may also be considered diffusion. Averaging across phases it was found that particles with $v \leq 2$ R_E/s drift outward, while particles with $v \geq 2.5$ R_E/s drift inward. Although there is no energy change for particles moving in purely magnetic fields, inward drift in GC theory is often considered to be equivalent to energy gain, and outward drift to energy loss. For most of the velocity range considered, the dependence of r_{min} and r_{max} on the initial phase was approximated very well by a cosine function. Using a Fourier transform it was verified that cosine is indeed the dominant coefficient in the expansion, comfortably exceeding the

next largest coefficient by an order of magnitude or more. This surprisingly simple dependence on the phase might help develop a semi-empirical formula for the diffusion coefficient, however, this study is left for future work.

6. Particle Motion in Three Dimensions in a Magnetic Dipole

In this chapter, we analyze the motion of charged particles that are initiated on the equatorial plane, but with an initial $v_z \neq 0$. Thus, the motion of the charged particle is now three-dimensional. The magnetic field used for modelling is a simple dipole, introduced in more detail in Section 6.1. Plasma particles in a magnetic dipole are free to move along the magnetic field lines to some extent. From the conservation of the magnetic moment, Equation (2.18), we know that as B increases so does $v_\perp$, and we know B increases towards the poles due to the fact that a dipole magnetic field line density increases towards the poles. Substituting $v_\perp = v\sin\alpha$ into Equation (2.18) it becomes clear that α tends to move toward $\pi/2$ or $3\pi/2$ as the particle travels along the field line, away from the equatorial plane. Once the pitch angle reaches $\pi/2$ or $3\pi/2$ the particle no longer has any parallel kinetic energy and is reflected at this mirror point due to the parallel component of the gradient force [1]. It is through this mechanism that high energetic plasma particles get trapped in the Earth's Van Allen Belts. Thus, the increase in B along the magnetic field lines results in some particles being reflected back towards the magnetic equator, which is known as a magnetic bottle. Particles not contained within this field effect are considered to be part of the loss cone. Conditions necessary to meet loss criteria are discussed in more detail in Section 6.3. In general, a particle is considered to be part of the loss cone when α is significantly small at the equator [39].

Under most circumstances, particles in of the loss cone travel along magnetic field lines to high latitudes where they are absorbed by Earth's atmosphere at roughly 100km above the surface, though this varies as Earth's atmosphere is thicker at higher latitudes. In some circumstances though, rapidly changing space weather conditions cause magnetic field lines to break and reconnect, which funnels a tremendous amount of particles towards Earth's poles. This process is responsible for the auroras seen at high latitudes around Earth's poles, of which loss cone particles contribute to. These charged particles precipitate into the upper atmosphere where they ionize stable elements such as O_2 and N_2, resulting in the formation of bands of colours in the sky. The colour of the aurora depends on the element ionized and the altitude of ionization, ionization which in turn is related to the energy of the precipitating particle [33].

Analyzing trapped plasma particles, we aim to scrutinize some assumptions in GC theory. Particularly, we focused on the question of whether the equatorial pitch angle α_{eq} remains constant at every equatorial crossing. This assumption is often used in the simplest implementation of the GC theory, even though it is known that α_{eq} does deviate at every equatorial crossing, even when $E = 0$ and the plasma is assumed to be collisionless [40]. Thus, we aim to quantify the deviation of the GC approximation by computing the real 3D trajectories of plasma particles.

6.1 Analysis of Three-Dimensional Magnetic Field

We now introduce the magnetic field used in this Chapter. The magnetic field of a dipole is given by Equation (4.1). Using the magnetic field line Equation (4.3) we generate a 3D plot of the field lines in Figure 6.1 for visualization purposes. In this figure blue represents magnetic field lines below the magnetic equatorial plane and red represents field lines above it.

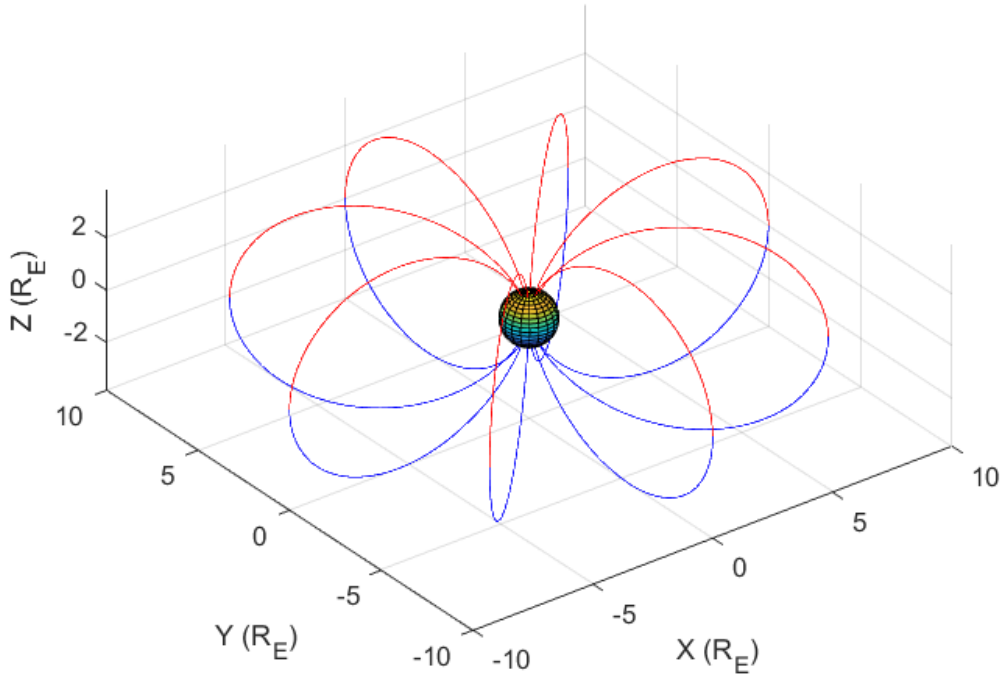

Figure 6.1: Eight 3D magnetic field lines crossing the equatorial plane at r = 10 R_E. The southern field lines are in blue and the northern field lines are in red. Earth is represented by the center sphere with a r =1 R_E.

For practical implementation of the code it is convenient to convert the magnetic field expression given by Equation (4.1) to cartesian coordinates. The result is given by Equation (6.1). This is done under the assumption that the magnetic dipole has no tilt. In this section we use the real dipole moment of the Earth, so M is given a value of $3.1 \cdot 10^{-5} T R_E^3$ and we assume all distances are measured in R_E [1].

$$\mathbf{B} = \frac{M}{r^5}(-3xz\,\hat{\mathbf{e}}_x, -3yz\,\hat{\mathbf{e}}_y, (x^2 + y^2 - 2z^2)\,\hat{\mathbf{e}}_z) \tag{6.1}$$

$$r = \sqrt{x^2 + y^2 + z^2} \tag{6.2}$$

Although it is easiest to solve the Equations of particle motion in cartesian coordinates, many analytical expressions involving the magnetic dipole appear simplest in spherical coordinates. The magnetic vector potential for this magnetic field is given by Equation (6.3), where θ is the colatitude defined as $\theta = \pi/2 - \lambda$.

$$\mathbf{A} = -\frac{M\sin(\theta)}{r^2}\hat{\mathbf{e}}_\varphi \tag{6.3}$$

6.2 Analytical Properties of 3D Trajectories

The magnetic vector potential is useful to determine the canonical momentum established in Equation (2.16). Since A does not depend on φ, the φ-component of the canonical momentum is conserved. Substituting Equation (6.12) into Equation (2.16), and only using the φ-component of velocity results in the expression for P_φ given by Equation (6.4).

$$P_\varphi = \rho\left(mv_\varphi - \frac{qM\sin\theta}{r^2}\right) \tag{6.4}$$

$$v_\varphi = \frac{xv_y - yv_x}{\rho} \tag{6.5}$$

Although the conservation of P_φ follows naturally from Lagrangian dynamics, where the canonical angular momentum is conjugate to the azimuthal angle φ, it is often called the Størmer's integral or invariant [36].

Similar to Section 4.1 we can use Equation (6.4) to determine the bounds of motion of the particle. Since the magnitude of v_φ cannot be larger than the magnitude of v we obtain Equations (6.6) and (6.7) for r_{min} and r_{max} respectively.

$$r_{min} = \frac{P_\varphi + \sqrt{P_\varphi^2 + 4mqMv\sin^3\theta}}{2mv\sin\theta} \tag{6.6}$$

$$r_{max} = \frac{-P_\varphi - \sqrt{P_\varphi^2 - 4mqMv\sin^3\theta}}{2mv\sin\theta} \tag{6.7}$$

An example of these radial bounds is given in Figure 6.2. In this figure we define $\rho_{min} = r_{min}\cdot\sin\theta$ and $\rho_{max} = r_{max}\cdot\sin\theta$ as it is often convenient to make the plots of the particle trajectory in cylindrical coordinates to view the particle from the meridian plane. In Figure 6.2 the solid black lines correspond to our ρ_{min} and ρ_{max} bounds, while the blue line is a ion initiated with $m_0 = 1.673\cdot10^{-27}$ kg, $q = 1.602\cdot10^{-19}$ C, $r_0 = [7, 0, 0]$ R_E and $v_0 = [0, v\sin\alpha, v\cos\alpha]$ R_E/s. In this example we use $v = 1$ R_E/s and $\alpha = \pi/4$. We use Matlab's events functionality to stop the calculation after half a bounce, which we define as the time until the particle first crosses the equatorial.

Unlike the situation described in Section 4.1 these bounds are not near the particle's trajectory at the equator. This is because the particle in this region has $v_\parallel$, and, therefore, v_φ cannot exceed $v_\perp$. In contrast, near the mirror point ρ_{min} and ρ_{max} provide tight bounds for the trajectory of the particle because right at the mirror point $v_\parallel = 0$. Providing tight bounds on the trajectory near the equatorial plane would require another conservation law which would allow us to constrain $v_\parallel$. Unfortunately, no such conservation law is known for 3D particle motion in a dipole field. In fact, no exact conservation law of this type likely exists as the problem is generally believed to be non-integrable. Thus, an exact solution for the first adiabatic invariant does not exist for 3D motion. However, the first adiabatic invariant can be approximated by Equation (2.18) and used as the additional conservation law [12]. We do not do this since all approximate expressions for the

adiabatic invariant lose accuracy for high velocity, which is the case we are interested in most. Therefore, we accept Equations (6.6) and (6.7), to provide strict bounds for the motion of a particle, if not always tight.

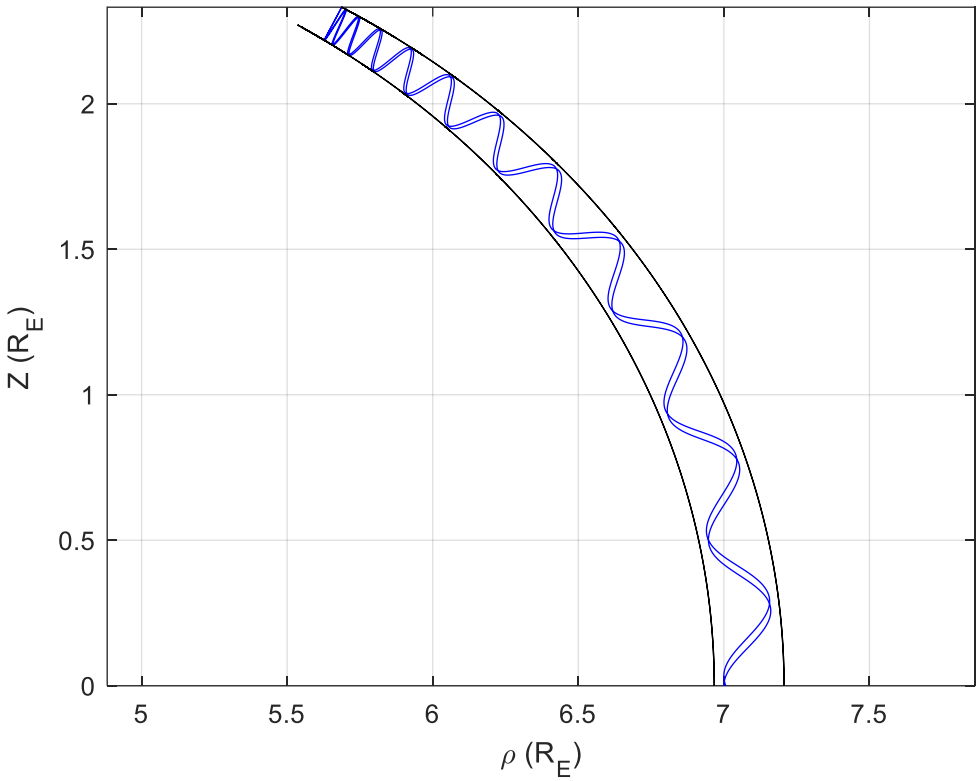

Figure 6.2: Illustration of ion trajectory and bounds for a half bounce period in ρ-z coordinates. The particle is initiated with $M = 3.1 \cdot 10^{-5}$ TR_E^3, $m_0 = 1.673 \cdot 10^{-27}$ kg, $q = 1.602 \cdot 10^{-19}$ C, $r_0 = [7, 0, 0]$ R_E and $v_0 = [0, 0.7071, 0.7071]$ R_E/s. The trajectory is shown with a blue line and ρ_{min} and ρ_{max} with a black solid line.

Analyzing our expression for r_{max} given by Equation (6.7) it is determined that a particle becomes unbound when $4mqMv\sin^3\theta > P_\varphi^2$, as r_{max} becomes undefined. In this thesis only bound particles are examined.

Lastly, it should be noted that exact expressions for the gyroperiod and drift period also do not exist for particles moving in three dimensions.

6.3 GC Approximation for the 3D Magnetic Dipole

For particles moving in three dimensions in a magnetic dipole the gradient curvature drift velocity (6.10) is calculated explicitly. The drift velocity is directed everywhere in the azimuthal direction and κ is the curvature of the magnetic field lines.

$$\mathbf{v_D} = \frac{m\left(v_{\parallel}^2 + \frac{1}{2}v_{\perp}^2\right)\boldsymbol{\kappa}}{qB}\,\hat{\mathbf{e}}_{\boldsymbol{\varphi}} \tag{6.8}$$

$$\boldsymbol{\kappa} = \mathbf{B}\cdot\nabla\mathbf{B} = \frac{3}{r}\left(\frac{\left(1+\cos^2\theta\right)\sin\theta}{\left(1+3\cos^2\theta\right)}\right)\hat{\mathbf{e}}_{\boldsymbol{\varphi}} \tag{6.9}$$

For particles that are trapped in the magnetic field, there is an approximate expression for the GC bounce period and frequency, this is given by Equations (6.10) and (6.11) respectively [1].

$$T_b = \frac{L_s R_E}{\sqrt{W/m}}\left(3.6 - 1.6\sin\alpha_{eq}\right) \tag{6.10}$$

$$\Omega_b = \frac{2\pi}{T_b} \tag{6.11}$$

In Equation (6.10) W is the kinetic energy of the particle and L_s is the shell parameter, or Mcllwainian parameter, defined as the distance from the center of the Earth to the point where a field line crosses the equatorial plane expressed in R_E [41]. α_{eq} is the equatorial pitch angle. For trapped plasma particles, there is an approximate expression for the GC drift period and frequency as well, this is given by Equations (6.12) and (6.13) respectively [1].

$$T_d = \frac{\pi q M R_E^2}{3L_s W}\left(0.35 + 0.15\sin\alpha_{eq}\right) \tag{6.12}$$

$$\Omega_d = \frac{2\pi}{T_d} \tag{6.13}$$

Note that in (6.10) and (6.12) the period only depends on the α_{eq}, W of the particle and the L_s shell. It is implicitly assumed that all these parameters remain constant for any given particle. Investigating the limits of this assumption is one of the goals of this Chapter.

Whether a particle is trapped in the magnetic bottle or is in the loss cone depends on the value of α_{eq}. In general, a particle is more likely to precipitate into the atmosphere if it has a small pitch angle or high parallel kinetic energy at the equatorial plane. This is because such particles must travel farther to reach the magnetic mirror point, and if the magnetic mirror is below 100 km from the surface of the Earth, then the particle is very likely to be absorbed by the atmosphere [1]. Additionally, a particle is more likely to remain trapped if its equatorial crossing is at a farther distance from the Earth as such particle must travel further to reach a 100 km altitude. The latitude of the magnetic mirror point λ_m for a particle is calculated under the GC approximation as a function of the equatorial pitch angle, it is given in Equation (6.14), where B_{eq} and B_m are the magnetic field strength at the equator and mirror point respectively [1].

$$\sin^2\alpha_{eq} = \frac{B_{eq}}{B_m} = \frac{\cos^6\lambda_m}{\sqrt{1+3\sin^2\lambda_m}} \tag{6.14}$$

This Equation is derived by assuming the magnetic moment, given by Equation (16) remains constant. Again, because Equation (2.18) is only approximate Equation (6.14) is not exact either. In Sections 6.6 through 6.8 we check with direct Lorentz calculation how accurately Equation (6.14) holds and if it remains approximately constant for the same particle during multiple bounces.

It is also convenient to reformat Equation (6.14) to calculate the loss cone pitch angle at the equatorial plane α_{lc} analytically. It is possible to do this with Equation (6.14) using B_{eq} and B_m, however, this requires knowing B_{eq} and B_m at every L_s shell. Instead, we format Equation (6.14) such that it only depends on the equatorial radial distance of the particle in R_E. This is given by Equation (6.15), where the value of 1.015679 R_E corresponds to 100 km above the surface of the Earth [39].

$$\sin^2 \alpha_{lc} = \left(\frac{1.015679\ R_E}{r_{eq}}\right)^3 \sqrt{\frac{1}{4 - 3\left(\frac{1.015679\ R_E}{r_{eq}}\right)}} \tag{6.15}$$

6.4 Particle Trajectory and Code Accuracy

Similar to the previous chapters we quantify the accuracy of the numerical integrator for this code before analyzing the particle trajectory in depth. We use the conserved quantities P_φ and v to check the accuracy of our numerical calculations. The resultant relative numerical error in these quantities for half a bounce period was determined to be on the order of 10^{-14} and 10^{-10} for P_φ and v respectively. This level of numerical accuracy is more than sufficient for our purposes.

To illustrate a typical three-dimensional trajectory of a particle, we consider the motion of a proton with the same initial conditions as Figure 6.2. Under these initial conditions the particle is initiated at r_{min} with a kinetic energy of 0.2124 MeV. The trajectory is visualized in Figure 6.3 in 3 dimensions. In this figure it is shown that the particle gyrates around and follows the curved field line. Additionally, as the particle moves away from the equatorial plane $v_\parallel$ decreases and $v_\perp$ increases, as its magnetic moment is approximately conserved. This continues until the particle only has a $v_\perp$, at this mirror point the particle is reflected back towards the equatorial plane.

For these initial conditions, the α_{eq} changed from α_{eq} = 0.7854 rad (π/4) to α_{eq} = 0.7880 rad, accounting for the direction of travel relative to the magnetic field line. At the same time the radial distance for the equatorial crossing changed from 7 R_E to 7.0061 R_E. This illustrates the errors inherent in the GC approximation. For example, when applying the approximate formulas (4.15) and (6.10), for the drift and bounce periods respectively, one needs to use the equatorial pitch angle of the particle and the magnetic field intensity at the location of the particle or its gyrocenter. If these parameters remain the same from one bounce to another, then there is no problem in applying these formulas. However, if the radial distance of the equatorial crossing and the pitch angle both slightly change at every bounce this creates uncertainty in the application of Equation (6.8). There is also a risk of accumulation of error over many bounces for some particles; this is examined further in Sections 6.6 through 6.8.

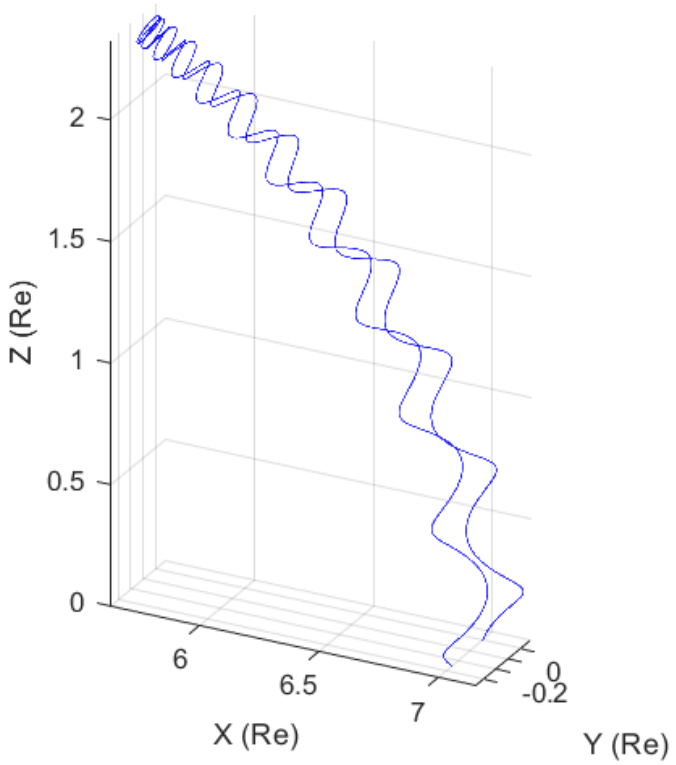

Figure 6.3: Example trajectory in 3D for half a bounce period. The particle is initiated with $M = 3.1 \cdot 10^{-5}$ TR_E^3, $m_0 = 1.673 \cdot 10^{-27}$ kg, $q = 1.602 \cdot 10^{-19}$ C, $r_0 = [7, 0, 0]$ R_E and $v_0 = [0, 0.7071, 0.7071]$ R_E/s.

We measure μ given by (2.18) at the final and initial position of the particle because μ_0 is a function of both α and B, which depends on r. Thus, we check to see if the μ returns to the same value at the equatorial crossing as the changes in α and B could offset each other. Plotting μ for the trajectory of the particle results in Figure 6.4 and more clearly shows that the final value of μ does not return exactly to the initial value. In this figure, the initial and final values correspond to $3.7650 \cdot 10^{-7}$ Am^2 and $3.7947 \cdot 10^{-7}$ Am^2 respectively. Additionally, this figure shows that the mean value about which the zeroth-order magnetic moment oscillates remains virtually constant, but that the amplitude of oscillation changes as the particles moves into stronger or weaker magnetic fields. The maximum amplitude occurs at the equatorial plane, where the magnetic field is the weakest, and the minimum amplitude occurs at the mirror point, where the magnetic field is strongest, as expected.

The following Sections are dedicated to analyzing the variations in α_{eq} and μ_0 for half a bounce period, the accumulation of α_{eq} deviations for multiple bounce periods and the $\Delta\alpha_{eq}$ in relation to the GC approximation of the loss cone for a range of velocities.

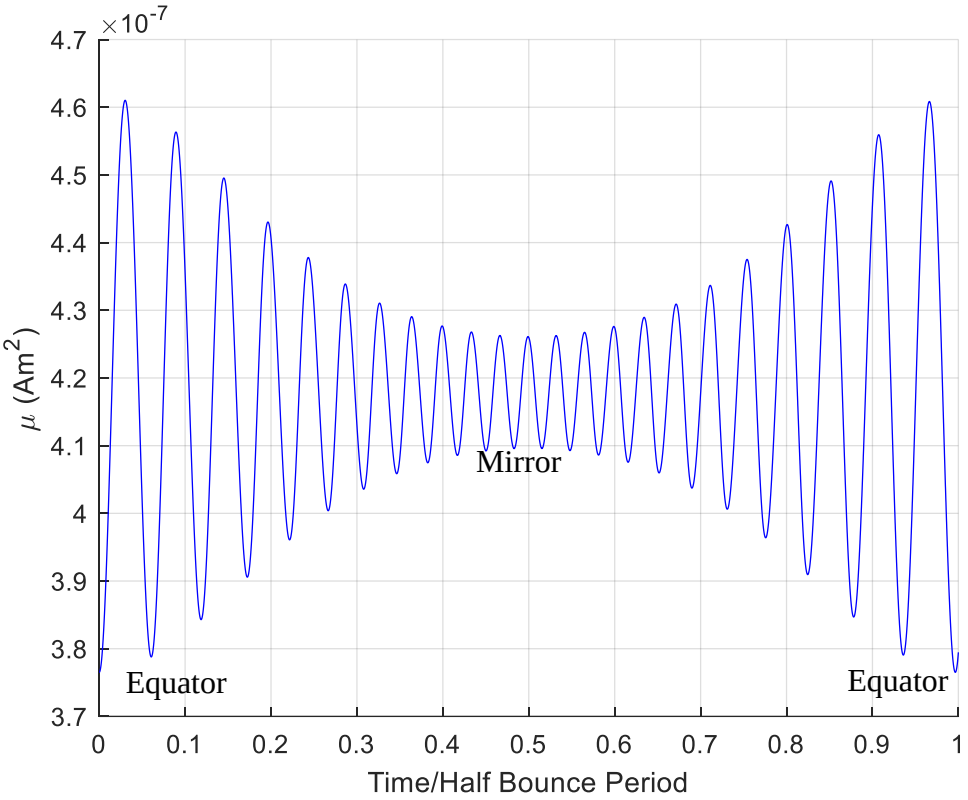

Figure 6.4: Magnetic moment for half a bounce period. The particle is initiated with $M = 3.1 \cdot 10^{-5}$ TR_E^3, $m_0 = 1.673 \cdot 10^{-27}$ kg, $q = 1.602 \cdot 10^{-19}$ C, r_0 = [7, 0, 0] R_E and v_0 = [0, 0.7071, 0.7071] R_E/s.

6.5 Phase Distribution Problem

Similarly to Chapter 5, we analyze the various phases of the particles because the loss of phase data is a limitation of GC theory. In Chapter 5 we were able to initialize an ensemble of particles which were different only in their initial phase value, while the energy, drift velocity, magnetic moment, canonical angular momentum and radial limits of motion were all the same. These particles were thus indistinguishable from the point of view of the GC theory. In three dimensions we would like to be able to initialize a similar ensemble of particles. This is more complicated since we also would like the particles to have the same α_{eq} and λ_m, in addition to all the quantities mentioned above. Figure 6.5 illustrates this difficulty, in this figure the two particles are initiated in the equatorial plane with the same values for energy, pitch angle and canonical angular momentum. Using the same canonical angular momentum allows us to restrict both particles to the same radial limits of motion. Therefore these two particles differ in only their initial velocity and initial position. The first particle, displayed in blue in Figure 6.5, has the same initial conditions as Figure 6.2, where r_0 = [7, 0, 0] R_E and v_0 = [$v$sin(δ), $v$sin(α_{eq})sin(δ), $v$cos(α_{eq})] R_E/s with our phase δ = 0, v = 1 R_E/s and, α_{eq} =π/4. The second particle, displayed in red in Figure 6.5, uses a phase value of $\delta = \pi$ to generate a new initial velocity vector. To generate a new r_0 we use Equation (4.10) from section 4.1, this results in r_0 = [7.1694, 0, 0] R_E. Overall, despite all the similarities between the two particles, it was found that they have different mirror points. Thus their trajectories differ.

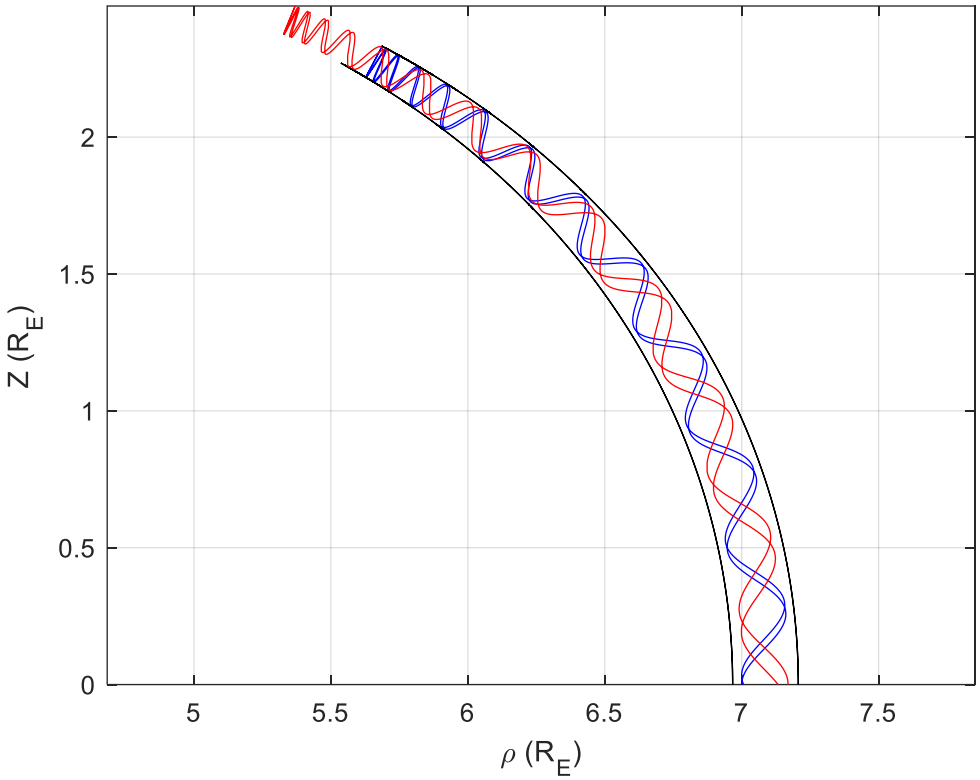

Figure 6.5: Illustration of the phase distribution problem. $M = 3.1 \cdot 10^{-5}$ TR$_E^3$. Particle in blue is initiated with r_0 = [7, 0, 0] R$_E$ and v_0 = [0, 0.7071, 0.7071] R$_E$/s. Particle in red is initiated with r_0 = [7.1694, 0, 0] R$_E$ and v_0 = [0, -0.7071, 0.7071] R$_E$/s. ρ_{min} and ρ_{max} are shown with black solid lines.

It is not immediately clear if this phase distribution problem has an elegant solution. The situation is further complicated by the fact that for particle motion in a three-dimensional dipole field there is no exact expression for the adiabatic invariant, only various approximations. Overall, this problem stems from a lack of Equations to constrain the degrees of freedom. Therefore, to simplify our initialization process in the rest of this Chapter we initialize our particles at the same location, r_0 = [7, 0, 0] R$_E$, with our initial velocity taking the form v_0 = [$v$sin(α_{eq})cos(ξ), $v$sin(α_{eq})sin(ξ), $v$cos(α_{eq})]. Here ξ is the azimuthal angle between $\boldsymbol{r}$ and $\boldsymbol{v}$ vectors measured counterclockwise as introduced in Section 4,1. ξ plays the role of the phase angle, although unlike Section 5.3 it represents the initial phase angle only approximately. For example, particles with the same initial location and α_{eq}, but different azimuthal angle ξ, would have different centers of curvature for their trajectories calculated using Equation (3.13). The rest of this chapter is dedicated to a systematic study of variations in v, α_{eq}, and ξ separately, while the other two variables are held constant.

6.6 Analysis of Variations in Velocity

In this section, we illustrate the dependence of the equatorial pitch angle and the magnetic moment on the magnitude of the velocity of the particle. Therefore, we hold the initial α_{eq}, and ξ constant and assign them values of $\pi/4$ and $\pi/2$ respectively. All other initial variables are the same

as in Figure 6.2. The upper range of velocity to be analyzed is determined from our bound velocity threshold condition established by r_{max} given by Equation (6.7). From this we know a particle becomes unbound when $4mqMv\sin^3\theta > P_\varphi^2$ [22]. Using this Equation, we found that the particle becomes unbound when $v_0 > 11.07$ R_E/s. Therefore, we analyze velocities from $v = 0.01$ to 10 R_E/s. Using 1000 velocities within this velocity range we measure $\Delta\alpha_{eq}$ for half a bounce period. The result is given below in Figure 6.6. At low velocities, the data in this figure does not have a high resolution due to the larger frequency of variation. In an attempt to solve this we considered increasing the number of velocities used within the lower range of analysis, however, this clusters more data points into a small area, resulting in data being indistinguishable. Thus, we did not increase the resolution. For similar figures encountered later in this chapter the same principle applies.

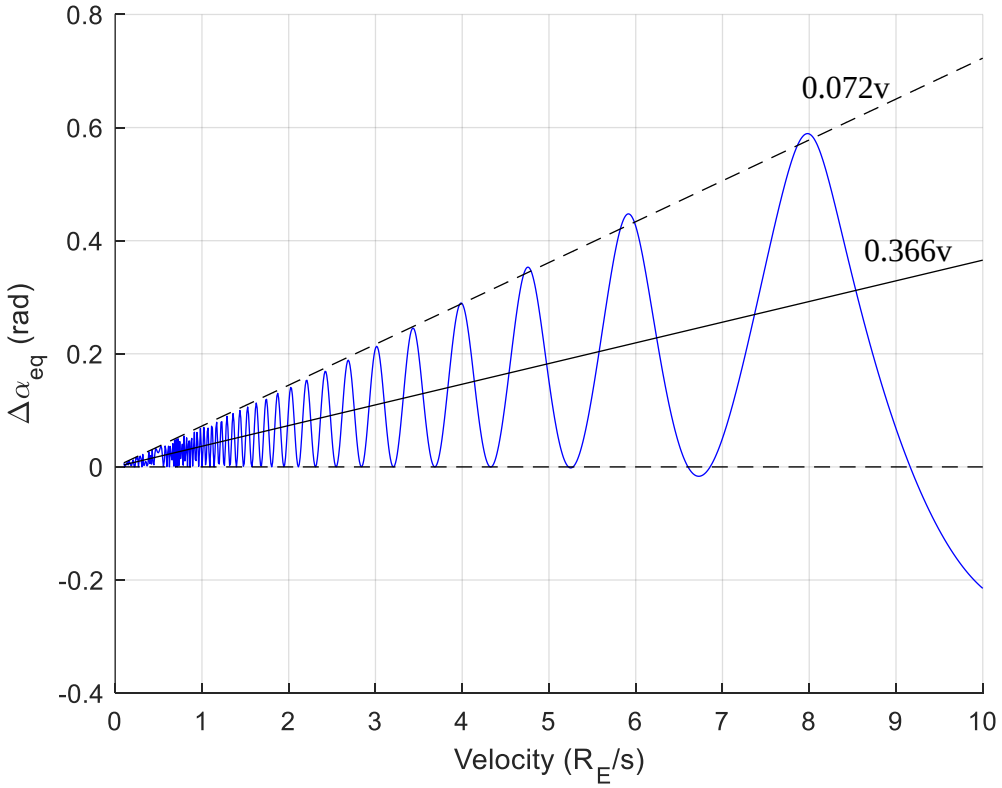

Figure 6.6: $\Delta\alpha_{eq}$ for 1000 velocities from $v = 0.01$ to 10 R_E/s. Integrated for half a bounce period. The particle is initiated with $M = 3.1\cdot10^{-5}$ TR_E^3, $m_0 = 1.673\cdot10^{-27}$ kg, $q = 1.602\cdot10^{-19}$ C, $r_0 = [7, 0, 0]$ R_E and $v_0 = v[\sin(\alpha_{eq})\cos(\xi), \sin(\alpha_{eq})\sin(\xi), \cos(\alpha_{eq})]$ R_E/s. $\alpha_0 = \pi/4$ and $\xi = \pi/2$. $\Delta\alpha_{eq}$ is in blue, minimum and maximum lines of best fit are black dashed lines and the average line of best fit is the black line.

In Figure 6.6 it is shown in blue that the $\Delta\alpha_{eq}$ is linearly proportional to velocity on average. However, it oscillates between 0 and some amplitude that is linearly proportional to v. The frequency of these oscillations increases as v approaches 0. The black line in Figure 6.6 represents the linear line of best fit, the slope of this line is $0.0366v$. This line represents the average error in modelling α_{eq} for every half bounce period and it demonstrates that even at relatively low velocities the particle deviates from GC approximation. The line of best fit was calculated using a least-squares method up to a velocity of $v = 9$ R_E/s, then extrapolated to $v = 10$ R_E/s afterwards. This was done to exclude the negative data above $v = 9$ R_E/s. The locations where $\Delta\alpha_{eq}$ crosses 0 simply illustrate when the final $v_\parallel$ is greater than the initial $v_\parallel$ and does not mark any significant transition.

The fact that $\Delta\alpha_{eq}$ remains positive over most velocities is due to the choice of the initial phase. Thus we add a dashed black line at 0 to illustrate the minimum error in modelling α_{eq}. The maximum error is also illustrated by a black dashed line, here we used the local peaks to fit another linear line of best fit, the slope of this line is $0.0720v$.

The behaviour of the change in the normalized magnetic moment $\Delta\mu/\mu_0$ as a function of v is similar, as shown in Figure 6.7. Again, there are some velocities for which $\Delta\mu/\mu_0 = 0$, thus we add a dashed black line at 0 to illustrate the minimum error. For the average and maximum error, in a solid and dashed black line respectively, we find that a quadratic function best fits the data. Following the same process that was used in Figure 6.7 we determined the average error to be proportional to $0.0085v^2 + 0.1098v - 0.0271$. The maximum error was determined to be proportional to $0.0452v^2 + 0.1295v + 0.0205$. We note that both y-intercepts should be 0 and that their value is only a result of the least-squares best fit method. Contrasting this slope with the $\Delta\alpha_{eq}$ slope we find that the change in a magnetic moment in Figure 6.7 is quadratic, while the change in pitch angle is linear in Figure 6.6. We attribute this to α in $v_\perp = (v\sin\alpha)^2$ being raised to the power of two from (2.18). The frequency of the oscillations, once again, increases as v decreases.

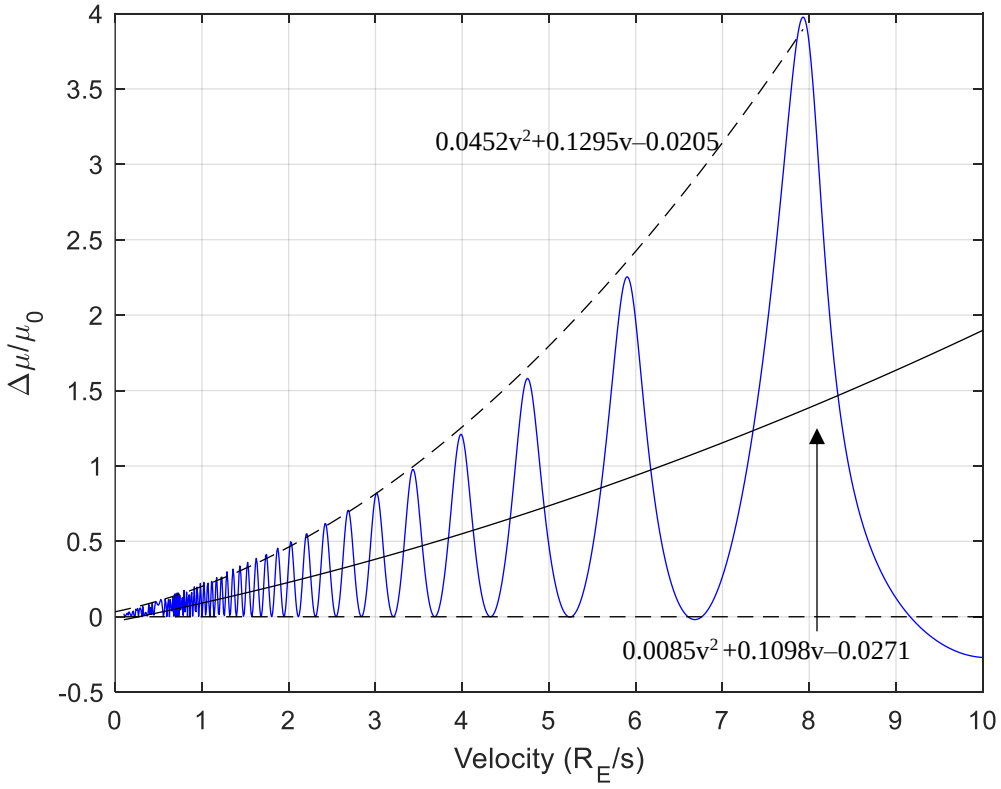

Figure 6.7: $\Delta\mu/\mu_0$ for 1000 velocities from v = 0.01 to 10 R_E/s. Integrated for half a bounce period The particle is initiated with $M = 3.1\cdot10^{-5}$ TR_E^3, $m_0 = 1.673\cdot10^{-27}$ kg, $q = 1.602\cdot10^{-19}$ C, r_0 = [7, 0, 0] R_E and $v_0 = v[\sin(\alpha_{eq})\cos(\xi), \sin(\alpha_{eq})\sin(\xi), \cos(\alpha_{eq})]$ R_E/s. $\alpha_0 = \pi/4$ and $\xi = \pi/2$. $\Delta\mu/\mu_0$ is in blue, minimum and maximum lines of best fit are black dashed lines and the average line of best fit is the black line.

We now investigate if the average $\Delta\alpha_{eq}$ from Figure 6.6 accumulates over multiple half-bounce periods. To do this it is convenient to first analyze only one velocity, thus we use v = 1 R_E/s from Sections 6.2 and 6.3. At this velocity, the bounce half period is 12.4s. Therefore we set the

integration time to 1300s to obtain at least 100 equatorial crossings. At every crossing, we recorded the value of α_{eq}. We note that it is possible to use Matlab's events functionality to stop the integration after a certain number of crossings. However, to generate 100 crossings a lot of code lines would be needed. This process is rather simple but tedious, therefore using a specified integration time was deemed sufficient. The results are displayed in Figure 6.8, where the first crossing corresponds to our initial pitch angle of $\pi/4$.

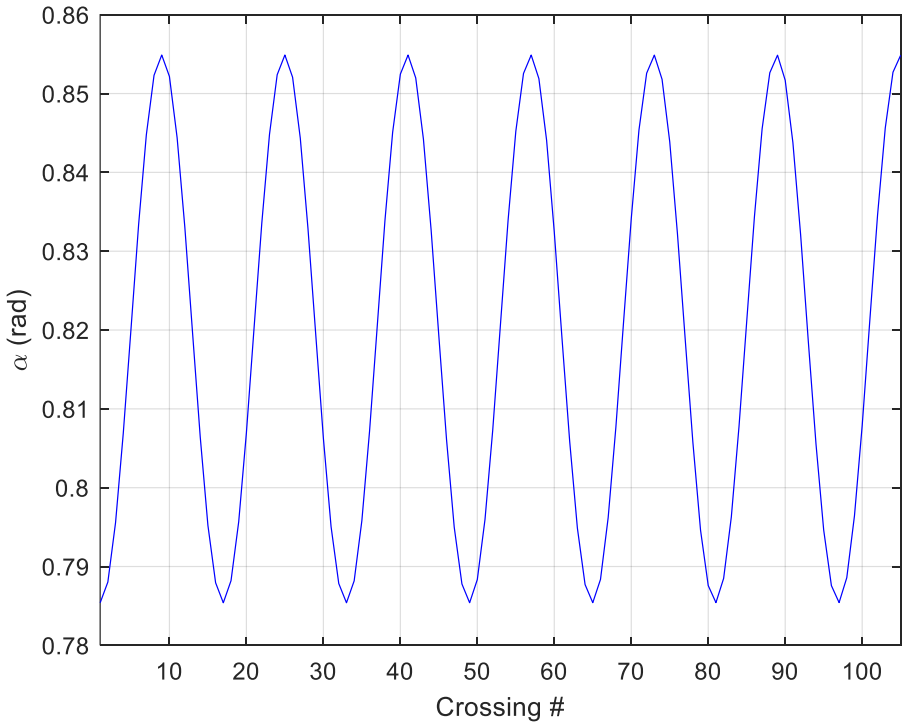

Figure 6.8: α_{eq} at every equatorial crossing for v = 1 R_E/s. Integration time = 1300s. The particle is initiated with $M = 3.1\cdot10^{-5}\,TR_E^3$, $m_0 = 1.673\cdot10^{-27}$ kg, $q = 1.602\cdot10^{-19}$ C, r_0 = [7, 0, 0] R_E and $v_0 = v[\sin(\alpha_{eq})\cos(\xi), \sin(\alpha_{eq})\sin(\xi), \cos(\alpha_{eq})]$ R_E/s. $\alpha_0 = \pi/4$ and $\xi = \pi/2$.

From Figure 6.8 we see that $\Delta\alpha_{eq}$ does not visibly accumulate for this velocity, but instead oscillates. The range of this oscillation is shown by the amplitude, which is 0.0695 rad in Figure 6.8. We now attempt to measure the oscillation period as a function of velocity. Before this, we must ensure that the sinusoidal pattern is consistent over multiple velocities. Thus we recreate Figure 6.8 for v = 3 R_E/s, v = 5 R_E/s and v = 7 R_E/s. We do this by dividing our integration time from Figure 6.8 by velocity, thus integration time = 1300/v. In addition to this, we also check to see if the amplitude of oscillation remains consistent when a different integration time is used. To check for this, we simply double our integration time to 2600/v. Overall Figure 6.9 illustrates the oscillations of α_{eq} as a function of equatorial crossings for v = 3 R_E/s, v = 5 R_E/s and v = 7 R_E/s. The left column corresponds to integration time = 1300/v, while the right column corresponds to 2600/v.

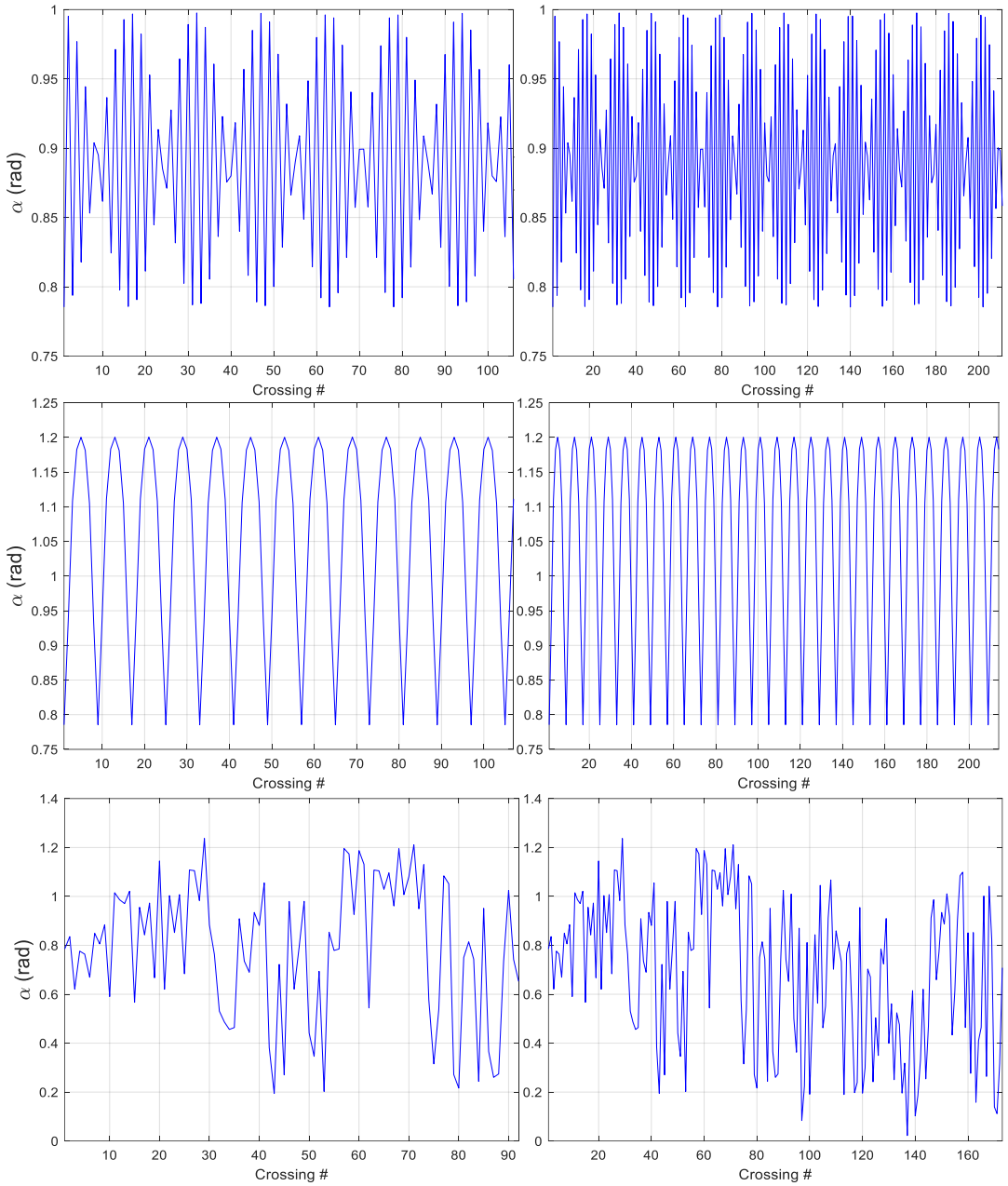

Figure 6.9: α_{eq} at every equatorial crossing for v = 1 R_E/s (top row), 3 R_E/s (middle row) and 7 R_E/s (bottom row). Integration time = 1300s/v (left column) and 2600/v (right column). The particle is initiated with M = $3.1 \cdot 10^{-5}$ TR_E^3, m_0 = $1.673 \cdot 10^{-27}$ kg, q = $1.602 \cdot 10^{-19}$ C, r_0 = [7, 0, 0] R_E and v_0 = v[sin(α_{eq})cos(ξ), sin(α_{eq})sin(ξ), cos(α_{eq})] R_E/s. α_0 = π/4 and ξ = π/2.

From Figure 6.9 we conclude, that for relatively low velocities, there is a clear repeating pattern in the oscillations in α_{eq}. This is demonstrated by the 1st and 2nd rows, where v = 3 R_E/s and v = 5 R_E/s respectively. Unfortunately, the shapes of these patterns, along with Figure 6.8, are not

consistent. Thus, a plot of oscillation period for different velocity cannot be generated, because coding a method to detect the end of an oscillation period would require a unique solution for various velocities. However, our implementation of integration time scaling did result in the same number of crossings for every velocity in Figure 6.8 and Figure 6.9 which showed a clear pattern in oscillation. Thus, for relatively low velocities, we know our bounce period is proportional to the velocity, as expected based on Equation (6.10). For the 3rd row of Figure 6.9, we note that no pattern of oscillation is evident for v = 7 R_E/s. Furthermore, we found that increasing integration time for this case resulted in the maximum amplitude of α_{eq} changing from 1.0427 rad to 1.2146 rad. This is significant as it implies that there is a velocity threshold above which the pattern in the variation of α between two equatorial crossings disappears. In fact, $\Delta\alpha_{eq}$ in this case looks fairly chaotic. Although chaotic trajectories of particles in a field of a magnetic dipole have been reported, this phenomenon appears not to have been studied substantially in the past [42] [43]. Therefore, we leave the details for future studies. In contrast, the amplitude change for v = 3 R_E/s was 0.2121 rad to 0.2122 rad, for v = 5 R_E/s it was 0.4150 rad to 0.4151 rad, both of which are much smaller than our results from v = 7 R_E/s. To explore this behaviour further we plot the maximum change in α_{eq} as a function of the entire velocity range of 0.01 R_E/s to 10 R_E/s in Figure 6.10. This was done for 1000 velocities using an integration time of 332s/v. We reduced the integration time to make our computational resources more efficient. In Figure 6.8 we know that slightly more than six oscillation periods are formed in 1300 s at v = 1 R_E/s. Thus an integration time of 332s/v should comfortably allow at least one oscillation period to form at every velocity.

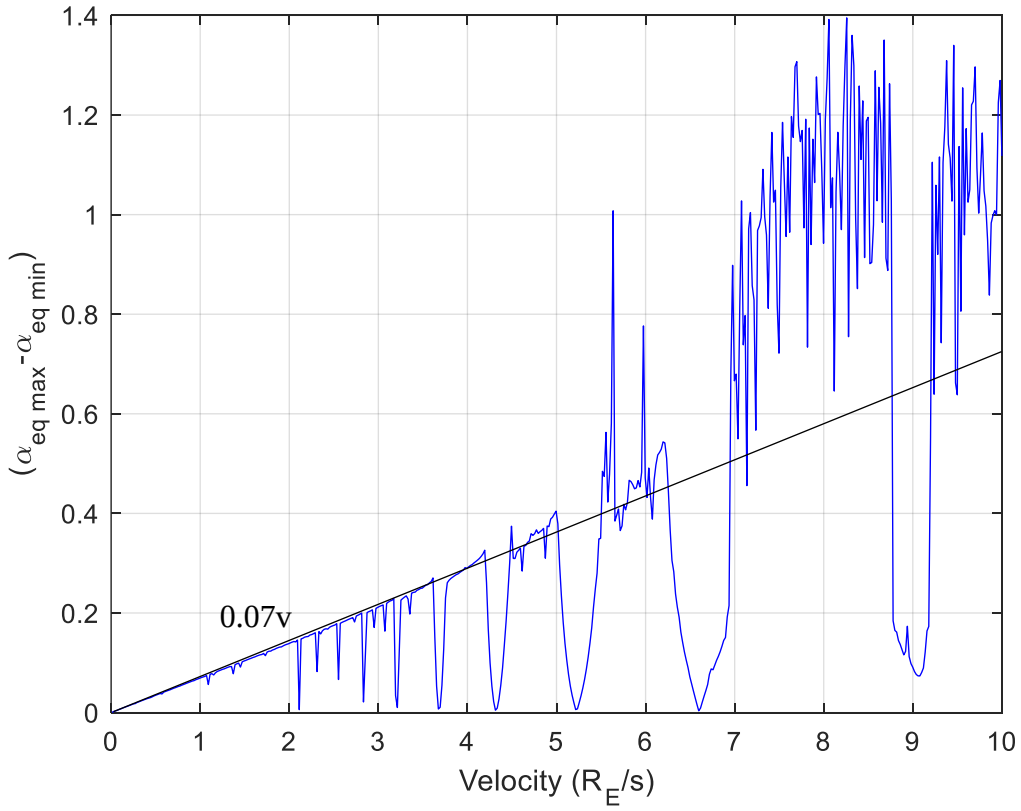

Figure 6.10: Maximum oscillation range of α_{eq} for 1000 velocities between v = 0.01 to 10 R_E/s. Integration time = 332s/v. The particle is initiated with $M = 3.1\cdot10^{-5}\,TR_E^3$, $m_0 = 1.673\cdot10^{-27}$ kg, $q = 1.602\cdot10^{-19}$ C, r_0 = [7, 0, 0] R_E and $v_0 = v[\sin(\alpha_{eq})\cos(\xi), \sin(\alpha_{eq})\sin(\xi), \cos(\alpha_{eq})]$ R_E/s. $\alpha_0 = \pi/4$ and $\xi = \pi/2$.

In Figure 6.10 there is a clear linear trend at lower velocities. As the velocity approaches 0 it is unsurprising that our range of α_{eq} variation approaches 0, as the GC approximation is accurate for lower energy particles. Analyzing the linear trend at lower velocities we obtain a slope value of $0.07v$. This aligns with our results from Figure 6.6, where the maximum $\Delta\alpha_{eq} = 0.0720v$ for a half bounce period. Thus, we know that, for relatively low-velocity particles, some particles reach their maximum $\Delta\alpha_{eq}$ in a single crossing. However, this does not continue to occur every subsequent crossing, instead the $\Delta\alpha_{eq}$ gradually gets smaller and then reaches this maximum again. This is illustrated by $v = 3$ R_E/s in Figure 6.6 and Figure 6.9. For other particles, $\Delta\alpha_{eq}$ is consistently small each crossing as the particle oscillates between maximum and minimum α_{eq} extremes, as illustrated by $v = 1$ R_E/s Figure 6.8.

Figure 6.10 also shows that there is a distinct transition in the type of variation of $\Delta\alpha_{eq}$ as the velocity passes the velocity of approximately 7 R_E/s. This further confirms the existence of a threshold velocity of some sort for the motion of the particles at approximately this value.

In regards to the 0 points in Figure 6.10, these align with the $\Delta\alpha_{eq} = 0$ from Figure 6.6. However, the 0 points in Figure 6.10 are sharper than the gradual oscillations toward 0 in Figure 6.6. This is attributed to the fact that a particle with a $\Delta\alpha_{eq} \approx 0$ for a half bounce period will continue to move within the oscillation maximum and minimum values of α_{eq}, eventually reaching a linear slope of maximum $\Delta\alpha_{eq} = 0.0720v$ after multiple bounces.

Figure 6.10 shows that the maximum range of oscillation in α_{eq} increases linearly for relatively small particle velocities. In addition, this trend remains the same regardless of the integration time used, as demonstrated in Figure 6.9. At some point, at a relatively high-velocity threshold, this range of oscillation in α_{eq} approaches $\pi/2$ as velocity or integration time is increased. Therefore, high-energy particles have the ability to approach $\alpha_{eq} = 0$ for some bounces and it is only a matter of time before they reach the loss cone. Applying our starting location of $\rho = 7$ R_E to the loss cone Equation (6.15) it was determined that the particle has a $\alpha_{lc} = 2.3^o$ or 0.04 rad. Figure 6.11 illustrates the approach $\alpha_{eq} = 0$ in the ρ-z plot for the relatively high velocity of $v = 9.52$ R_E/s. This corresponds to the particle having a kinetic energy of 19.88 MeV. The initial equatorial pitch angle of this particle was $\pi/4$, which is very far from the loss cone. However, as shown in Figure 6.11, there is some point in time when the particle penetrates very deeply into the dipole field and would be lost to the upper atmosphere of Earth. In Figure 6.11 we set the integration time to stop when the particle reaches the radial distance of 1.015679 R_E, which is 100 km above the surface of Earth. In this case, it took 154.03s for this particle to be absorbed by the atmosphere of Earth, this is based on purely statistical changes in the mirror point location from one bounce to the next.

This is an interesting result as it puts an upper limit on the energy of particles that can remain within the Van Allen belts, even if their velocities are below our unbound condition of $v =$ 11.07 R_E/s. Above a certain velocity threshold, we have illustrated a new diffusion process in which the random scattering of α_{eq} results in a loss cone being reached. In addition, if our initial pitch angle is closer to the loss cone condition then the probability of scattering also increases [40]. We have also shown in Figure 6.10 that α_{eq} oscillates within a range that, if close to the loss cone, would result in diffusion into the loss cone. Overall these two facts blur the boundaries of the loss cone. We believe a statistical model could be built to modify our current understanding of diffusion into the loss cone to account for our range of variation in α_{eq} as a function of velocity. We note that collision probability with neutrals would likely play a role here. We leave this for future work, however, we aim to further demonstrate the benefit of such work later in this section.

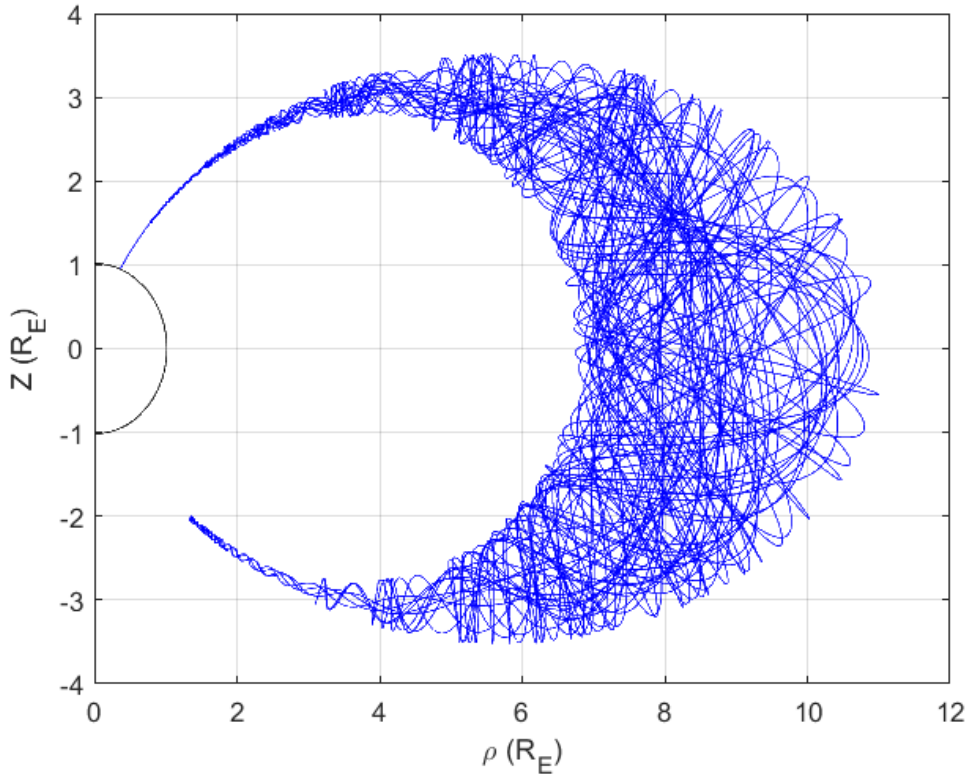

Figure 6.11: ρ-z plot for v = 9.52 R_E/s. Integration time = 154.03s. The particle is initiated with $M = 3.1 \cdot 10^{-5}$ TR_E^3, $m_0 = 1.673 \cdot 10^{-27}$ kg, $q = 1.602 \cdot 10^{-19}$ C, r_0 = [7, 0, 0] R_E and $v_0 = v[\sin(\alpha_{eq})\cos(\xi), \sin(\alpha_{eq})\sin(\xi), \cos(\alpha_{eq})]$ R_E/s. $\alpha_0 = \pi/4$ and $\xi = \pi/2$.

It should be noted that the situation opposite to Figure 6.11 is also possible. There are some particles which preserve their equatorial pitch angle with much greater consistency than could have been expected. For example, Figure 6.12 shows the trajectories of two particles initiated at v = 4.34 R_E/s and v = 9 R_E/s, integrated for 1300s/v, for which the equatorial pitch angle remains virtually unchanged from one bounce to another. In Figure 6.11 these points are where the maximum $\Delta\alpha_{eq} \approx 0$, as briefly discussed earlier. The orbits of such particles would be extremely stable with regard to pitch angle diffusion, and as a consequence, such particles may be over-represented in the terrestrial magnetosphere under certain conditions. Note, that the velocity of one of these particles is quite high. Comparing the left and right panels of Figure 6.12 it is also concluded that the number of trajectory inflection points decreases as velocity increases for these types of particles

Next we analyze the Equations for λ_m (6.14), T_b (6.10) and T_d (6.12), which are all obtained from the GC approximation. We now use Matlab's events functionality set to the calculation time to half a bounce period for the remainder of this section. To start we use Equation (6.14) to determine the location of λ_m numerically and analytically. Numerically we use initial B_{eq} and B_m along the particle's trajectory. Analytically we use the GC assumption that α_{eq} remains constant and apply our $\alpha_{eq} = \pi/4$ starting condition across our entire velocity range. In addition, we wish to modify our analytical approach to illustrate the dynamic nature of α_{eq} established in previous figures To do this we use our average $\Delta\alpha_{eq} = 0.0366v$ from Figure 6.6 to modify our initial $\alpha_{eq} = \pi/4$. We choose to add this average $\Delta\alpha_{eq}$ because the data from Figure 6.6 was positive, indicating

that α_{eq} increased. Thus, we apply $\alpha_{eq} = \pi/4 + \pi/4\ (0.0366v)$ to Equation (6.14) to determine λ_m. The result of all three methods for determining λ_m is given in Figure 6.13 as a function of velocity. In this figure, blue corresponds to our numerical approach, red to standard GC theory and green to our attempt at modifying the GC theory.

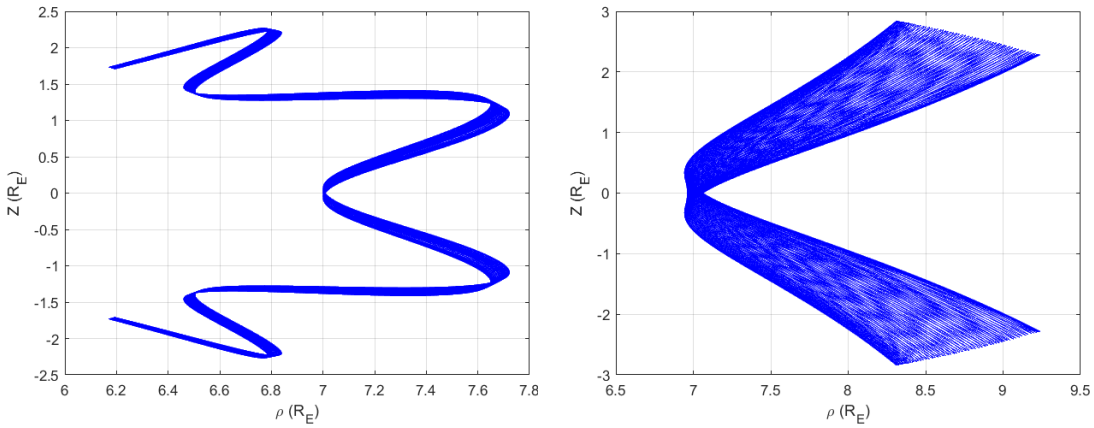

Figure 6.12: ρ-z plot for v = 4.34 R_E/s (left) and v = 9 R_E/s (right). Integration time = 1300s/v. The particle is initiated with $M = 3.1\cdot10^{-5}\ TR_E^3$, $m_0 = 1.673\cdot10^{-27}$ kg, $q = 1.602\cdot10^{-19}$ C, r_0 = [7, 0, 0] R_E and $v_0 = v[\sin(\alpha_{eq})\cos(\xi), \sin(\alpha_{eq})\sin(\xi), \cos(\alpha_{eq})]$ R_E/s. $\alpha_0 = \pi/4$ and $\xi = \pi/2$.

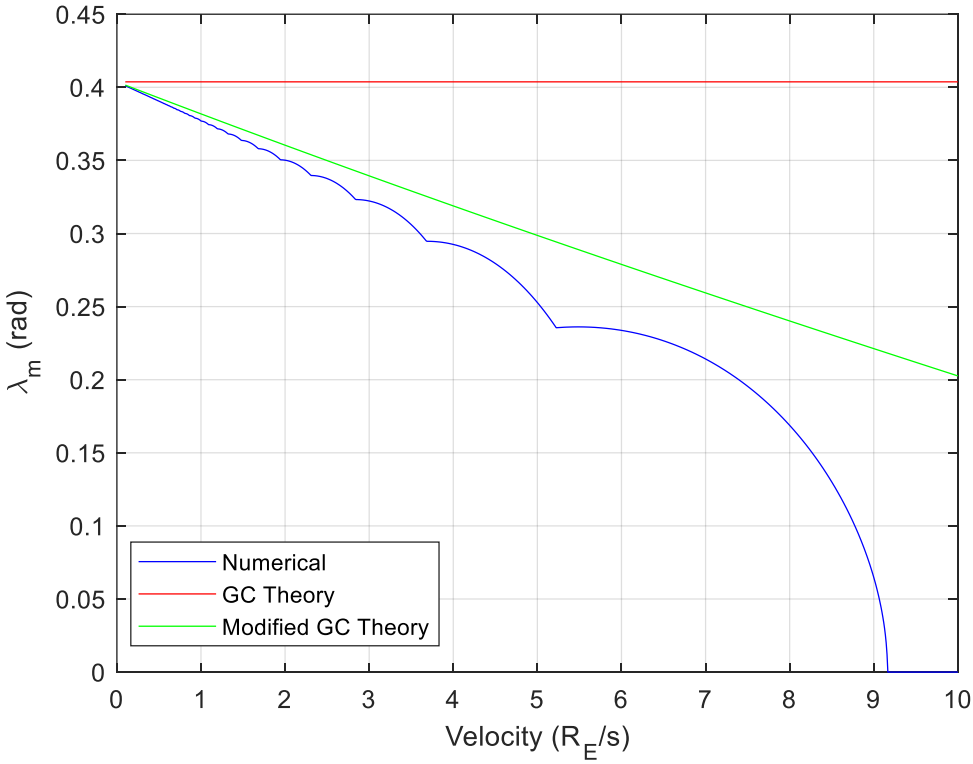

Figure 6.13: Calculation of λ_m using GC approximation for velocities from v = 0.01 to 10 R_E/s. Integrated for half a bounce period. The particle is initiated with $M = 3.1\cdot10^{-5}\ TR_E^3$, $m_0 = 1.673\cdot10^{-27}$ kg, $q = 1.602\cdot10^{-19}$ C, r_0 = [7, 0, 0] R_E and $v_0 = v[\sin(\alpha_{eq})\cos(\xi), \sin(\alpha_{eq})\sin(\xi), \cos(\alpha_{eq})]$ R_E/s. $\alpha_0 = \pi/4$ and $\xi = \pi/2$. The numerical solution is in blue, GC theory is in red and our modification to GC theory is in green

Figure 6.13 shows that as velocity decreases the numerical results approach the GC approximation for λ_m, as the blue line approaches the red line, which is equal to our initial condition of $\alpha_{eq} = \pi/4$. This result is unsurprising since similar studies have been conducted showing that the λ_m deviates from the GC approximation for high-energy protons [44]. However, for high-energy electrons, the deviations were negligible, and thus the results are mass-dependent [44], though this mass dependence is not examined in this thesis. The green line shows an improvement when applying our modification to the GC theory. This illustrates that a more thorough statistical model could be developed to improve the GC approximation by rewriting α_{eq} in Equation (6.14) as a function of velocity. Lastly, the cusps in Figure 6.13 do not correspond to points on any other figures and thus are deemed insignificant.

We now compare the GC approximation bounce and drift period, given by Equations (6.10) and (6.12) respectively, against our numerical calculations of the real trajectory. Again, we also use $\alpha_{eq} = \pi/4 + 0.0366v$ to modify GC theory. To calculate the numerical bounce period, we simply multiply our integration time by a factor of two, as our events functionality models half a bounce period. For the drift period, we calculate the angle between the positive x-axis and the particles stopping location after a half bounce period. This gives us the $\Delta\varphi$ the particle experiences during our half-bounce constriction. Using this we multiply our integration time by $2\pi/\Delta\varphi$ to get our numerical drift period. The results of this process are displayed in Figure 6.14 and Figure 6.15 for the bounce and drift periods respectively. These figures show that the GC Equations are only approximate, as the periods for the numerical integration oscillate around both GC solutions for all velocities analyzed. It should be noted that the numerical calculations were all performed for $\xi = \pi/2$. If ξ is varied, the area between the GC theory and numerical curves will likely be filled with numerical results, however, the maximum difference between the numerical and analytical results is likely to be comparable to that shown in Figure 6.14 and Figure 6.15

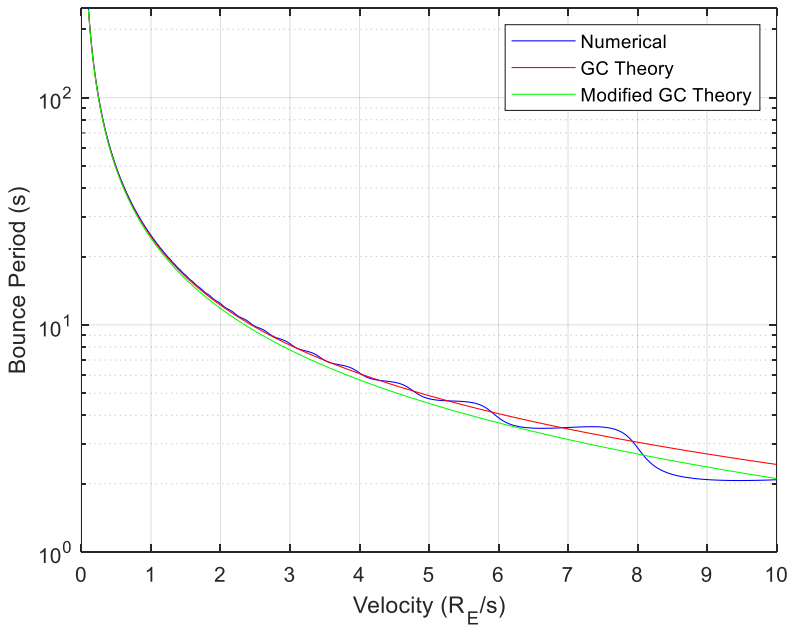

Figure 6.14: Calculation of T_b using GC approximation for velocities from v = 0.01 to 10 R_E/s. Integrated for half a bounce period. The particle is initiated with $M = 3.1\cdot10^{-5}\,TR_E^3$, $m_0 = 1.673\cdot10^{-27}$ kg, $q = 1.602\cdot10^{-19}$ C, r_0 = [7, 0, 0] R_E and $v_0 = v[\sin(\alpha_{eq})\cos(\xi), \sin(\alpha_{eq})\sin(\xi), \cos(\alpha_{eq})]$ R_E/s. $\alpha_0 = \pi/4$ and $\xi = \pi/2$. The numerical solution is in blue, GC theory is in red and our modification to GC theory is in green.

In Figure 6.14 it is interesting to note that, for higher velocities, the numerical curve forms almost flat steps where the bounce period is almost independent of the particle velocity for a while, and then rapidly drops to the next relatively flat step. We currently do not have an explanation for this behaviour. In regards to our modification to the GC theory, it is impossible to determine if the green line more accurately represents the numerical results than the red. Thus, we sum the numerical data in blue and subtract the sum of both GC theory and our modification to compare accuracy. We then divide by our iteration to average the data. The absolute average difference between the GC theory and our modification was 1.61s vs 0.73s. Again, this illustrates that a statistical model could be developed to improve the GC approximation by accounting for variations in α_{eq}.

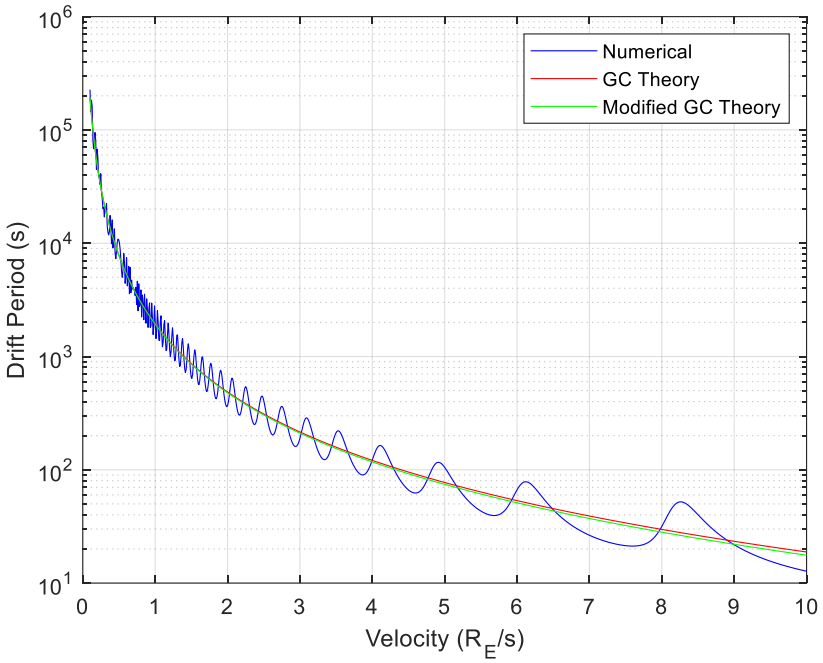

Figure 6.15: Calculation of T_d using GC approximation for velocities from v = 0.01 to 10 R_E/s. The particle is initiated with $M = 3.1 \cdot 10^{-5}$ TR_E^3, $m_0 = 1.673 \cdot 10^{-27}$ kg, $q = 1.602 \cdot 10^{-19}$ C, r_0 = [7, 0, 0] R_E and $v_0 = v[\sin(\alpha_{eq})\cos(\xi), \sin(\alpha_{eq})\sin(\xi), \cos(\alpha_{eq})]$ R_E/s. $\alpha_0 = \pi/4$ and $\xi = \pi/2$. The numerical solution is in blue, GC theory is in red and our modification to GC theory is in green.

The results of Figure 6.15 indicate that at relatively high velocities, such as v = 6 R_E/s, the difference between the GC approximation and numerically computed drift periods varies by a factor of two. In addition, we also wish to test our modification to the GC theory. Again, we sum the numerical data in blue and subtract the sum of both GC theory and our modification to determine accuracy. We then divide by the number of data points to average the data. The absolute average difference between the GC theory and our modification was $4.04 \cdot 10^4$s vs $4.36 \cdot 10^4$s. Indicating that our modification did not improve the accuracy of measuring the drift period.

6.7 Analysis of Variations in Pitch Angle

In this section, we vary the equatorial pitch angle while holding the initial v, and ξ constant. Here we use the values of v = 5 R_E/s and $\xi = \pi/2$ respectively. All other initial conditions are the same as those in Figure 6.2. We chose v = 5 R_E/s because this value is sufficiently large so that deviations from the GC are sufficiently clear, yet it is still significantly smaller than the threshold at which the motion becomes unbounded. Also, at this speed, the scattering of a particle into the loss cone is not very likely. In regards to our pitch angle range, we use an upper bound of 89° or 1.5333 rad, as 90° would result in equatorially mirroring particles. These were already extensively discussed in Chapter 5. For our lower limit, we choose a value of 0° to study if the loss cone threshold angle α_{lc} calculated using Equation (6.15) is indeed 2.3°. Using 1000 pitch angles between 0° and 89° we measure $\Delta\alpha_{eq}$ for our half bounce period. The result is given below in Figure 6.16. Similar to the results for varying velocity we find points where the $\Delta\alpha_{eq} = 0$. The frequency of the oscillations in $\Delta\alpha_{eq}$ decreases as α_0 approaches $\pi/2$. For small values of α_0, we clearly do not resolve these oscillations accurately, doing so would require many more points at lower values of α_0, which would result in the data being clustered. Overall, it does not affect our ability to draw conclusions from the data.

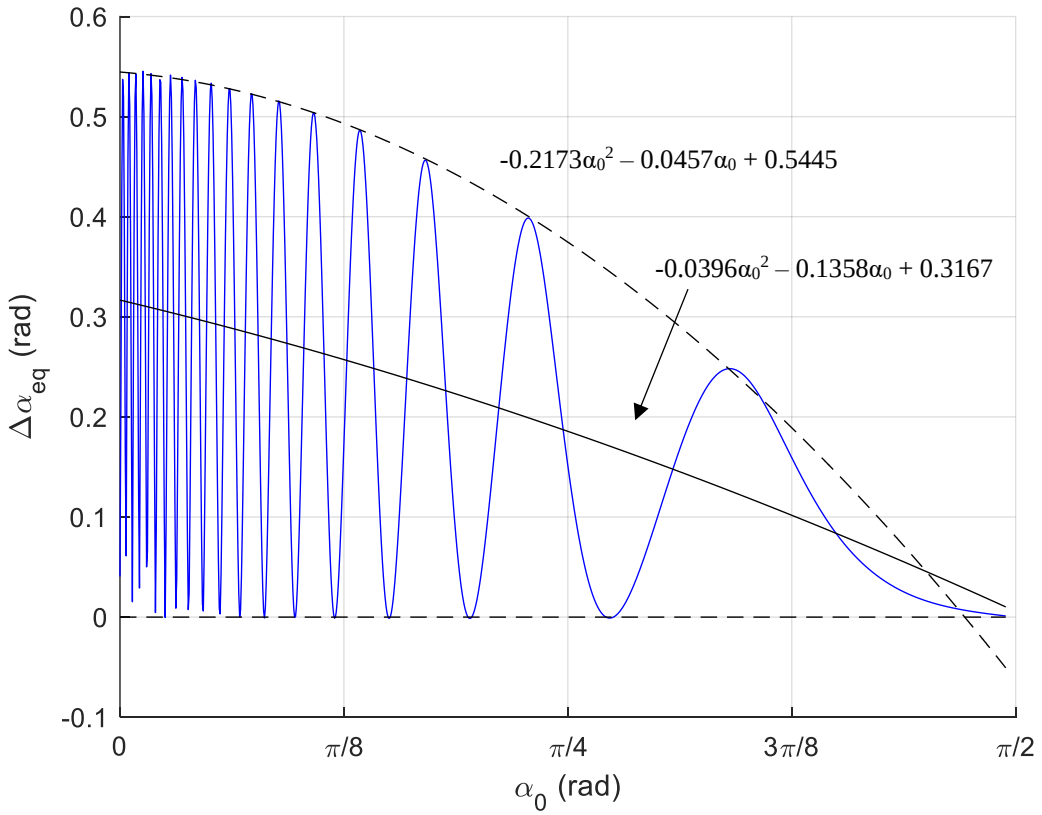

Figure 6.16: $\Delta\alpha_{eq}$ for 1000 pitch angles from α_0 = 0 to 89°. Integrated for half a bounce period. The particle is initiated with $M = 3.1\cdot10^{-5}$ TR_E^3, $m_0 = 1.673\cdot10^{-27}$ kg, $q = 1.602\cdot10^{-19}$ C, r_0 = [7, 0, 0] R_E and $v_0 = v$[sin(α_{eq})cos(ξ), sin(α_{eq})sin(ξ), cos(α_{eq})] R_E/s. v = 5 R_E/s and $\xi = \pi/2$. $\Delta\alpha_{eq}$ is in blue, minimum and maximum lines of best fit are black dashed lines and the average line of best fit is the black line.

Figure 6.16 shows that $\Delta\alpha_{eq}$ approaches 0 as α_{eq} approaches $\pi/2$. This is natural, since when $\alpha_{eq} = \pi/2$ the particles become restricted to the equatorial plane, and thus, their pitch angle cannot change. On the other hand, as α_0 approaches zero the frequency of the oscillation grows and the amplitude of the oscillations reaches the maximum. This corresponds to a value of 0.5445 rad as the line of best fit for peak data, represented by the black dashed line, is proportional to the quadratic $-0.2173\alpha_0^2 - 0.0457\alpha_0 + 0.5445$. To represent the minimum, we put a black dashed line along the 0 horizontal. To represent the average $\Delta\alpha_{eq}$ we fit a quadratic line to this data, shown in black in Figure 6.16. For this line of best fit we find that $\Delta\alpha_{eq} = -0.0396\alpha_0^2 - 0.1358\alpha_0 + 0.3167$.

We now analyze the $\Delta\mu/\mu_0$ as a function of our α_0, this is illustrated in Figure 6.17. Similar to Figure 6.16 the data oscillates, and the frequency of these oscillations increases as α_0 approaches zero. Due to the nature of the data, we plot it on a log-log scale, Similar to Section 6.6 there are some points where $\Delta\mu/\mu_0 \approx 0$, thus we add a line of best fit in black. The slope of this line is proportional to $\alpha_0^{-1.407}e^{-1.3814}$.

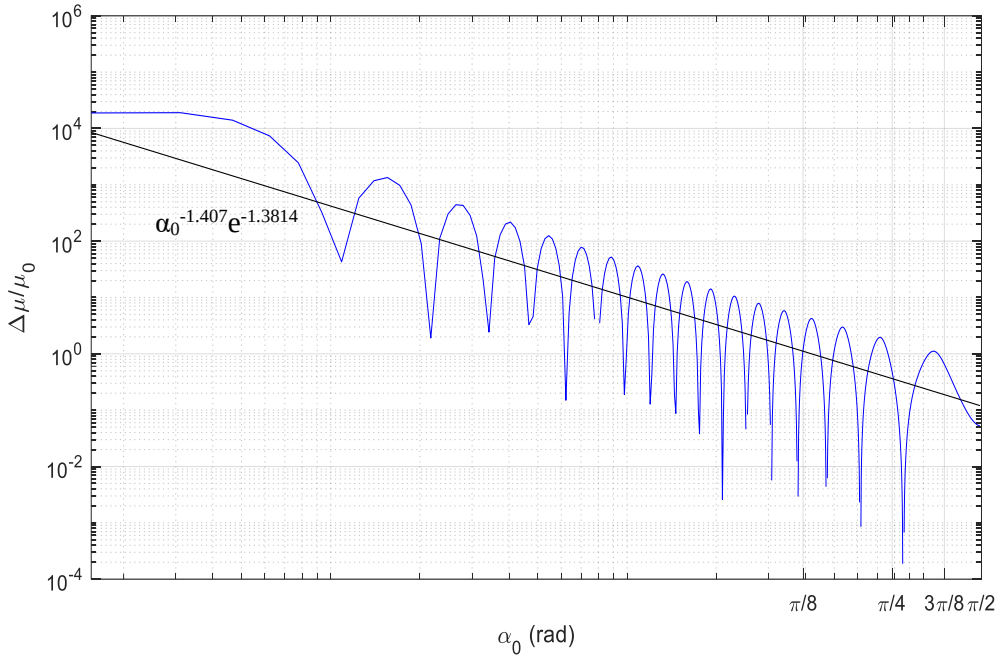

Figure 6.17: $\Delta\mu/\mu_0$ for 1000 pitch angles from $\alpha_0 = 0$ to 89°. Integrated for half a bounce period. The particle is initiated with $M = 3.1\cdot10^{-5}$ TR$_E^3$, $m_0 = 1.673\cdot10^{-27}$ kg, $q = 1.602\cdot10^{-19}$ C, $r_0 = [7, 0, 0]$ R$_E$ and $v_0 = v[\sin(\alpha_{eq})\cos(\xi), \sin(\alpha_{eq})\sin(\xi), \cos(\alpha_{eq})]$ R$_E$/s. $v = 5$ R$_E$/s and $\xi = \pi/2$. $\Delta\alpha_{eq}$ is in blue, minimum and maximum lines of best fit are black dashed lines and the average line of best fit is the black line.

From Section 6.6 we know that $\Delta\alpha_{eq}$ does not accumulate, but oscillates, between a range of α_{eq}, at least for relatively small velocities. To determine the range of oscillation in α_{eq} we remove our events functionality and graph the maximum $\Delta\alpha_{eq}$ for multiple equatorial crossing by using a specified integration time. We do not correct for the use of a higher velocity and simply use the same integration time = 332s/v from Section 6.6. Using a velocity of $v = 5$ R$_E$/s in this section results in an integration time of 66.4s. Overall, the results of this process are displayed in Figure 6.18.

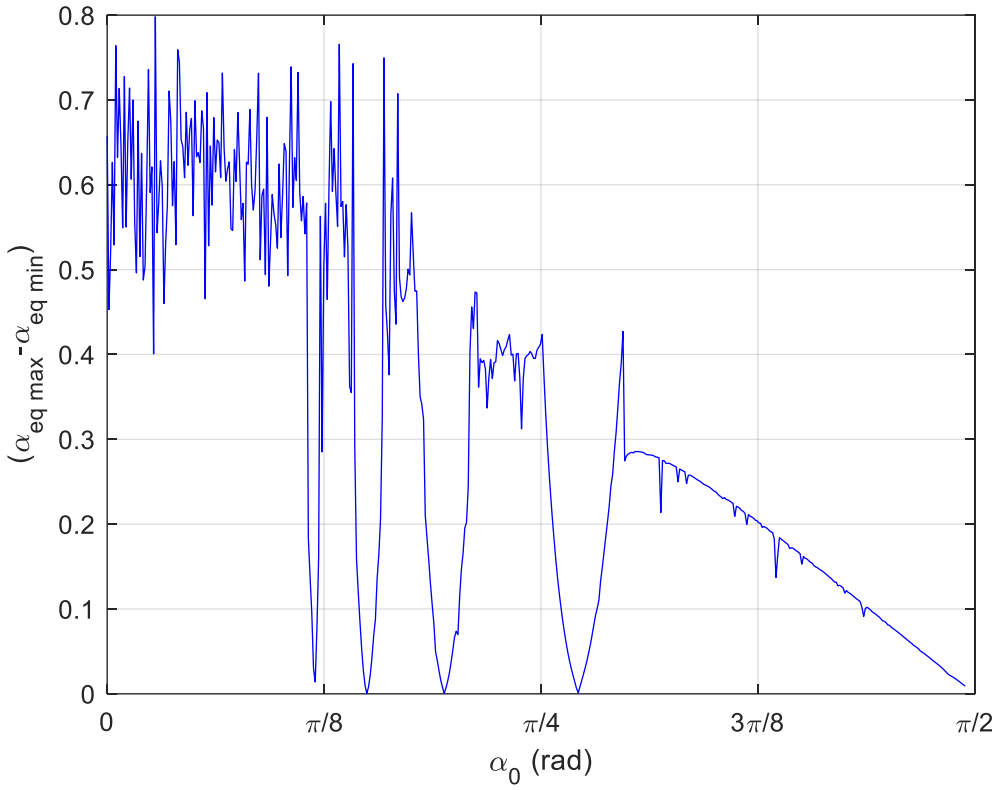

Figure 6.18: Maximum oscillation range of α_{eq} for 1000 pitch angles from α_0 = 0 to 89°. Integration time = 66.4s. The particle is initiated with $M = 3.1 \cdot 10^{-5}$ TR$_E^3$, $m_0 = 1.673 \cdot 10^{-27}$ kg, $q = 1.602 \cdot 10^{-19}$ C, r_0 = [7, 0, 0] R$_E$ and v_0 = v[sin(α_{eq})cos(ξ), sin(α_{eq})sin(ξ), cos(α_{eq})] R$_E$/s. v = 5 R$_E$/s and $\xi = \pi/2$.

In Figure 6.18 we show similar results to that of varying velocity from Figure 6.9, except that in this case the data is downward sloping. Like Figure 6.9 the downward deviations from the linear trend on the right side of Figure 6.18 correspond to the points where $\Delta\alpha_{eq} = 0$. These occurrences line up with our results from Figure 6.16 and Figure 6.17. Therefore, they are a result of the particle traversing a similar path between r_{min} and r_{max} every bounce. This was illustrated in Section 6.6 in Figure 6.12. Again, similarly to Figure 6.9, the upwards deviations in Figure 6.18 correspond to plasma particles that have a wide range of oscillation in α_{eq}. Due to this large oscillation range, small α_0, particularly those already close to the loss cone, have the ability to approach α_{lc}. This process was illustrated in Figure 6.11 where the complicated trajectory eventually reaches a loss cone angle purely based on statistical probability. This is an interesting result as we expect particles close to the loss cone approximation, in our case 0.04 rad, to be lost. However, Figure 6.18 clearly shows, at least for this velocity, that initial pitch angles as high as 0.5 rad also get lost after multiple bounce periods. Detailed analysis of these trajectories is left for future work. Overall, the results of varying α_0 produced results with similar patterns to varying velocity. Thus, we know that the maximum line of best fit from Figure 6.16 corresponds to the slope on the right end of Figure 6.18.

Having quantified the average variation in α_{eq} as a function of α_0 we now measure the numerical solution against the GC approximation for Equations for λ_m (6.14), T_b (6.10) and T_d

(6.12). We also set Matlab's events functionality back to half a bounce period to analyze these Equations. Similar to section 6.6 we calculate λ_m using Equation (6.14) and use our numerical results to determine B_{eq} and B_m. The result of this process is given in Figure 6.20 in blue. In red we use our value of α_0 for α_{eq} in Equation (6.14) to demonstrate GC theory. Lastly, we modify Equation (6.14) by using the average variation in α_{eq} from Figure 6.16. Since all data in Figure 6.16 is positive we add our average variation in α_{eq}. Thus we apply $\alpha_{eq} = \alpha_0 + (-0.0396\alpha_0^2 - 0.1358\alpha_0 + 0.3167)$ to Equation (6.14) to determine λ_m. The modified result is displayed in green in Figure 6.19 below.

Figure 6.19 shows that as α_0 increases the numerical results in blue approach the GC approximation in red, as to be expected. However, the red GC approximation fails to accurately model the numerical results throughout the range of α_0. This is especially true as α_0 approaches 0 since our results for the GC theory in red approach 1.3 rad or 75°. This latitude too high for dipole field line mapping, and is typically only reached In aurora precipitation which requires magnetic field line breaking and reconnection as discussed in the beginning of this chapter. Thus we show that the standard application GC theory does not produce logical result when attempting to estimate λ_m at low α_0. The green line shows a significant improvement when applying our correction factor to the GC theory. Overall, this illustrates that a more thorough statistical model could be developed to improve the approximation of λ_m when applying (6.14). This is left for future work.

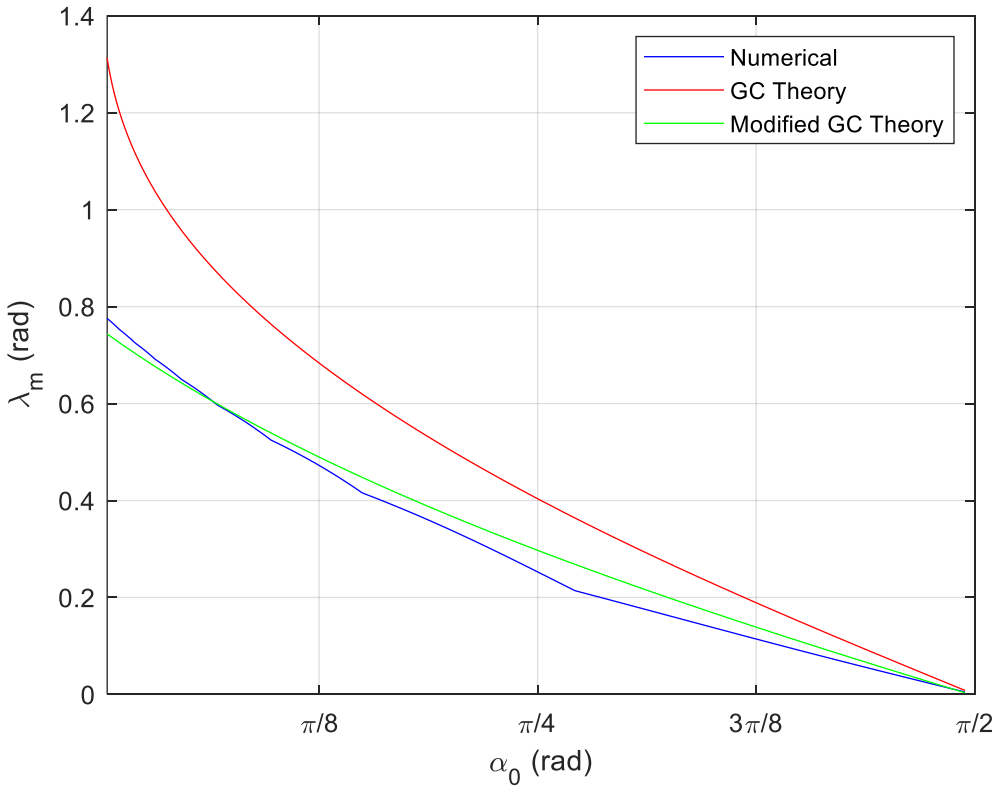

Figure 6.19: Calculation of λ_m using GC approximation for 1000 pitch angles from α_0 = 0 to 89°. The particle is initiated with $M = 3.1\cdot10^{-5}$ TR$_E^3$, $m_0 = 1.673\cdot10^{-27}$ kg, $q = 1.602\cdot10^{-19}$ C, r_0 = [7, 0, 0] R$_E$ and $v_0 = v$[sin(α_{eq})cos(ξ), sin(α_{eq})sin(ξ), cos(α_{eq})] R$_E$/s. v = 5 R$_E$/s and $\xi = \pi/2$. The numerical solution is in blue, GC theory is in red and our modification to GC theory is in green.

Lastly, we compare the GC approximation bounce and drift period Equations, (6.10) and (6.12) respectively, against our numerical calculations of the real trajectory. Again we express α_{eq} as a function of α_0 to account for average variation and apply this to the GC Equations. The calculation of the numerical bounce and drift period is the same discussed previously in section 6.6. With the numerical results in blue, the GC approximation in red and our modification of the GC approximation in green we generate Figure 6.20 and Figure 6.21 for the bounce and drift periods respectively.

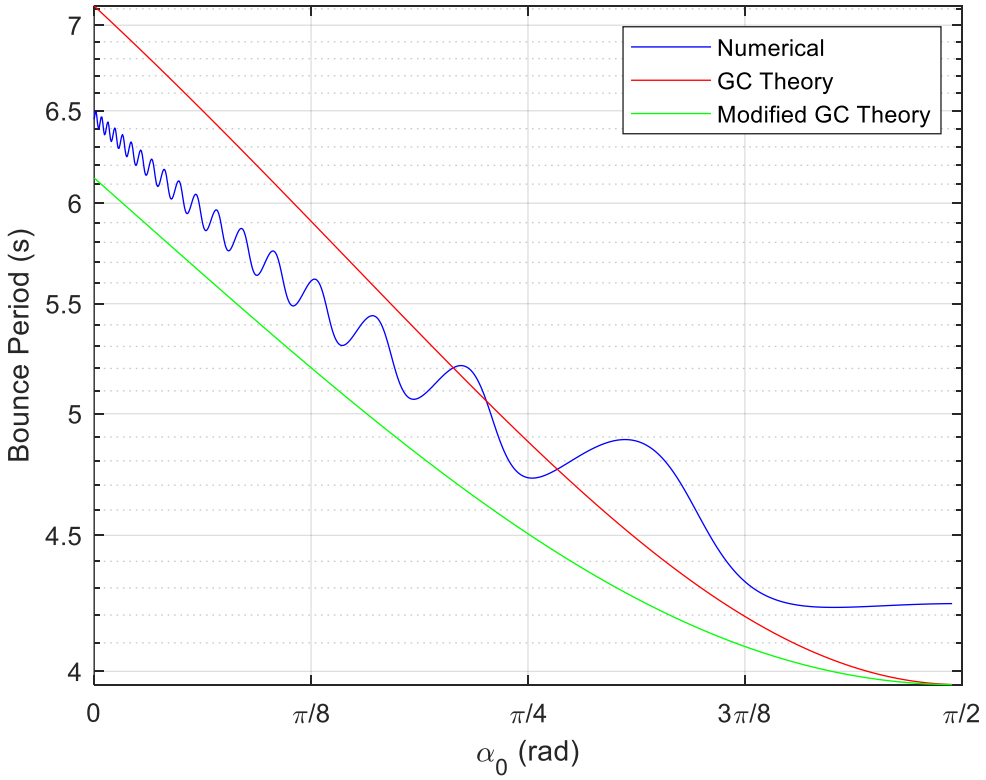

Figure 6.20: Calculation of T_b using GC approximation for 1000 pitch angles from α_0 = 0 to 89°. The particle is initiated with $M = 3.1\cdot10^{-5}$ TR$_E^3$, $m_0 = 1.673\cdot10^{-27}$ kg, $q = 1.602\cdot10^{-19}$ C, r_0 = [7, 0, 0] R$_E$ and $v_0 = v$[sin(α_{eq})cos(ξ), sin(α_{eq})sin(ξ), cos(α_{eq})] R$_E$/s. v = 5 R$_E$/s and $\xi = \pi/2$. The numerical solution is in blue, GC theory is in red and our modification to GC theory is in green.

For the bounce period Figure 6.20 clearly shows that our modification did not improve upon the GC approximation, though it is below the numerical results in blue by a consistent deviation across all α_0. In contrast, the discrepancy of the red curve grows for small pitch angles, but is more accurate for large pitch angles. Overall, the inaccuracy of both GC curves is attributed to a relatively high velocity. To quantify the difference in accuracy we sum the numerical data in blue and subtract the sum of both GC curves, to average the data, we then divide by our iterations. Across the entire range of α_0 we find that the GC approximation had a value of 0.08s and our modification to the GC expression had a value of 0.34s. The higher accuracy of the red curve is attributed to crossing the numerical results, while our modification did not.

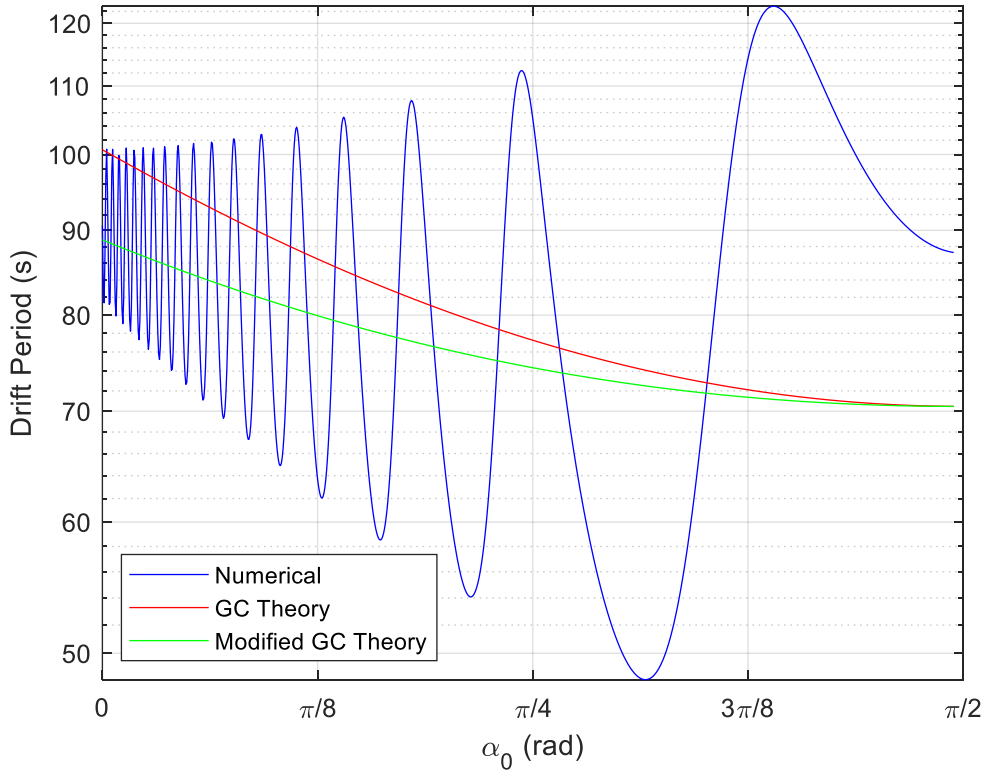

Figure 6.21: Calculation of T_d using GC approximation for 1000 pitch angles from α_0 = 0 to 89°. Integrated for half a bounce period. The particle is initiated with $M = 3.1 \cdot 10^{-5}$ TR$_E^3$, $m_0 = 1.673 \cdot 10^{-27}$ kg, $q = 1.602 \cdot 10^{-19}$ C, r_0 = [7, 0, 0] R$_E$ and $v_0 = v$[sin(α_{eq})cos(ξ), sin(α_{eq})sin(ξ), cos(α_{eq})] R$_E$/s. v = 5 R$_E$/s and $\xi = \pi/2$. The numerical solution is in blue, GC theory is in red and our modification to GC theory is in green.

For the drift period Figure 6.21 shows that our modification in green improved the GC approximation, as the curve is more centred around the numerical results. However, using our quantitative analysis conducted in Figure 6.20 we find the red curve to be more accurate. Across the entire range of α_0 we find that the GC approximation had a drift period error of 3.26s and our modified expression had a drift period error of 7.21s.

Overall, we have shown that α_{eq} does depend on α_0 and used the average rate of oscillation in α_{eq} to improve upon the GC approximations Equation for α_{eq}, while demonstrating the potential for improvement for T_b and T_d. Similar to the results for the varying velocity we found pitch angles that result in scattering into the loss and cone and initial pitch angles in which the conservation of α_{eq} is extremely consistent.

6.8 Analysis of Variations in Azimuthal Angle

In this section, we vary the azimuthal angle ξ while holding v and α_{eq} constant. They are assigned values of 5 R$_E$/s and $\pi/4$ respectively. All other initial variables are the same as in Figure 6.2. We choose v = 5 R$_E$/s for consistency with section 6.7. We choose $\alpha_{eq} = \pi/4$ for consistency with section 6.6, and because it is one of the lowest pitch angles that remains trapped for v = 5

R_E/s, as established in Figure 6.18. In regards to our azimuthal range, we use 1000 points between 0 and 2π for ξ. We start by analyzing our $\Delta\alpha_{eq}$ for our ξ range and display the results in Figure 6.22 for half a bounce period.

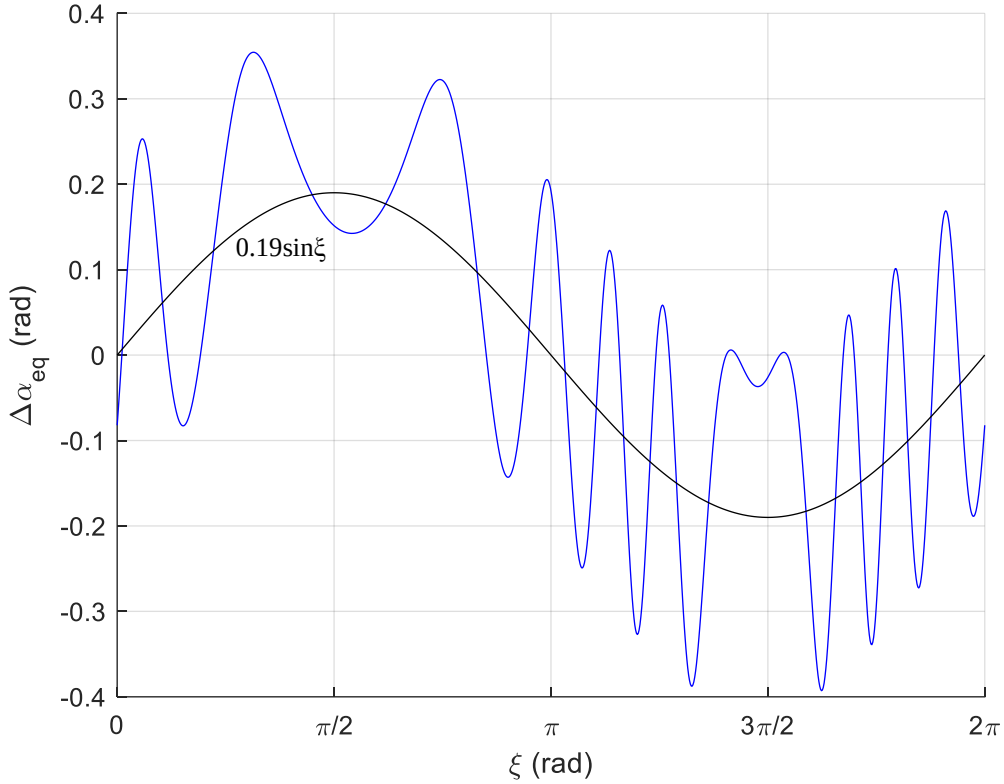

Figure 6.22: $\Delta\alpha_{eq}$ for 1000 azimuthal angles from ξ = 0 to 2π. Integrated for half a bounce period. The particle is initiated with $M = 3.1\cdot10^{-5}$ TR$_E^3$, $m_0 = 1.673\cdot10^{-27}$ kg, $q = 1.602\cdot10^{-19}$ C, r_0 = [7, 0, 0] R$_E$ and $v_0 = v$[sin(α_{eq})cos(ξ), sin(α_{eq})sin(ξ), cos(α_{eq})] R$_E$/s. v = 5 R$_E$/s and $\alpha_0 = \pi/2$. $\Delta\alpha_{eq}$ is in blue and the line of best fit is the black.

Figure 6.22 shows a clear dependence of $\Delta\alpha_{eq}$ on ξ. Naturally, the curve in Figure 6.22 is periodic as ξ changes from 0 to 2π. While there are numerous oscillations, the overall waveform seems to follow the form of a sine function. To confirm this trend, we plotted the same curve for v = 0.15 R$_E$/s and v = 1.5 R$_E$/s, again we find the overall waveform seems to follow the form of a sine function, as illustrated in Figure 6.23. The black line of best fit in Figure 6.22 shows that the average variation in $\Delta\alpha_{eq}$ = 0.19sin(ξ). This curve of best fit was determined using a least-squares method, with amplitude accuracy limited to two decimal points. Observing this we conclude that the maximum deviation of α_{eq} from its initial value after half-a-bounce bounce occurs around ξ = π/2 and ξ = 3π/2, when the velocity is initially directed in the φ direction. In contrast, the minimum deviation of α_{eq} occurs around ξ = 0 and π, when the velocity is initially directed in the radial direction. Lastly, we sum the data of the blue line and divide it by the number of iterations to determine if there is an average positive or negative result. The result is a value of 0.0277 rad. This indicates that the particle is slightly more likely to have α_{eq} increase after a half-bounce period which means that most particles at this velocity are scattered away from the loss cone

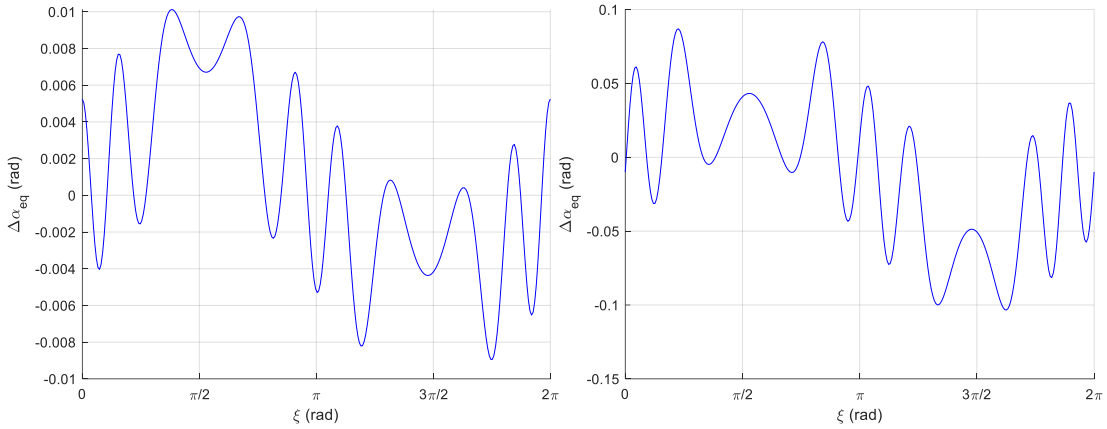

Figure 6.23: $\Delta\alpha_{eq}$ for 1000 azimuthal angles from $\xi = 0$ to 2π for $v =$ 0.15 R_E/s (left), 1.5 R_E/s (right). Integrated for half a bounce period. The particle is initiated with $M = 3.1\cdot10^{-5}$ TR_E^3, $m_0 = 1.673\cdot10^{-27}$ kg, $q = 1.602\cdot10^{-19}$ C, $r_0 = [7, 0, 0]$ R_E and $v_0 = v[\sin(\alpha_{eq})\cos(\xi), \sin(\alpha_{eq})\sin(\xi), \cos(\alpha_{eq})]$ R_E/s. $\alpha_0 = \pi/2$.

Next we analyze normalized $\Delta\mu$ as a function of ξ, the results are displayed in Figure 6.24 for half a bounce period.

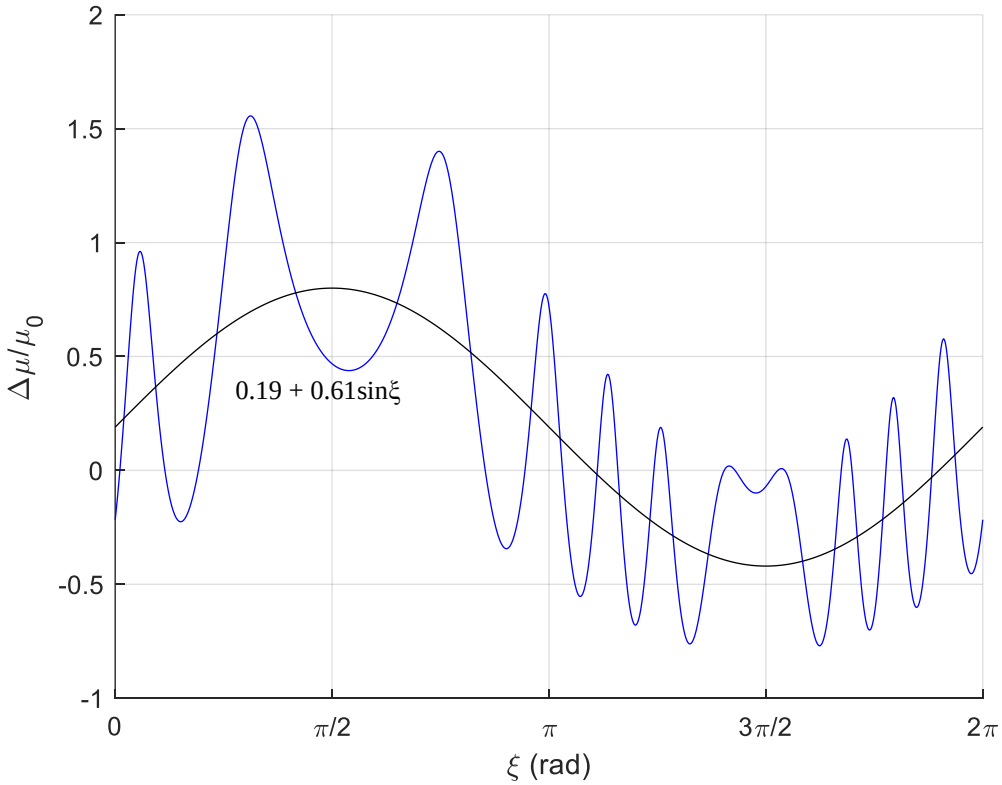

Figure 6.24: $\Delta\mu/\mu_0$ as for 1000 azimuthal angles from $\xi = 0$ to 2π. Integrated for half a bounce period. The particle is initiated with $M = 3.1\cdot10^{-5}$ TR_E^3, $m_0 = 1.673\cdot10^{-27}$ kg, $q = 1.602\cdot10^{-19}$ C, $r_0 = [7, 0, 0]$ R_E and $v_0 = v[\sin(\alpha_{eq})\cos(\xi), \sin(\alpha_{eq})\sin(\xi), \cos(\alpha_{eq})]$ R_E/s. $v = 5$ R_E/s and $\alpha_0 = \pi/2$. $\Delta\alpha_{eq}$ is in blue and the line of best fit is the black.

The curve in Figure 6.24 is similar to that in Figure 6.22. Using a least-squares method we determine the amplitude of a sine function to fit the data. In regards to the y shift of 0.19, this was determined by averaging the data in blue. We find the best approximation to be $0.19 + 0.61\sin(\xi)$, shown as a black line in Figure 6.24. Compared to Figure 6.24 the oscillations are shifted upwards. Thus, the particle is slightly more likely to have μ increase after a half-bounce period.

Similar to Figure 6.10 and Figure 6.18, from Sections 6.6 and 6.7 respectively, we attempted to analyze the maximum range of oscillation in α_{eq} for multiple bounce periods. However, due to the periodic nature of the azimuthal angle, the results were simply too noisy and did not provide relevant data.

We now plot the difference in our numerical solution vs the GC approximation for λ_m (6.14) T_b (6.10) and T_d (6.12). Again we modify our GC approximation to try and improve the results. However, unlike Sections 6.6 and 6.7, we do not have a graph of the maximum oscillation range in α_{eq} to validate that our average $\Delta\alpha_{eq}$ from Figure 6.22 should be applied. Instead, we note, that this is simply a trial to see if the GC approximation benefits from writing α_{eq} as a function of ξ. In addition, this is also done for consistency with previous Sections. Overall, we also apply $\alpha_{eq} = \alpha_0 + 0.19\sin(\xi)$ to Equation (6.14) to determine λ_m. The result of this process is given in Figure 6.25.

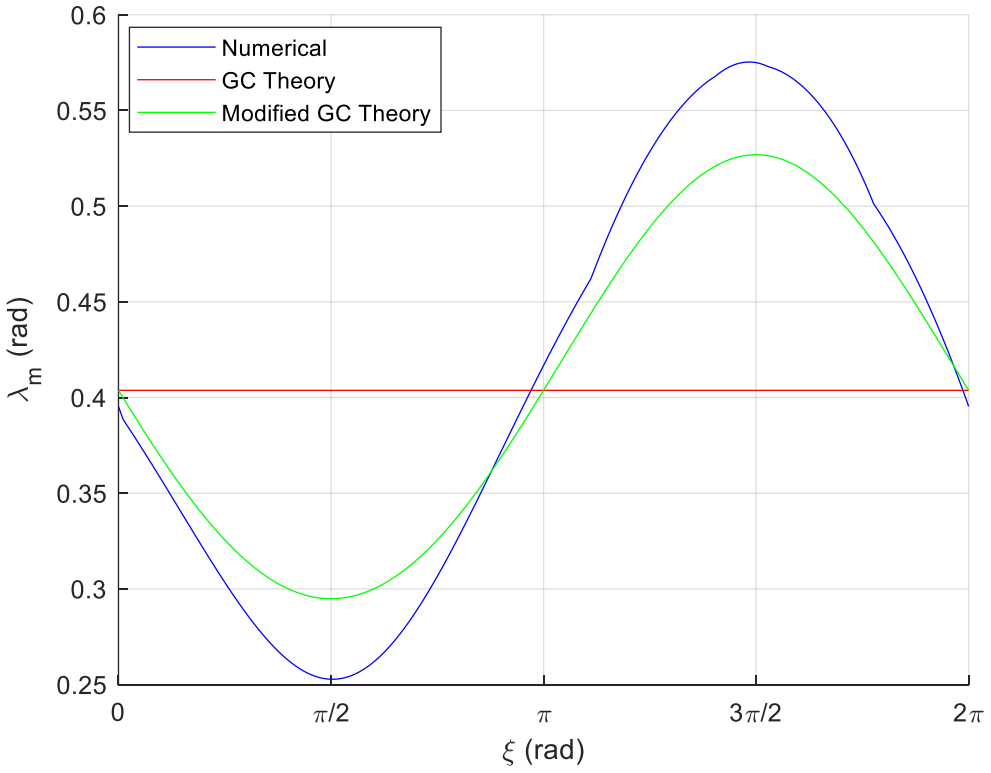

Figure 6.25: Calculation of λ_m using GC approximation for 1000 azimuthal angles from $\xi = 0$ to 2π. Integrated for half a bounce period. The particle is initiated with $M = 3.1\cdot10^{-5}\,TR_E^3$, $m_0 = 1.673\cdot10^{-27}$ kg, $q = 1.602\cdot10^{-19}$ C, $r_0 = [7, 0, 0]\,R_E$ and $v_0 = v[\sin(\alpha_{eq})\cos(\xi), \sin(\alpha_{eq})\sin(\xi), \cos(\alpha_{eq})]\,R_E/s$. $v = 5\,R_E/s$ and $\xi = \pi/2$. The numerical solution is in blue, GC theory is in red and our modification to GC theory is in green.

Figure 6.25 shows that the GC approximation in red does a fairly good job at averaging the changes that result from a periodic variation in λ_m. However, the modification to the GC approximation demonstrates a significant increase in predicting the numerical results of λ_m.

It should be noted here that the dependence of ξ on the GC Equation for the mirror point was studied in a paper by Porazik [39]**,** where they used the 2nd order Taylor expansion of μ, given by Equation (2.19), to formulate an expression for the loss cone Equation that depends on varying values of ξ and initial α_{eq}. For future work, this Equation could be modified to determine λ_m as a function of ξ, or used in combination with section 6.6 to include the velocity variable.

Lastly, we compare the GC approximation bounce and drift period Equations, (6.10) and (6.12) respectively, against our numerical calculations. Following the same procedure, we again modify Equations (6.10) and (6.12) by applying $\alpha_{eq} = \alpha_0 + 0.19\sin(\xi)$. The calculation of the numerical bounce and drift period is the same discussed previously in Section 6.6. Since T_b and T_d do not depend on ξ the result is a horizontal line. With the numerical results in blue, the conventional analytical expression in red and our modified analytical expression in green we generate Figure 6.26 and Figure 6.27 for the bounce and drift periods respectively.

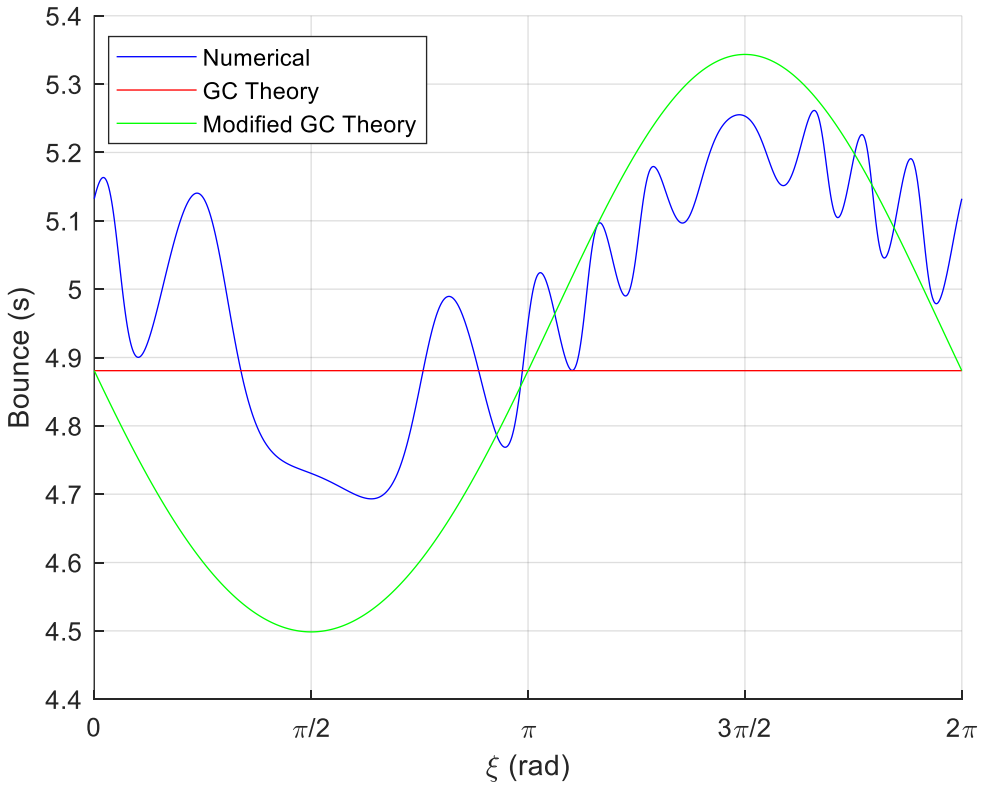

Figure 6.26: Calculation of T_b using GC approximation for 1000 azimuthal angles from $\xi = 0$ to 2π. Integrated for half a bounce period. The particle is initiated with $M = 3.1\cdot10^{-5}$ TR$_E^3$, $m_0 = 1.673\cdot10^{-27}$ kg, $q = 1.602\cdot10^{-19}$ C, $r_0 = [7, 0, 0]$ R$_E$ and $v_0 = v[\sin(\alpha_{eq})\cos(\xi), \sin(\alpha_{eq})\sin(\xi), \cos(\alpha_{eq})]$ R$_E$/s. $v = 5$ R$_E$/s and $\xi = \pi/2$. The numerical solution is in blue, GC theory is in red and our modification to GC theory is in green.

Figure 6.26 shows that variation in ξ does cause changes in the bounce period. However, the variation in the bounce period is rather small, on the order of 10^{-1}s. On average the GC solution in red is below the mean of the numerical oscillations. Again modifying the GC Equation with our sine function seems to have improved the approximation. To quantify the inaccuracy of both methods we average the difference in sums between the numerical data in blue and both GC approximations. For the red line, this results in a value of 0.116s, for the green curve this is 0.096s, thus validating the improvement of T_b when α_{eq} is made a function of ξ.

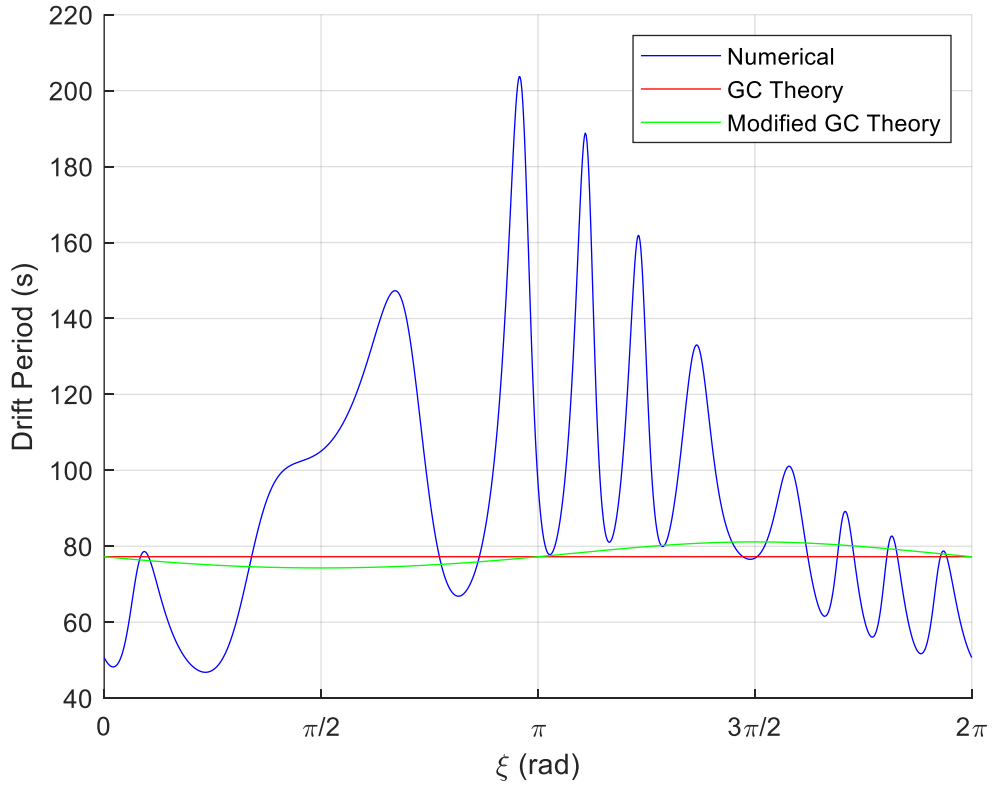

Figure 6.27: Calculation of T_d using GC approximation for 1000 pitch angles from α_0 = 0 to 89°. Integrated for half a bounce period. The particle is initiated with $M = 3.1\cdot10^{-5}$ TR$_E^3$, $m_0 = 1.673\cdot10^{-27}$ kg, $q = 1.602\cdot10^{-19}$ C, r_0 = [7, 0, 0] R$_E$ and $v_0 = v$[sin(α_{eq})cos(ξ), sin(α_{eq})sin(ξ), cos(α_{eq})] R$_E$/s. v = 5 R$_E$/s and $\xi = \pi/2$. The numerical solution is in blue, GC theory is in red and our modification to GC theory is in green.

Figure 6.27 shows the dependence of the drift period ξ. The drift period calculated numerically reaches a maximum around $\xi = \pi$ and a minimum at $\xi = 0$. The drift period given by (6.12) is, of course, independent of ξ. It is shown by the horizontal red line. In addition, our modification made a negligible difference in approximating the drift period. The results of the numerical solution are hypothesized to be based on the initial position of the particle and the charge. First, we know an ion gyrates counterclockwise with an initial B_z in the positive direction, which is the case here. With x_0 on the positive x-axis, the ion must initially gyrate into a positive y-position if the initial v is directed towards the origin, which it is with $\xi = \pi$. Thus this results in a small $\Delta\varphi$ over our half bounce period constriction, which in turn affects our drift period calculation, as $T_d = 2\pi/\Delta\varphi$.

Nothing in the GC approximation depends on the angle ξ, however, our calculations demonstrate that λ_m, T_b and T_d a do depend on the value of ξ. This clearly illustrates the approximate nature of the GC theory. While this dependence decreases with the particle velocity, it might have to be taken into account in some calculations

.

6.9 Conclusion

In this chapter, we analyzed the motion of plasma particles in a three-dimensional dipole. One of the main focuses of our study was to test the GC assumption that the equatorial pitch angle remains constant. Since the GC approximation is dependent on the conservation of the magnetic moment, which is also dependent on pitch angle, this is an important test of the GC accuracy. In our analysis, we found multiple ways in which α_{eq} deviates from the GC approximation. Under certain conditions, this resulted in particles diffusing into the loss cone, despite α_0 being far from the expected loss cone requirements. Using these deviations in α_{eq} we then illustrated the potential for improving the GC Equations for α_{eq} (6.14), T_b (6.10) and T_d (6.12). Much of this was left for future work, as though we covered a lot of ground, the results in this Chapter are only preliminary and require much more time to study in detail. Overall this analysis is relevant to understanding the characteristics of trapped radiation belt particles and the precipitation of loss cone particles into the ionosphere.

We began by deriving the particle's bounds of motion in an attempt to analyze an ensemble of particles that only differed in phase. Since phases are indistinguishable under GC theory this would allow for a more in-depth analysis. Unfortunately, the complexity of 3D motion only allowed for our radial constraints to be tight at the magnetic mirror point. This is in part attributable to the fact that no analytical solutions exist for particle motion in a 3D dipole. This resulted in a lack of enough independent Equations to constrain our system. For the same reason, we did not find a simple way to distribute particles between r_{min} and r_{max} so that they shared common parameters in everything but the initial phase. For example, two particles with the same bounds of motion end up having different initial pitch angles, which in turn results in two separate mirror points. After one reflection at a mirror point, the particles no longer move together and thus can not be used for phase analysis. As a way to address this issue, we introduced the azimuthal angle ξ to mimic differences in phases. Although the azimuthal angle is not exactly the phase angle, in the GC approximation it does not affect the location of the mirror point. Then we proceeded to analyze the parameters of v, α_{eq} and ξ separately. Thus we were able to form conclusions on the variation of one parameter at a time. This is a notable limitation in our analysis. In future work, a more in-depth analysis would compile the variation in these three parameters into unifying statistical or analytical expression to estimate the deviation of GC theory in regards to the conservation α_{eq}. Unfortunately, the time allotted to complete this Master's thesis does not allow for such time-consuming analysis.

For variations in velocity, we found that $\Delta\alpha_{eq}$ over a half bounce oscillated between 0 and a maximum amplitude which increased linearly with v, and thus so too did the average change in $\Delta\alpha_{eq}$. In addition, the frequency of these oscillations decreased with v. Similar results were found for the $\Delta\mu/\mu_0$, except the $\Delta\mu/\mu_0$ increased quadratically with v. We also observed that there are some particular velocities for which $\Delta\alpha_{eq} = 0$ and we found that these particles conserve their α_{eq} extremely well, even over multiple bounce periods, and thus could make up a disproportionate percent of trapped radiation belt particles under some conditions. For all other particles, we found

that the $\Delta\alpha_{eq}$ oscillated between a maximum range over multiple bounces, up until a velocity threshold of $v \approx 7$ R_E/s where a transition to chaos trajectoies occurred. Below this threshold, the maximum range of oscillation over multiple bounce periods corresponded to the maximum range in $\Delta\alpha_{eq}$ over a half bounce period. Indicating that the oscillation of α_{eq} between the minimum and maximum values is not always gradual, as some particles, some of the time, make the maximum $\Delta\alpha_{eq}$ in a single equatorial crossing. Above a velocity threshold of $v \approx 7$ R_E/s we found that the maximum $\Delta\alpha_{eq}$ increases with time and thus it is only a matter of time before these high-energy particles diffuse into the loss cone. Lastly, using the GC approximations for λ_m, T_b and T_g we showed that the numerical results deviate from GC approximation, especially λ_m. In an attempt to improve these results we used the average change in $\Delta\alpha_{eq}$ to demonstrate that GC theory can be more accurate if α_{eq} is written as a function of v, and not assumed as a constant.

When analyzing the dependence of variation in α_{eq} on the pitch angle itself we found very similar results to the ones found in our variation in the velocity section. For example, we found that, over multiple bounce periods, relatively small values in α_0 resulted in the maximum $\Delta\alpha_{eq}$ increasing with time, while values of α_0 approaching $\pi/2$ were accurately modelled by our maximum line of best fit from our $\Delta\alpha_{eq}$ over a half bounce. This is inverse to our velocity results because the GC approximation converges towards our numerical results as v is decreased or when α_0 is increased, as the particle approaches equatorial mirroring. We also found points within our α_0 range for which $\Delta\alpha_{eq} = 0$ holds, resulting in particles conserving their α_{eq} extremely well, even over multiple bounce periods. The line of best fit for $\Delta\alpha_{eq}$ as a function of α_0 over a half bounce period was proportionate to a parabolic function. However, this parabolic line was relatively lat and thus was not a huge deviation from a linear line of best fit. Using this average line of best fit for $\Delta\alpha_{eq}$, as a function of α_0, we were again able to demonstrate that the GC approximations for λ_m, T_b and T_g have the potential to be improved upon. In addition, we also highlighted the deviation of the GC approximation from numerical results. Illustrating that underlying assumptions in GC theory, at times, do not reproduce accurate approximation, especially at relatively low values of α_0.

For variations in the azimuthal angle, ξ, we found that the average change in $\Delta\alpha_{eq}$ was similar to a sine function. Using the Equation for our curve of the best fit we analyzed the GC approximations for λ_m, T_b and T_g. Unlike variations in velocity and initial pitch, these Equations are not functions of ξ. This is because the GC approximation assumes phases are indistinguishable, though ξ does not represent phase directly, it is our proxy for it. Through our analysis we found that λ_m, T_b and T_g do change as a function of ξ, and thus this illustrates a limitation of GC theory. Lastly, we made the GC approximation a function of ξ by applying our average change in $\Delta\alpha_{eq}$. This resulted in significant improvement in the approximation of λ_m and T_b, however, this did not affect the results for T_g in any significant way.

7. Summary

In this thesis we investigated the limits of the GC approximation. To this end we compared particle trajectories with the GC approximation in various magnetic fields and analyzed the dependence of various parameters, such as the particle speed, direction of the velocity and pitch angle. We also studied various strategies for selecting the initial position for the GC depending on the initial particle position and velocity exclusively. Whenever possible, we used analytical results applicable to motion in different fields.

We started with the examination of GC initialization options and GC approximation accuracy for high-energy particles moving in a magnetic field with a constant gradient in the x-direction. Although this is a very simple field, it can be used to locally approximate any two-dimensional magnetic field.

We sought a GC initialization method which relied solely on the initial position and velocity vectors of the particle. This is advantageous as it does not rely on using analytical results that are only available for specific magnetic fields or numerically tracing a particle over at least one gyroperiod. The simplest method is to just use the particle's position as the starting point for GC integration. However, this is the least accurate method and our calculations show that the error, in this case, is proportional to v^3. A better, commonly used option is to start the GC integration at the location of the gyroradius calculated by using the magnetic field at the position of the particle. This approach results in the error being proportional to v^4. We attempted to improve the accuracy further by introducing iterations to our calculation of the gyrocenter position. This reduced the error further by a factor of 17, although it did not change the scaling of the error with v.

For the magnetic field with a constant gradient there were exact solutions, which were used to find the exact locations where the expressions for the magnetic moment, gyroperiod and drift velocity became exact. It was found that these three x-positions shared no overlap for a range of velocities, except for their convergence towards each other at low velocities. Thus only one of the magnetic moment, gyroperiod or drift velocity can be evaluated exactly when applying GC at high velocities. Since the typical application of the GC approximation focuses on the transport of the particles the drift velocity may be considered the most desirable GC starting point in most applications.

A crucial aspect of the GC theory is the conservation of the magnetic moment. For the magnetic field with a constant gradient an exact expression for the first adiabatic invariant is available, however, most practical calculations use the approximation of $\mu_0 = mv_\perp^2/B$, which is just the first term in a Taylor series expansion of the exact expression. Thus, we analyzed different strategies for evaluating the magnetic moment for this field as well. Of course, using μ_0 with the magnetic field evaluated at the particle position is the least accurate, with the error being proportional to v^3. This is improved if the expression for μ_0 is evaluated using a magnetic field at either the 1st gyrocenter or the converged gyrocenter. The scaling of the error in both of these cases was v^4. Another possibility is to use the expression for the second-order Taylor series expansion. This gave an error proportional to v^4 and v^5 when evaluating B at the converged gyrocenter and particle position respectively. Comparing the results on a log plot it was found that the application of μ_0 at the converged gyrocenter is the most accurate method of calculating the magnetic moment at or above a velocity of roughly 6.5. For velocities less than 6.5 the application of the Taylor series

expansion using B at the particle trajectory was the most accurate.

In Chapter 4 we examined GC initialization options and GC approximation accuracy for high energy particles in the equatorial plane of a magnetic dipole. Similar to Chapter 3 we relied on magnetic field symmetry to determine particle trajectory bounds. The results of Chapter 4 apply to modelling high-energy particles in the inner magnetosphere of Earth, such as inner Van Allen Belt particles.

Similar to Chapter 3 we investigated different options for initializing GC in the equatorial plane of a magnetic dipole. The results were similar to those of Chapter 3 as well, initializing the GC calculation at the position of the particle gave an error proportional to v^3, while the first approximation to the gyrocenter resulted in the error proportional to v^4. Using iterations to improve the estimation of the gyrocenter reduced the error by a factor of 3 for most velocities, but did not change its scaling with v. Based on the agreement between the two different fields we believe this scaling with v to be universal. One difference between the two Chapters is that the gyrocenter iterations diverged for sufficient high v in the equatorial plane of a magnetic dipole. At sufficiently large velocities approaching the divergence threshold we found the 1st gyrocenter to have smaller errors than the converged gyrocenter.

In the equatorial plane of a magnetic dipole there also exist exact analytical expressions for the magnetic moment, gyroperiod and drift period. Similar to Chapter 3 we used these exact formulations with the actual magnetic moment, gyroperiod and drift period to determine an initial radial position that corresponded to these exact solutions. It was found that these three radial positions shared no overlap for a range of velocities, except for their convergence at low velocities. Thus only one of the magnetic moment, gyroperiod or drift period can be conserved exactly when applying GC approximation at high velocities.

Overall the GC initialization results of Chapters 3 and 4 allow us to envision GC initialization, dependent only on the initial position and velocity vectors, to be conducted as follows. First, one needs to determine ∇B for a given magnetic field, which is required for GC formalism anyway. Second, one needs to initialize a plasma particle using either (3.28) or (4.22), as the accurate reproduction of drift velocity or period is usually preferred. Overall this procedure accounts for both the magnetic field strength and its gradient in GC initialization, and is expected to work well for general magnetic fields This hypothesis should be verified for a variety of fields by future work.

The existence of the exact expression for the magnetic moment also allowed us to measure the accuracy of the GC approximation in the equatorial plane of a dipole. The results were generally similar to those of Chapter 3, except for the different scaling of the errors when using the Taylor series expansion form of μ. Evaluating B at the converged gyrocenter and particle trajectory resulted in the errors proportionate to v^3 and v^4 respectively, one less than they were for the magnetic field with a constant gradient. We believe that this is due to the field of Chapter 3 being too simple, some terms in the expansion are likely to equal zero, which affects the scaling. Thus, the scaling of the errors obtained in Chapter 4 is believed to be more general. In Chapter 4 evaluating μ_0 at the converged gyrocenter was found to have the least error across the entire velocity range examined.

In Chapters 3 and 4 the background magnetic field had symmetry and therefore the canonical momentum of the particle was conserved. This conservation law allowed us to derive

the limits of particle motion analytically. In general, most magnetic fields do not have symmetry. Therefore, we introduce some asymmetry to the equatorial field of a magnetic dipole in Chapter 5. This asymmetry mimics the stretching of the magnetosphere on the nightside. On the dayside the magnetic field in our model remains dipolar, this allowed us to use the exact expressions for the canonical momentum and adiabatic invariant in this region. We considered three different models of the magnetotail to illustrate the effects of the magnetic gradient steepness. Two of these magnetotails had smooth variations in the magnetic field strength as a function of position, while the other magnetotail was modelled by a piece-wise linear function. These magnetotail models allowed us to illustrate the effects of the magnetic gradient on particle motion.

In Chapter 5 we focus on the changes in the canonical momentum and the adiabatic invariant as the particle passes through the magnetotail region. Here it was found that the initial and final values for both P_φ and μ_{Exact} remain approximately the same after crossing the magnetotail. For the adiabatic invariant this behaviour is expected due to the dawn-dusk symmetry of the magnetic field. However, this is a significant result for P_φ, as the only expectation for the canonical momentum is that it will return to a constant value in the dipolar region. Measuring the difference between the final and initial values of P_φ and μ_{Exact} allowed us to quantify the secular error the GC approximation accumulates every drift. The ΔP_φ and $\Delta\mu_{Exact}$ were calculated for a range of initial phases and velocities. For a smooth variation of the magnetic field, we found that the change in the canonical momentum and the adiabatic invariant was an exponentially small function of the velocity. For our magnetotail with piecewise linear variations, it was found that secular error was proportional to v^3. Such radical difference in the level of conservation of the adiabatic invariants is not surprising, it is well known that the level of their conservation depends on whether the variation of external parameters is smooth or not. Similar effects for the canonical momentum were found, it seems that this is a new discovery and is therefore of considerable theoretical interest.

This research may provide the foundation for future theoretical studies in the area of classical mechanics as well as plasma physics. In addition to small secular changes in P_φ and μ_{Exact}, we also observed similar small changes in the average position of the particle after crossing the magnetotail, this results in a radial drift. In GC theory inward drift is often equivalent to an energy gain, with outward drift being equivalent to an energy loss. However, we know that because magnetic fields can not do work on a particle that this is not the case. These small secular changes can, most likely, be statistically modelled as diffusion. Thus, this aspect of our study indicates yet another way in which the GC approximation breaks down.

For this equatorial non-axisymmetric magnetic field we generated an ensemble of particles which differ only in their initial phase. These particles share identical values for all other parameters, such as the particle's energy, canonical momentum, magnetic moment and the ranges of motion. The analysis of phase dependence clearly illustrates deviations from the GC approximation, as the GC approximation assumes all phases are collapsed onto the GC, and thus are indistinguishable.

In Chapter 6 we considered motion in a three-dimensional dipole. The problem, in this case, becomes considerably more complicated than the 2D motion studied up to this point. First of all, no analytical solutions exist in three dimensions. Even more importantly, the size of the parameter space increases, as we need to analyze the dependence on the pitch angle as well. Although our simulations covered a lot of ground, the results in this Chapter are only preliminary and require much more time to study in detail. We found multiple deviations from the standard GC

theory and illustrated them as a function of the initial particle speed, equatorial pitch angle and the azimuthal angle, which plays the role of the initial phase in 3D. These deviations from the GC theory included variations in the equatorial pitch angle between consecutive bounces of a particle and associated variations in the mirror point positions. In some cases, these variations were substantial enough for a particle to 'diffuse' into the loss cone. Such results have applications to the dynamics of the radiation belt particles and their precipitation into the ionosphere. In some cases the dynamics of particles in the dipole magnetic field appear to be chaotic which also requires more detailed investigation in the future. Deviations for the bounce and drift periods from their standard GC calculations were also demonstrated. Of course, all the violations of the GC theory approach zero as the velocity of the particles becomes small. Future work in this area would focus on quantifying the GC inaccuracies better for all possible combinations of the particle's initial velocity, equatorial pitch angle, azimuthal angle and position. Lastly, we attempted to improve upon the GC approximations of λ_m, T_b, and T_g by including the average $\Delta\alpha_{eq}$ as a function of velocity, initial pitch and the azimuthal angle separately. In many cases, this showed significant improvement and thus we believe corrections could be developed to further improve the GC approximation by conglomerating the patterns in α_{eq} oscillations found in this paper.

8. References

[1] Baumjohann W. and Treumann R. *Basic Space Plasma Physics*, Imperial College Press. 1997, p. 1-328.

[2] Thomas D.K. *The Van Allen Radiation Belts*. University of London. 1961, p. 1-344.

[3] Goebel D. and Katz I. *Fundamentals of Electric Propulsion: Ion and Hall Thrusters*. Jet Propulsion Laboratory California Institute of Technology. 2008, p. 37-89.

[4] Yu J., Li L.Y., Cao J. B., Reeves G.D., Baker H.N. and Spence H. *The influences of solar wind pressure and interplanetary magnetic field on global magnetic field and outer radiation belt electrons*. Geophysical Research Letters: Space Physics 43(14), 7319-7327 (2016); https://doi.org/10.1002/2016GL069029

[5] Landau L.D. and Lifshitz E.M. *Mechanics: Course of Theoretical Physics.* Butterworth-Heinemann. 1976 p. 1-167.

[6] Zeng F., Kabin K. and Wang X. *et al*. *Epicycloid fits to trajectories of particles confined to the equatorial plane of a magnetic dipole*. Physics of Plasmas 28, 102505 (2021); https://doi.org/10.1063/5.0054393

[7] B.J. Anderson, R.B. Decker, N.P. Paschalidis and T. Sarris. *Onset of nonadiabatic particle motion in the near-Earth*. Journal of Geophysical Research 102, 17,553-17,569 (1997); 0148-0227/97/97JA-00798509.00

[8] Northrop T.G. *The Adiabatic Motion of Charged Particles*. Interscience Publishers. 1963, p.1-109.

[9] Konstantinidis K. and Sarris T. *Calculations of the integral invariant coordinates I and L* in the magnetosphere and mapping of the regions where I is conserved, using a particle tracer (ptr3D v2.0), LANL*, SPENVIS, and IRBEM*. Geoscientific Model Development 8(9), 2967–2975 (2015); https://doi.org/10.5194/gmd-8-2967-2015

[10] Kabin K. *Two examples of exact calculations of the adiabatic invariant for charged particle motion in non-uniform axisymmetric magnetic fields*. Physics of Plasmas 26, 012114 (2019); https://doi.org/10.1063/1.5054594

[11] Kabin K. *Adiabatic invariant of a charged particle moving in a magnetic field with a constant gradient*. Physics of Plasmas 28, 122101 (2021); https://doi.org/10.1063/5.0063755

[12] Gardner C.S. *Magnetic Moment to Second Order for Axisymmetric Static Field*. The Physics of Fluids 9, 1997 (1966); https://doi.org/10.1063/1.1761557

[13] La Rocca M. *Advanced Algorithms and Data Structures*. Manning Publications. 2021, p. 1-768

[14] Siambis J. and Northrop T. *Magnetic Field Geometry and the Adiabatic Invariants of Particle Motion*. Physic of Fluids 9, 2001 (1966); https://doi.org/10.1063/1.1761558

[15] Northrop T.G., Liu C.S. and Kruskal M.D. *First Correction to the Second Adiabatic Invariant of Charged-Particle Motion*. Physic of Fluids 9, 1503 (1966); https://doi.org/10.1063/1.1761885

[16] Northrop T.G. and Teller E. *Stability of the Adiabatic Motion of Charged Particles in the Earth's Field*. Physical Review 117(1), 215 (1960); https://link.aps.org/doi/10.1103/PhysRev.117.215

[17] Shampine L. and Reichelt M. *The Matlab ODE Suite*. SIAM Journal on Scientific Computing, 18, 1-35 (1997); 10.1137/S1064827594276424

[18] Prasolov V. and Solovyev Y. *Elliptic Functions and Elliptic Integrals*. American Mathematical Society. 1997, p. 1-198.

[19] Brizard A.J. *On the validity of the guiding-center approximation in the presence of strong magnetic gradients*. Physics of Plasmas 24, 042115 (2017); https://doi.org/10.1063/1.4981217

[20] Seymour P. W. *Drift of a Charged Particle in a Magnetic Field of Constant Gradient*.

[21] Bruce J.W. and Giblin P.J. *Curves and Singularities*. Cambridge University Press. 1984, p. 1-235.

[22] Kabin K., Kalugin K., Spanswick E. and Donovan E. *Threshold speed for two-dimensional confinement of charged particles in certain axisymmetric magnetic fields*. Canadian Journal of Physics, 96, 519–523 (2018); http://dx.doi.org/10.1139/cjp-2017-0415

[23] Kabin K., Kalugin G., Donovan E. and Spanswick E. *Particle Energization by Sunstorm Dipolarization*. Journal of Geophysical Research: Space Physics 122, 349-367 (2017); doi:10.1002/2016JA023459.

[24] Li X., Baker D. N., Temerin M., Reeves G. D. and Belian R. D. *Simulation of dispersionless injections and drift echoes of energetic electrons associated with substorms*. Geophysical Research Letters 25(20), 3763– 3766 (1998).

[25] Li X., Sarris T. E., Baker D. N., Peterson W. K. and Singer H. J. *Simulation of energetic particle injections associated with a substorm*. Geophysical Research Letters 30(1), 1004 (2003); doi:10.1029/2002GL015967.

[26] Sarris T. and Li X. *Evolution of the dispersionless injection boundary associated with substorms*. Annals Geophysics 23, 877– 884 (2005).

[27] Sarris T. E., Li X., Tsaggas N. and Paschalidis N. *Modeling energetic particle injections in dynamic pulse fields with varying propagation speeds*. Journal of Geophysical Research 107(A3), 1033 (2002); doi:10.1029/2001JA900166.

[28] Avrett E.H. *Particle Motion in the Equatorial Plane of a Dipole Magnetic* Field. Journal of Geophysical Research 67(1), 53-58 (1962).

[29] Juarez, A.R. *Periods of Motion in Periodic Orbits in the Equatorial Plane of a Magnetic Dipole*. Physical Review 75(1), 137-139 (1949)

[30] Brizard A.J and Markowski D.G. *On the validity of the guiding-center approximation in a magnetic dipole field*. Physics of Plasmas, 1-11 (2022); https://doi.org/10.48550/arXiv.2111.05353

[31] Dorman L. *Cosmic Rays in Magnetospheres of the Earth and other Planets*. Springer. 2009, p. 1-358.

[32] Kabin K., Spanswick E., Rankin R, Donovan E. and Samson J. C. *Modeling the relationship between substorm dipolarization and dispersionless injection*. Journal of Geophysical Research 116, A04201 (2011); doi:10.1029/2010JA015736

[33] Liang J., Shen Y., Knudsen D., Spanswick E., Burchill J. and Donovan E. *e-POP and Red Line Optical Observations of Alfvénic Auroras*. JPR Space Physics 124(6), 4672-4696 (2019); https://doi.org/10.1029/2019JA026679

[34] Littlewood J.E. *Lorentz's Pendulum Problem*. Annals of Physics 21, 233-249 (1963); http://dx.doi.org/10.1016/0003-4916(63)90107-6

[35] Chandrasekhar S. *Plasma Physics: a course given at the University of Chicago.* University of Chicago Press. 1960, p. 1-217.

[36] Gombosi T.I. *Physics of the Space Environment*. Cambridge University Press. 2004, p. 1-357.

[37] Walt M. *Introduction to Geomagnetically Trapped Radiation*. Cambridge University Press. 2005, p. 1-192.

[38] Konskinen H. and Kilpua E. *Physics of Earth's radiant belts*. Springer. 2022, p. 1-271.

[39] Porazik P., Johnson J.R., Kaganovivh I. and Sanchez E. *Modification of the Loss Cone for Energetic Particles*. Geophysical Research Letters 41, 8107–8113 (2014); doi:10.1002/2014GL061869.

[40] Schulz M. and Lanzerotti L.J. *Particle Diffusion in the Radiation Belts: Pitch-Angle Diffusion*. Physics and Chemistry in Space 7. 46-80 (1974) https://doi.org/10.1007/978-3-642-65675-0_3

[41] Mcllwainian C.E. *Coordinates for mapping the distribution of magnetically trapped particles*. Journal of Geophysical Research 66(11), 3681-3691 (1961); https://doi.org/10.1029/JZ066i011p03681

[42] Xie Y. and Liu S. *From period to quasiperiod to chaos: A continuous spectrum of orbits of charged particles trapped in a dipole magnetic field*. Chaos 30, 123108 (2020); https://doi.org/10.1063/5.0028644

[43] De Alcantara Bonfim O.F., Griffiths D.J. and Hinkley S. *Chaotic and Hyperchaotic Motion of a charged particle in a Magnetic Dipole Field*. International Journal of Bifurcation and Chaos 10(1), 265-271 (2000); https://doi.org/10.1063/5.0028644

[44] Soni P.K., Kakad B. and Kakad A. *L-shell and energy dependence of magnetic mirror point of charged particles trapped in Earth's magnetosphere*. Earth Planets Space 72, 129 (2020); https://doi.org/10.1186/s40623-020-01264-5

9. Appendix: Matlab Code

https://github.com/mathew-staikos/A-Comparison-of-Lorentz-Trajectories-with-the-Guiding-Center-Approximation-for-High-Energy-Particles.git